Data Mining to Constrain New Physics in the Top Sector

Stephen Edward Brown

Supervised by Dr. David J. Miller and Dr. Andy Buckley

Submitted in fulfilment of the requirements for the degree of
Doctor of Philosophy

April 2025

School of Physics and Astronomy
College of Science and Engineering
University of Glasgow

Abstract

We explore the Standard Model Effective Field Theory as a (mostly) model agnostic route to obtaining data–driven limits on new physics. After briefly covering some foundational concepts, we introduce a modular and extensible framework that enables data acquisition, analysis, and the fitting of EFT operators to experimental data from particle colliders. A global fit to top quark data is then performed, finding good agreement with the Standard Model in most cases, and competitive results compared to a contemporaneous study. We then investigate, through the lens of top partial compositeness and anomalous weak top quark couplings, the expected limiting factors for both HL–LHC and FCC–hh. We find the key factors in sensitivity in these scenarios to be theoretical uncertainties. We lastly explore the use of graph neural networks to boost sensitivity to EFT contributions, via what amounts to non–rectangular phase space cuts based on model classification, finding significant improvements to be possible in both individual and profiled constraints.

Declaration of originality

This thesis is my own work, except where explicit attribution to others is made. Chapters 5 to 7 are based on the following publications:

Chapter 5:

S. Brown et al., "*TopFitter: Fitting top-quark Wilson Coefficients to Run II data*", PoS **ICHEP2018**, 293 (2019), arXiv:1901.03164 [hep-ph]

S. Brown et al., "*New results from TopFitter*", PoS **ICHEP2020**, 322 (2021)

Chapter 6:

S. Brown et al., "*Electroweak top couplings, partial compositeness, and top partner searches*", Phys. Rev. D **102**, 075021 (2020), arXiv:2006.09112 [hep-ph]

Chapter 7:

O. Atkinson et al., "*Improved constraints on effective top quark interactions using edge convolution networks*", JHEP **04**, 137 (2022), arXiv:2111.01838 [hep-ph]

The calculations and tables presented in Appendix A are the results of work carried out by Dr. Peter Galler [5].

Acknowledgments

I'd firstly like to express my deepest gratitude to my supervisor, David Miller, for his support, encouragement, and trust. His willingness to allow the space to fail, learn, and grow whilst providing just–out–of–sight guardrails did not go unnoticed; I learned a lot *from* him, but even more *because of* him.

The PPT group at Glasgow is a truly special place that I'm lucky to have known; I'd like to thank David, Christine Davies, Christoph Englert, and Chris Bouchard for fostering and maintaining such a people–first and curiosity–led environment.

Thanks also to Andy Buckley for his guidance and incredibly welcoming nature, as well as Peter Galler — my closest collaborator for the work herein — who is an excellent, knowledgeable, and infectiously enthusiastic colleague.

Dan[1], Dan, Will, Euan, and Panos — I'm genuinely lucky to have met each of you. Although scattered across continents, "we'll always have ~~Paris~~ Room 526".

I'd like to thank my parents, Eddie and Frances, for their endless love, patience, and inexplicable trust that I'd (eventually) find my own way. A job well done, I'd say.

Finally, in an emotional sense, embarking on a PhD was far from a solitary endeavour. Linsay, thank you for being there. This thesis wouldn't exist if not for you.

Epigraphs

The quotations at the beginning of Chapters 1–4 are from the following sources:

Chapter 1: S. Weinberg, *Scientist: Four Golden Lessons*, Nature (2003)

Chapter 2: K. Popper, *The Open Universe: An Argument for Indeterminism* (1992)

Chapter 3: T. Van Sant quoting R.P. Feynman, *No Ordinary Genius*, BBC (1993)

Chapter 4: P. Ginsparg quoting K.G. Wilson, *Renormalized After-Dinner Anecdotes*, Journal of Statistical Physics (2014)

[1] You're both first.

"I believe," he said, speaking more slowly now, "that there is a whole world of sound about us all the time that we cannot hear. It is possible that up there in those high–pitched inaudible regions there is a new exciting music being made, with subtle harmonies and fierce grinding discords, a music so powerful that it would drive us mad if only our ears were tuned to hear the sound of it."

Roald Dahl, The Sound Machine

Contents

Chapter 1

The Standard Model of Particle Physics

I managed to get a quick PhD — though when I got it I knew almost nothing about physics. But I did learn one big thing: that no one knows everything, and you don't have to.

Steven Weinberg

Equal parts impressive and infuriating in its stubborn agreement with measurement, the Standard Model of particle physics (SM) encompasses our current best guess as to the fundamental nature of Nature outwith gravity.

An example of a relativistic quantum field theory[1] (QFT), the model describes — with incredible accuracy — the dynamics of the electromagnetic, weak, and strong forces. Comprised of local quantum fields, associated with the elementary particles illustrated in Fig. 1.1, the theory provides a unified framework describing the behaviour of and interactions between said fields — matter (*fermions*), force–carriers (*gauge bosons*), and the (scalar) Higgs boson.

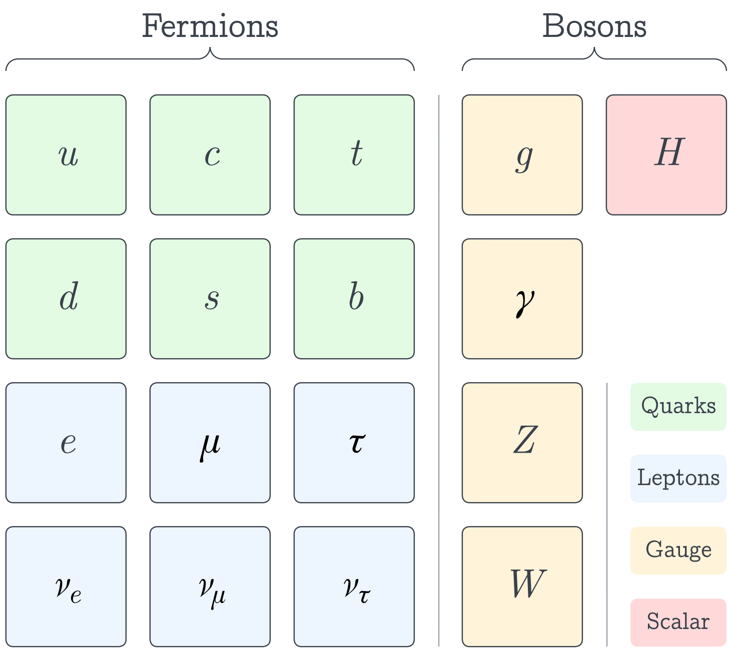

Figure 1.1: Fundamental particles of the Standard Model.

In this chapter we will touch upon the components, parameters, and limitations of the Standard Model; the constituent pieces of the Standard Model are introduced in Section 1.1, the parameters required for the model to be predictive and their currently accepted values are discussed in Section 1.2, and finally a brief discussion of some reasons to believe the Standard Model is incomplete is provided in Section 1.3.

[1] Pedagogical introductions can be found in, e.g., Refs. [6, 7].

1.1 The Rule of Three

He ain't heavy, he's my brother.

The Hollies

At its core the Standard Model consists of two theories, encapsulating the dynamics of the fundamental strong, weak, and electromagnetic forces, and their (in)direct interaction with the (deservedly) much–celebrated Higgs mechanism…

Quantum Chromodynamics (QCD): The theory of the strong interaction, described by a gauge group respecting local $SU(3)_C$ symmetry with *colour* charge, C. QCD describes any interaction between quarks that is mediated by the gluon.

The Electroweak Theory: A unified model of the electromagnetic and weak interactions via the gauge group $SU(2)_L \times U(1)_Y$ with the charges being weak isospin, L, and weak hypercharge, Y. Under this theory the electroweak interactions are mediated by the non-physical W_1, W_2, W_3, and B bosons, with the theory becoming physical only when the electroweak symmetry is broken.

The Higgs Mechanism: A complex scalar field doublet with four degrees of freedom and a non-zero minimum — the *vacuum expectation value* (vev) — which induces spontaneous breaking of the above electroweak symmetry into a $U(1)$ group with the electromagnetic coupling as its charge; this group describes Quantum Electrodynamics (QED), the theory of (charged) particle interactions involving the photon. The four degrees of freedom give mass to the $W^{\pm}$ and Z bosons and produce the Higgs boson, a massive scalar particle.

We have, then, that the Higgs mechanism is directly involved in QED via electroweak symmetry breaking (EWSB); this gives rise to weak processes, involving the now–massive $W^{\pm}$ and Z bosons, such as β and μ decay.

The gluon, however, is massless — it does not interact directly with the Higgs field. Instead the Higgs mechanism impacts QCD indirectly as fermions acquire mass after EWSB by way of interactions with the Higgs field, named Yukawa interactions.

Combining these pieces yields the Standard Model. Symmetric under gauge group $\mathcal{G}_{\text{SM}} = SU(3)_C \times SU(2)_L \times U(1)_Y$, the SM Lagrangian,

$$\begin{aligned}
\mathcal{L}_{\text{SM}}^{(4)} = & \underbrace{-\frac{1}{4}G_{\mu\nu}^A G^{A\mu\nu} - \frac{1}{4}W_{\mu\nu}^I W^{I\mu\nu} - \frac{1}{4}B_{\mu\nu}B^{\mu\nu}}_{\text{Gauge sector}} \\
& + \underbrace{i(\bar{l}\not{D}l + \bar{e}\not{D}e + \bar{q}\not{D}q + \bar{u}\not{D}u + \bar{d}\not{D}d)}_{\text{Fermion sector}} \\
& + \underbrace{(D_\mu\varphi)^\dagger(D^\mu\varphi) - \mu^2\varphi^\dagger\varphi - \lambda(\varphi^\dagger\varphi)^2}_{\text{Higgs sector}} \\
& + \underbrace{(\bar{l}Y_e e\varphi + \bar{q}Y_u u\tilde{\varphi} + \bar{q}Y_d d\varphi + \text{h.c.})}_{\text{Yukawa sector}},
\end{aligned}$$

provides an impressively concise — though by no means simple — way to encapsulate three of the four known fundamental forces by way of the four sectors highlighted above. These highlighted sectors, with additional reference to Fig. 1.1, are:

Gauge sector: Comprised of gluon fields, $G_\mu^{1,\dots,8}$, and the electroweak boson fields, $W_\mu^{1,\dots,3}$ and B_μ, this sector encapsulates the dynamics of the gauge bosons, or *force–carriers*; the strong interaction is mediated by the gluon (g), weak by $W^\pm$ and Z bosons, and electromagnetism by the photon (γ).

Fermion sector: Dictates the properties and behaviour of quarks and (charged) leptons, or *matter*, with both interacting with QED but only quarks having involvement with QCD. The fields are the left–handed and right–handed leptons l and e, the left–handed quarks q, and the up–type and down–type right–handed quarks u and d.

Higgs sector: The Higgs mechanism which induces EWSB, resulting in the physical (massless) photon γ and (massive) W^+, W^-, and Z bosons. The sole field here is the Higgs field, φ.

Yukawa sector: Describes the interaction between fermions and the Higgs field, which — after EWSB — are the processes by which matter acquires mass. The fields are the Higgs and fermion fields, with the Y_f terms being Yukawa coupling constants.

In addition to the local gauge symmetries, the SM Lagrangian is constructed such that it is consistent with special relativity, being Lorentz invariant; the physical manifestations of $\mathcal{L}_{\text{SM}}^{(4)}$ are independent of observer frame of reference, or are *observationally symmetric*. The Standard Model admits a number of 'free' parameters, the values of which cannot be known *a priori* and must instead be determined by experiment. We will now briefly introduce and discuss these parameters.

1.2 Free Parameters

'Cause I'm as free as a bird now,
and this bird you cannot change.

LYNYRD SKYNYRD

In the case of a single generation of fermions the eight free, or *fundamental*, parameters of the Standard Model are: three gauge couplings g_s, g, and g'; two Higgs potential parameters (μ and λ); three Yukawa coupling constants (y_u, y_d, and y_e). These parameters are commonly expressed as terms more amenable to measurement:

$$
\begin{aligned}
\tan\theta_W &= \frac{g'}{g}, \\
e &= g\sin\theta_W, \\
m_H &= \sqrt{2}\mu = \sqrt{2\lambda}v, \\
m_W &= \frac{g\mu}{2\sqrt{\lambda}} = \frac{gv}{2}, \text{ and} \\
m_f &= \frac{y_f\mu}{\sqrt{2\lambda}} = \frac{y_f}{\sqrt{2}}v.
\end{aligned}
$$

We therefore have, in this simplified regime, that the interaction strengths of the strong and electroweak sectors of the Standard Model are fixed by one and seven parameters respectively. In reality, however, we have not one but three generations of fermions; this introduces additional complexity due to our three–generation Yukawa couplings being a 3×3 matrix rather than three scalar values.

We must, then, include off-diagonal terms V_{ij} which induce *mixing* of quark flavours and do not violate the requirement of gauge–invariance. This matrix, called the Cabibbo-Kobayashi-Maskawa (CKM) matrix [8, 9], is expressed as

$$
V_{\text{CKM}} = \begin{bmatrix} V_{ud} & V_{us} & V_{ub} \\ V_{cd} & V_{cs} & V_{cb} \\ V_{td} & V_{ts} & V_{tb} \end{bmatrix},
$$

with the probability of a quark of flavour j transitioning to an i-type quark being $|V_{ij}|^2$. As of 2022, the most recent values for $|V_{ij}|$ are [10]

$$
\begin{bmatrix} |V_{ud}| & |V_{us}| & |V_{ub}| \\ |V_{cd}| & |V_{cs}| & |V_{cb}| \\ |V_{td}| & |V_{ts}| & |V_{tb}| \end{bmatrix} = \begin{bmatrix} 0.97435 \pm 0.00016 & 0.225 \pm 0.00067 & 0.00369 \pm 0.00011 \\ 0.22486 \pm 0.00067 & 0.97349 \pm 0.00016 & 0.04182^{+0.00085}_{-0.00074} \\ 0.00857^{+0.00020}_{-0.00018} & 0.04110^{+0.00083}_{-0.00072} & 0.999118^{+0.000031}_{-0.000036} \end{bmatrix}.
$$

A common parameterisation of the CKM matrix uses Wolfenstein parameters [11],

$$V_{\text{CKM}} = \begin{bmatrix} 1-\lambda^2/2 & \lambda & A\lambda^3\left(\rho - i\eta\right) \\ -\lambda & 1-\lambda^2/2 & A\lambda^2 \\ A\lambda^3\left(1-\rho-i\eta\right) & 1-A\lambda^2 & 1 \end{bmatrix} + \mathcal{O}\left(\lambda^4\right).$$

We then have that the three–generation Standard Model, neglecting neutrino masses and mixing[1], has eighteen[2] free parameters:

- The eight parameters of the single-generation model.
- Six additional Yukawa couplings, three for each generation.
- Four Wolfenstein parameters — A, $\bar{\rho}$, λ, and $\bar{\eta}$ — in the CKM matrix, which determine the coupling strengths between quark generations.

The latest values for these parameters are provided in Table 1.1 [10].

Coupling Constants		**Lepton Masses**	
α	$1/137.035999084(21)$	m_e	$0.510998950(15)$ MeV
α_s	$0.1179(9)$	m_μ	$105.6583755(23)$ MeV
G_F	$1.1663788(6) \times 10^{-5}$ GeV^{-2}	m_τ	1776.86 ± 0.12 MeV
Quark Masses			
m_u	$2.16^{+0.49}_{-0.26}$ MeV	m_s	$93.4^{+8.6}_{-3.4}$ MeV
m_d	$4.67^{+0.48}_{-0.17}$ MeV	m_t	172.69 ± 0.30 GeV
m_c	1.27 ± 0.02 GeV	m_b	$4.18^{+0.03}_{-0.02}$ GeV
Boson Masses			
m_H	125.25 ± 0.17 GeV	m_W	$80.377(12)$ GeV
Wolfenstein Parameters			
A	$0.826^{+0.018}_{-0.015}$	$\bar{\rho}$	0.159 ± 0.01
λ	$0.225(67)$	$\bar{\eta}$	0.348 ± 0.01

Table 1.1: Free parameters of the Standard Model.

[1] For this work we consider neutrinos to be massless, though note that massive neutrinos require seven further parameters — three neutrino masses, three mixing angles, and a phase angle. These angles constitute the PMNS matrix [12], the neutrino equivalent of the CKM matrix.

[2] There also exists a nineteenth parameter, the QCD vacuum angle θ_{QCD}, which does not contribute to perturbation theory but would give rise to a neutron electric dipole moment that has yet to be observed.

1.3 Here Be Dragons

All nature is but art unknown to thee.

ALEXANDER POPE

Impressive as the Standard Model is with respect to agreement with experiment there are strong reasons to believe the model is, at the very least, incomplete. Broadly speaking, these problems can be split into two categories; aesthetic concerns — aspects of the theory that *work* but lack sufficient motivation or explanation so as to be satisfactory — and problems that arise from observed phenomena that are not explained by the model. Here we briefly discuss a (non-exhaustive) selection of challenges to the Standard Model in both of these categories.

First among the aesthetic considerations are the free parameters described in Section 1.2. These parameters are, in a sense, arbitrary and at present admit no reasons as to why the values are what they are; we would expect a truly fundamental description of Nature to provide an explanation, if not admit *a priori* prediction of these values. Another challenge — or, indeed, *class* of challenges - is what is known as fine-tuning; instances where a parameter seems to admit a range of values but necessitates a very specific value when set against observed phenomena. Two well-known examples of fine-tuning in the Standard Model are:

The strong CP problem: Where a term respecting all SM symmetries gives rise to an electric dipole moment for the neutron that has not yet been measured experimentally. This is solved by tuning θ_{QCD} such that the term disappears.

The hierarchy problem: The as-yet unanswered question as to why the Higgs mass, $m_H \approx 125\text{GeV}$, is so small. With no known symmetry to "protect" the mass by cancelling out corrections, we would naively expect it to be much larger than measured; this implies a significant amount of fine-tuning, which is unsatisfactory when set alongside appeals to naturalness.

In addition to aesthetic — or theoretical — issues with the Standard Model, there also exist multiple observed phenomena that the model simply does not explain. Most prominent is the absence of a quantum description of gravity, as we would expect there to exist some fundamental theory that captures and explains all physical phenomena rather than two individual models. The Standard Model also provides no predictions or explanations of Dark Matter, Dark Energy, the amount of matter–antimatter asymmetry, or (without deliberate extension) massive neutrinos.

Chapter 2

Effective Field Theories

Science may be described as the art of systematic over-simplification — the art of discerning what we may with advantage omit.

Karl Popper

In the study of physical phenomena, it is often useful to approach systems using methods appropriate to the length or energy scale of the process in question. For example in studying the thermal properties of gases it is crucial to deal with average motions and energies rather than explicitly calculating the interactions of each individual molecule. Such approaches, called *effective theories*, aim to model the observed behaviour of a system in a given regime without having to explicitly describe the full set of underlying causes of said effects. Effective theories are useful both in simplifying the calculation of low energy dynamics when the full model is known and the modelling of phenomena in the case that said model remains illusive.

In the context of quantum field theory such an approach takes the form of an effective *field* theory[1] (EFT), allowing the description of physics at a given energy or distance scale without necessarily calculating — or even knowing! — the properties or dynamics of particles or interactions that may exist at higher energies [15]. Rather than model–building, this approach uses the fact that the effects of physics at high energy can — at energies well separated from some cut–off scale Λ — be captured via the introduction of so–called *effective operators* describing some set of interactions and scalar values, referred to as *Wilson coefficients*, which contain information as to the underlying physics above the cut–off scale. A brief discussion of the roots of and general approach to constructing an EFT are provided in Section 2.1.

As in the general case of effective theories, an effective field theory should accurately capture the dynamics observed at the energies at which the theory is constructed to describe. Effective field theories also admit the same dual purposes introduced above in that they can be used in simplifying low–energy calculations when the physics above Λ are known, as well as in capturing the effects of *unknown* but well–separated New Physics (NP) in a model–independent way. These methods of construction are called *top–down* and *bottom–up* respectively. Explicit examples of both approaches in the context of Fermi's interaction, an EFT describing the weak interaction for $E \ll \Lambda = m_W$, are provided in Section 2.2.

In Section 2.3 we will discuss the idea that our current understanding can, under the assumption that physics beyond the Standard Model (BSM) resides at high–energy scales, itself be interpreted as a low–energy effective field theory of some yet to be discovered fundamental physics.

[1] For a more rigorous treatment see, e.g., [13, 14].

2.1 Principles

The procedure for building an EFT is similar to that of building a QFT; they still decide on constituent fields — the 'degrees of freedom' in the theory — and a relevant group of symmetries, but instead of writing the most general *renormalisable* action which is consistent with the desired symmetries, it is simply the most general symmetry–respecting action which is written.

The removal of the renormalisability criterion is, at least in part, a result of epistemological considerations; it represents an admission, or an acknowledgement of the possibility, that the theory is valid only between some bounds in energy scale. In renormalisable field theories there is a maximum dimension terms in the action can have, resulting in a finite number of terms. This is not the case in EFTs where the most general action involves infinitely many terms which, in the strictest sense, should be dealt with if the theory is to be predictive.

Effective field theories, then, rely on three ingredient types [16]:

1. **Particle Content:** The fields describing the relevant degrees of freedom in the EFT, with at the very least all particles with mass $m \ll \Lambda$ included.

2. **Symmetries:** Observed symmetric properties of physics at the energy scale in question should be respected; be they gauge (e.g. $SU(3) \times SU(2) \times U(1)$ in the SM), spacetime (e.g. Lorentz symmetry), or otherwise.

3. **Counting scheme:** Once the first two ingredients are in place, there will be infinitely many operators which can be included in the EFT — a counting scheme is used to decide which of these can be omitted. Since the action, $S = \int d^dx\mathcal{L}$, is a scalar if and only if $\mathcal{L}$ is of mass dimension d, we require operators with mass dimension $D > d$ to be suppressed by $1/\Lambda^{D-d}$.

Once these ingredients are in place, a physical theory can be assembled. Owing to its generality, this approach has found wide and varied uses in physics and astronomy, with effective field theories being used in the search for Dark Matter [17, 18], in attempting to explain inflation and cosmic acceleration [19–21], and in nuclear physics [22, 23]. A classic example of such a theory within particle physics dealing with the weak interaction is found in Fermi's interaction, which we will now discuss.

2.2 Fermi's Interaction

Fermi theory describes the weak interactions at energies below the mass of the W boson, m_W. Whereas in the Standard Model (SM) the weak interaction is mediated by the W boson, at low energies this W propagator can be 'integrated out' and replaced with an effective four fermion contact interaction with coupling constant G_F. Although originally proposed to describe only beta decay, an example of a process accurately captured by Fermi theory is muon decay [24], with typical energy scales $E = m_\mu$ being well below the upper limit of the theory $\Lambda = m_W$. This process is illustrated in Figure 2.1.

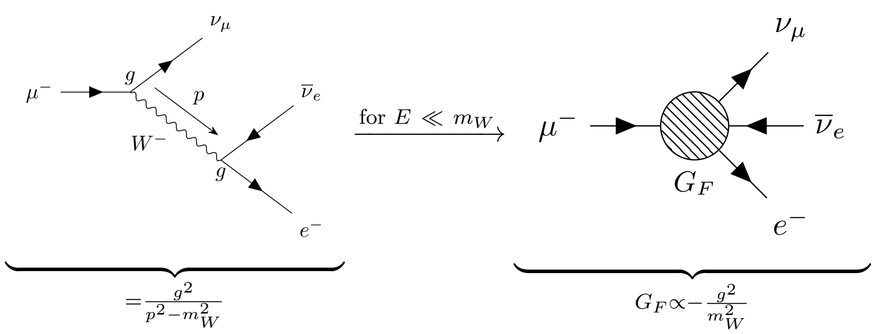

Figure 2.1: Standard Model (*left*) and Fermi Theory (*right*) muon decay[1].

As the momenta involved in the process increase, though, Fermi theory becomes less accurate; at $E \gtrapprox m_W$ the Standard Model allows for the creation of on–shell W bosons, a particle that doesn't exist in Fermi theory — as mentioned previously, well–separated scales are an essential component of any EFT.

The construction of an effective theory can be approached from either end of these separated scales to obtain an effective Lagrangian of the general form

$$\mathcal{L}_{\text{Eff}} = \text{kinetic terms} + \text{mass terms} + \sum_{i,D} \frac{C_{i,D}}{\Lambda^{D-d}} O_i,$$

where $C_{i,D}$ is the Wilson coefficient of the operator O_i in the term suppressed by Λ^{D-d} — this will be non–zero for only one such suppression term — and D, d are defined as in Section 2.1.

[1]All Feynman diagrams were produced using TikZ-FeynHand [25].

2.2.1 Top–Down Construction

In the top–down case, the Wilson coefficients of an EFT can be calculated directly and used in subsequent, simplified, calculations. Top–down effective theories must be matched with the underlying theory, which is a procedure by which it is ensured that at some ‘matching scale’ the full and effective theories are in agreement to corrections suppressed by $1/\Lambda^n$. The matching procedure involves dividing the particle content of the underlying theory into light and heavy fields, and ‘integrating out’ the heavy fields [26] with $m > \Lambda$.

Starting with the ‘full’ underlying theory, the Standard Model, we can construct a top–down effective field theory of the weak interaction. Following the recipe in Section 2.1 with the renormalisable SM having $d = 4$, then, we need to have our ingredients in place; our particle content consists of quarks, leptons, and the W boson. We must then determine all Feynman diagrams containing a single W boson[1] — our ‘heavy’ field, along with the top quark since $m_t > m_W = \Lambda$ — and evaluate the resulting path integral, integrating out the heavy fields. There turns out to be only one such diagram,

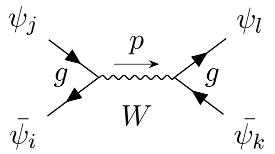

$$= \left(\bar{\psi}_i \frac{ig}{\sqrt{2}} \frac{1-\gamma_5}{2} \gamma^\mu \psi_j\right) \frac{-g_{\mu\nu}}{p^2 - m_W^2} \left(\bar{\psi}_k \frac{ig}{\sqrt{2}} \frac{1-\gamma_5}{2} \gamma^\nu \psi_l\right)$$

$$= \frac{g^2 \left(\bar{\psi}_i \left(1-\gamma_5\right) \gamma^\mu \psi_j\right) \left(\bar{\psi}_k \left(1-\gamma_5\right) \gamma_\mu \psi_l\right)}{8\left(p^2 - m_W^2\right)}.$$

We have $p \ll m_W = \Lambda$, giving

$$\frac{C_W}{\Lambda^2} O_W = \frac{g^2}{8m_W^2} \left(\bar{\psi}_i \left(1-\gamma_5\right) \gamma^\mu \psi_j\right) \left(\bar{\psi}_k \left(1-\gamma_5\right) \gamma_\mu \psi_l\right) + \mathcal{O}\left(1/\Lambda^4\right)$$

which, after setting $\Lambda = m_W$ and the Wilson coefficient $C_W = g^2/8$, yields the Lagrangian

$$\mathcal{L}_{\text{Eff}} = \underbrace{i\bar{\psi}_i \gamma^\mu \partial_\mu \psi_i}_{\text{Kinetic term}} - \underbrace{m_i \bar{\psi}_i \psi_i}_{\text{Mass term}} + \frac{g^2}{8m_W^2} \underbrace{\left(\bar{\psi}_i \left(1-\gamma_5\right) \gamma^\mu \psi_j\right) \left(\bar{\psi}_k \left(1-\gamma_5\right) \gamma_\mu \psi_l\right)}_{\text{Effective operator}}.$$

This is Fermi’s interaction, with $g^2/8m_W^2 = G_F/\sqrt{2}$. A similar process can be used for any theory, and would allow any proposed fundamental BSM theory to be quickly checked against phenomenologically constrained Wilson coefficient values.

[1] Strictly, loop and self–interaction diagrams should also be included. However, these terms are suppressed by a factor of $1/\Lambda^4$ and can therefore be safely omitted.

2.2.2 Bottom–up Construction

The bottom–up approach involves capturing the physical phenomena at a low scale without knowing the specifics of the high scale physics. In this situation, the field/particle content of a theory is used to construct an (infinite) ladder of higher dimensional operators with unknown coefficients — the coefficients which could be directly calculated if the underlying theory was known. The value of these coefficients is then determined by experiment, with Fermi's interaction as originally proposed being an example of this kind of theory [27].

To provide a concrete example of how such a theory is constructed we will now run through another sketch of Fermi theory, this time from the opposite direction. First, we must assume no knowledge of the W boson and run through the three ingredients of an EFT as outlined in Chapter 2. The relevant degrees of freedom above Λ_{QCD} are leptons and all quarks except the top, the relevant symmetries are Lorentz invariance and charge, lepton number, and baryon number conservation, and we will choose to keep only the lowest dimension operators which respect these symmetries.

The Lagrangian formed solely with the fermion kinetic and mass expressions contains dimension four terms. The lowest dimension that contains terms that respect our required symmetries is six, with seven four–fermion operators being found there. After removing terms which fail symmetry considerations, we are left with a single effective operator,

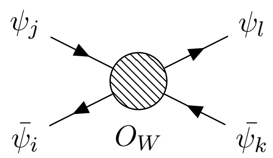

$$= \frac{C_W}{\Lambda^2}\left(\bar{\psi}_i\left(1-\gamma_5\right)\gamma^\mu\psi_j\right)\left(\bar{\psi}_k\left(1-\gamma_5\right)\gamma_\mu\psi_l\right),$$

which leads us to our bottom–up Lagrangian given by

$$\mathcal{L}_{\text{Eff}} = \underbrace{i\bar{\psi}_i\gamma^\mu\partial_\mu\psi_i}_{\text{Kinetic term}} - \underbrace{m_i\bar{\psi}_i\psi_i}_{\text{Mass term}} + \frac{C_W}{\Lambda^2}\underbrace{\left(\bar{\psi}_i\left(1-\gamma_5\right)\gamma^\mu\psi_j\right)\left(\bar{\psi}_k\left(1-\gamma_5\right)\gamma_\mu\psi_l\right)}_{\text{Effective operator}}.$$

This is Fermi theory, where the coefficient $C_W/\Lambda^2 = G_F/\sqrt{2} = 1.16\times10^{-5}\ \text{GeV}^{-2}$ is determined by observation. It is worth noting here that, with a bottom–up approach, C and Λ^2 can not be decoupled — that is, the exact scale of the new physics cannot be determined.

2.3 Standard Model Effective Field Theory

The Standard Model itself can also be approached as a low-energy EFT, and there are good reasons to believe it is so — that is, that there exists some Beyond the Standard Model (BSM) physics at higher energy scales; the observation of neutrino oscillations, for example, requires that neutrinos have some small but non–zero mass. This is not accounted for within the SM, and so the theory *cannot* be complete. The existence of Dark Matter (DM) is another such reason; if it turns out to be the case that DM is particle–like in nature, it should be captured by any fundamental theory of particle physics.

The lack of new physics (NP) signals thus far at the LHC indicates that if there is indeed NP to be discovered it is well separated from the SM in mass, further motivating an effective approach. It should, however, be said that both our current detectors and the EFT approach can only capture the effects of heavy degrees of freedom, and as such cannot rule out the possibility of exotic light degrees of freedom[1].

$$\mathcal{L}_{\text{Eff}} = \mathcal{L}_{\text{SM}} + \sum_{n=1}^{\infty} \sum_{i} \frac{C_i^{(n)}}{\Lambda^n} \mathcal{O}_i^{(n)}.$$

A model–independent approach is found in a bottom–up EFT with a cut off on mass dimension.

For dimension 5 there turns out to be only one operator, which will not be covered here as it has no bearing on the physics studied in this project. Although it is perhaps interesting to note that this operator — the first deviation from the SM in our EFT — provides Majorana neutrino mass terms. With the observation of neutrino oscillations, requiring massive neutrinos, this fact may lend credence to EFT as an approach to the constraint of BSM physics. The single $D = 5$ operator,

$$\begin{aligned} O_{\nu\nu} &= \epsilon_{jk} \varepsilon_{mn} \varphi^j \varphi^m (\ell'^k_{Lp})^T \mathbb{C} \ell'^n_{Lr} \\ &\equiv \left(\widetilde{\varphi}^\dagger \ell'^k_{Lp}\right)^T \mathbb{C} \left(\widetilde{\varphi}^\dagger \ell'_{Lr}\right), \end{aligned}$$

is critical in maintaining consistency between the Standard Model and observation due to it generating neutrino masses and mixing, measured but not allowed by $\mathcal{L}_{\text{SM}}^{(4)}$.

[1] Either way, though, the SM captures neither!

Dimension six does, however, include relevant operators, and this is the limit set here. A complete list of 80 dimension six operators, formed by SM fields and respecting the Lorentz and $SU(3) \times SU(2) \times U(1)$ symmetries, was first written down in 1985 [28], and this was subsequently reduced to 59 independent operators by spotting and removing redundancies in the original list [29, 30]. This means we can extend the SM Lagrangian by adding the individual operator terms,

$$\mathcal{L}_{O_i} = \frac{C_i}{\Lambda^2} O_i \implies \mathcal{L}_{D6} = \sum_i \frac{C_i}{\Lambda^2} O_i \, .$$

Our new effective Lagrangian is then given by

$$\begin{aligned} \mathcal{L}_{\text{Eff}} &= \mathcal{L}_{\text{SM}} + \mathcal{L}_{D5} + \mathcal{L}_{D6} \\ &= \mathcal{L}_{\text{SM}} + \frac{C_{\nu\nu}}{\Lambda} O_{\nu\nu} + \sum_i \frac{C_i}{\Lambda^2} O_i \, , \end{aligned}$$

where C_i are the (dimensionless) Wilson coefficients of the dimension six operators O_i, and Λ is defined as before. There are three popular bases used in writing these operators; the "Warsaw" basis [30], the SILH convention [31], and the HISZ basis [32]. It is the first of these that we will be using here as it is particularly useful in top quark EFTs due to simplifying modifications to fermion couplings. The full set of non–redundant dimension–six operators are listed in Tables 2.1 and 2.2.

The Wilson coefficients must be determined from experiment, but once they have been sufficiently constrained the theory can be used to make predictions of future events and provide a fast route to check the validity of proposed BSM theories. The simultaneous constraint of 59 operators would prove intractable, however not all of these operators have a role to play in every physical process — subsets of this set of dimension six operators apply to different sectors.

At dimension–eight there are $\mathcal{O}(1,000)$ operators, a number too large to be dealt with in the current study. Additionally, there has not yet been a full treatment in resolving redundancies for $D > 6$ and as such we will impose a well–motivated limit of dimensionality at six here.

X^3		φ^6 and $\varphi^4 D^2$		$\psi^2\varphi^3$	
O_G	$f^{ABC} G_\mu^{A\nu} G_\nu^{B\rho} G_\rho^{C\mu}$	O_φ	$(\varphi^\dagger\varphi)^3$	$O_{e\varphi}$	$(\varphi^\dagger\varphi)(\bar l'_p e'_r \varphi)$
$O_{\widetilde G}$	$f^{ABC} \widetilde G_\mu^{A\nu} G_\nu^{B\rho} G_\rho^{C\mu}$	$O_{\varphi\Box}$	$(\varphi^\dagger\varphi)\Box(\varphi^\dagger\varphi)$	$O_{u\varphi}$	$(\varphi^\dagger\varphi)(\bar q'_p u'_r \widetilde\varphi)$
O_W	$\varepsilon^{IJK} W_\mu^{I\nu} W_\nu^{J\rho} W_\rho^{K\mu}$	$O_{\varphi D}$	$\left(\varphi^\dagger D^\mu\varphi\right)^* \left(\varphi^\dagger D_\mu\varphi\right)$	$O_{d\varphi}$	$(\varphi^\dagger\varphi)(\bar q'_p d'_r \varphi)$
$O_{\widetilde W}$	$\varepsilon^{IJK} \widetilde W_\mu^{I\nu} W_\nu^{J\rho} W_\rho^{K\mu}$				
$X^2\varphi^2$		$\psi^2 X\varphi$		$\psi^2\varphi^2 D$	
$O_{\varphi G}$	$\varphi^\dagger\varphi\, G^A_{\mu\nu} G^{A\mu\nu}$	O_{eW}	$(\bar l'_p \sigma^{\mu\nu} e'_r)\tau^I \varphi W^I_{\mu\nu}$	$O^{(1)}_{\varphi l}$	$(\varphi^\dagger i \overleftrightarrow{D}_\mu \varphi)(\bar l'_p \gamma^\mu l'_r)$
$O_{\varphi\widetilde G}$	$\varphi^\dagger\varphi\, \widetilde G^A_{\mu\nu} G^{A\mu\nu}$	O_{eB}	$(\bar l'_p \sigma^{\mu\nu} e'_r)\varphi B_{\mu\nu}$	$O^{(3)}_{\varphi l}$	$(\varphi^\dagger i \overleftrightarrow{D}^I_\mu \varphi)(\bar l'_p \tau^I \gamma^\mu l'_r)$
$O_{\varphi W}$	$\varphi^\dagger\varphi\, W^I_{\mu\nu} W^{I\mu\nu}$	O_{uG}	$(\bar q'_p \sigma^{\mu\nu} \mathcal{T}^A u'_r)\widetilde\varphi\, G^A_{\mu\nu}$	$O_{\varphi e}$	$(\varphi^\dagger i \overleftrightarrow{D}_\mu \varphi)(\bar e'_p \gamma^\mu e'_r)$
$O_{\varphi\widetilde W}$	$\varphi^\dagger\varphi\, \widetilde W^I_{\mu\nu} W^{I\mu\nu}$	O_{uW}	$(\bar q'_p \sigma^{\mu\nu} u'_r)\tau^I \widetilde\varphi\, W^I_{\mu\nu}$	$O^{(1)}_{\varphi q}$	$(\varphi^\dagger i \overleftrightarrow{D}_\mu \varphi)(\bar q'_p \gamma^\mu q'_r)$
$O_{\varphi B}$	$\varphi^\dagger\varphi\, B_{\mu\nu} B^{\mu\nu}$	O_{uB}	$(\bar q'_p \sigma^{\mu\nu} u'_r)\widetilde\varphi\, B_{\mu\nu}$	$O^{(3)}_{\varphi q}$	$(\varphi^\dagger i \overleftrightarrow{D}^I_\mu \varphi)(\bar q'_p \tau^I \gamma^\mu q'_r)$
$O_{\varphi\widetilde B}$	$\varphi^\dagger\varphi\, \widetilde B_{\mu\nu} B^{\mu\nu}$	O_{dG}	$(\bar q'_p \sigma^{\mu\nu} \mathcal{T}^A d'_r)\varphi\, G^A_{\mu\nu}$	$O_{\varphi u}$	$(\varphi^\dagger i \overleftrightarrow{D}_\mu \varphi)(\bar u'_p \gamma^\mu u'_r)$
$O_{\varphi WB}$	$\varphi^\dagger \tau^I \varphi\, W^I_{\mu\nu} B^{\mu\nu}$	O_{dW}	$(\bar q'_p \sigma^{\mu\nu} d'_r)\tau^I \varphi\, W^I_{\mu\nu}$	$O_{\varphi d}$	$(\varphi^\dagger i \overleftrightarrow{D}_\mu \varphi)(\bar d'_p \gamma^\mu d'_r)$
$O_{\varphi\widetilde W B}$	$\varphi^\dagger \tau^I \varphi\, \widetilde W^I_{\mu\nu} B^{\mu\nu}$	O_{dB}	$(\bar q'_p \sigma^{\mu\nu} d'_r)\varphi\, B_{\mu\nu}$	$O_{\varphi ud}$	$i(\widetilde\varphi^\dagger D_\mu\varphi)(\bar u'_p \gamma^\mu d'_r)$

Table 2.1: $D = 6$ bosonic and single-fermion current operators.

$(\bar L L)(\bar L L)$		$(\bar R R)(\bar R R)$		$(\bar L L)(\bar R R)$	
O_{ll}	$(\bar l'_p \gamma_\mu l'_r)(\bar l'_s \gamma^\mu l'_t)$	O_{ee}	$(\bar e'_p \gamma_\mu e'_r)(\bar e'_s \gamma^\mu e'_t)$	O_{le}	$(\bar l'_p \gamma_\mu l'_r)(\bar e'_s \gamma^\mu e'_t)$
$O^{(1)}_{qq}$	$(\bar q'_p \gamma_\mu q'_r)(\bar q'_s \gamma^\mu q'_t)$	O_{uu}	$(\bar u'_p \gamma_\mu u'_r)(\bar u'_s \gamma^\mu u'_t)$	O_{lu}	$(\bar l'_p \gamma_\mu l'_r)(\bar u'_s \gamma^\mu u'_t)$
$O^{(3)}_{qq}$	$(\bar q'_p \gamma_\mu \tau^I q'_r)(\bar q'_s \gamma^\mu \tau^I q'_t)$	O_{dd}	$(\bar d'_p \gamma_\mu d'_r)(\bar d'_s \gamma^\mu d'_t)$	O_{ld}	$(\bar l'_p \gamma_\mu l'_r)(\bar d'_s \gamma^\mu d'_t)$
$O^{(1)}_{lq}$	$(\bar l'_p \gamma_\mu l'_r)(\bar q'_s \gamma^\mu q'_t)$	O_{eu}	$(\bar e'_p \gamma_\mu e'_r)(\bar u'_s \gamma^\mu u'_t)$	O_{qe}	$(\bar q'_p \gamma_\mu q'_r)(\bar e'_s \gamma^\mu e'_t)$
$O^{(3)}_{lq}$	$(\bar l'_p \gamma_\mu \tau^I l'_r)(\bar q'_s \gamma^\mu \tau^I q'_t)$	O_{ed}	$(\bar e'_p \gamma_\mu e'_r)(\bar d'_s \gamma^\mu d'_t)$	$O^{(1)}_{qu}$	$(\bar q'_p \gamma_\mu q'_r)(\bar u'_s \gamma^\mu u'_t)$
		$O^{(1)}_{ud}$	$(\bar u'_p \gamma_\mu u'_r)(\bar d'_s \gamma^\mu d'_t)$	$O^{(8)}_{qu}$	$(\bar q'_p \gamma_\mu \mathcal{T}^A q'_r)(\bar u'_s \gamma^\mu \mathcal{T}^A u'_t)$
		$O^{(8)}_{ud}$	$(\bar u'_p \gamma_\mu \mathcal{T}^A u'_r)(\bar d'_s \gamma^\mu \mathcal{T}^A d'_t)$	$O^{(1)}_{qd}$	$(\bar q'_p \gamma_\mu q'_r)(\bar d'_s \gamma^\mu d'_t)$
				$O^{(8)}_{qd}$	$(\bar q'_p \gamma_\mu \mathcal{T}^A q'_r)(\bar d'_s \gamma^\mu \mathcal{T}^A d'_t)$

$(\bar L R)(\bar R L)$ and $(\bar L R)(\bar L R)$		B-violating	
O_{ledq}	$(\bar l_p^{\prime j} e'_r)(\bar d'_s q_t^{\prime j})$	O_{duq}	$\varepsilon^{\alpha\beta\gamma}\varepsilon_{jk}\left[(d_p^{\prime\alpha})^T \mathbb{C} u_r^{\prime\beta}\right]\left[(q_s^{\prime\gamma j})^T \mathbb{C} l_t^{\prime k}\right]$
$O^{(1)}_{quqd}$	$(\bar q_p^{\prime j} u'_r)\varepsilon_{jk}(\bar q_s^{\prime k} d'_t)$	O_{qqu}	$\varepsilon^{\alpha\beta\gamma}\varepsilon_{jk}\left[(q_p^{\prime\alpha j})^T \mathbb{C} q_r^{\prime\beta k}\right]\left[(u_s^{\prime\gamma})^T \mathbb{C} e'_t\right]$
$O^{(8)}_{quqd}$	$(\bar q_p^{\prime j} \mathcal{T}^A u'_r)\varepsilon_{jk}(\bar q_s^{\prime k} \mathcal{T}^A d'_t)$	O_{qqq}	$\varepsilon^{\alpha\beta\gamma}\varepsilon_{jn}\varepsilon_{km}\left[(q_p^{\prime\alpha j})^T \mathbb{C} q_r^{\prime\beta k}\right]\left[(q_s^{\prime\gamma m})^T \mathbb{C} l_t^{\prime n}\right]$
$O^{(1)}_{lequ}$	$(\bar l_p^{\prime j} e'_r)\varepsilon_{jk}(\bar q_s^{\prime k} u'_t)$	O_{duu}	$\varepsilon^{\alpha\beta\gamma}\left[(d_p^{\prime\alpha})^T \mathbb{C} u_r^{\prime\beta}\right]\left[(u_s^{\prime\gamma})^T \mathbb{C} e'_t\right]$
$O^{(3)}_{lequ}$	$(\bar l_p^{\prime j} \sigma_{\mu\nu} e'_r)\varepsilon_{jk}(\bar q_s^{\prime k} \sigma^{\mu\nu} u'_t)$		

Table 2.2: Four-fermion operators.

Chapter 3

Collider Physics

Oh, you don't trust me?

Richard P. Feynman

In Chapters 1 and 2 we introduced the required theoretical underpinnings of the work presented here, but what about *observed* phenomena?

The what *is*, rather than what *could be*, of fundamental particle physics is studied using the measurement and analysis of the results of high–energy collisions of particle beams, the physics of which is very briefly[1] introduced in this chapter.

Serving simultaneously as our best way to probe Nature and scrutinise accepted and proposed theories it would be hard to overestimate the importance and utility — not to mention the technical achievements — of modern particle colliders, detectors, and analysis tooling.

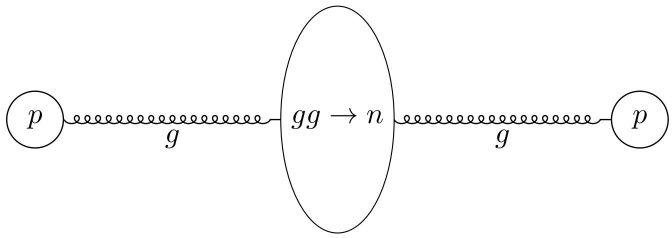

Figure 3.1: Illustration of pp collision leading to a $2 \to n$ scattering process.

The structure of this chapter is as follows: Section 3.1 provides a brief outline of relativistic kinematics to serve as the basis for later discussion; in Section 3.2 we introduce the concepts of total and differential scattering cross–sections with reference to the matrix element, parton density, and scale–dependence; in Section 3.3 we discuss sources of systematic uncertainty in hadron collider scattering cross–section calculations which can, broadly speaking, be grouped in to three categories — scale dependence, parton distribution function (PDF) uncertainties, and the finite-accuracy of Standard Model parameters; Section 3.4 places collider measurements in the context of searches for signs of New Physics (NP), provides indirect searches as motivation for an EFT approach, and sketches commonly-used physical quantities — inclusive cross–sections, differential cross–sections, decay observables, and asymmetries — in the pursuit of said searches.

[1] For a practical and in–depth introduction to collider physics see, e.g., Ref. [33].

3.1 Relativistic Kinematics

We must take relativistic effects into account at the speeds involved in particle collisions, and as such will here introduce the notation and properties of four–vectors. Firstly we have the spacetime position of a particle expressed as

$$x^\mu = (ct,\, x,\, y,\, z)\,,$$

with μ indicating the vector component — i.e. $x^0 = ct$. From this, we then have that the four–momentum is given by

$$p^\mu \equiv m\frac{\partial x^\mu}{\partial \tau}$$

where τ is the proper time — the time experienced by the particle at rest — which, if the particle is *not* at rest, is dilated by γ such that

$$t = \gamma\tau,\;\; \gamma = \left(1 - \frac{v^2}{c^2}\right)^{-1/2}\,,$$

with $v = |\mathbf{v}|$ being the magnitude of the particles *non-relativistic* three-velocity. This allows us to write the four-momentum of the particle as

$$p^\mu = \left(\frac{E}{c},\, \mathbf{p}\right)\,,$$

with

$$E = \gamma mc^2,\;\; \mathbf{p} = \gamma m\mathbf{v}$$

being the *relativistic* energy and three-momentum respectively.

The above can in turn be used to construct observable quantities that allow more granular study, and comparison to experimental measurement of (differential) scattering cross-sections, of the kinematic properties of a given theory. Inclusive and differential cross-sections are introduced in Section 3.2.

3.2 Scattering Cross–sections

The scattering cross–section, σ, relates to the probability of a given process occurring as the consequence of particles — or beams of particles — colliding, with the result depending on the properties of the colliding entities. In the context of particle colliders this probability is related to the event rate

$$\frac{\mathrm{d}N}{\mathrm{d}t} = \mathcal{L}(t)\sigma\,,$$

where $\mathcal{L}(t)$ is the instantaneous luminosity. The cross–section for colliding beams of a– and b–type particles is given by

$$\sigma = \frac{1}{N_a \mathcal{F}_b}\frac{\delta N}{\delta t}\,,$$

where N_a is the number of a particles, $\mathcal{F}_b$ is the flux of b particles.

Calculation of scattering amplitudes begins with the S-matrix, composed of scattering piece T and trivial non-scattering piece $\mathbb{1}$,

$$S = \mathbb{1} + iT = \mathbb{1} + i\delta^4(p_f - p_i)\mathcal{M}_{fi}\,,$$

where $\delta^4(p_f - p_i)$ imposes momentum conservation and can be factored out to extract the matrix element $\mathcal{M}_{fi}$. We then have cross-section

$$\sigma(a_1(p_1)a_2(p_2) \to X) = \frac{1}{\Phi}\int d\Pi_n |\mathcal{M}_{fi}|^2\,, \tag{3.1}$$

where $\Phi = |v_{a_1} - v_{a_2}|(2E_{a_1})(2E_{a_2})$ is the flux factor and

$$\int d\Pi_n = \int \prod_{i=1}^{n} \frac{d^3 k_i}{(2\pi)^3 2E_{k_i}} = \int d\mathrm{LIPS}(X)$$

is the Lorentz–invariant phase space.

We then calculate the full hadronic cross-section

$$\sigma(p(k_1)p(k_2) \to X) = \sum_{i,j}\int_0^1 dx_1 dx_2 f_i(x_1,\mu_F^2) f_j(x_2,\mu_F^2)\hat{\sigma}_{ij}(x_1,x_2,s,\alpha_s(\mu_R,Q^2))\,,$$

where $\hat{\sigma}_{i,j\to X}$ is the cross-section for the partonic subprocess $ij \to X$, f_i are parton density functions (PDFs), μ_R and μ_F are the (arbitrary) renormalisation and factorisation scales respectively.

Given some observable property of the final state(s) X the differential cross–section is related to the Lorentz–invariant matrix element $\mathcal{M}$ by

$$\frac{d\sigma}{dX} = \int d\Pi_{\mathrm{LIPS}}\delta^{(4)}(X - X')|\mathcal{M}|^2\,,$$

with $d\Pi_{\mathrm{LIPS}} \sim dX'$. Commonly studied kinematic observables are introduced in Section 3.4.

3.3 Sources of Uncertainty

Scale Dependence

Calculations beyond leading–order (LO) in QFT often exhibit ultraviolet (UV) divergences induced by the inclusion of intermediate states of arbitrarily high momentum. A common method used to deal with these UV divergences is to define some *renormalisation scale*, μ_R, which imposes separation of low–energy and unknown high–energy (short–distance) physics. The renormalisation scale should be arbitrary and have no effect on predictions of physical quantities; indeed, the variation — or *running* — of renormalised coupling values is dictated by the renormalisation group equations (RGEs) such that measured/predicted quantities are independent of μ_R. However fixed–order calculations, where the perturbative expansion is truncated, result in the *incomplete* cancellation of μ_R in the resulting predictions meaning there remains a residual μ_R dependence which is proportional to the next (discarded) order in the expansion.

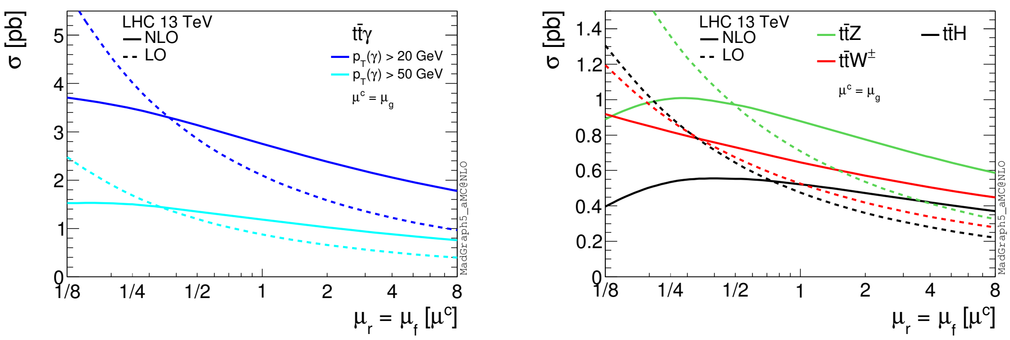

Figure 3.2: The scale dependence, at LO and NLO in QCD, of $pp \to t\bar{t}V$ total cross–sections at 13 TeV [34].

At the other end of energy scales involved in a given process we must also deal with infrared (IR) effects, which is done by imposing one more separation of scales. Here we choose a value for the *factorisation scale*, μ_F, of a given process; this scale determines the energy at which the "hard" — parton–parton — and "soft" — hadron–hadron — scattering processes are defined, with the hard (high–momentum) scattering cross-section being subsequently calculated using (fixed–order) perturbation theory and any initial state with $E < \mu_F$ being (re)absorbed into the hadron. The severity of the above scale dependencies are reduced as the chosen order of truncation is increased, as illustrated in Fig. 3.2, though higher-order calculations are (as ever) increasingly involved and difficult to carry out.

Parton Density

When dealing with hadron collisions, we must take into account the composite nature of the colliding particles. Hadrons are comprised of quarks and gluons, or *partons*, and we include the distribution using PDFs. These functions, generally fit to measurements of well–understood processes and applied more generally, encode the probability of finding some parton i with fraction x of total hadron momentum; the probabilities for low– and high–momentum transfer can be found in Fig. 3.3.

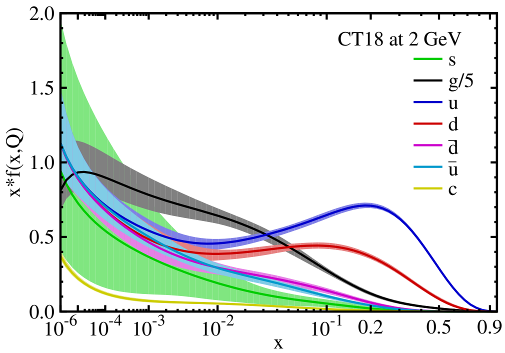

(a) Low momentum transfer $Q = 2$ GeV.

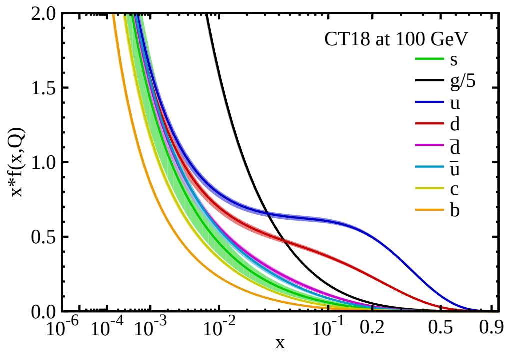

(b) High momentum transfer $Q = 100$ GeV.

Figure 3.3: The CT18 parton distribution functions [35].

The above plots include uncertainties arising from the fitting procedure used to produce PDFs — and, indeed, nature of the problem. These uncertainties are commonly handled by providing PDFs as an *ensemble* of fit results for varying input parameters, alongside some well–defined prescription for the method used to calculate PDF uncertainties.

Standard Model Parameters

Whilst the largest contributions to theoretical uncertainties in hadron collider cross–section calculations come from μ_R, μ_F, and PDF choices the finite measurement precision of the Standard Model parameters in Table 1.1 gives rise to an additional source of uncertainty. The impact of these parameters varies depending on the process under study, with the most relevant for this study being α_s and m_t. While α_s and m_t have been measured to significant accuracy, interpretation of direct top quark mass measurements is an open issue (see, e.g, Ref. [36] for a recent review). Treatment of uncertainties is discussed further in Section 5.3.

3.4 New Physics Searches

To date, the probing of fundamental particle physics at colliders has proved stubborn in its refusal to admit direct measurement of new particles. This lack of direct detection, coupled with the known limitations outlined in Section 1.3 and an acknowledgement of the possibility that our current experimental methods *can't* provide direct measurement of new signals provides strong motivation for *indirect* approaches to the detection or constraint of New Physics (NP). There are broadly speaking two scenarios that could explain our inability to detect new particles; that said particles are *light*, where additional degrees of freedom reside at energy scales that are currently probed but exhibit weak or as–yet unknown coupling to SM fields or *heavy*, residing at energy scales that we have not (yet) been able to probe directly. It is the latter scenario that lends itself to the approach taken here, where the indirect effects of unknown physics at high energy scales result, as long as they couple sufficiently strongly to SM fields, in deviations from Standard Model predictions at lower relative energies that are currently amenable to study at particle colliders.

The simplest case in the indirect search for signs of new physics is found in the comparison of measured and predicted values for inclusive cross–section; this involves calculating the total production cross–section of a given particle, or set of particles, for the theory in question — the Standard Model, for example — and comparing the result to the observed cross–section extracted from collider data. A selection of inclusive cross–section measurements are shown alongside SM predictions in Fig. 3.4.

The study of cross-section as a function of one or more kinematic final-state properties allows for additional means to test proposed models, as they can carry much more information than total cross–section alone. In the case of multiple final–states one commonly measured property is the invariant mass

$$m^2 = \left(\sum_i E_i\right)^2 - \left(\sum_i \mathbf{p}_i\right)^2,$$

where i denotes final-state particles. For a single final–state standard measurements include the transverse momentum

$$p_\perp^2 = p_x^2 + p_y^2$$

and rapidity

$$y = \frac{1}{2}\ln\left(\frac{E+p_z}{E-p_z}\right).$$

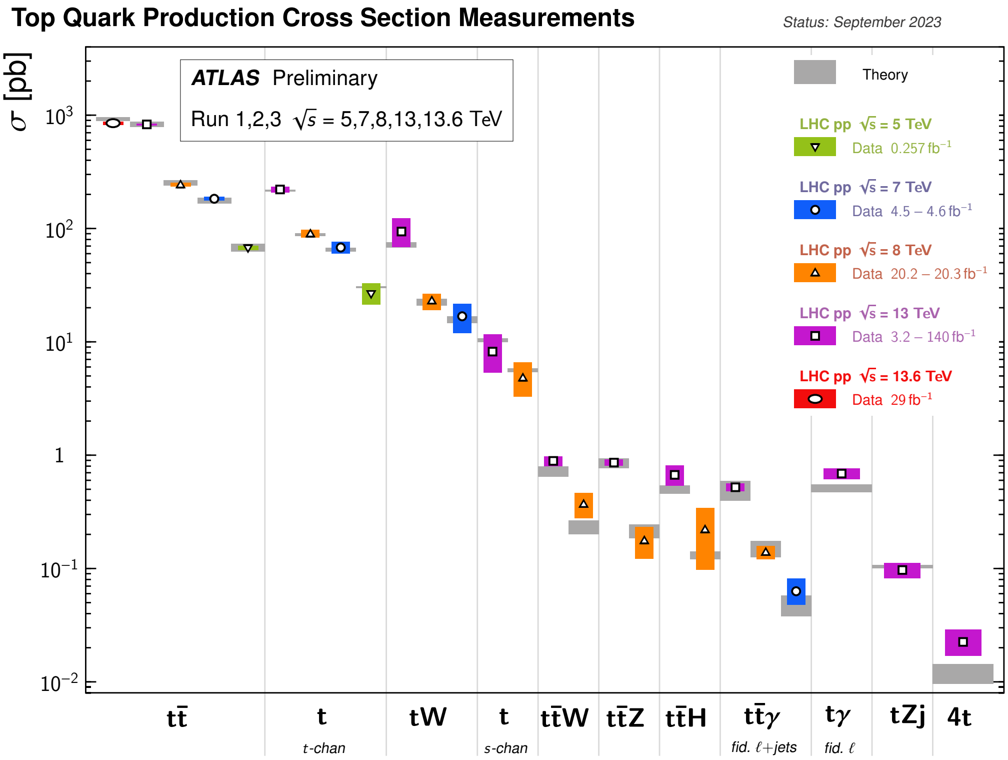

Figure 3.4: Inclusive top quark production cross–section results [37].

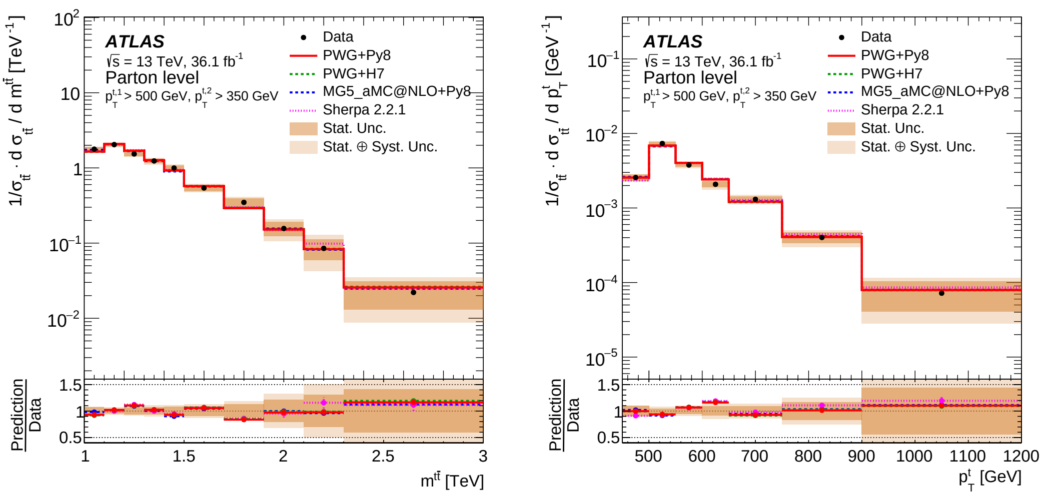

(a) Top–pair invariant mass $m_{t\bar{t}}$.

(b) Top quark transverse momentum p_T.

Figure 3.5: Normalised differential $pp \to t\bar{t}$ cross–sections [38].

Differential cross–sections are often expressed as normalised distributions

$$\frac{1}{\sigma}\frac{\partial\sigma}{\partial X},$$

as the normalisation step allows for the (partial) cancellation of common systematic uncertainties in the ratio of total and differential cross–sections. This is particularly useful in the context of indirect searches, as the relative reduction in uncertainty can increase sensitivity to deviations from observed results.

In addition to cross–section measurements, indirect searches can be carried out via the study of observables arising from particle decay. For top quark decay one might look for deviations between predicted and measured values of the decay width Γ_t, the probability per unit time that a given top quark will decay. W-boson helicity fractions — the proportion of top quarks decaying to W-bosons of left-handed (F_L), right-handed (F_R), or zero (F_0) chirality — can also be used in indirect searches. These fractions, at leading order and with a massive b quark, are

$$F_0 = \frac{(1-y^2)^2 - x^2(1+y^2)}{(1-y^2)^2 + x^2(1-2x^2+y^2)}$$

$$F_L = \frac{x^2(1-x^2+y^2) + \sqrt{\lambda}}{(1-y^2)^2 + x^2(1-2x^2+y^2)}$$

$$F_R = \frac{x^2(1-x^2+y^2) - \sqrt{\lambda}}{(1-y^2)^2 + x^2(1-2x^2+y^2)}$$

where $x = M_W/m_t$, $y = m_b/m_t$, and $\lambda = 1 + x^4 + y^4 - 2x^2y^2 - 2x^2 - 2y^2$.

Owing to the fact $\Gamma_t \gg \frac{\Lambda^2_{\mathrm{QCD}}}{m_t} \approx 0.1$ MeV correlation between top quark spins and the spin of decay products is preserved. We can extract information about this spin correlation via, for example, the study of $\cos\theta_{l^+}\cos\theta_{l^-}$, where $\theta_{l^\pm}$ is the angle of a charged lepton in the rest frame of the parent top (anti)quark in a given basis.

Useful quantities to measure are asymmetries — in large part due to the cancellation of systematic uncertainties in the numerator and denominator — of the general form

$$A(X,\alpha) = \frac{N(X>\alpha) - N(X<\alpha)}{N(X>\alpha) + N(X<\alpha)},$$

where N is the number of events meeting a given criteria for some observable X and threshold value α. Examples include forward-backward asymmetry for asymmetric ($p\bar{p}$) colliders

$$A_{\mathrm{FB}} = \frac{N(\Delta y>0) - N(\Delta y<0)}{N(\Delta y>0) + N(\Delta y<0)}$$

where $\Delta y = y_t - y_{\bar{t}}$ and the symmetric (pp) collider analogue charge asymmetry A_{C}, where $\Delta|y| = |y_t| - |y_{\bar{t}}|$ takes the place of Δy in A_{FB}.

Chapter 4

The TopFitter Framework

You shouldn't choose a problem on the basis of the tool. You start by thinking about the physics problem, and the computational method should be a tool like any other.

Kenneth G. Wilson

In Chapters 2 and 3 we introduced and motivated the conceptual approach whereby the Standard Model can be treated as the low–energy limit of some as–yet unknown underlying theory. Indeed, the lack of *direct* observation of New Physics signals at energies probed at past and current collider experiments can — under the assumption that no exotic, weakly–coupled light degrees of freedom exist — be taken as a hint that if indeed Beyond the Standard Model (BSM) physics is to be found it is well–separated from typical collider energy scales.

How, then, do we best accommodate the detection of *indirect* signals of high–scale physics? The approach taken here is to leverage the model–independent, kinematically–sensitive nature of the SMEFT Lagrangian and the significant amount of experimental measurements to produce phenomenologically-derived limits on what new physics is possible; put another way, to determine the range of effective operator coefficients produces predictions consistent with observed behaviour using the modular, end–to–end framework outlined in Fig. 4.1.

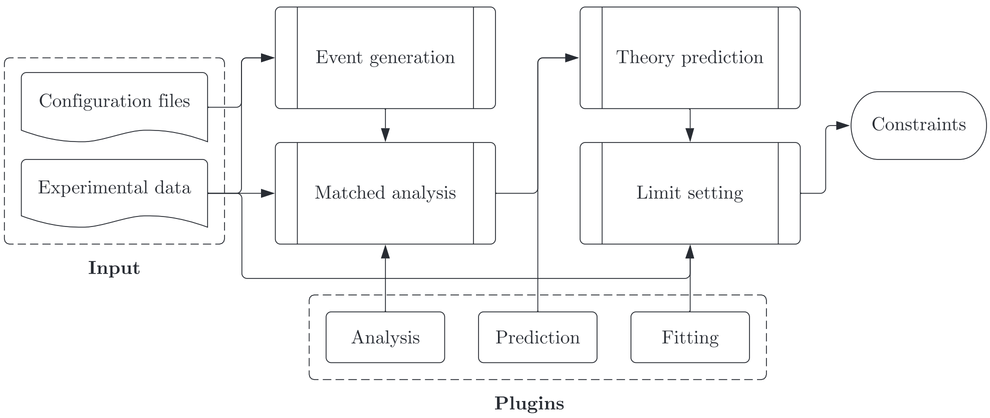

Figure 4.1: Framework overview flowchart.

The structure of this chapter is as follows: in Section 4.1 we lay the foundations of the TopFitter approach, introducing the piecewise (re)construction of SMEFT matrix element as the basis upon which subsequent architectural and methodological decisions are built; in Section 4.2 we discuss the overall architecture of the framework, the motivation and design of the underlying data structure based on said piecewise construction, and the extensible plugin–driven design implemented to allow for rapid iteration of and adaptation to new ideas and/or data; finally, Section 4.3 describes the approach in procuring raw event data and performing experimentally–matched analyses, the plugin–driven prediction and limit setting framework.

4.1 The Physics Problem

From Eq. (3.1) we have that cross–section is related to the matrix element $\mathcal{M}$. Recall also that, neglecting the single dimension–five operator, our extended SMEFT Lagrangian is given by

$$\begin{aligned}\mathcal{L}_{\text{Eff}} &= \mathcal{L}_{\text{SM}} + \mathcal{L}_{D6} \\ &= \mathcal{L}_{\text{SM}} + \sum_i \frac{C_i}{\Lambda^2} O_i \,.\end{aligned} \tag{4.1}$$

Since the final–state phase space has no dependence on the matrix element, $\mathcal{M}$, we can express any cross–section following from Eq. (4.1) as

$$\sigma = \sigma_{\text{SM}} + \frac{C_i}{\Lambda^2}\sigma_i^{(1)} + \frac{C_i C_j}{\Lambda^4}\sigma_{ij}^{(2)} \,, \tag{4.2}$$

where C_i are the Wilson coefficients and Λ is the New Physics (NP) scale. Deviations from SM predictions, then, are induced by altered scattering amplitudes arising due to extra terms in the EFT matrix element. The inclusion of dimension–six operators results in matrix element $\mathcal{M} = \mathcal{M}_{\text{SM}} + \mathcal{M}_{\text{D6}}$, giving a squared amplitude of the form

$$|\mathcal{M}|^2 = |\mathcal{M}_{\text{SM}}|^2 + \underbrace{2\,\text{Re}\,(\mathcal{M}_{\text{SM}}\mathcal{M}_{\text{D6}}^*)}_{\mathcal{O}(1/\Lambda^2)} + \underbrace{|\mathcal{M}_{\text{D6}}|^2}_{\mathcal{O}(1/\Lambda^4)}, \tag{4.3}$$

where $\mathcal{M}_{\text{SM}}$ denotes the pure–SM amplitude, the $\mathcal{O}(\Lambda^{-2})$ term captures interference between SM and NP amplitudes, and the $\mathcal{O}(\Lambda^{-4})$ term is the pure–NP amplitude.

More generally, the squared EFT contributions to the matrix element are of the form

$$|\mathcal{M}|^2\Big|_{\Lambda^{-4}} = \sum_{i,j}^{n} \left[C_i C_j^* \mathcal{M}_i \mathcal{M}_j^* + (1+\delta_{ij})\text{Re}\left[C_i C_j \mathcal{M}_{ij}\mathcal{M}_{\text{SM}}^*\right]\right], \tag{4.4}$$

where n is the number of operators contributing to the given process, $\mathcal{M}_{\text{SM}}$ is the pure-SM amplitude, and the subscripts i, j denote the operators O_i and O_j. $\mathcal{M}_i$ denotes an amplitude with one insertion of the operator $\mathcal{O}_i$ per Feynman diagram where the Wilson coefficient C_i is factored out. $\mathcal{M}_{ij}$ with $\mathcal{M}_{ij} = \mathcal{M}_{ji}$ denotes an amplitude with insertion of two operators $\mathcal{O}_i$ and $\mathcal{O}_j$ (the case $i = j$ is allowed) per Feynman diagram where the Wilson coefficients C_i and C_j are factored out. In general the Wilson coefficients can be complex, $C_j = C_j^R + i\,C_j^I$.

The $\mathcal{O}(\Lambda^{-4})$ contribution to the matrix element in Eq. (4.4) is a quadratic form

$$Q(C_1^R, C_1^I, C_2^R, C_2^I, ..., C_n^R, C_n^I) = \mathbf{C}^T M \mathbf{C}\,, \tag{4.5}$$

with

$$\mathbf{C} = \begin{pmatrix} C_1^R \\ C_1^I \\ \vdots \\ C_n^R \\ C_n^I \end{pmatrix} = \begin{pmatrix} \tilde{C}_1 \\ \tilde{C}_2 \\ \vdots \\ \tilde{C}_{2n-1} \\ \tilde{C}_{2n} \end{pmatrix} \tag{4.6}$$

and M a symmetric $N \times N$ matrix with $N = 2n$. The $\tilde{}$ notation was introduced to represent the Wilson coefficients with a joint index for real and imaginary parts. Odd indices represent real parts and even indices imaginary parts. By evaluating the $\mathcal{O}(\Lambda^{-4})$ contribution of the squared matrix element for different choices of Wilson coefficients we can extract all components of the matrix M. This allows us to evaluate the matrix element for an arbitrary point $\mathbf{C}$ in the Wilson coefficient parameter space by simply calculating the right hand side of Eq. (4.5).

The matrix M has $N(N+1)/2$ degrees of freedom which can be extracted using N equations for the diagonal entries of M

$$Q(0, \cdots, 0, \tilde{C}_j = 1, 0, \cdots, 0) = M_{jj} \tag{4.7}$$

and $\binom{N}{2} = \frac{N!}{(N-2)!2!}$ equations for the off-diagonal entries of M

$$Q(0, \cdots, 0, \tilde{C}_j = 1, 0, \cdots, 0, \tilde{C}_k = 1, 0, \cdots, 0) = 2M_{jk} + M_{jj} + M_{kk}\,. \tag{4.8}$$

Specific examples, of both single and double operator insertions, of M and the extraction of squared EFT contributions for real and complex Wilson coefficients in the illustrative case of just two operators are given in Section 4.2.1 and Section 4.2.2 respectively.

Run config	Coupling order	C_a	C_b	Contribution
R_{SM}	-	-	-	$\lvert\mathcal{M}_{\text{SM}}\rvert^2$
R_0^a	`NP^2==1`	1	0	$2\text{Re}[\mathcal{M}_{\text{SM}}\mathcal{M}_a^*]$
R_0^b	`NP^2==1`	0	1	$2\text{Re}[\mathcal{M}_{\text{SM}}\mathcal{M}_b^*]$
$R_1^{(1)a}$	`NP==1`	1	0	$\lvert\mathcal{M}_a\rvert^2$
$R_1^{(1)b}$	`NP==1`	0	1	$\lvert\mathcal{M}_b\rvert^2$
$R_2^{(1)}$	`NP==1`	1	1	$R_1^a + R_1^b + 2\text{Re}[\mathcal{M}_a\mathcal{M}_b^*]$

Table 4.1: Accessing EFT contributions using MadGraph.

4.2 The Computational Method

Given the rather general structure of contributions outlined in Section 4.1, the task at hand is to design and implement a computational method, or framework, that allows said structure to be exploited in the pursuit of data–driven, phenomenologically–derived bounds on EFT contributions.

Recall from Eq. (4.3) that, in addition to the squared EFT contributions covered in Section 4.2.1, we also require the SM and SM–NP interference pieces of the full squared amplitude $|\mathcal{M}|^2$. Taking the simple case of two dimension–six operators O_a and O_b, with real–valued C_a and C_b, in order to set the stage we must then obtain the contributions outlined in Table 4.1.[1]

Event samples are produced using MadGraph5_aMC@NLO [39, 40] which allows for direct access to SM and EFT contributions — more detail on this is provided in Section 4.3.4. Using the contributions in Table 4.1 we have that

$$\begin{aligned}|\mathcal{M}|^2 = R_{\text{SM}} + C_a R_0^a + C_b R_0^b + C_a^2 R_1^{(i)a} \\ + C_b^2 R_1^{(i)b} + C_a C_b (R_2^{(i)} - R_1^{(i)a} - R_1^{(i)b})\end{aligned} \quad (4.9)$$

where R_{SM} is the pure-SM contribution and R_i is the run configuration defined using the coupling order and setting the corresponding Wilson coefficient $C_i = 1$.

This means we can reach any point in our Wilson coefficient space simply by generating and analysing the SM and EFT events separately, choosing values for C_a and C_b, and produce our theory predictions by linear combination of the resulting distributions.

[1]The coupling order syntax is that used by MadGraph, with `NP^2==1` and `NP==1` being the $\mathcal{O}(\Lambda^{-2})$ and $\mathcal{O}(\Lambda^{-4})$ contributions respectively.

Contribution	Example	Contribution	Example
$\lvert\mathcal{M}_a\rvert^2$	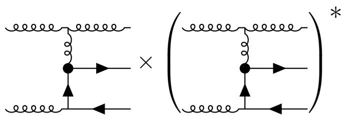	$\mathcal{M}_{aa}\mathcal{M}^*_{\mathrm{SM}}$	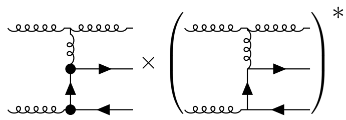
$\lvert\mathcal{M}_b\rvert^2$	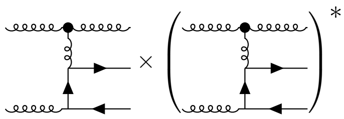	$\mathcal{M}_{bb}\mathcal{M}^*_{\mathrm{SM}}$	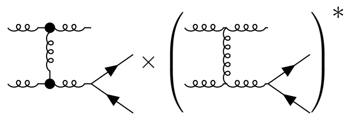
$\mathcal{M}_a\mathcal{M}^*_b$	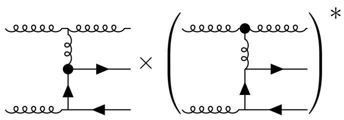	$\mathcal{M}_{ab}\mathcal{M}^*_{\mathrm{SM}}$	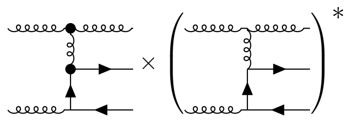

Table 4.2: $\mathcal{O}(\Lambda^{-4})$ contributions to $|\mathcal{M}|^2$.

4.2.1 Real Wilson Coefficients

As a first simple example let us consider two operators $\mathcal{O}_a$ and $\mathcal{O}_b$ with real Wilson coefficients C_a and C_b. The matrix M is given by

$$M = \begin{pmatrix} |\mathcal{M}_a|^2 + 2\mathrm{Re}[\mathcal{M}_{aa}\mathcal{M}^*_{\mathrm{SM}}] & \mathrm{Re}[\mathcal{M}_a\mathcal{M}^*_b] + \mathrm{Re}[\mathcal{M}_{ab}\mathcal{M}^*_{\mathrm{SM}}] \\ \mathrm{Re}[\mathcal{M}_a\mathcal{M}^*_b] + \mathrm{Re}[\mathcal{M}_{ab}\mathcal{M}^*_{\mathrm{SM}}] & |\mathcal{M}_b|^2 + 2\mathrm{Re}[\mathcal{M}_{bb}\mathcal{M}^*_{\mathrm{SM}}] \end{pmatrix} . \qquad (4.10)$$

There are six contributions to the $\mathcal{O}(\Lambda^{-4})$ part of the squared matrix element which are listed in Table 4.2 together with illustrative examples.

Each component of M has one contribution from single operator insertions and one from double operator insertions. We can extract the components of M using Eqs. (4.7) and (4.8).

This is achieved by running MadGraph with different settings for the coupling order and Wilson coefficients as shown in Table 4.3. For the case where two operator insertions are neglected we use runs R_1–R_3 in Table 4.3

$$|\mathcal{M}|^2\Big|_{\Lambda^{-4}} = C_a^2|\mathcal{M}_a|^2 + C_b^2|\mathcal{M}_b|^2 + 2C_aC_b\mathrm{Re}[\mathcal{M}_a\mathcal{M}^*_b] .$$

For the case in which two operator insertions are included we use the runs R_4–R_6

$$|\mathcal{M}|^2\Big|_{\Lambda^{-4}} = C_a^2R_4 + C_b^2R_5 + C_aC_b(R_6 - R_4 - R_5) . \qquad (4.11)$$

If one is interested in a comparison between these two cases all six runs R_1–R_6 have to be used.

Run config	Coupling order	C_a	C_b	Contribution
R_1	`NP==1`	1	0	$\lvert\mathcal{M}_a\rvert^2$
R_2	`NP==1`	0	1	$\lvert\mathcal{M}_b\rvert^2$
R_3	`NP==1`	1	1	$R_1 + R_2 + 2\mathrm{Re}[\mathcal{M}_a\mathcal{M}_b^*]$
R_4	`NP^2==2`	1	0	$\lvert\mathcal{M}_a\rvert^2 + 2\mathrm{Re}[\mathcal{M}_{aa}\mathcal{M}_{\mathrm{SM}}^*]$
R_5	`NP^2==2`	0	1	$\lvert\mathcal{M}_b\rvert^2 + 2\mathrm{Re}[\mathcal{M}_{bb}\mathcal{M}_{\mathrm{SM}}^*]$
R_6	`NP^2==2`	1	1	$R_4 + R_5 + 2\left(\mathrm{Re}[\mathcal{M}_a\mathcal{M}_b^*] + \mathrm{Re}[\mathcal{M}_{ab}\mathcal{M}_{\mathrm{SM}}^*]\right)$

Table 4.3: Extracting individual contributions at $\mathcal{O}(\Lambda^{-4})$ by evaluating the squared matrix element with specific choices for the Wilson coefficients and MadGraph coupling order.

4.2.2 Complex Wilson Coefficients

In the case that we have two operators $\mathcal{O}_a$ and $\mathcal{O}_b$ with complex Wilson coefficients C_a and C_b, we define the Wilson coefficient vector as

$$\mathbf{C} = \begin{pmatrix} C_a^R \\ C_a^I \\ C_b^R \\ C_b^I \end{pmatrix} \tag{4.12}$$

such that the matrix M is given by

$$M = \begin{pmatrix} |\mathcal{M}_a|^2 + 2\mathrm{Re}[\tilde{\mathcal{M}}_{aa}^{\mathrm{SM}}] & -2\mathrm{Im}[\tilde{\mathcal{M}}_{aa}^{\mathrm{SM}}] & \mathrm{Re}[\tilde{\mathcal{M}}_a^b] + \mathrm{Re}[\tilde{\mathcal{M}}_{ab}^{\mathrm{SM}}] & \mathrm{Im}[\tilde{\mathcal{M}}_a^b] - \mathrm{Im}[\tilde{\mathcal{M}}_{ab}^{\mathrm{SM}}] \\ -2\mathrm{Im}[\tilde{\mathcal{M}}_{aa}^{\mathrm{SM}}] & |\mathcal{M}_a|^2 - 2\mathrm{Re}[\tilde{\mathcal{M}}_{aa}^{\mathrm{SM}}] & -\mathrm{Im}[\tilde{\mathcal{M}}_a^b] - \mathrm{Im}[\tilde{\mathcal{M}}_{ab}^{\mathrm{SM}}] & \mathrm{Re}[\tilde{\mathcal{M}}_a^b] - \mathrm{Re}[\tilde{\mathcal{M}}_{ab}^{\mathrm{SM}}] \\ \mathrm{Re}[\tilde{\mathcal{M}}_a^b] + \mathrm{Re}[\tilde{\mathcal{M}}_{ab}^{\mathrm{SM}}] & -\mathrm{Im}[\tilde{\mathcal{M}}_a^b] - \mathrm{Im}[\tilde{\mathcal{M}}_{ab}^{\mathrm{SM}}] & |\mathcal{M}_b|^2 + 2\mathrm{Re}[\tilde{\mathcal{M}}_{bb}^{\mathrm{SM}}] & -2\mathrm{Im}[\tilde{\mathcal{M}}_{bb}^{\mathrm{SM}}] \\ \mathrm{Im}[\tilde{\mathcal{M}}_a^b] - \mathrm{Im}[\tilde{\mathcal{M}}_{ab}^{\mathrm{SM}}] & \mathrm{Re}[\tilde{\mathcal{M}}_a^b] - \mathrm{Re}[\tilde{\mathcal{M}}_{ab}^{\mathrm{SM}}] & -2\mathrm{Im}[\tilde{\mathcal{M}}_{bb}^{\mathrm{SM}}] & |\mathcal{M}_b|^2 - 2\mathrm{Re}[\tilde{\mathcal{M}}_{bb}^{\mathrm{SM}}] \end{pmatrix},$$

where in the interest of brevity we introduce the notation $\tilde{\mathcal{M}}_i^j = \mathcal{M}_i\mathcal{M}_j^\star$.

Allowing only a single operator insertion per diagram, M is given by

$$M = \begin{pmatrix} |\mathcal{M}_a|^2 & 0 & \mathrm{Re}[\mathcal{M}_a\mathcal{M}_b^*] & \mathrm{Im}[\mathcal{M}_a\mathcal{M}_b^*] \\ 0 & |\mathcal{M}_a|^2 & -\mathrm{Im}[\mathcal{M}_a\mathcal{M}_b^*] & \mathrm{Re}[\mathcal{M}_a\mathcal{M}_b^*] \\ \mathrm{Re}[\mathcal{M}_a\mathcal{M}_b^*] & -\mathrm{Im}[\mathcal{M}_a\mathcal{M}_b^*] & |\mathcal{M}_b|^2 & 0 \\ \mathrm{Im}[\mathcal{M}_a\mathcal{M}_b^*] & \mathrm{Re}[\mathcal{M}_a\mathcal{M}_b^*] & 0 & |\mathcal{M}_b|^2 \end{pmatrix}.$$

Run config	Coupling order	C_a^R	C_a^I	C_b^R	C_b^I	Contribution
R_1	`NP==1`	1	0	0	0	$\lvert\mathcal{M}_a\rvert^2$
R_2	`NP==1`	0	0	1	0	$\lvert\mathcal{M}_b\rvert^2$
R_3	`NP==1`	1	0	1	0	$R_1 + R_2 + 2\mathrm{Re}[\mathcal{M}_a \mathcal{M}_b^*]$
R_4	`NP==1`	1	0	0	1	$R_1 + R_2 + 2\mathrm{Im}[\mathcal{M}_a \mathcal{M}_b^*]$
R_5	`NP^2==2`	1	0	0	0	$\lvert\mathcal{M}_a\rvert^2 + 2\mathrm{Re}[\mathcal{M}_{aa}\mathcal{M}_{\mathrm{SM}}^*]$
R_6	`NP^2==2`	0	1	0	0	$\lvert\mathcal{M}_a\rvert^2 - 2\mathrm{Re}[\mathcal{M}_{aa}\mathcal{M}_{\mathrm{SM}}^*]$
R_7	`NP^2==2`	0	0	1	0	$\lvert\mathcal{M}_b\rvert^2 + 2\mathrm{Re}[\mathcal{M}_{bb}\mathcal{M}_{\mathrm{SM}}^*]$
R_8	`NP^2==2`	0	0	0	1	$\lvert\mathcal{M}_b\rvert^2 - 2\mathrm{Re}[\mathcal{M}_{bb}\mathcal{M}_{\mathrm{SM}}^*]$
R_9	`NP^2==2`	1	1	0	0	$R_5 + R_6 - 2\mathrm{Im}[\mathcal{M}_{aa}\mathcal{M}_{\mathrm{SM}}^*]$
R_{10}	`NP^2==2`	1	0	1	0	$R_5 + R_7 + \mathrm{Re}[\mathcal{M}_a\mathcal{M}_b^*] + \mathrm{Re}[\mathcal{M}_{ab}\mathcal{M}_{\mathrm{SM}}^*]$
R_{11}	`NP^2==2`	1	0	0	1	$R_5 + R_8 + \mathrm{Im}[\mathcal{M}_a\mathcal{M}_b^*] + \mathrm{Im}[\mathcal{M}_{ab}\mathcal{M}_{\mathrm{SM}}^*]$
R_{12}	`NP^2==2`	0	1	1	0	$R_6 + R_7 - \mathrm{Im}[\mathcal{M}_a\mathcal{M}_b^*] - \mathrm{Im}[\mathcal{M}_{ab}\mathcal{M}_{\mathrm{SM}}^*]$
R_{13}	`NP^2==2`	0	1	0	1	$R_6 + R_8 + \mathrm{Re}[\mathcal{M}_a\mathcal{M}_b^*] - \mathrm{Re}[\mathcal{M}_{ab}\mathcal{M}_{\mathrm{SM}}^*]$
R_{14}	`NP^2==2`	0	0	1	1	$R_7 + R_8 - 2\mathrm{Im}[\mathcal{M}_{bb}\mathcal{M}_{\mathrm{SM}}^*]$

Table 4.4: Extract individual contributions to the squared matrix at $\mathcal{O}(\Lambda^{-4})$.

Again, the components of M can be extracted by using Eq. (4.7) and Eq. (4.8) as shown in Table 4.4 If two operator insertions are neglected we obtain

$$\begin{aligned} |\mathcal{M}|^2\Big|_{\Lambda^{-4}} = &\left[(C_a^R)^2 + (C_a^I)^2\right] R_1 + \left[(C_b^R)^2 + (C_b^I)^2\right] R_2 \\ &+ \left[C_a^R C_b^R + C_a^I C_b^I\right](R_3 - R_1 - R_2) \\ &+ \left[C_a^R C_b^I - C_a^I C_b^R\right](R_4 - R_1 - R_2)\,, \end{aligned} \tag{4.13}$$

and if two operator insertions are included we instead obtain

$$\begin{aligned} |\mathcal{M}|^2\Big|_{\Lambda^{-4}} = &(C_a^R)^2 R_5 + (C_a^I)^2 R_6 + (C_b^R)^2 R_7 + (C_b^I)^2 R_8 \\ &+ C_a^R C_a^I (R_9 - R_5 - R_6) + C_a^R C_b^R (R_{10} - R_5 - R_7) \\ &+ C_a^R C_b^I (R_{11} - R_5 - R_8) + C_a^I C_b^R (R_{12} - R_6 - R_7) \\ &+ C_a^I C_b^I (R_{13} - R_6 - R_8) + C_b^R C_b^I (R_{14} - R_7 - R_8)\,. \end{aligned} \tag{4.14}$$

4.3 A Tool Like Any Other

4.3.1 Data Structure

With the structure outlined in Section 4.1 and uncertainties introduced in Section 3.3 as inspiration, the TopFitter framework is designed and built around an equivalent data structure. This structure, illustrated in Fig. 4.2, is a three-dimensional array with axes corresponding to measurement, contribution, and variation. The underlying data structure leverages xarray [41] – a Python package which provides labelled and performant N-dimensional arrays. The choice of library and design carries with it a few immediate and longer-term benefits, namely:

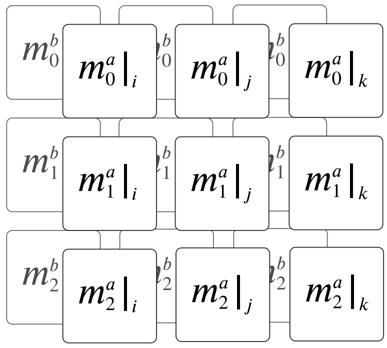

Figure 4.2: Data structure illustration.

Maintainability: Labelled, clean API allows for an expressive and easily understood codebase as well as the rapid addition of new or improved analysis/observable plugins as and when required.

Ease of use: As above, though with additional benefit of interoperability with widely-used package Pandas [42] and, indeed, the wider 'scientific' Python stack.

Extensibility: Easy addition and manipulation of measurements, EFT contributions, and systematic variations. This allows the rapid inclusion of improvements in terms of both experimental data coverage/quality and theoretical advances – be they in higher-order (in QCD or SMEFT expansion) EFT models or, e.g., improved PDF sets.

Performance: The underlying, contiguous array is amenable to vectorised/single instruction multiple data (SIMD) numerical operations and, if desired, the use of just-in-time (JIT) compilers such as Numba [43].

Scalability: Built-in support for parallel and distributed processing. Whilst distributed compute is not currently used it may become important at a later date if resource constraints become dominant. The TopFitter framework is well–placed to handle such eventualities.

With this core object in place we can then proceed to "build out" a framework that is both general and modular in the context of input, compute, and output.

4.3.2 Plugins

In keeping with our as-general-as-possible approach to constructing a viable and useful EFT analysis toolset, the TopFitter framework is implemented with plugin-driven architecture around our core data structure. The currently implemented plugins belong, broadly speaking, to four categories; here we will discuss each in turn.

Observables: Used to analyse event samples and produce aggregate results such as total/differential cross-sections or the required pieces for, e.g., asymmetry measurements.

Systematics: Used to calculate systematic uncertainties using the set of prediction variations according to a user–defined prescription for error estimation.

Post-hooks: Used to include predictions or carry out tasks which are not directly linked to event samples. Examples are analytical predictions, inclusion of higher-order/decay corrections, calculation of cross-measurement ratios, asymmetries, etc.

Limit-setting: These plugins allow for changes and/or improvements in the *fitting* piece of our EFT workflow. Examples include loss functions, minimisation routines/algorithms, and bound-finding algorithms.

4.3.3 User Input

The framework architecture allows for a lot of automation which is exploited by the use of low/no–code human–readable configuration files to drive common tasks, lowering friction and allowing for rapid iteration, experimentation, and updating of results as new experimental input or theoretical improvements become available.

The main tasks exposed via no–code configuration are in the definition of experimental analyses, colliders, processes, and global/targeted fits; an outline of the configuration files is provided here.

Analysis Description File

The definition and experimental results of analyses is provided using an Analysis Description File (ADF) for each analysis, with the configuration blocks being:

Metadata: General information (title, INSPIRE ID) as well as specific values used when obtaining event samples (top quark mass, collider, unfolding).

Processes: User-provided set of processes studied in a given analysis, allowing for multi-process analyses to be handled. Each process also lists which measurements should enter fits, any phase-space cuts to be applied when generating events, and any cross-measurement/whole-dataset correlation or covariance matrices.

Observables: The set of measurements in the analysis, each containing information essential to setting limits (observed results and correlation/covariance matrices) and generating a matching theory analysis (binning, units, scaling).

Correlations: An analysis-level field allowing for the inclusion of any cross-process correlation or covariance data in addition to bin–to–bin or cross–distribution matrices within a single process.

The use of ADFs — the core configuration input to TopFitter — to drive event generation and analysis is described in more detail in Sections 4.3.4 and 4.3.5.

Additionally, simple YAML files can be used to define:

Collider: Define the beam types (e.g., pp or $p\bar{p}$), beam energies, and/or collider-specific cuts to be passed through to the event generator.

Processes: Used to list relevant operators, event generation configuration such as which model to use, decay channels, and process definitions. Process definition can be split between SM/EFT, e.g., direct decay product syntax for LO (EFT) and not for NLO (SM) when using MadGraph.

Fits: Used to list analyses to be included, data configuration such as order in Λ, maximum operator insertions per diagram, and fit settings — loss function, optimisation method, dynamic subset selection.

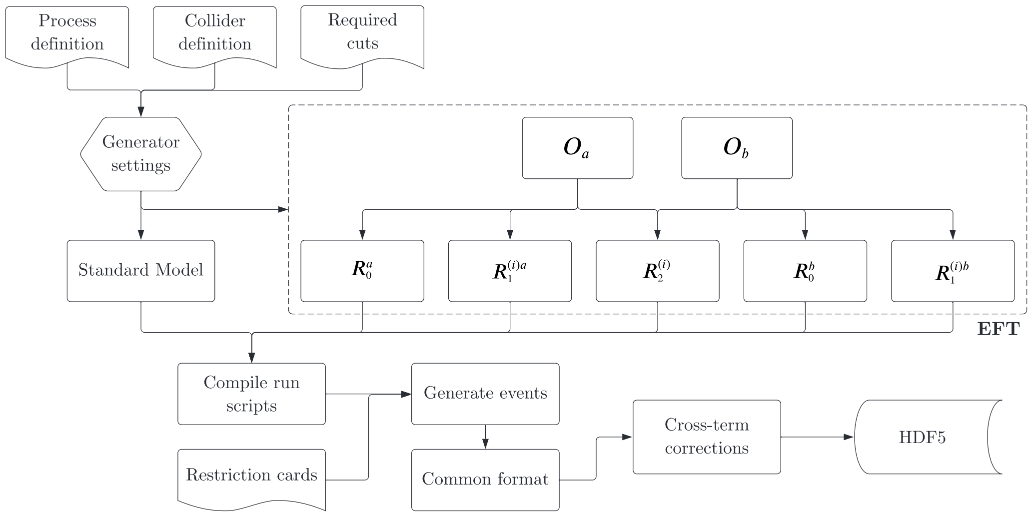

Figure 4.3: Contribution event generation illustration.

4.3.4 Event Generation

The event generation process, outlined in Fig. 4.3, uses the configuration files introduced in Section 4.3.3 to determine generator settings, pull the relevant operators from pre-defined processes, generate all required submission files, and submits the jobs to be processed in parallel.

Restriction cards are used to increase performance by removing unnecessary diagrams before event generation, with said cards being automatically generated if not present.

Standard Model events are generated using the default MadGraph NLO model and passed through a custom MadAnalysis [44] routine to produce weighted samples; this enables the direct computation of per–measurement NLO corrections during the analysis step. EFT events are generated using the SmeftSim [45] model, provided via the Universal FeynRules Output (UFO) [46] format, by default though this is configurable.

Due to the need for showering of NLO SM event samples involving decay processes, all contributions — SM and EFT — for these processes pass through a generation workflow involving MadSpin [47], showering via Pythia8 [48], and a custom general–purpose Rivet [49] analysis which produces unweighted parton-level event samples.

4.3.5 Matched Analyses

Using the Analysis Description File (ADF) outlined in Section 4.3.3 we can automatically build an analysis routine that matches the experimental analysis. This routine is then applied to event samples for all relevant contributions to produce per-contribution, per-variation results to be used in producing theory predictions.

In addition to the raw observable values, this step allows for the automatic injection of any required parameters in the case that post-hooks will be required to make predictions or apply specific corrections.

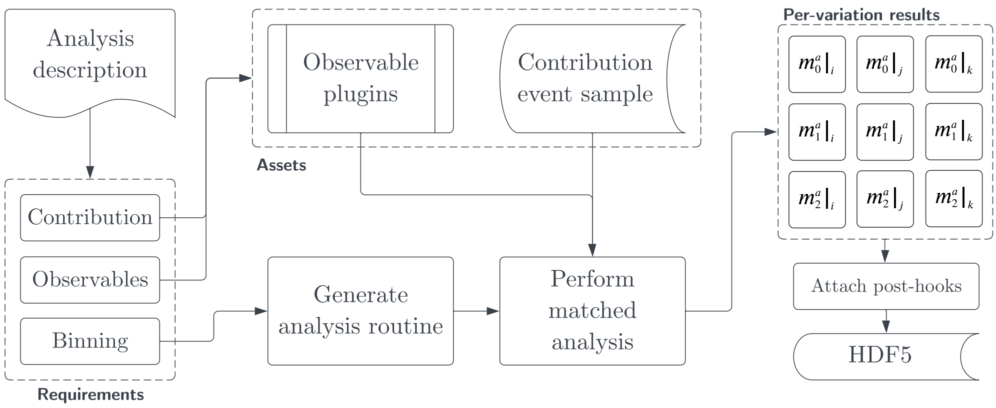

Figure 4.4: Per-contribution matched analysis illustration.

The form taken by a given analysis depends on the level of unfolding required to match the experimental analysis, with parton-level analyses being handled by TopFitter and particle-level analyses handled by Rivet.

One edge case does exist, in that parton-level analyses of processes involving top quark decay requires both tools; parton-level events are showered using Pythia and MadSpin, then piped through a custom Rivet routine which produces unweighted, LHE-esque[1] event samples which are used by TopFitter to perform the analysis.

The framework also has support for the direct use of Rivet analyses, be that for particle–level results or to avoid the requirement of complex and/or numerous observable plugins for a small number of parton–level analyses.

[1] The Les Houches Event (LHE) format [50, 51] is a standardised data exchange format for process and event information.

4.3.6 Theory Predictions

The theory prediction pipeline is outlined in Fig. 4.5, with

$$p_\alpha^\beta|_\gamma = \frac{C_\beta}{C_\beta^{\text{fix}}} m_\alpha^\beta|_\gamma$$

being the per-contribution, per-variation predictions where C_β is the desired Wilson coefficient value and C_β^{fix} the fixed value, typically $C_\beta^{\text{fix}} = 1$, used to generate the events entering our per-contribution analysis step;

$$p_\alpha^{\text{th.}}|_\gamma = \sum_\beta p_\alpha^\beta|_\gamma$$

is the per-variation prediction with all SMEFT contributions combined.

Finally, we have our theory predictions and uncertainties

$$\left\{p_\alpha^{\text{th.}}, \delta p_\alpha^{\text{th.}}\right\} = F(P_\alpha)\,,$$

where F is a user-defined uncertainty estimator acting on the set of per-variation predictions $P_\alpha = \left\{p_\alpha^{\text{th.}}|_0, \ldots, p_\alpha^{\text{th.}}|_n\right\}$ that have optionally been passed through additional processing steps, e.g., the computing of ratios or application of higher-order corrections.

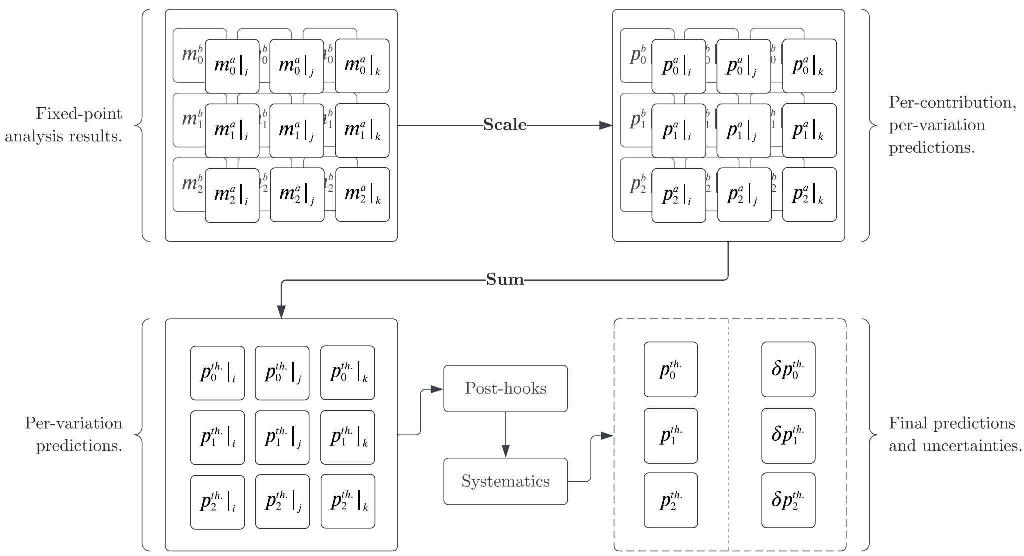

Figure 4.5: SMEFT prediction illustration.

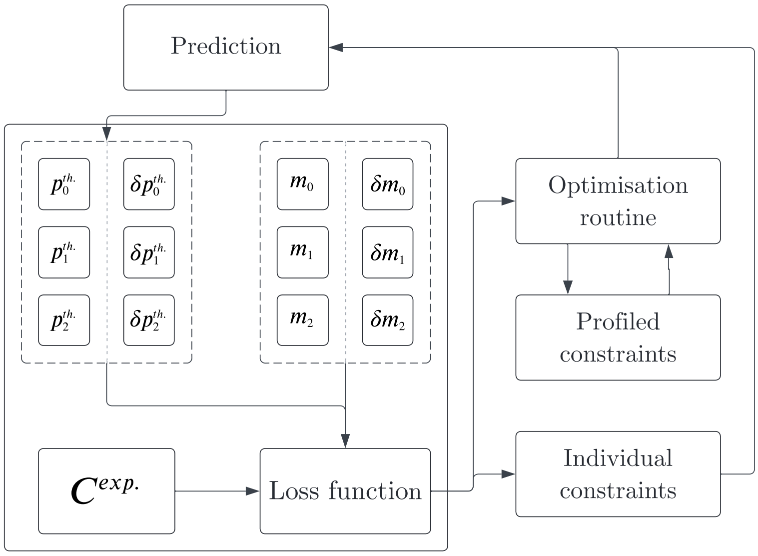

Figure 4.6: SMEFT constraint flowchart.

4.3.7 Limit Setting

In order to carry out limit–setting, a data structure of the form illustrated in Section 4.3.1 is first constructed using a list of analysis IDs. This structure also merges and exposes correlation/covariance, higher–order correction, and experimental reference data in a standardised way.

Implementation–specific abstractions are provided to expose any given loss function plugin results to existing optimisation routines provided by, for example, SciPy [52]. The flow illustrated in Fig. 4.6 can then be followed to determine the individual and/or profiled bounds for a given operator or set of operators; the difference between these bound types is shown in Fig. 4.7, where it can be seen that individual bounds correspond to the intersection of a given confidence area/volume with the axis represented by the parameter under study, and profiled bounds correspond to the projection of said volume on to the axis.

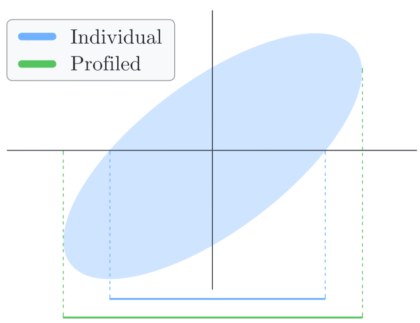

Figure 4.7: Illustration of bound types.

Chapter 5

Global Fit to Top Sector Measurements

In Chapters 1 and 2 we introduced the Standard Model as our current — and frustratingly experimentally consistent — ‘best guess’ as to the fundamental nature of Nature and discussed the motivations of using effective field theory approaches to, in a (mostly) model-independent way, capture the low-energy effects of as-yet unknown high-energy physics. Chapter 3 provided a brief overview of physics in a particle-collider context and the use of measured scattering cross-sections as a means to perform indirect searches for New Physics, with particular attention paid to physics involving the top quark. The general architecture and statistical methodologies underpinning the TopFitter framework were covered in Chapter 4, beginning with the mathematical structure of our dimension-six extended SMEFT Lagrangian and matrix elements, passing through analysis definition, event sample generation, and limit-setting via SMEFT predictions of experiment-matched sets of analyses. Bringing this together, then, this chapter will cover a *specific* application of the framework to perform a set of fits — global and more targeted in nature — sharing a common statistical treatment.

This chapter has the following structure: we will introduce the comprehensive set of top-relevant experimental measurements entering these fits in Section 5.1. Section 5.2 describes the numerical and analytical theory predictions involved, as well as higher-order QCD corrections and treatment of EFT-induced changes in decay process predictions. We will then cover with more specificity the statistical treatment of uncertainties, and measures taken to avoid over- or underestimating EFT effects via the careful handling of correlated measurements, in Section 5.3. Section 5.4 provides an overview of the data selection and limit setting methodology used to obtain phenomenologically-derived bounds on the EFT operators provided and discussed in Section 5.5, with a summary of results and outlook provided in Section 5.6.

5.1 Experimental Input

The experimental measurements entering the fit listed in Table 5.1 comprise 823 individual measurements from a number of top-relevant processes and drawn from Tevatron and LHC — 7, 8, and 13 TeV — analyses. All data considered in this first global fit are at parton–level, though we note that particle–level fits are possible using the TopFitter framework.

In addition to top production observables, top decay observables such as spin and angular measurements are included; this allows the study of different operator sets, specifically the inclusion of lepton–top operators, as well as complementary views on operators previously studied in the context of top quark data.

5.2 Theoretical Input

Top-Relevant Operators

Considering operators in Tables 2.1 and 2.2 involving at least one top quark field and respecting the assumptions of flavour symmetry $U(2)_q \times U(2)_u \times U(2)_d$ in the first two quark generations, lepton universality and lepton flavour conservation, $\mathcal{B}$ and $\mathcal{CP}$ conservation, leaves 42 effective operators. From these we include all dipole operators, charged and neutral current operators, heavy–light four–quark operators, and lepton–top operators.

In addition to said operators with direct involvement of the top quark the non-top operator O_G which, though well–constrained by jet physics [125, 126], contributes to the gluon channel in top–pair production and is therefore included. This leaves a total of 31 operators to be studied, listed in Table 5.2 along with indications of to which processes, and at which order, each contributes.

Predictions

Although the majority of predictions are made via the analysis of event samples as described in Chapter 4, we use analytical results where possible. This currently includes the top quark decay width, Γ_t, as well as W boson helicity fractions F_0, F_L, and F_R.

Experiment	arχiv	Process	N_{dof}	Experiment	arχiv	Process	N_{dof}
ATLAS	1201.1889 [53]	$t\bar{t}$	1		1503.05027 [89]	tj	1
	1205.2067 [54]	$t\bar{t}$	1		1709.04894 [90]	$t\bar{t}$	6
	1205.2484 [55]	$t\bar{t}$	2			$t\bar{t}$ $(\ell\ell)$	1
	1211.7205 [56]	$t\bar{t}$	1	CMS	1203.6810 [91]	$t\bar{t}$	1
	1311.6724 [57]	$t\bar{t}$	16		1209.4533 [92]	tj	1
	1406.5375 [58]	$t\bar{t}$	2		1211.2220 [93]	$t\bar{t}$	22
	1406.7844 [59]	tj	18		1301.5755 [94]	$t\bar{t}$	1
	1407.0371 [60]	$t\bar{t}$	12		1302.0508 [95]	$t\bar{t}$	1
	1407.0573 [61]	$t\bar{t}$	1		1308.3879 [96]	$t\bar{t}$	2
	1407.4314 [62]	$t\bar{t}$ $(\ell\ell)$	2		1402.3803 [97]	$t\bar{t}$ $(\ell\ell)$	6
	1509.05276 [63]	$t\bar{t}W$	1		1403.7366 [98]	tj	2
		$t\bar{t}Z$	1		1505.04480 [99]	$t\bar{t}$	23
	1510.07478 [64]	$t\bar{t}$ $(\ell\ell)$	7		1510.01131 [100]	$t\bar{t}W$	1
	1512.06092 [65]	$t\bar{t}$	1			$t\bar{t}Z$	1
	1606.02699 [66]	$t\bar{t}$	1		1511.02138 [101]	tj (μ)	10
	1607.07281 [67]	$t\bar{t}$	15		1601.01107 [102]	$t\bar{t}$ $(\ell\ell)$	187
	1609.03920 [68]	tj	3		1602.09024 [103]	$t\bar{t}$	2
	1612.02577 [69]	$t\bar{t}$	2		1603.02303 [104]	$t\bar{t}$	2
	1612.07231 [70]	tW	1		1603.06221 [105]	$t\bar{t}$ $(\ell\ell)$	104
	1702.08309 [71]	tj (ℓ)	7		1605.09047 [106]	$t\bar{t}$	2
	1702.08839 [72]	$t\bar{t}$	1		1701.06228 [107]	$t\bar{t}$	1
	1707.05393 [73]	tj	1		1703.01630 [108]	$t\bar{t}$	56
	1709.04207 [74]	$t\bar{t}$	1		1708.07638 [109]	$t\bar{t}$	24
	1710.03659 [75]	tZj	1		1711.02547 [110]	$t\bar{t}W$	1
	1901.03584 [76]	$t\bar{t}W$	1			$t\bar{t}Z$	1
		$t\bar{t}Z$	1		1805.07399 [111]	tW	1
	1903.07570 [77]	$t\bar{t}$ $(e\mu)$	20		1811.06625 [112]	$t\bar{t}$	34
	2002.07546 [78]	tjZ $(\ell\ell)$	1		1812.05900 [113]	tjZ $(\ell\ell)$	1
ATLAS,	1709.05327 [79]	$t\bar{t}$	1		1812.10505 [114]	$t\bar{t}$	1
CMS	1902.07158 [80]	tW	2		1812.10514 [115]	tj	3
		tb	1		1904.05237 [116]	$t\bar{t}$	33
CDF	0903.2850 [81]	$t\bar{t}$	10		1907.03729 [117]	$t\bar{t}$ $(\ell\ell)$	110
	1211.4523 [82]	$t\bar{t}$	2		1907.11270 [118]	$t\bar{t}Z$ $(\ell\ell)$	7
	1306.2357 [83]	$t\bar{t}$	5	DØ	1011.6549 [119]	$t\bar{t}$	2
	1308.4050 [84]	$t\bar{t}$	1		1201.4156 [120]	tj	1
	1410.4909 [85]	tj, tb	1		1308.6690 [121]	$t\bar{t}$ $(\ell\ell)$	3
	1602.09015 [86]	$t\bar{t}$	2		1401.5785 [122]	$t\bar{t}$	14
CDF, DØ	1309.7570 [87]	$t\bar{t}$	1		1405.0421 [123]	$t\bar{t}$	4
	1402.5126 [88]	tb	1		1605.06168 [124]	$t\bar{t}$	1
						Total:	823

Table 5.1: Experimental results entering the fit.

	Top Pair Production			Single Top Production				Top Decay Processes			
	$t\bar{t}$	$t\bar{t}W$	$t\bar{t}Z$	tb	tj	tW	tZj	$t\bar{t}$ $(\ell\ell)$	$t\bar{t}Z$ $(\ell\ell)$	tj (ℓ)	tjZ $(\ell\ell)$
O_G	$\oplus$		$\oplus$					$\oplus$	$\oplus$		
O_{dW}^{33}		$\ominus$	$\ominus$	$\ominus$	$\ominus$	$\ominus$	$\ominus$	$\ominus$	$\ominus$	$\ominus$	$\ominus$
$O_{\varphi q}^{(1)33}$			$\oplus$				$\oplus$		$\oplus$		$\oplus$
$O_{\varphi q}^{(3)33}$		$\ominus$	$\oplus$	$\oplus$	$\oplus$	$\oplus$	$\oplus$	$\oplus$	$\oplus$	$\oplus$	$\oplus$
$O_{\varphi u}^{33}$			$\oplus$				$\oplus$		$\oplus$		$\oplus$
$O_{\varphi ud}^{33}$		$\ominus$		$\ominus$	$\ominus$	$\ominus$	$\ominus$	$\ominus$		$\ominus$	$\ominus$
O_{uB}^{33}			$\oplus$				$\oplus$		$\oplus$		$\oplus$
O_{uG}^{33}	$\oplus$	$\oplus$	$\oplus$			$\oplus$		$\oplus$	$\oplus$		
O_{uW}^{33}		$\ominus$	$\oplus$	$\oplus$	$\oplus$	$\oplus$	$\oplus$	$\oplus$	$\oplus$	$\oplus$	$\oplus$
$O_{qd}^{(1)33ii}$	$\ominus$		$\ominus$					$\ominus$	$\ominus$		
$O_{qd}^{(8)33ii}$	$\oplus$		$\oplus$					$\oplus$	$\oplus$		
$O_{qq}^{(1)i33i}$	$\oplus$	$\oplus$	$\oplus$	$\oplus$	$\oplus$		$\oplus$	$\oplus$	$\oplus$	$\oplus$	$\oplus$
$O_{qq}^{(1)ii33}$	$\ominus$	$\ominus$	$\ominus$					$\ominus$	$\ominus$		
$O_{qq}^{(3)i33i}$	$\oplus$	$\oplus$	$\oplus$	$\oplus$	$\oplus$		$\oplus$	$\oplus$	$\oplus$	$\oplus$	$\oplus$
$O_{qq}^{(3)ii33}$	$\ominus$	$\ominus$	$\ominus$	$\oplus$	$\oplus$		$\oplus$	$\ominus$	$\ominus$	$\oplus$	$\oplus$
$O_{qu}^{(1)33ii}$	$\ominus$		$\ominus$					$\ominus$	$\ominus$		
$O_{qu}^{(1)ii33}$	$\ominus$	$\ominus$	$\ominus$					$\ominus$	$\ominus$		
$O_{qu}^{(8)33ii}$	$\oplus$		$\oplus$					$\oplus$	$\oplus$		
$O_{qu}^{(8)ii33}$	$\oplus$	$\oplus$	$\oplus$					$\oplus$	$\oplus$		
$O_{ud}^{(1)33ii}$	$\ominus$		$\ominus$					$\ominus$	$\ominus$		
$O_{ud}^{(8)33ii}$	$\oplus$		$\oplus$					$\oplus$	$\oplus$		
O_{uu}^{i33i}	$\oplus$		$\oplus$					$\oplus$	$\oplus$		
O_{uu}^{ii33}	$\ominus$		$\ominus$					$\ominus$	$\ominus$		
O_{eu}^{ii33}									$\oplus$		$\oplus$
O_{ledq}^{ii33}								$\ominus$	$\ominus$	$\ominus$	$\ominus$
$O_{lequ}^{(1)ii33}$								$\ominus$	$\ominus$	$\ominus$	$\ominus$
$O_{lequ}^{(3)ii33}$								$\ominus$	$\ominus$	$\ominus$	$\ominus$
$O_{lq}^{(1)ii33}$									$\oplus$		$\oplus$
$O_{lq}^{(3)ii33}$								$\oplus$	$\oplus$	$\oplus$	$\oplus$
O_{lu}^{ii33}									$\oplus$		$\oplus$
O_{qe}^{33ii}									$\oplus$		$\oplus$

Table 5.2: The operators included and processes to which they contribute. Operators contributing at $\mathcal{O}(\Lambda^{-2})$ are denoted by $\oplus$ and those contributing at only $\mathcal{O}(\Lambda^{-4})$ by $\ominus$.

Corrections

Higher-order QCD Corrections

In order to maintain control over and enable the accurate calculation of systematic uncertainties on SMEFT predictions, event samples for each contribution are generated to the highest order available where all scale and PDF variations can be included, summarised in Table 5.3 and discussed below.

Whilst recent advances now mean EFT contributions can be calculated at NLO [127], and the TopFitter framework is designed to be model agnostic, the results here have all EFT contributions at leading order only. Inclusion of NLO effects on EFT contributions via the swap from SmeftSim to Smeft@NLO [127] as the input model is, though entirely possible, out of scope for this study. Standard Model contributions are at NLO in most cases, however total cross-section measurements for top-pair and single-top production processes are calculated at NNLO using Hathor [128].

Contribution	Process	Observable	QCD order	Source
Standard Model	$t\bar{t}$, tj, tb	σ_{tot}	NNLO	Hathor
	All else	All else	NLO	MadGraph
EFT	All	All	LO	MadGraph

Table 5.3: Higher-order QCD correction breakdown

Whereas prior TopFitter results [129, 130] applied NLO corrections calculated for the central variation/PDF member only, we now extract NLO k-factors for all variations entering systematic uncertainty estimates on a per-measurement basis.

To mitigate the impact of missing NNLO corrections for differential cross-section measurements we use only normalised results, i.e., for observable X the distribution is of the form $\frac{1}{\sigma}\frac{\partial\sigma}{\partial X}$. The lack of NNLO SM effects does however force us to omit any measurements of the forward-backward asymmetry, A_{FB}, from the fit — these measurements cannot be included here in good faith as the impact of higher-order SM corrections is known to be significant and as such NLO predictions are known to be mis-modelled.

Decay Observables

Whilst the inclusion of processes involving top decay carries the dual benefits of increased data points and access to lepton–top operator constraints, it also carries with it an additional complication — these processes have a dependence on the top quark width, Γ_t. In the narrow–width approximation of the top quark propagator we have that

$$\frac{1}{(p^2 - m_t^2) - \Gamma_t^2 m_t^2} \to \frac{\pi}{\Gamma_t m_t}\delta(p^2 - m_t^2)\,, \tag{5.1}$$

meaning each decaying top quark contributes a factor of $\frac{1}{\Gamma_t}$. The top width itself depends on the values of (some[1]) Wilson coefficients, such that

$$\Gamma_t = \Gamma_t^{\mathrm{SM}} + C_i \Gamma_{t,i}^{(1)} + C_i C_j \Gamma_{t,ij}^{(1)}\,. \tag{5.2}$$

This behaviour invalidates the piecewise approach used for processes with no top decay involved, as we must also include EFT–induced changes in the top decay width. Fortunately Γ_t has no kinematic dependence and therefore factors out of the cross-section,

$$\sigma(pp \to n \times t \to \text{decay products}) = \frac{\tilde{\sigma}}{\Gamma_t^n}\,,$$

where n is the number of top (anti)quarks and $\tilde{\sigma}$ is the cross-section in the narrow width approximation with the top decay width factored out.

We can therefore compute the polynomial coefficients of $\tilde{\sigma}$ and Γ_t once and construct our cross-section prediction, σ, for any point in our Wilson coefficient space, $\mathbb{C}$, as

$$\sigma(\mathbb{C}) = \frac{\tilde{\sigma}^{\mathrm{SM}} + C_i \tilde{\sigma}_i^{(1)} + C_i C_j \tilde{\sigma}_{ij}^{(2)}}{\left(\Gamma_t^{\mathrm{SM}} + C_i \Gamma_{t,i}^{(1)} + C_i C_j \Gamma_{t,ij}^{(2)}\right)^n} = \frac{\tilde{\sigma}(\mathbb{C})}{\Gamma_t(\mathbb{C})}\,.$$

So in order to make our theory predictions for processes involving top decay we generate the results using the method expressed in Eq. (4.9) using the SM top width, Γ_t^{SM}, and add the additional step of correcting for top width changes after the usual scaling of contributions to make the prediction at the point $\mathbb{C}$. Specifically, we then have

$$\sigma(\mathbb{C}) = \left(\frac{\Gamma_t^{\mathrm{SM}}}{\Gamma_t(\mathbb{C})}\right)^2 \tilde{\sigma}(\mathbb{C})\,.$$

The validity of this correction process has been confirmed numerically for both inclusive and differential cross-sections. Further details, and tabulated results, can be found in Appendix A.

[1]Specifically, changes in Γ_t are induced by non-zero values of C_{uW}^{33}, C_{dW}^{33}, $C_{\varphi ud}^{33}$, and $C_{\varphi q}^{(3)33}$.

5.3 Statistical Treatment

Our statistical treatment is chosen to minimise any additional assumptions entering the fit, as well as avoiding under- or overestimating sensitivity to SMEFT contributions. This section discusses the approaches used for handling uncertainties and the use of experimental correlation matrices to maximise numerical stability and minimise assumptions that could otherwise induce double-counting of events.

5.3.1 Treatment of Uncertainties

Experimental Uncertainties

Although we have little control over experimental uncertainties we do, owing to the need for symmetric uncertainties in our loss function, shift the value to the center of the reported uncertainty bounds if asymmetric errors are provided.

If reported separately all sources of experimental uncertainty are added in quadrature, with the exception that the final uncertainty is extracted from the covariance matrix if provided. Where correlation data is provided this is used in the fit, with care taken to avoid imposing any assumptions as outlined in Section 5.3.2.

Theoretical Uncertainties

The theory uncertainties included follow the PDF4LHC prescription [131], using all members of the `PDF4LHC15_nlo_30_pdfas` PDF set to obtain PDF uncertainties and varying the renormalisation and factorisation scales independently as $\mu_{r,f}/2 < \mu_{r,f} < 2\mu_{r,f}$. We choose $\mu_{r,f} = m_t = 172.5$ GeV[1] as the central scale, and the systematic theory uncertainties are arrived at using

$$\delta^{\mathrm{PDF}+\alpha_s+\mu_{r,f}}\sigma = \sqrt{(\delta^{\mathrm{PDF}}\sigma)^2 + (\delta^{\alpha_s}\sigma)^2 + (\delta^{\mu_{r,f}}\sigma)^2}\,,$$

where

$$\delta^{\mathrm{PDF}}\sigma = \sqrt{\sum_{k=1}^{N_{\mathrm{mem}}}(\sigma^{(k)} - \sigma^{(0)})^2},$$

$$\delta^{\alpha_s}\sigma = \frac{\sigma(\alpha_s = 0.1195) - \sigma(\alpha_s = 0.1165)}{2}\,,$$

and $\delta^{\mu_{r,f}}\sigma$ is taken as the envelope of values produced by the nine scale variations.

[1] This is the default value, although m_t is set to match that used in the experimental analysis where provided.

5.3.2 Treatment of Correlated Measurements

Measurement Pooling

In order to avoid imposing correlation/covariance assumptions, we treat each analysis as a 'pool' of measurements,

$$P_{\text{total}} = \{P_{\text{full}},\, P_{\text{partial}},\, P_{\text{none}}\}\ ,$$

where the subscripts on the RHS denote the completeness of the covariance data. Analyses providing partial, or bin-to-bin, covariances are treated as a pool of distributions and analyses with no experimental covariance data as a pool of individual bins. The subset entering the fit is then $A_{\text{fit}} = P_{\text{full}} \cup A_{\text{partial}} \cup A_{\text{none}}$, where

$$\begin{aligned} A_{\text{partial}} &= \left\{ \underset{\text{dist.}}{\text{select}}\, f(\text{dist.}) \,|\, \text{dist.} \in X,\, X \in P_{\text{partial}} \right\}, \\ A_{\text{none}} &= \left\{ \underset{\text{bin}}{\text{select}}\, f(\text{bin}) \,|\, \text{bin} \in X,\, X \in P_{\text{none}} \right\}, \end{aligned}$$

for some selection operator acting on the result of arbitrary function f.

This means that even if we have a substantial dataset in principle from a given analysis, we take the conservative decision to include only a single bin in the event that no correlation data is available. We operate under the assumption that analyses are statistically independent and therefore uncorrelated, with care being taken to avoid the inclusion of superseded results.

Distributions

All differential distributions entering the fit are normalised to unity resulting in the covariance matrix for each distribution being necessarily singular, i.e.

$$b_j = 1 - \sum_{i \neq j}^{N} b_i\, .$$

for a distribution comprised of N bins, b. This means that, for each normalised distribution, we must drop precisely one bin. We choose as our selection criteria the numerical stability of the resulting covariance matrix as measured by the condition number,

$$\kappa(A) = \|A\| \|A^{-1}\|\, .$$

In choosing the optimal bin to drop we compute the condition numbers of all possible outcomes and select the result with the most well-conditioned covariance matrix. In the event that more than one choice exhibits the same condition number we drop the bin with the largest relative experimental uncertainty.

5.4 Limit Setting

5.4.1 Dynamic Subset Selection

Given that we need to choose some subset of the overall experimental input to the fit to avoid double-counting of events or incorrectly estimating our sensitivity to EFT effects as outlined in Section 5.3.2, we need to decide *how* to choose said subset. Two examples of selection criteria, based on sensitivity and precision, are discussed here.

Operator Sensitivity

The first of our input selection methods is to choose a minimal-assumption set of measurements based on sensitivity to the operator in question. Here we compare the prediction at a fixed value[1] to the Standard Model prediction, 'blinding' the process to avoid biasing the selection with experimental data. We then choose from each pool the bin/distribution which produces the most significant deviation,

$$A_x = \left\{ \arg\max_x f(x) \,|\, x \in X,\, X \in P_x \right\},$$

where

$$f(x) = \frac{\left(O_i - C_i^{\mathrm{SM}}\right)^2}{\sigma_i^2}\,.$$

The resulting subset is then used to place constraints on that operator. This selection method was used to produce the results in this study.

Measurement Precision

Another approach is to select input based on experimental precision rather than theoretical sensitivity. This is achieved by selecting from each pool the member exhibiting the smallest relative measurement uncertainties,

$$A_x = \left\{ \arg\min_x f(x) \,|\, x \in X,\, X \in P_x \right\},$$

where

$$f(x) = \frac{\sum_i^N \sigma_x^i}{N}\,.$$

This method is more generally applicable for, e.g., multi-operator optimisation as it produces a (much) more stable parameter space than 'true' dynamic subset selection using sensitivity as the metric.

[1]The default fixed point is $C_i/\Lambda^2 = 10$ TeV^{-2}.

5.4.2 Fitting Procedure

The loss function to be minimised is

$$\chi^2 = R^T C^{-1} R\,, \tag{5.3}$$

where $R = V_{\text{exp.}} - V_{\text{theory}}$ is a vector of residuals and C is the covariance matrix of the data. We calculate C for each prediction according to

$$C_{ij} = \frac{S_{ij}}{E_i E_j}\,,$$

where S is the block-diagonal experimental correlation matrix, formed using bin-to-bin correlations where provided, and $E_a = \sqrt{E^2_{\text{a,exp}} + E^2_{a,\text{theory}}}$ are the combined theoretical and experimental uncertainties for bin a.

The optimisation/minimisation method is again plugin-driven, with a modular approach taken to allow for arbitrary custom or third-party routines. The default plugin wraps the `optimize` function provided by SciPy [52], which provides easy access to various popular optimisation methods.

Once the best-fit point is found, we determine the confidence interval/area as the region for which

$$\Delta\chi^2 \leq 1 - F(\chi^2; k)\,,$$

where

$$F(\chi^2; k) = \frac{\gamma(\frac{k}{2}, \frac{\chi^2}{2})}{\Gamma(\frac{k}{2})}$$

is the cumulative distribution function of a chi-square distribution with k degrees of freedom and

$$\Delta\chi^2 = \chi^2 - \chi^2_{\text{min}}$$

is the difference between the global minimum of the χ^2 distribution and the value for a given set of parameter values.

With this approach, k is simply the number of parameters (operators) being studied – i.e. $k = 1$ for the one-dimensional confidence interval for a given coefficient (operator), C_i (O_i). This has the added benefit of ‘washing out’ any measurements in the fit which arise from processes with no diagrams containing O_i, allowing the entire dataset to be used with no need to curate input to avoid artificially diluting our sensitivity.

5.5 Wilson Coefficient Constraints

We will now present constraints obtained by carrying out a global fit according to the methodology and framework presented in previous sections, using the experimental results outlined in Table 5.1. Both individual (where only the target coefficient can take non–zero values) and profiled (all coefficients can take non–zero values) results are presented, expressed using the dimensionless 'barred' notation $\bar{C}_i = C_i \frac{v^2}{\Lambda^2}$.

The nominal[1] results for dipole, charged/neutral current, and four–quark operators are presented in Fig. 5.1 and tabulated in Table 5.11. We find all operators to be well constrained on an individual basis, with excellent agreement with Standard Model predictions in all but the four–quark octet operators $O_{qq}^{(8)iiii}$ (more on this later). Broadly speaking, the strength of constraints reflects how well–studied the processes to which an operator contributes as is to be expected; the strongest bounds are on operators contributing to top pair production, for example, as that is the process for which the availability of differential measurements is highest and experimental uncertainties lowest.

Profiled constraints show good agreement with SM predictions in all cases where they have been found, with most operators being well constrained using the data available. These constraints are wider than individual results for all operators, due to counteracting contributions to inclusive and differential predictions when the full, 31–dimensional parameter space is available.

The lack of profiled results for $O_{\varphi q}^{(1)33}$ and $O_{\varphi u}^{33}$, and the weakness of profiled constraints for O_{uB}^{33}, are explained by their contributing only to processes involving top production in association with neutral bosons. All three contribute to associated Z production, with O_{uB}^{33} also contributing to top production in association with the photon (e.g. $t\bar{t}\gamma$). No associated photon production analyses are included here, with associated Z boson production measurements comprising just 14 of the 823 measurements entering the fit; seven of which are total cross–section measurements and all of which also have contributions from multiple operators.

Obtaining or improving profiled bounds will require the inclusion of additional measurements of associated production processes, ideally involving differential distributions to allow the possibility of decoupling of operators via their kinematic effects in disparate regions. The considerable impact of including differential measurements is shown in Fig. 5.6 and the discussion thereof.

[1]Here "nominal" refers to fits performed using all available data, allowing up to two operator insertions per diagram, and including $\mathcal{O}(\Lambda^{-4})$ terms.

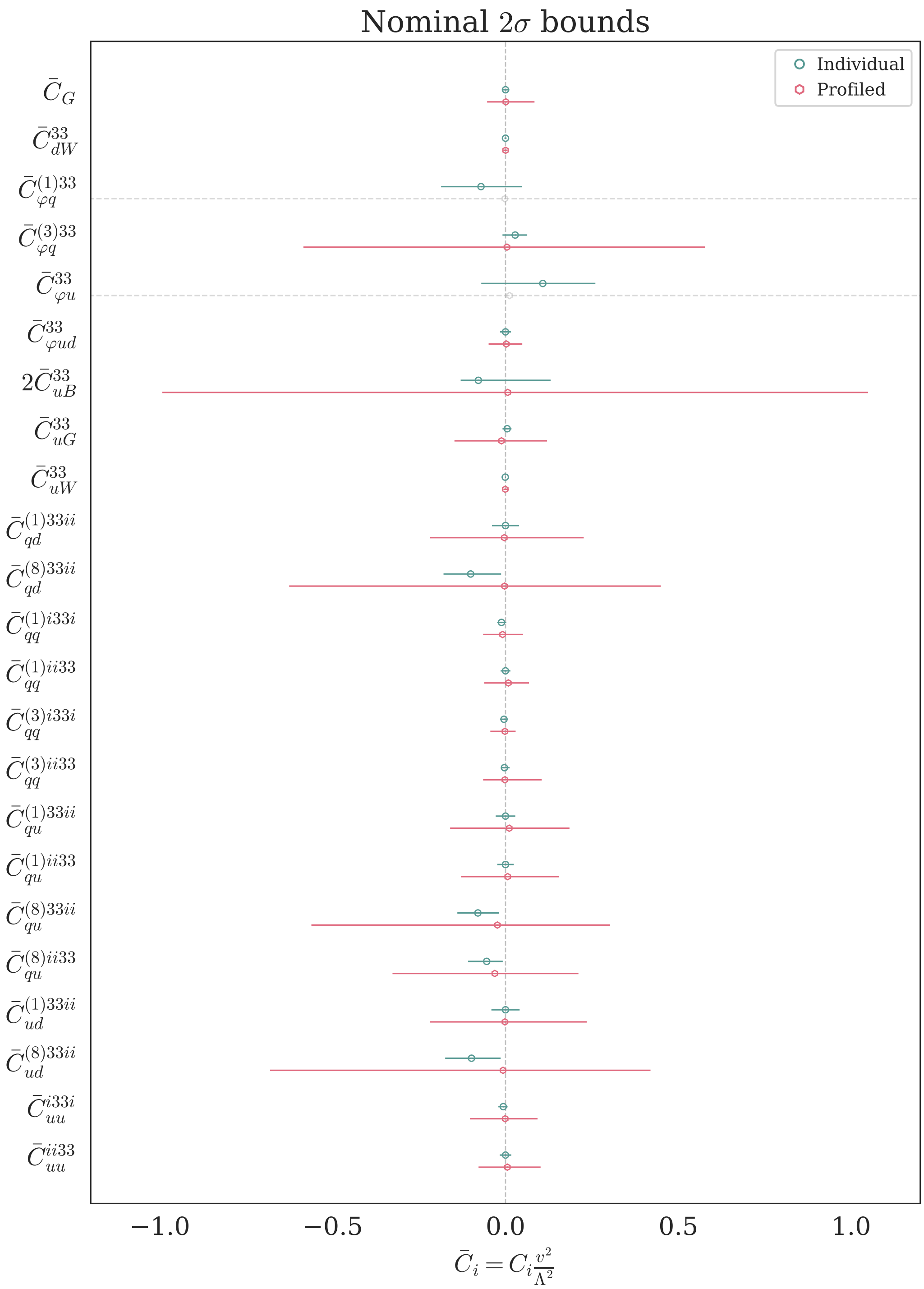

Figure 5.1: The 2σ confidence intervals obtained using the full data set presented in Table 5.1. Note that $2\bar{C}^{33}_{uB}$ is used here for legibility, with values for $\bar{C}^{33}_{uB}$ provided in Table 5.11.

The 95% confidence intervals for the eight lepton–top operators are presented in Fig. 5.2 and tabulated in Table 5.11. We find that the operators O_{ledq}^{ii33}, $O_{lequ}^{(1)ii33}$, $O_{lequ}^{(3)ii33}$, and $O_{lq}^{(3)ii33}$ are well constrained on an individual basis, though only $O_{lequ}^{(3)ii33}$ admits profiled bounds. The remaining, poorly constrained[1], operators contribute only to top decay processes with associated Z production as shown in Table 5.2; these amount to just nine of the 823 measurements entering the fit.

The lepton–top operators here, alongside the most weakly constrained operators from Fig. 5.1 also contributing to associated production and decay processes, may provide an argument for the further study and addition of inclusive and differential measurements relating to such processes.

Although not fully constrained, the results are worthy of inclusion as they are newly available from a purely top sector perspective; they also offer both the possibility of complementarity and a baseline for further study as new experimental results become available.

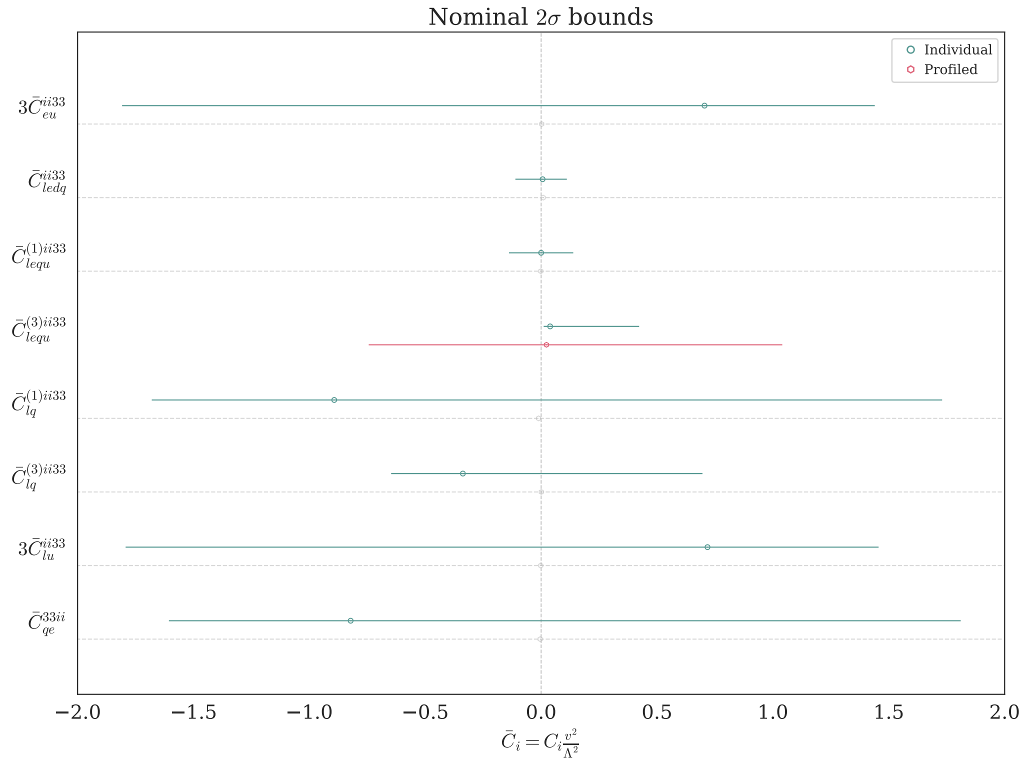

Figure 5.2: The 2σ confidence intervals obtained using the full data set presented in Table 5.1. Note that $3\bar{C}_{eu}^{ii33}$ and $3\bar{C}_{lu}^{ii33}$ are used here for legibility, with unscaled values for both provided in Table 5.11.

[1] These operators are, in fact, effectively unconstrained by available measurements due to admitting values outside the range of validity — $|C_i| \leq 4\pi$, or $|\bar{C}_i| \lesssim 0.76$ — for the EFT expansion.

	$\bar{C}_{qd}^{(8)33ii}$	$\bar{C}_{qu}^{(8)33ii}$	$\bar{C}_{qu}^{(8)ii33}$	$\bar{C}_{ud}^{(8)33ii}$
Best fit	-0.0874	-0.0629	-0.0289	-0.0848
95% CL	$(-0.1828, 0.0247)$	$(-0.1340, 0.0063)$	$(-0.0896, 0.0177)$	$(-0.1765, 0.0196)$

Table 5.4: Individual 2σ octet bounds with Ref. [116] omitted.

As highlighted at the opening of this section, there is an apparent preference for the four–fermion octet operators, uniform in direction, to be pulled away from the Standard Model — indeed the individual bounds have the SM hypothesis *outside* the 95% CL as shown in Fig. 5.1. This discrepancy allows use of another benefit of the TopFitter framework, namely the ability to carry out granular investigations of our parameter space through direct exploration and the reporting of per–parameter contributions to the loss function for a given point in said space.

We first use the framework to make predictions for each of the octet operators in turn, using the unrealistically large value of $\bar{C}_i = 10$ to ensure significant deviations from the SM for measurements where C_i induces change, and capture the dominant contributions to the overall loss. Results are shown in Tables 5.5 to 5.8, where see that the main source of deviation is a single bin in the $\frac{1}{\sigma}\frac{d\sigma}{dm_{t\bar{t}}d|\Delta\eta_{t\bar{t}}|}$ distribution of Ref. [116]. It is interesting that another measurement of the same region, though at $\sqrt{s} = 8$ TeV rather than 13 TeV, in Ref. [108] is also a major factor for three of the four operators though with better agreement between experiment and prediction. Whilst this discrepancy warrants further investigation, the impact of removing Ref. [116] is shown in Table 5.4 where the SM hypothesis is indeed recaptured.

			Overall			Breakdown	
arχiv	Process	Observable	χ^2/N_{dof}	$\chi^2_{\text{SM}}/N_{\text{dof}}$	N_{dof}	Bin	χ^2
1904.05237	$t\bar{t}$	$\frac{1}{\sigma}\frac{d\sigma}{dm_{t\bar{t}}d\|\Delta\eta_{t\bar{t}}\|}$	133.55	13.93	1	[(650, 1500), (0.0, 0.4)]	133.55
1703.01630	$t\bar{t}$	$\frac{1}{\sigma}\frac{d\sigma}{dm_{t\bar{t}}d\|\Delta\eta_{t\bar{t}}\|}$	12.25	1.74	11	[(650, 1500), (0.0, 0.4)]	49.61
1512.06092	$t\bar{t}$	A_C ($m_{t\bar{t}} > 750$ GeV)	10.98	0.72	1	–	10.98
1709.05327	$t\bar{t}$	A_C (LHC7)	10.10	0.07	1	–	10.10
1505.04480	$t\bar{t}$	$\frac{1}{\sigma}\frac{d\sigma}{dm_{t\bar{t}}}$	8.96	1.18	1	(820, 1100)	8.96
1907.11270	$t\bar{t}Z$ ($\ell\ell$)	σ_{tot} ($m_{ll} \leq 110$ GeV)	8.61	1.03	1	–	8.61
1311.6724	$t\bar{t}$	A_C	8.12	0.02	1	–	8.12
1407.4314	$t\bar{t}$ ($\ell\ell$)	C_{hel}	7.46	8.14	1	–	7.46

Table 5.5: Dominant contributions to χ^2 for $\bar{C}_{ud}^{(8)33ii} = 10$.

			Overall			Breakdown	
arχiv	Process	Observable	χ^2/N_{dof}	$\chi^2_{\mathrm{SM}}/N_{\mathrm{dof}}$	N_{dof}	Bin	χ^2
1904.05237	$t\bar{t}$	$\frac{1}{\sigma}\frac{d\sigma}{dm_{t\bar{t}}d\lvert\Delta\eta_{t\bar{t}}\rvert}$	133.22	13.93	1	[(650, 1500), (0.0, 0.4)]	133.22
1512.06092	$t\bar{t}$	A_C ($m_{t\bar{t}} > 750$ GeV)	27.52	0.72	1	–	27.52
1907.11270	$t\bar{t}Z$ ($\ell\ell$)	σ_{tot} ($m_{ll} \leq 110$ GeV)	24.60	1.03	1	–	24.60
1901.03584	$t\bar{t}Z$	σ_{tot}	13.73	0.32	1	–	13.73
1703.01630	$t\bar{t}$	$\frac{1}{\sigma}\frac{d\sigma}{dm_{t\bar{t}}d\lvert\Delta\eta_{t\bar{t}}\rvert}$	12.25	1.74	11	[(650, 1500), (0.0, 0.4)]	49.66
1711.02547	$t\bar{t}Z$	σ_{tot}	11.67	0.71	1	–	11.67
1306.2357	$t\bar{t}$	$a_l^{(1)}$	10.15	4.10	1	–	10.15
1509.05276	$t\bar{t}Z$	σ_{tot}	9.82	0.49	1	–	9.82

Table 5.6: Dominant contributions to χ^2 for $\bar{C}_{qd}^{(8)33ii} = 10$.

			Overall			Breakdown	
arχiv	Process	Observable	χ^2/N_{dof}	$\chi^2_{\mathrm{SM}}/N_{\mathrm{dof}}$	N_{dof}	Bin	χ^2
1904.05237	$t\bar{t}$	$\frac{1}{\sigma}\frac{d\sigma}{dm_{t\bar{t}}d\lvert\Delta\eta_{t\bar{t}}\rvert}$	173.16	13.93	1	[(650, 1500), (0.0, 0.4)]	173.16
1512.06092	$t\bar{t}$	A_C ($m_{t\bar{t}} > 750$ GeV)	58.86	0.72	1	–	58.86
1907.11270	$t\bar{t}Z$ ($\ell\ell$)	σ_{tot} ($m_{ll} \leq 110$ GeV)	39.47	1.03	1	–	39.47
1306.2357	$t\bar{t}$	$a_l^{(1)}$	37.44	4.10	1	–	37.44
1709.05327	$t\bar{t}$	A_C (LHC7)	30.32	0.07	1	–	30.32
1901.03584	$t\bar{t}Z$	σ_{tot}	22.34	0.32	1	–	22.34
1711.02547	$t\bar{t}Z$	σ_{tot}	19.97	0.71	1	–	19.97
1703.01630	$t\bar{t}$	$\frac{1}{\sigma}\frac{d\sigma}{dm_{t\bar{t}}d\lvert\Delta\eta_{t\bar{t}}\rvert}$	18.87	1.74	11	[(650, 1500), (0.0, 0.4)]	85.45

Table 5.7: Dominant contributions to χ^2 for $\bar{C}_{qu}^{(8)33ii} = 10$.

			Overall			Breakdown	
arχiv	Process	Observable	χ^2/N_{dof}	$\chi^2_{\mathrm{SM}}/N_{\mathrm{dof}}$	N_{dof}	Bin	χ^2
1904.05237	$t\bar{t}$	$\frac{1}{\sigma}\frac{d\sigma}{dm_{t\bar{t}}d\lvert\Delta\eta_{t\bar{t}}\rvert}$	181.33	13.93	1	[(650, 1500), (0.0, 0.4)]	181.33
1512.06092	$t\bar{t}$	A_C ($m_{t\bar{t}} > 750$ GeV)	75.73	0.72	1	–	75.73
1907.11270	$t\bar{t}Z$ ($\ell\ell$)	σ_{tot} ($m_{ll} \leq 110$ GeV)	57.07	1.03	1	–	57.07
1709.05327	$t\bar{t}$	A_C (LHC7)	45.23	0.07	1	–	45.23
1711.02547	$t\bar{t}W$	σ_{tot}	43.20	0.32	1	–	43.20
1901.03584	$t\bar{t}W$	σ_{tot}	41.36	0.91	1	–	41.36
1306.2357	$t\bar{t}$	$a_l^{(1)}$	40.86	4.10	1	–	40.86
1607.07627	$t\bar{t}$ (ℓj)	$\mathcal{P}_t^{\mathrm{hel}}$	35.31	2.65	1	–	35.31

Table 5.8: Dominant contributions to χ^2 for $\bar{C}_{qu}^{(8)ii33} = 10$.

We now turn our attention to the impact of allowing a maximum of one or two operator insertions on the resulting bounds. Interestingly, the impact of allowing an additional insertion per diagram is significant for (some) lepton–top operators even on an individual basis; that is, diagrams involving two insertions of the same operator results in larger responses (deviations) when scanning that axis. This behaviour is shown in Fig. 5.3, where only individual bounds are shown due to insufficient control of lepton–top operators on a profiled basis.

This behaviour is not seen in the other operators studied here, with little–to–no change in constraining power for individual bounds between one and two insertions per diagram; additional operator insertions do, however, have a measurable impact on profiled bounds for most as shown in Fig. 5.4. The effect is most pronounced for $O_{\varphi q}^{(3)33}$, which goes from well–constrained to weakly constrained from above and unbounded from below when a maximum of one insertion is allowed, and O_{uB}^{33} which goes from weakly constrained to unconstrained. This is due to the importance of $(\mathcal{O}(\Lambda^{-4}))$ cross–terms, where they exist, when multiple operators exist with non–zero coefficients in a given scenario.

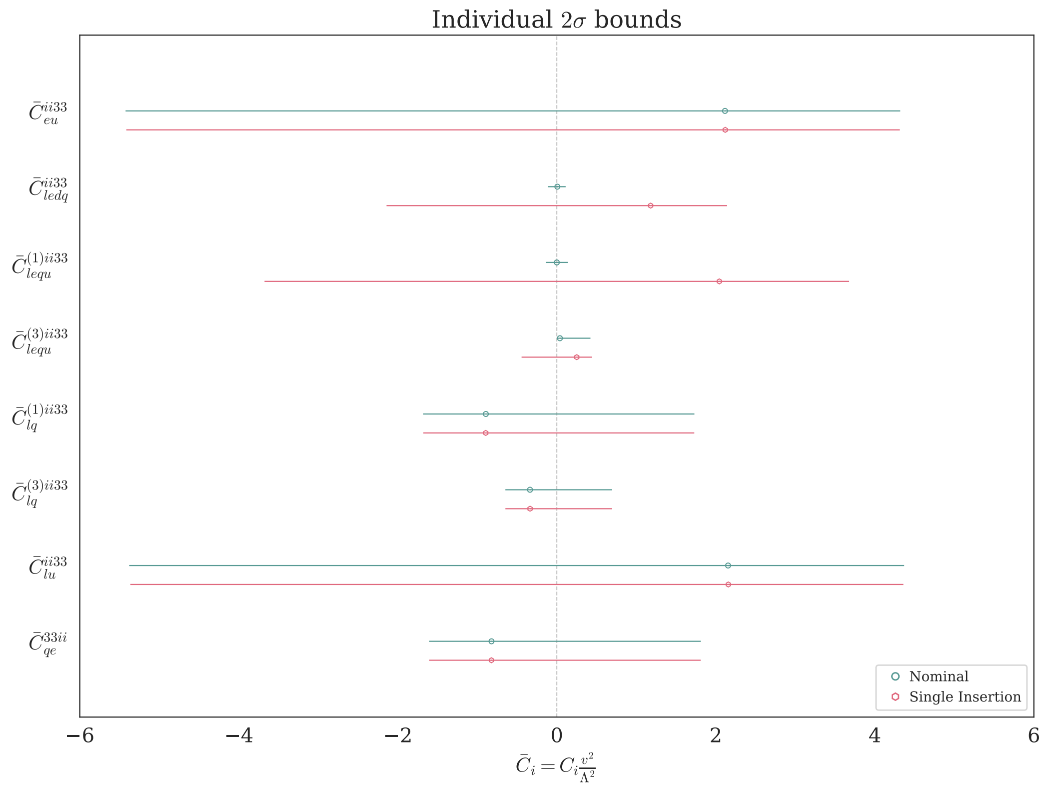

Figure 5.3: Impact of insertion limit on lepton–top operators.

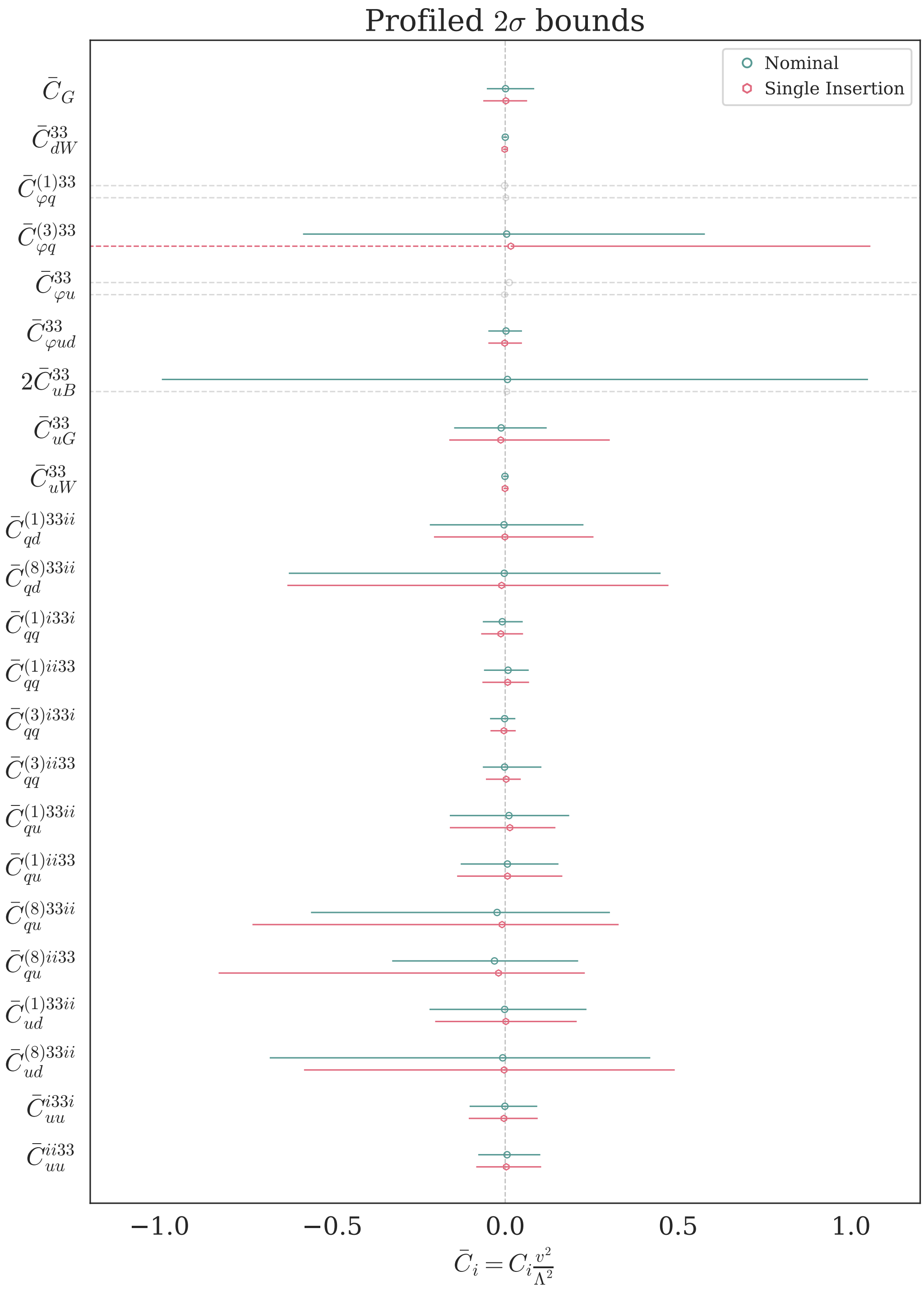

Figure 5.4: Impact of allowing up to two operator insertions per diagram. Note that $2\bar{C}_{uB}^{33}$ is used here for legibility.

Our final investigation on the impact of contributions and data on constraints, and penultimate sanity check of the fit and framework, is on the importance of differential measurements in constraining New Physics with an EFT approach.

It would seem to make intuitive sense that differential data should add constraining power to such a fit; inclusive cross–section predictions can only be pushed up or down, meaning there's greater scope for a set of operators to cancel each other out. Differential measurements, on the other hand, allow a more granular view of the kinematic effects of higher–dimensional operators whilst (hopefully) making said operators distinguishable from one another.

This intuition is, thankfully, borne out here. In Figs. 5.5 and 5.6 we see that the use of differential data has a significant impact on limits for most operators. It is worth highlighting that the operators with the smallest difference are also those least controlled in Figs. 5.1 and 5.2, perhaps indicating some benefit in pursuing new kinematic observables or regions.

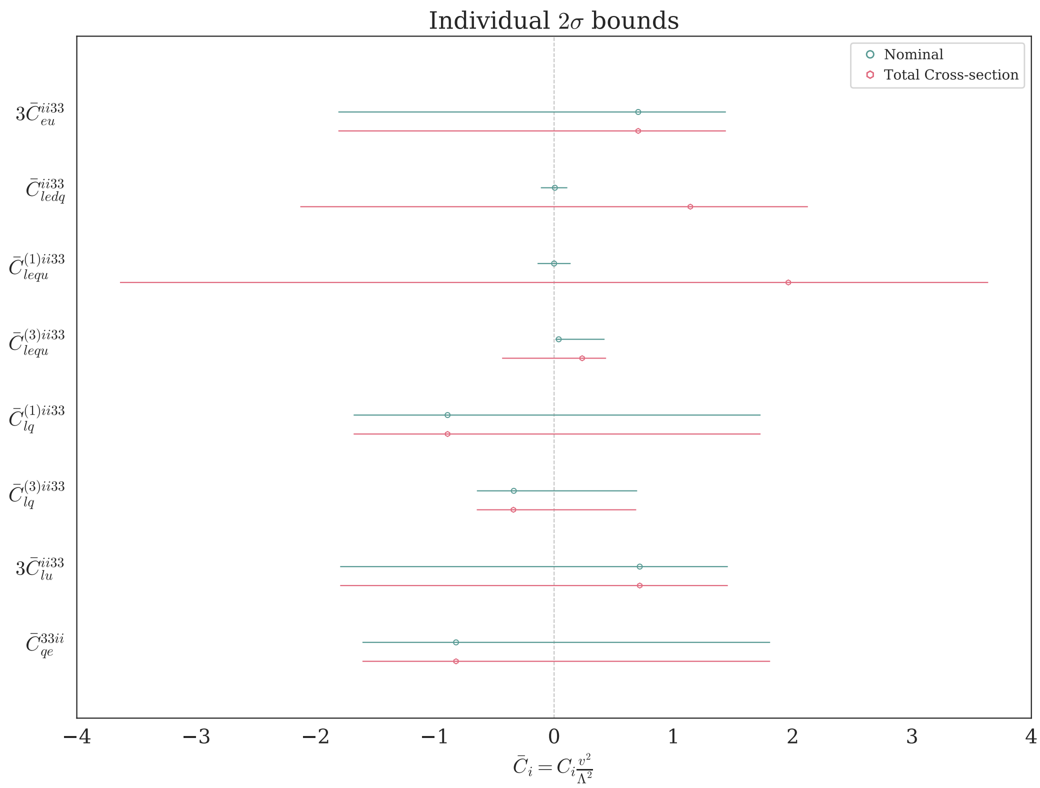

Figure 5.5: Impact of including differential cross–section measurements in the fit. Note that $3\bar{C}_{eu}^{ii33}$ and $3\bar{C}_{lu}^{ii33}$ are used here for legibility.

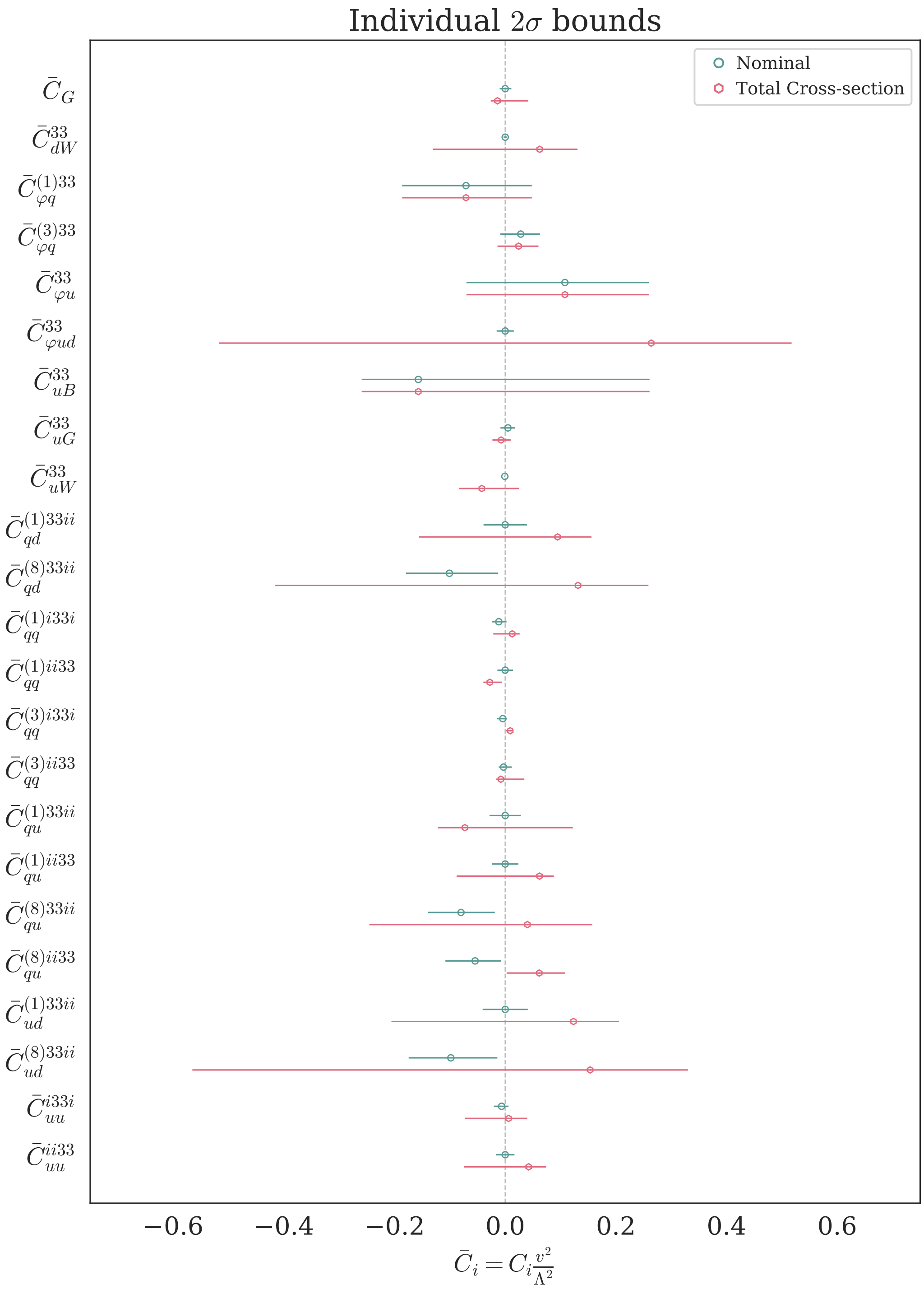

Figure 5.6: Impact of including differential cross–section measurements in the fit.

Finally, we compare results from TopFitter to a contemporaneous EFT study of the top sector, SMEFiT [132], with similar aims but a significantly different approach. In doing so we can also highlight another feature of the framework presented here, that being the ability to define arbitrary maps between (combinations of) Wilson coefficients; these can be used to perform fits using the same underlying data.

Aligning with SMEFiT by using the degrees of freedom in Table 5.9 we find excellent agreement in most cases and TopFitter to be competitive in many, as shown in Fig. 5.7 and Table 5.10. Only individual bounds are compared here, as they admit direct comparison more readily than profiled or marginalised results.

It is, perhaps, notable that both approaches — differing in both statistical methodology and dataset — seem to have some qualitative similarities as regards the previously discussed octet operators.

	$C_{qd}^{(1)33ii}$	$C_{qd}^{(8)33ii}$	$C_{qq}^{(1)i33i}$	$C_{qq}^{(1)ii33}$	$C_{qq}^{(3)i33i}$	$C_{qq}^{(3)ii33}$	$C_{qu}^{(1)33ii}$	$C_{qu}^{(1)ii33}$	$C_{qu}^{(8)33ii}$	$C_{qu}^{(8)ii33}$	$C_{ud}^{(1)33ii}$	$C_{ud}^{(8)33ii}$	C_{uu}^{i33i}	C_{uu}^{ii33}
c_{Qd}^{1}	1													
c_{Qd}^{8}		1												
$c_{Qq}^{1,8}$			1		3									
$c_{Qq}^{1,1}$			$\frac{1}{6}$	1	$\frac{1}{2}$									
$c_{Qq}^{3,8}$			1		-1									
$c_{Qq}^{3,1}$			$\frac{1}{6}$		$-\frac{1}{6}$	1								
c_{Qu}^{1}							1							
c_{tq}^{1}								1						
c_{Qu}^{8}									1					
c_{tq}^{8}										1				
c_{td}^{1}											1			
c_{td}^{8}												1		
c_{tu}^{8}													2	
c_{tu}^{1}													$\frac{1}{3}$	1

(a) Heavy-light.

	C_{dW}^{33}	$C_{\varphi q}^{(1)33}$	$C_{\varphi q}^{(3)33}$	$C_{\varphi u}^{33}$	$C_{\varphi ud}^{33}$	C_{uB}^{33}	C_{uG}^{33}	C_{uW}^{33}
c_{bW}	1							
$c_{\varphi Q}^{-}$		1	-1					
$c_{\varphi Q}^{3}$			1					
$c_{\varphi t}$				1				
$c_{\varphi tb}$					1			
c_{tZ}						$-s_W$		c_W
c_{tG}							1	
c_{tW}								1

(b) Heavy-boson.

	C_{eu}^{ii33}	C_{ledq}^{ii33}	$C_{lequ}^{(1)ii33}$	$C_{lequ}^{(3)ii33}$	$C_{lq}^{(1)ii33}$	$C_{lq}^{(3)ii33}$	C_{lu}^{ii33}	C_{qe}^{33ii}
$c_{te}^{(l)}$	1							
$c_{b}^{S(l)}$		1						
$c_{t}^{S(l)}$			1					
$c_{t}^{T(l)}$				1				
$c_{Ql}^{-(l)}$					1	-1		
$c_{Ql}^{3(l)}$						1		
$c_{tl}^{(l)}$							1	
$c_{Qe}^{(l)}$								1

(c) Heavy-lepton.

Table 5.9: LHC Top EFT working group degrees of freedom [133].

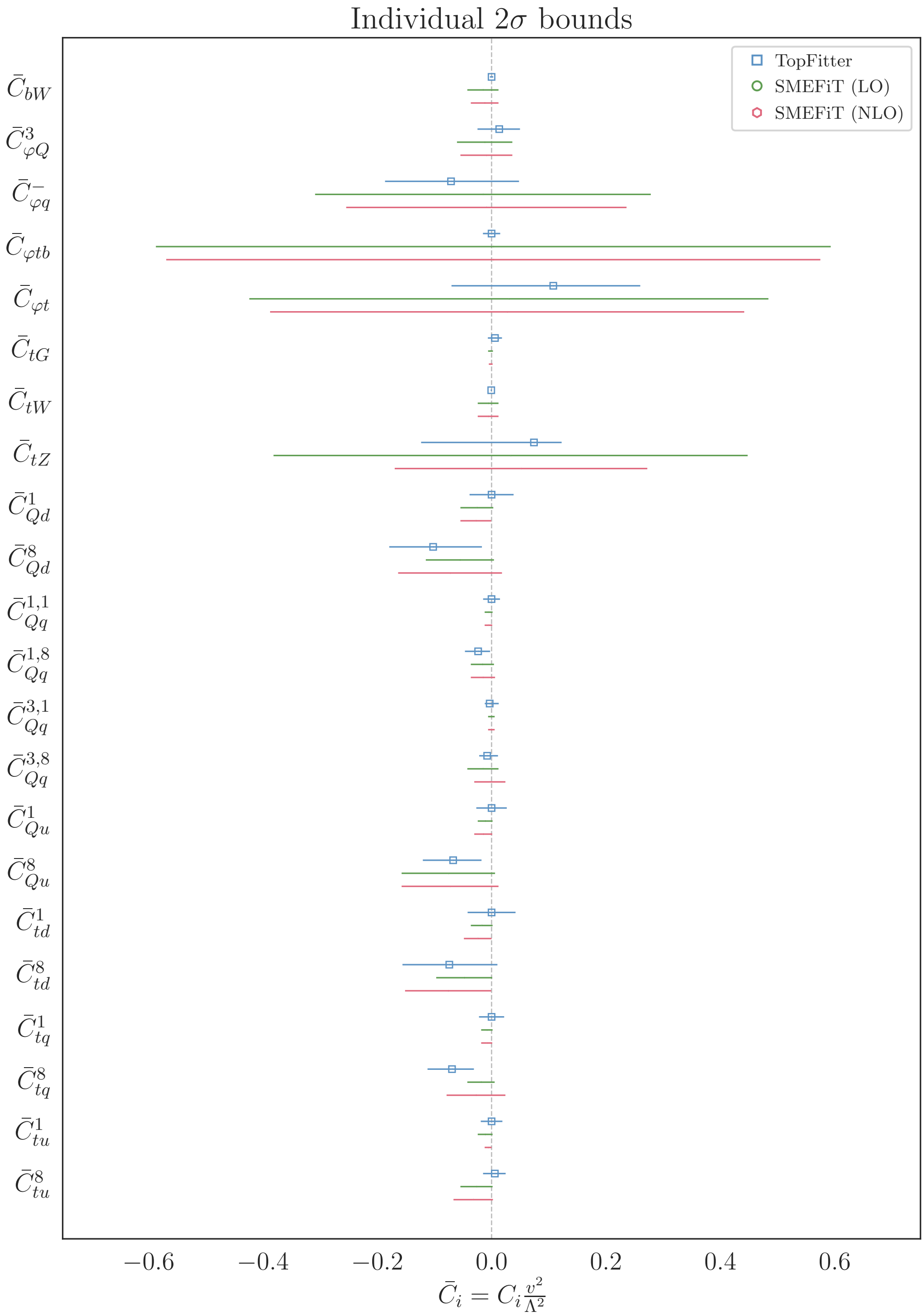

Figure 5.7: Individual bounds compared to SMEFiT [132] results with EFT contributions at both leading–order (LO) and next–to–leading–order (NLO) in QCD.

	TopFitter		SMEFiT	
	Best	95% CL	LO	NLO
$\bar{C}_{bW}$	0.0000	$(-0.0029, 0.0029)$	$(-0.0424, 0.0121)$	$(-0.0363, 0.0121)$
$\bar{C}^{3}_{\varphi Q}$	0.0134	$(-0.0246, 0.0497)$	$(-0.0605, 0.0363)$	$(-0.0545, 0.0363)$
$\bar{C}^{-}_{\varphi q}$	-0.0709	$(-0.1863, 0.0480)$	$(-0.3086, 0.2784)$	$(-0.2542, 0.2360)$
$\bar{C}_{\varphi tb}$	0.0000	$(-0.0151, 0.0151)$	$(-0.5870, 0.5931)$	$(-0.5689, 0.5749)$
$\bar{C}_{\varphi t}$	0.1079	$(-0.0701, 0.2600)$	$(-0.4236, 0.4841)$	$(-0.3873, 0.4418)$
$\bar{C}_{tG}$	0.0059	$(-0.0065, 0.0182)$	$(-0.0061, 0.0024)$	$(-0.0048, 0.0018)$
$\bar{C}_{tW}$	-0.0006	$(-0.0016, 0.0004)$	$(-0.0242, 0.0121)$	$(-0.0242, 0.0121)$
$\bar{C}_{tZ}$	0.0741	$(-0.1232, 0.1225)$	$(-0.3813, 0.4478)$	$(-0.1694, 0.2723)$
$\bar{C}^{1}_{Qd}$	0.0000	$(-0.0385, 0.0385)$	$(-0.0545, 0.0030)$	$(-0.0545, -0.0006)$
$\bar{C}^{8}_{Qd}$	-0.1022	$(-0.1789, -0.0169)$	$(-0.1150, 0.0042)$	$(-0.1634, 0.0182)$
$\bar{C}^{1,1}_{Qq}$	-0.0001	$(-0.0148, 0.0147)$	$(-0.0121, 0.0018)$	$(-0.0121, 0.0012)$
$\bar{C}^{1,8}_{Qq}$	-0.0235	$(-0.0466, -0.0026)$	$(-0.0363, 0.0042)$	$(-0.0363, 0.0061)$
$\bar{C}^{3,1}_{Qq}$	-0.0033	$(-0.0119, 0.0125)$	$(-0.0061, 0.0054)$	$(-0.0061, 0.0054)$
$\bar{C}^{3,8}_{Qq}$	-0.0077	$(-0.0216, 0.0112)$	$(-0.0424, 0.0121)$	$(-0.0303, 0.0242)$
$\bar{C}^{1}_{Qu}$	-0.0000	$(-0.0267, 0.0266)$	$(-0.0242, 0.0018)$	$(-0.0303, 0.0012)$
$\bar{C}^{8}_{Qu}$	-0.0672	$(-0.1202, -0.0176)$	$(-0.1573, 0.0061)$	$(-0.1573, 0.0121)$
$\bar{C}^{1}_{td}$	0.0000	$(-0.0419, 0.0419)$	$(-0.0363, 0.0018)$	$(-0.0484, 0.0000)$
$\bar{C}^{8}_{td}$	-0.0739	$(-0.1558, 0.0102)$	$(-0.0968, 0.0012)$	$(-0.1513, -0.0006)$
$\bar{C}^{1}_{tq}$	0.0000	$(-0.0220, 0.0220)$	$(-0.0182, 0.0018)$	$(-0.0182, 0.0012)$
$\bar{C}^{8}_{tq}$	-0.0692	$(-0.1120, -0.0309)$	$(-0.0424, 0.0054)$	$(-0.0787, 0.0242)$
$\bar{C}^{1}_{tu}$	0.0000	$(-0.0189, 0.0189)$	$(-0.0242, 0.0018)$	$(-0.0121, 0.0000)$
$\bar{C}^{8}_{tu}$	0.0057	$(-0.0149, 0.0246)$	$(-0.0545, 0.0018)$	$(-0.0666, 0.0024)$
$\bar{C}^{3}_{Ql}$	-0.2751	$(-0.5315, 0.5699)$	–	–
$\bar{C}^{-}_{Ql}$	-0.8927	$(-1.6800, 1.7303)$	–	–
$\bar{C}_{bS}$	0.0064	$(-0.1110, 0.1110)$	–	–
$\bar{C}_{tS}$	0.0000	$(-0.1387, 0.1387)$	–	–
$\bar{C}_{tT}$	0.0389	$(0.0108, 0.4200)$	–	–
$\bar{C}_{te}$	2.1152	$(-5.4240, 4.3191)$	–	–
$\bar{C}_{tl}$	2.1538	$(-5.3785, 4.3684)$	–	–

Table 5.10: Individual bounds compared to SMEFiT results [132].

	Individual		Profiled	
	Best	95% CL	Best	95% CL
$\bar{C}_{G}$	0.0000	$(-0.0100, 0.0111)$	0.0010	$(-0.0532, 0.0839)$
$\bar{C}_{dW}^{33}$	0.0000	$(-0.0030, 0.0030)$	0.0002	$(-0.0062, 0.0061)$
$\bar{C}_{\varphi q}^{(1)33}$	-0.0709	$(-0.1863, 0.0480)$	-0.0019	–
$\bar{C}_{\varphi q}^{(3)33}$	0.0280	$(-0.0087, 0.0628)$	0.0042	$(-0.5847, 0.5774)$
$\bar{C}_{\varphi u}^{33}$	0.1079	$(-0.0701, 0.2600)$	0.0117	–
$\bar{C}_{\varphi ud}^{33}$	0.0000	$(-0.0155, 0.0155)$	0.0023	$(-0.0488, 0.0485)$
$\bar{C}_{uB}^{33}$	-0.1570	$(-0.2594, 0.2609)$	0.0131	$(-1.9858, 2.0982)$
$\bar{C}_{uG}^{33}$	0.0049	$(-0.0086, 0.0173)$	-0.0117	$(-0.1477, 0.1200)$
$\bar{C}_{uW}^{33}$	-0.0007	$(-0.0017, 0.0003)$	-0.0007	$(-0.0061, 0.0101)$
$\bar{C}_{qd}^{(1)33ii}$	0.0000	$(-0.0392, 0.0392)$	-0.0034	$(-0.2180, 0.2263)$
$\bar{C}_{qd}^{(8)33ii}$	-0.1008	$(-0.1793, -0.0127)$	-0.0027	$(-0.6258, 0.4493)$
$\bar{C}_{qq}^{(1)i33i}$	-0.0116	$(-0.0242, 0.0024)$	-0.0085	$(-0.0648, 0.0507)$
$\bar{C}_{qq}^{(1)ii33}$	-0.0001	$(-0.0141, 0.0141)$	0.0083	$(-0.0614, 0.0680)$
$\bar{C}_{qq}^{(3)i33i}$	-0.0043	$(-0.0154, 0.0032)$	-0.0016	$(-0.0439, 0.0293)$
$\bar{C}_{qq}^{(3)ii33}$	-0.0031	$(-0.0117, 0.0118)$	-0.0018	$(-0.0647, 0.1047)$
$\bar{C}_{qu}^{(1)33ii}$	-0.0000	$(-0.0284, 0.0283)$	0.0108	$(-0.1602, 0.1851)$
$\bar{C}_{qu}^{(1)ii33}$	0.0000	$(-0.0238, 0.0238)$	0.0063	$(-0.1287, 0.1540)$
$\bar{C}_{qu}^{(8)33ii}$	-0.0799	$(-0.1393, -0.0188)$	-0.0235	$(-0.5616, 0.3028)$
$\bar{C}_{qu}^{(8)ii33}$	-0.0544	$(-0.1081, -0.0080)$	-0.0310	$(-0.3269, 0.2110)$
$\bar{C}_{ud}^{(1)33ii}$	0.0000	$(-0.0408, 0.0408)$	-0.0016	$(-0.2189, 0.2350)$
$\bar{C}_{ud}^{(8)33ii}$	-0.0983	$(-0.1745, -0.0142)$	-0.0072	$(-0.6809, 0.4195)$
$\bar{C}_{uu}^{i33i}$	-0.0065	$(-0.0207, 0.0060)$	-0.0009	$(-0.1029, 0.0927)$
$\bar{C}_{uu}^{ii33}$	0.0000	$(-0.0167, 0.0167)$	0.0054	$(-0.0780, 0.1015)$
$\bar{C}_{eu}^{ii33}$	2.1152	$(-5.4240, 4.3191)$	0.0078	–
$\bar{C}_{ledq}^{ii33}$	0.0064	$(-0.1110, 0.1110)$	0.0090	–
$\bar{C}_{lequ}^{(1)ii33}$	0.0000	$(-0.1387, 0.1387)$	-0.0015	–
$\bar{C}_{lequ}^{(3)ii33}$	0.0389	$(0.0109, 0.4230)$	0.0231	$(-0.7439, 1.0406)$
$\bar{C}_{lq}^{(1)ii33}$	-0.8927	$(-1.6800, 1.7303)$	-0.0110	–
$\bar{C}_{lq}^{(3)ii33}$	-0.3376	$(-0.6471, 0.6962)$	0.0008	–
$\bar{C}_{lu}^{ii33}$	2.1538	$(-5.3785, 4.3684)$	-0.0048	–
$\bar{C}_{qe}^{33ii}$	-0.8218	$(-1.6061, 1.8105)$	-0.0040	–

Table 5.11: Top–line individual and profiled results using the full data set presented in Table 5.1, with up to two insertions per diagram.

5.6 Summary and Outlook

In this chapter we have carried out an extensive and statistically–rigorous fit using a large proportion of available top–relevant measurements from Tevatron and LHC analyses to obtain data–driven limits on all dipole, charged and neutral current, and heavy–light four–quark dimension six operators in the SMEFT with a role in top physics. We also include processes involving top quark decay, introducing the method by which we corrected predictions by analytical calculation of the top quark decay width Γ_t, and allowing the study of lepton–top operators.

In total, 823 experimental measurements were used to target 31 operators. The fit was carried out with care to avoid statistical assumptions or double counting, selecting only uncorrelated data or data with reported correlation matrices. Using dynamic subset selection based on operator sensitivity, we selected the subset of data with the largest response to changes in the coefficient under study.

We find the results to be consistent with the Standard Model hypothesis within 95% confidence limits in most cases, with a slight and unresolved tension among light–heavy four–quark octet operators and said hypothesis. The importance of differential distributions and multiple operator insertions per diagram was demonstrated, and finally the framework and statistical methodology tested against a contemporaneous study using a different approach with good agreement found.

The outlook for such an approach seems positive on a number of fronts. First, as the number and variety of analyses of associated production processes increases it is likely that the least well–controlled operators will see some improvement. Second, the increasing frequency of full published correlation/covariance matrices for experimental analyses may increase the impact each set of results has on EFT interpretations due to the ability to use the full and granular kinematic picture provided. The possibility of including particle–level analyses in future fits, as well as improvements to parton distribution functions and models used to generate events for Standard Model and EFT contributions all add possible upside in the not–too–distant future.

The modular, extensible design of the TopFitter allows it to be well–placed for any of the above eventualities; it is model–agnostic, prescriptions for systematics can be implemented easily, and the inclusion of new experimental results and matched theory analyses is similarly simple. Another possibly fruitful path would be to use the framework to perform targeted fits, matched to specific UV scenarios where it is known that only a subset of operators admit non–zero coefficients.

Chapter 6

Electroweak Top Couplings, Partial Compositeness and Top Partner Searches

In case the SM's UV completion is both weakly coupled and scale separated to the extent that modifications of the low-energy SM Lagrangian become non-resolvable in the light of expected theoretical and experimental limitations, the EFT approach will become as challenged as measurements in the full model-context that the EFT can approximate. If, on the other hand, new physics is actually strongly coupled at larger energy scales, EFT-based methods are suitable tools to capture the UV completions' dynamics and symmetry. Prime examples of such theories are models with strong electroweak symmetry breaking (EWSB, see [134–137] for recent reviews).

Whereas a global fit to top measurements was presented in Chapter 5, this chapter covers a more targeted investigation of a specific UV scenario. A brief introduction providing the motivation for this study is given in Section 6.1. In Section 6.2, we review the basics of the composite top scenario. Our approach to constraining anomalous top couplings to W and Z bosons in this model is outlined in Section 6.3. Following this strategy we discuss in Section 6.4 the indirect sensitivity reach of top measurements to coupling deformations as expected in top compositeness theories at the LHC and also provide projections for a 100 TeV FCC-hh [138] (see also [139, 140]). In Section 6.5, we focus on a resonance search in a representative $pp \to TX, T \to t(Z \to \ell^+\ell^-)$ final state, where T is the top partner and X is either an additional T or a third generation quark. This analysis directly reflects the region where top-partial compositeness leads to new resonant structures as a consequence of modified weak top interactions. The sensitivity of this direct search is compared with the indirect sensitivity reach to demonstrate how top fits and concrete resonance searches both contribute to a more detailed picture of top-partial compositeness at hadron colliders. Conclusions are given in Section 6.6.

6.1 Partial Compositeness

Partial top quark compositeness is an important aspect of theories involving strong electroweak symmetry breaking which predict, in addition to heavy top partners that lift the top quark mass to its observed value, correlated modifications of top quark electroweak couplings. Although the microscopic structure of UV models of compositeness varies[1], they admit some common phenomenological similarities that are encapsulated by Minimal Composite Higgs Models (MCHMs) [143–145] (see also [146–149]). These similarities arise due to two necessary ingredients of pseudo-Nambu Goldstone boson (pNGB) theories involving the Higgs boson; the explicit breaking of a global symmetry by weakly gauging a global (flavour) subgroup in the confining phase of a "hypercolour" interaction and partial fermion compositeness [150–153], with the latter providing an additional source of global symmetry breaking. These effects together result in an effective low energy Higgs potential [134, 142–145] of the form

$$V(h) = f^4 \left(\beta \sin^2 \frac{h}{f} - \frac{\alpha + 2\beta}{4} \right)^2$$

where f is Goldstone boson decay constant, h is a custodial isospin singlet for a given embedding of $SU(2)_L \times SU(2)_R$, and α, β are low energy constants (LECs) related to two- and four-point correlation functions of the (extended) hypercolour theory [154, 155]. The vacuum expectation value is determined by

$$\sin^2 \frac{\langle h \rangle}{f} = \frac{\alpha + 2\beta}{4\beta} = \frac{v^2}{f^2} = \xi \tag{6.1}$$

where ξ parametrises the model-dependent modifications of the physical Higgs boson to SM matter (see, e.g., Ref. [156] for an overview). The physical Higgs mass is related to the LECs by

$$m_h^2 = f^2 \left(8\beta - 2\frac{\alpha^2}{\beta} \right) . \tag{6.2}$$

Symmetry breaking $\xi > 0$ in Eq. (6.1) constrains the LECs $\alpha, \beta \neq 0$, and experimental Higgs and electroweak boson measurements imply

$$0.258 \simeq \frac{m_h^2}{v^2} = 8(2\beta - \alpha) , \tag{6.3}$$

limiting the parameter range that must be reproduced by a realistic theory. The region $\xi \ll 1$ — which is required to have SM-like Higgs interactions as indicated

[1] See, e.g., Refs. [141, 142].

by LHC measurements — is accessed by $\alpha \simeq -2\beta$, further narrowing the selected region in LEC parameter space.

While this is often taken as an indication of fine–tuning, it can be shown that all linear combinations of α, β are sensitive to four–point correlation functions [155]. Additional phenomenological input is needed to constrain concrete scenarios [155], given the current status of lattice calculations[1]. This shows that there is (so far) no fine–tuning of the electroweak scale in these scenarios but instead an incomplete understanding of UV dynamics, as can be expected when performing calculations in the interpolating hyperbaryon and meson picture. Indirect constraints on — or even the observation of — partial compositeness in the top sector would provide complementary phenomenological input, and the purpose of this work is to re–interpret existing LHC searches along these lines. The potential of the high-luminosity (HL-)LHC (13 TeV) and a future circular hadron-hadron collider (FCC-hh) to further constrain the strong interaction parameter space will also, via extrapolation of current searches, be discussed.

6.2 Strong Coupling Imprints in Top Interactions

For a given global symmetry breaking pattern, $\mathcal{G} \to \mathcal{H}$, composite Higgs theories can be described using a Callen, Coleman, Wess, Zumino (CCWZ) construction of Refs. [163, 164][2]. Taking $\hat{T}^A$, T^a as the generators of $\mathcal{G}/\mathcal{H}$ and $\mathcal{H}$ respectively, we have that the associated non-linear sigma model field

$$\Sigma = \exp\{i\hat{\phi}^A\hat{T}^A/f\} \in \mathcal{G}$$

captures the transformation properties of the (would-be) Goldstone bosons $\hat{\phi}^A$ under $g \in \mathcal{G}$ as

$$\Sigma \to g\Sigma h^\dagger(g, \hat{\phi}) \,. \tag{6.4}$$

Kinetic terms can then be defined by considering the $\mathcal{G}/\mathcal{H}$ piece of

$$\Sigma^\dagger \partial_\mu \Sigma = v_\mu^a T^a + p_\mu^A \hat{T}^A = v_\mu + p_\mu \,, \tag{6.5}$$

[1] Lattice calculations of baryon four–point functions is highly involved, however progress has been made toward understanding realistic composite Higgs theories using lattice simulations in Refs. [157–162].

[2] For a review of the foundations and related electroweak phenomenology of the construction see, e.g., Ref. [135].

which transforms as $p_\mu \to h p_\mu h^\dagger$ [164]. From Eq. (6.4) we have that this transformation will — in general — be non–linear due to the $\hat{\phi}$– and $\mathcal{G}$–dependence of h, though admits reduction to linear transformations for $g \in \mathcal{H}$. Where there is an automorphism A: $A(T^a) = T^a$, $A(\hat{T}^A) = -\hat{T}^A$, meaning $\mathcal{G}/\mathcal{H}$ is a symmetric space, we can consider a simplified object [163],

$$U = \Sigma A(\Sigma)^\dagger \,,$$

which lies in $\mathcal{G}/\mathcal{H}$ but transforms linearly under $\mathcal{G}$.

In this work we will consider a specific ultraviolet completion of MCHM5 [145], which is based on $SO(5) \to SO(4)$. Concrete UV completions of $\mathcal{G} = SO(5) \times U(1) \to SO(4) \times U(1) = \mathcal{H}$ necessitate a larger symmetry, for example $SU(5) \to SO(5) \supset SO(4)$ [142, 154, 165–167] and therefore typically lead to richer pNGB and hyperbaryon phenomenologies [155, 159, 168–171]. In this case the automorphism is related to complex conjugation and [165]

$$U = \Sigma\Sigma^T = \exp\{2i\hat{\phi}^A\hat{T}^A/f\}$$

with kinetic term

$$\mathcal{L} \supset \frac{f^2}{16}\mathrm{Tr}(\partial_\mu U \partial^\mu U^\dagger)\,.$$

Weak gauging of a (sub)group of H can, in the lowest order in the Goldstone boson expansion, be achieved by replacing the partial derivatives with covariant ones [31, 164], enabling the derivation of Higgs interactions with weak gauge bosons. We will not be exploring this in more depth here, instead carrying on under the assumption that this extension of MCHM5 does indeed make contact with concrete UV extensions; this, technically, means that we impose a fundamental assumption that top partners are the lightest states in the TeV regime when correlating top partner masses with top-electroweak coupling modifications in Section 6.4.

In strongly–coupled composite Higgs theories, EWSB depends upon the presence of additional sources of global symmetry breaking; this is due to the fact that weak gauging of the $SU(2)_L \times U(1)_Y$ will dynamically align the vacuum in the symmetry–preserving direction.[1] An elegant solution to this requirement is found in partial compositeness [152, 153, 172, 173], which posits that the fermion mass hierarchy is the result of the mixing of massless elementary fermions with composite hyperbaryons of the strong interactions. This simultaneously shifts the vacuum

[1] While gauging QED in the pion sector leads to an excellent description of the π^+, π^0 mass splitting QED remains exact. See [153] for a detailed discussion of this instructive example.

away from the $SU(2)_L \times U(1)_Y$ direction, rendering the Higgs a pseudo-Nambu Goldstone boson, and lifts the top and bottom masses to their observed values. From a phenomenological perspective this induces strong correlation between top and Higgs interactions, providing a non–perturbative example of the strong relationship between Higgs and top–quark interactions in generic BSM theories.

In light of $Z\bar{b}_L b_L$ coupling constraints [145], and considering a scenario based on $SU(5)/SO(5)$ [165] with similarities to the $SO(5)/SO(4)$ pattern with symmetric mass terms, we have that a minimal effective Lagrangian of partial compositeness is given by

$$-\mathcal{L} \supset M\bar{\Psi}\Psi + \lambda_q f \bar{\hat{Q}}_L \Sigma \Psi_R + \lambda_t f \bar{\hat{t}}_R \Sigma^* \Psi_L \\ + \sqrt{2}\mu_b \mathrm{Tr}(\bar{\hat{Q}}_L U \hat{b}_R) + \text{h.c.}, \tag{6.6}$$

where Ψ represents the vector-like composite baryons in the low energy effective theory that form a **5** of $SO(5)$ and transform in the fundamental representation of $SU(3)_C$

$$\Psi = \frac{1}{\sqrt{2}} \begin{pmatrix} iB - iX \\ B + X \\ iT + iY \\ -T + Y \\ \sqrt{2} i R \end{pmatrix} . \tag{6.7}$$

Ψ decomposes into a bi-doublet and a singlet under $SU(2)_L \times SU(2)_R$ [174] thus implementing the custodial $SU(2)$ mechanism of Ref. [175]. Under the SM gauge interactions, $SU(3)_C \times SU(2)_L \times U(1)_Y$, these fields transform as $(T, B) \in (\mathbf{3}, \mathbf{2})_{1/6}$, $R \in (\mathbf{3}, \mathbf{1})_{2/3}$, and $(X, Y) \in (\mathbf{3}, \mathbf{2})_{7/6}$. $\hat{Q}_L \supset (t_L, b_L)$, $\hat{t}_R \supset t_R$, and $\hat{b}_R \supset b_R$ are $SO(5)$ spurions

$$\hat{Q}_L = \begin{pmatrix} ib_L \\ b_L \\ it_L \\ -t_L \\ 0 \end{pmatrix}, \quad \hat{t}_R = \begin{pmatrix} 0 \\ 0 \\ 0 \\ 0 \\ t_R \end{pmatrix}, \quad \hat{b}_R = \begin{pmatrix} 0 \\ 0 \\ 0 \\ 0 \\ b_R \end{pmatrix}.$$

This additional source of $SO(5)$ breaking implies a finite contribution to the effective Higgs potential, lifting the $\sim f\lambda_q\lambda_t v/M$ in the large M limit, and leading to EWSB.

We can expand the Lagrangian of Eq. (6.6) to obtain the top partner mass mixing

$$\mathcal{M}_T = \begin{pmatrix} 0 & \frac{\lambda_q}{2} f(1+c_h) & \frac{\lambda_q}{2} f(1-c_h) & \frac{\lambda_q}{\sqrt{2}} f s_h \\ \frac{\lambda_t}{\sqrt{2}} f s_h & M & 0 & 0 \\ -\frac{\lambda_t}{\sqrt{2}} f s_h & 0 & M & 0 \\ \lambda_t f c_h & 0 & 0 & M \end{pmatrix}, \tag{6.8}$$

where $c_h = \cos(h/f)$ and $s_h = \sin(h/f)$. Expanding c_h, s_h around $\langle h \rangle$ gives rise to the Higgs-top (partner) interactions. The mass mixing in the bottom sector reads

$$\mathcal{M}_B = \begin{pmatrix} \mu_b s_h c_h & \lambda_q f \\ 0 & M \end{pmatrix}. \tag{6.9}$$

The mass eigenstates are obtained through bi-unitary transformations, which modify the weak and Higgs couplings of the physical top and bottom quarks compared to the SM by "rotating in" some of the top and bottom partner's weak interaction currents[1] (following the notation of [165])

$$\mathcal{L} \supset \bar{\Psi}\gamma^\mu \left(\frac{2}{3} e A_\mu - \frac{2}{3} t_w e Z_\mu + v_\mu + K p_\mu \right) \Psi \tag{6.10}$$

with v_μ, p_μ arising from Eq. (6.5) after gauging and K being an additional, undetermined, LEC. This leads to currents

$$\begin{aligned} J_Z^\mu / e = {} & c_{XX} \bar{X}\gamma^\mu X + c_{TT} \bar{T}\gamma^\mu T + c_{YY} \bar{Y}\gamma^\mu Y \\ & + c_{RR} \bar{R}\gamma^\mu R + c_{BB} \bar{B}\gamma^\mu B + (c_{RT} \bar{R}\gamma^\mu T + \text{h.c.}) \\ & + (c_{RY} \bar{R}\gamma^\mu Y + \text{h.c.}) + (c_{TY} \bar{T}\gamma^\mu Y + \text{h.c.}) \end{aligned} \tag{6.11a}$$

and

$$\begin{aligned} J_{W^+}^\mu / e = {} & c_{XT} \bar{X}\gamma^\mu T + c_{XY} \bar{X}\gamma^\mu Y + c_{XR} \bar{X}\gamma^\mu R \\ & + c_{TB} \bar{T}\gamma^\mu B + c_{YB} \bar{Y}\gamma^\mu B + c_{RB} \bar{R}\gamma^\mu B \,, \end{aligned} \tag{6.11b}$$

[1] Similar correlations are observed in models that target dark matter and B anomalies, see Ref. [176].

with coefficients c_i

$$\begin{aligned}
c_{XX} &= \frac{1}{s_w c_w}\left(\frac{1}{2} - \frac{5}{3}s_w^2\right) \\
c_{TT} &= -\frac{2}{3}t_w + \frac{c_h}{2 s_w c_w} \\
c_{YY} &= -\frac{2}{3}t_w - \frac{c_h}{2 s_w c_w} \\
c_{RR} &= -\frac{2}{3}t_w \\
c_{BB} &= \frac{1}{s_w c_w}\left(-\frac{1}{2} + \frac{1}{3}s_w^2\right) \\
c_{TY} &= 0 \\
c_{RT} = c_{RY} &= K\frac{s_h}{2\sqrt{2} s_w c_w}\,.
\end{aligned} \tag{6.12}$$

Similarly, the W couplings are

$$\begin{aligned}
c_{XT} = c_{YB} =& \frac{1 - c_h}{2\sqrt{2} s_w} \\
c_{XY} = c_{TB} =& \frac{1 + c_h}{2\sqrt{2} s_w} \\
c_{RB} = -c_{XR} =& K\frac{s_h}{2 s_w}\,,
\end{aligned} \tag{6.13}$$

where s_w, c_w, t_w are the sine, cosine and tangent of the Weinberg angle, respectively.

Due to mixing with heavy top partners, a non–vanishing K leads to significant changes in the tight correlation between the top partner mass and coupling modifications of the top. For $K = 0$ small top partner masses must, in order to lift the mass of the elementary top to its measured value, be balanced by increased mixing between top and top partners. The electroweak coupling deviations of the top quark in the mass eigenbasis are then determined by the mixing angle and, for $K = 0$, top partner mass and top coupling deviations are strongly correlated. If, however, K is allowed to take values $K \neq 0$ this correlation is weakened; this additionally admits momentum enhanced decays $T \to ht$ [165]. In Section 6.4 we leverage indirect searches to study the dependence of this sensitivity on the parameter K; this information is subsequently used to discuss the sensitivity gap with direct searches in Section 6.5.

As well as the above coupling changes, propagating top partners provide another source of amplitude corrections; a short EFT analysis of this effect, up to mass dimension eight, is provided in Appendix B.1. These additional propagating degrees of freedom result in "genuine" higher–dimensional effects in the mass basis, and are therefore suppressed relative to dimension–four top–coupling modifications. Using a concrete UV scenario this relative suppression has been verified using a full simulation of propagating top partners in the non–resonant limit, and these contributions are therefore omitted from our coupling analysis; the relevance of resonance searches are, however, revisited in Section 6.5.

6.3 Electroweak Top Property Constraints

The weak couplings of the SM top and bottom quarks are modified due to mixing with the top and bottom partners in the mass eigenbasis. These modifications, specifically, are of the left– and right–handed vectorial couplings to the W and Z bosons and can be expressed as

$$\begin{aligned}\mathcal{L} \quad &\supset \quad \bar{t}\gamma^\mu \left[g_L^t P_L + g_R^t P_R\right] tZ_\mu \\ &+ \quad \bar{b}\gamma^\mu \left[g_L^b P_L + g_R^b P_R\right] bZ_\mu \\ &+ \quad \left(\bar{b}\gamma^\mu \left[V_L P_L + V_R P_R\right] tW_\mu^+ + \text{h.c.}\right) . \end{aligned} \tag{6.14}$$

The anomalous couplings of the top quark — the relative deviation with respect to the SM — are denoted by δ

$$g_L^t = -\frac{g}{2\cos\theta_W}\left(1 - \frac{4}{3}\sin^2\theta_W\right)\left[1 + \delta_{Z,L}^t\right], \tag{6.15}$$

$$g_R^t = \frac{2g\sin^2\theta_W}{3\cos\theta_W}\left[1 + \delta_{Z,R}^t\right], \tag{6.16}$$

$$V_L = -\frac{g}{\sqrt{2}}\left[1 + \delta_{W,L}\right], \tag{6.17}$$

$$V_R = -\frac{g}{\sqrt{2}}\delta_{W,R}\,, \tag{6.18}$$

where g is the weak coupling constant associated with the $SU(2)_L$ gauge group and θ_W is the Weinberg angle. Note that $\delta_{W,R}$ is normalised to the left–handed SM coupling of the top quark to the W boson. In this study we implement these anomalous couplings in terms of Wilson coefficients in an effective Lagrangian constructed with dimension–six operators, with the relationship between δ parameters and Wilson coefficients in the Warsaw basis [30] given in Appendix B.2. Expressing anomalous couplings in terms of Wilson coefficients allows the use of the updated version of the TopFitter framework described in Chapter 4 to obtain constraints on the anomalous couplings of the top quark. The anomalous couplings of bottom quarks to Z bosons are, by construction, of lower phenomenological relevance [145].

Analysis	$\sqrt{s}$ [TeV]	Observables	dof
Single top t-channel			
1503.05027 [177]	1.96	σ_{tot}	1
1406.7844 [178]	7	$\frac{\sigma_t}{\sigma_{\bar{t}}}$,	1
		$\frac{1}{\sigma}\frac{\mathrm{d}\sigma}{\mathrm{d}p_\perp^t}$, $\frac{1}{\sigma}\frac{\mathrm{d}\sigma}{\mathrm{d}p_\perp^{\bar{t}}}$,	8
		$\frac{1}{\sigma}\frac{\mathrm{d}\sigma}{\mathrm{d}\lvert y_t\rvert}$, $\frac{1}{\sigma}\frac{\mathrm{d}\sigma}{\mathrm{d}\lvert y_{\bar{t}}\rvert}$	6
1902.07158 [179]	7, 8	σ_{tot}	2
1609.03920 [180]	13	σ_t, $\frac{\sigma_t}{\sigma_{\bar{t}}}$	2
1812.10514 [181]	13	$\frac{\sigma_t}{\sigma_{\bar{t}}}$, σ_t	2
Single top s-channel			
1402.5126 [88]	1.96	σ_{tot}	1
1902.07158 [179]	7, 8	σ_{tot}	2
tW			
1902.07158 [179]	7, 8	σ_{tot}	2
1612.07231 [182]	13	σ_{tot}	1
1805.07399 [183]	13	σ_{tot}	1
tjZ			
1710.03659 [184]	13	σ_{tot}	1
1812.05900 [185]	13	σ_{tot}	1

Analysis	$\sqrt{s}$ [TeV]	Observables	dof
$t\bar{t}Z$			
1509.05276 [186]	8	σ_{tot}	1
1510.01131 [187]	8	σ_{tot}	1
1901.03584 [188]	13	σ_{tot}	1
1907.11270 [118]	13	σ_{tot}, $\frac{1}{\sigma}\frac{\mathrm{d}\sigma}{\mathrm{d}p_\perp^Z}$,	4
		$\frac{1}{\sigma}\frac{\mathrm{d}\sigma}{\mathrm{d}\cos\theta_Z^*}$	3
W boson helicity fractions			
1211.4523 [189]	1.96	F_0, F_R	2
1205.2484 [190]	7	F_0, F_L, F_R	3
1308.3879 [191]	7	F_0, F_L, F_R	3
1612.02577 [192]	8	F_0, F_L	2
Top quark decay width			
1201.4156 [193]	1.96	Γ_t	1
1308.4050 [194]	1.96	Γ_t	1
1709.04207 [195]	8	Γ_t	1

Table 6.1: Experimental analyses used to determine constraints on anomalous top quark couplings. tjZ denotes single-top t-channel production in association with a Z boson.

Anomalous coupling constraints are obtained by comparing resulting predictions to experimental measurements of observables known to be sensitive to the vectorial weak couplings of the top quark. The fit used to constrain anomalous couplings here includes 21 experimental analyses [88, 118, 177–195], which are described in Table 6.1 and provide a total of $N = 54$ degrees of freedom.

The methodology employed when performing this fit mirrors the approach described in Chapter 5. No parton shower or detector simulation is required here, owing to the fact that the results in Table 6.1 are unfolded to parton level. Instead of the χ^2 loss function of Eq. (5.3) we will here instead express results in terms of likelihood.

The likelihood provided by TopFitter is defined as

$$-2\log L(\boldsymbol{\delta}) = \sum_{i,j=1}^{N} \left(X_i^{\mathrm{exp}} - X_i^{\mathrm{th}}(\boldsymbol{\delta})\right) (V^{-1})_{ij} \left(X_j^{\mathrm{exp}} - X_j^{\mathrm{th}}(\boldsymbol{\delta})\right) , \tag{6.19}$$

where X_i^{exp} is the experimental result for the observable X_i and $X_i^{\mathrm{th}}(\boldsymbol{\delta})$ is the theoretical prediction which depends on the anomalous couplings $\delta^t_{Z,L}$, $\delta^t_{Z,R}$, $\delta_{W,L}$ and $\delta_{W,R}$ collectively denoted by $\boldsymbol{\delta}$. The inverse covariance matrix, denoted by V^{-1}, takes into account bin-to-bin correlations where included in results published by experimental collaborations. The statistical treatment of correlations and uncertainties is as described in Section 5.3. Contributions that are quadratic and bilinear are taken into account in the anomalous couplings, though have been verified to cause only a small effect on the likelihood.

The likelihood in Eq. (6.19) is used to exclude anomalous couplings at a confidence level (CL) of 95%. A point $\boldsymbol{\delta}$ in the parameter space of the anomalous couplings is considered excluded if

$$1 - \mathrm{CL} > \int_{-2\log L(\boldsymbol{\delta})}^{\infty} \mathrm{d}x\, f_{\chi^2}(x,k)\,, \tag{6.20}$$

where $f_{\chi^2}(x,k)$ is the χ^2 probability distribution and $k = N$ is the number of degrees of freedom.

Due to the imposition of strong correlations between anomalous couplings by partial compositeness results cannot be obtained or expressed, as in Section 5.5, as individual or profiled bounds; this limit–setting approach would neglect these correlations and therefore lead to the incorrect exclusion of regions of our parameter space. We scan over the model's parameter space, calculating the corresponding anomalous top couplings for each sample point. We determine whether the parameter points are excluded at 95% confidence based on Eq. (6.20) using the likelihood in Eq. (6.19) which includes the experimental input in Table 6.1 and is implemented by TopFitter. This procedure takes the correlations between the anomalous couplings into account because the scan is performed in the parameter space of the underlying model and then mapped to the weak vectorial top couplings.

In Section 6.4 we give details about the parameter scan and present the results, contrasting the current experimental situation with projections to larger integrated luminosities and future colliders.

6.4 Indirect Signs of Partial Compositeness: Present and High Energy Frontier

Before turning to the results and implications of the fit described in Section 6.3 and its extrapolations, we will comment on additional constraints that could be imposed by non–top data. One such category of phenomenologically relevant, non–top data sources are precision Higgs measurements, which are sensitive to top partial compositeness due to their modified Yukawa interactions. Whilst the Yukawa sector probes different aspects of the model than gauge interactions Eqs. (6.8) and (6.11), they are also impacted by admixtures of vector-like top quarks and are therefore correlated. The CMS projections provided in Ref. [196], for example, can be used to comment on the relevance of the Higgs signal strength constraints; of all processes, $gg \to h, h \to ZZ$ provides the most stringent constraint when correlated with the top coupling deviations.[1] The expected signal strength constraint at 3/ab of 4.7% translates into a range of e.g. $|\delta_{W,L}| \lesssim 0.18$. The 100 TeV extrapolation of Ref. [138] of $\lesssim 2\%$ translates into $|\delta_{W,L}| \lesssim 0.1$.

Additionally, there are constraints from electroweak precision measurements, e.g. [197], which amount to a limit $|\delta g_{Z,L}| \lesssim 8\%$; flavour measurements provide an additional avenue to obtain limits on partial compositeness [198, 199]. Noting the above, however, we will here focus on a comparison of direct top measurements at hadron colliders.

The parameters of the Lagrangian in Eq. (6.6) are scanned, as described in Section 6.3, with the space scanned subject to the following mass constraints: existing top partner searches [200] are, loosely, reflected by imposing $M > 1.5$ TeV; the parameter combination $\lambda_t \lambda_q$ is restricted by $m_t \simeq 173$ GeV; and the parameter μ_b is restricted by the b quark mass $m_b \simeq 4.7$ GeV, scanning $|K| \lesssim 4\pi$. In addition to these constraints a reasonable parameter range is pre–selected through consideration of Higgs boson decay modifications. We require that $H \to ZZ, \gamma\gamma$ decay rates reproduce the SM predictions to within 30%, with the Higgs mass fixed to $m_H = 125$ GeV and $v \simeq 246$ GeV in our scan; this leaves ξ, and therefore f, as a free parameter. Whilst the Higgs mass has direct links to top and top partner spectra we, when considering partial–compositeness of the top, assume cancellations of the associated LEC parameters as expressed in Eq. (6.3).

[1] We note that derivative interactions $\sim K\,\bar{t}\gamma^\mu t\,\partial_\mu h$ [165] do not impact the loop-induced $h \to \gamma\gamma, gg$ amplitudes.

The degree of top compositeness is determined by the bi-unitary transformation of Eq. (6.8) with the right–chiral top quark, receiving 70%–90% admixture from the hyperbaryon spectrum, exhibiting the largest degree of compositeness in our scan; our scan finds that, in comparison, the left–chiral top is $\lesssim 30\%$ composite. The right–chiral gauge coupling properties of the top become particularly relevant when we look to constrain this scenario, especially given that they are not present in the SM (see below).

We find that current LHC and Tevatron measurements, given the results reported in Table 6.1, do not admit improved constraints on the parameter space described in Section 6.2 when compared to the limits already taken into account when performing the scan. Current Higgs signal constraints, for example, provide tighter limits on parameters; this is not particularly surprising, however, as top measurements are still at a relatively early stage in the LHC programme owing in part to top final state phenomenology being more involved than their Higgs counterparts.

Noting these limitations, then, it is perhaps more interesting to consider how the sensitivity provided by the current analysis programme of Table 6.1 will evolve in the future. The results of a parameter scan for the HL–LHC is presented in Fig. 6.1; these results are again produced using the experimental results in Table 6.1, though with statistical and experimental systematic uncertainties entering the scan reduced. We specifically rescale statistical uncertainties to 3/ab and, applying the statistical rescaling $\sim \sqrt{L_{\text{LHC}}/L_{\text{HL-LHC}}} \approx 0.2$ using the largest accumulated luminosity among the analyses in Table 6.1, reduce experimental systematics by 80%. We assume no theoretical uncertainties for now, with their impact discussed below. In order to mirror the LHC study as closely as possible, the 7 and 8 TeV analyses in Table 6.1 are reproduced at 13 TeV. The total degrees of freedom for the projection of experimental results to $\sqrt{s} = 13$ TeV and $L = 3/\text{ab}$ is reduced to $N = 30$, owing to the inclusion of a single projection per–observable rather than several measurements. We include the experimental bin–to–bin correlations as reported in their respective analyses [1]. In Fig. 6.1 points excluded by the parameter scan are coloured in red while the allowed region is shaded in green, with the shading indicating the value of the parameter K. As discussed in Section 6.2, the value of K loosens the correlation between the top partner mass and the associated electroweak top coupling modification. Fig. 6.1 also demonstrates that, with higher luminosity and a not–unreasonable reduction of current systematic uncertainties, we begin

[1]The correlations were confirmed to have only a small effect on the likelihood.

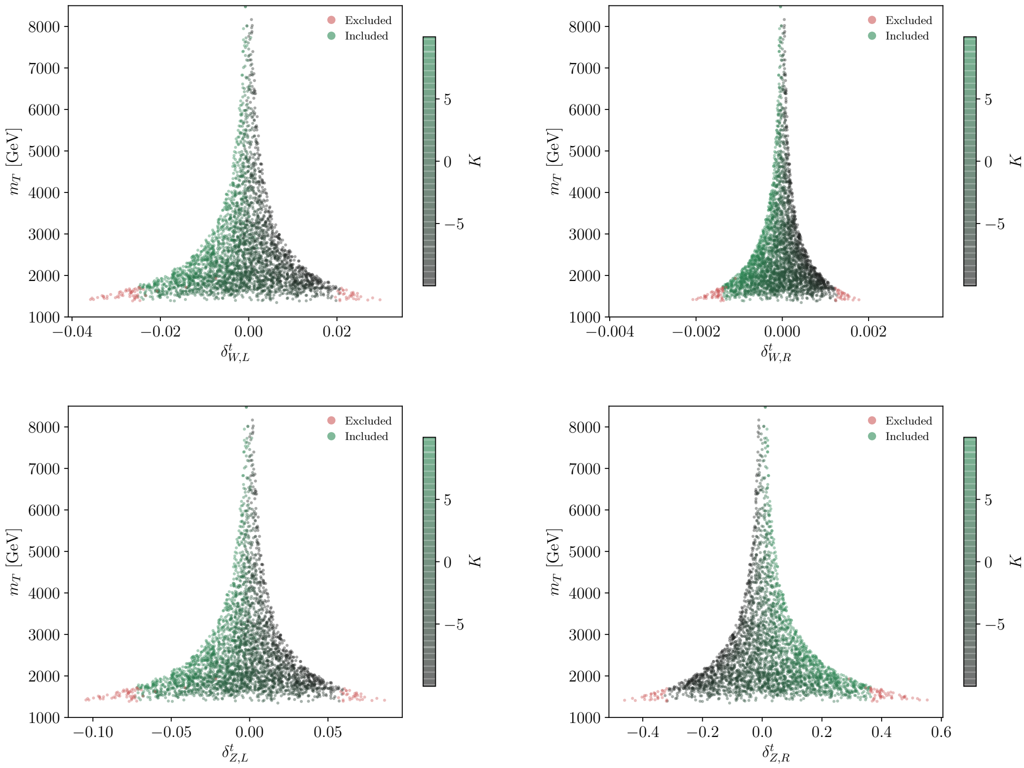

Figure 6.1: Correlation between top partner mass m_T and anomalous top quark couplings in the light of LHC sensitivity extrapolated to 3/ab. Points shown in green are allowed while point in red are excluded at 95% confidence level by this analysis.

to achieve constraints on the parameter space with large $|K| \sim 10$ and associated coupling deviations in the percent range and the right-handed Z coupling in the 30% range.

In Fig. 6.2 we study the impact of theoretical uncertainty assumptions on the maximal top partner mass m_T and the minimal $|K|$ that can be excluded. Whilst these are not strict exclusion limits, and smaller m_T and larger $|K|$ might still be allowed, Fig. 6.2 represents a measure of the maximum sensitivity that could be probed at the HL-LHC in terms of the above quantities. The sensitivity of indirect searches crucially depends, as can be seen in Fig. 6.2, on the expected theoretical uncertainty that will be achievable at the 3/ab stage. As with all channels that are not statistically limited at hadron colliders, the theoretical error quickly becomes the main factor in determining the level at which indirect searches will not provide

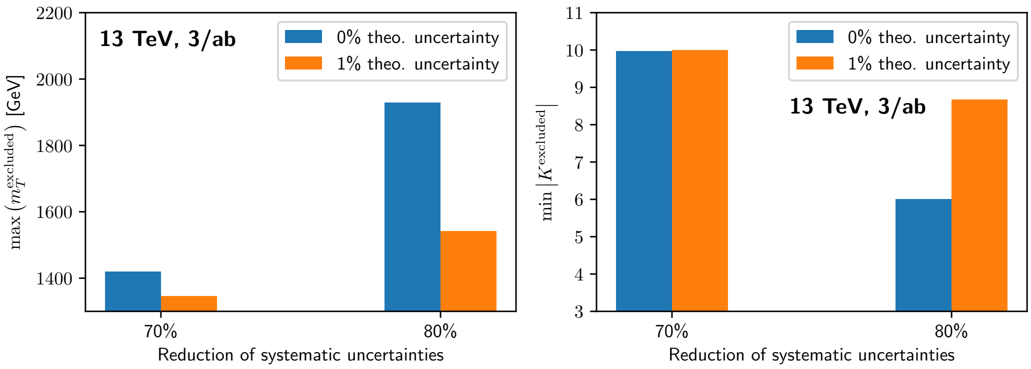

Figure 6.2: Left: Maximum excluded top partner mass m_T vs. reduction in experimental systematic uncertainties. The bars indicate different choices for relative theoretical uncertainties. Right: Minimal $|K|$ in the excluded region of the parameter scan vs. reduction in experimental systematic uncertainty.

complementary information even at moderate top partner masses.

A common practice [201, 202] for estimating projections for theoretical uncertainties at the HL-LHC is to apply a factor of 1/2 to the current theoretical uncertainties at the LHC. According to this prescription, the projected theory uncertainties at the HL-LHC for the observables studied in the analyses in Table 6.1 are $\sim 1-5\%$.

Whilst approximate due to the granularity of the scan, it is instructive to compare the bounds on the anomalous couplings obtained in Fig. 6.1,

$$\begin{aligned}
\delta_{W,L} &\in [-0.025, 0.02]\,, \quad \delta_{W,R} \in [-0.0014, 0.0013]\,,\\
\delta^t_{Z,L} &\in [-0.073, 0.06]\,, \quad \delta^t_{Z,R} \in [-0.33, 0.37]
\end{aligned}$$

with 95% CL profiled limits obtained from a model–agnostic fit, performed using the TopFitter framework described in Chapter 4, using the same experimental projections. These limits were found to be

$$\begin{aligned}
\delta_{W,L} &\in [-0.029, 0.019]\,, \quad \delta_{W,R} \in [-0.009, 0.009]\,,\\
\delta^t_{Z,L} &\in [-0.639, 0.277]\,, \quad \delta^t_{Z,R} \in [-1.566, 1.350]\,.
\end{aligned}$$

Comparing both sets of results for $\delta_{W,R}$, $\delta^t_{Z,L}$, and $\delta^t_{Z,R}$ in particular illustrates the fact that constraints on anomalous couplings — Wilson coefficients in the context of EFT — are likely to be stronger where analyses include correlations imposed by consideration of a concrete model. This suggests recent multi–dimensional parameter fits [130, 132, 203–207] are perhaps more sensitive to concrete realisations of high-scale new physics than is suggested by current, model–agnostic, profiled or marginalised constraints; this will be further enhanced as we move through the high–statistics realm of the LHC and, indeed, whichever high energy frontier awaits beyond.

Having covered possible HL-LHC implications, we now turn to an extrapolation of the analyses in Table 6.1 to a future FCC-hh. In this study the observables in Table 6.1 were reproduced at $\sqrt{s} = 100$ TeV; to reflect the increased reach of future 100 TeV analyses we also include the overflow bins for p_T distributions, resulting in a total number of degrees of freedom at $\sqrt{s} = 100$ TeV of $N = 35$. We additionally rescale statistical uncertainties from the analyses in Table 6.1 to 30/ab, reduce experimental systematic uncertainties to 1% of their measured values, and assume no theoretical uncertainties. A detailed comparison of the impact of uncertainties and experimental systematics is given in Fig. 6.4. Due to bin–to–bin correlations having a small impact on the exclusion of parameter points in 13 TeV analyses, we also assume no correlation between measurements and bins in the 100 TeV analyses. The results for this study, presented in Fig. 6.3, show that the FCC-hh can further improve on the LHC sensitivity by a factor of $\lesssim 3$ in terms of indirectly exploring the top partner mass in the scenario considered here.

As in the HL-LHC extrapolation we find that theoretical uncertainties are the key factors in sensitivity limits, with no fixed convention for theoretical uncertainty projections to FCC-hh. However according to Ref. [208], at least with respect to QCD processes, "*1% is an ambitious but justified target*". A 100 TeV FCC-hh can, in principle, reach $K = \mathcal{O}(1)$ values as shown in Fig. 6.4. This is the perturbative parameter region where $T \to tZ$ direct searches (cf. [209]) are relevant, and we will therefore focus on $|K| < 1$ when we study this phenomenologically relevant channel in a representative top partner search in Section 6.5.

Figs. 6.2 and 6.4 further demonstrate that uncertainties are the key limiting factors of indirect BSM sensitivity in the near future. Whilst this could be taken as painting a dire picture for the BSM potential, it is worth stressing that data–driven approaches, e.g. [210, 211], together with the application of new statistical tools to reduce the impact of uncertainties [212–215] will provide further paths to constraints beyond "traditional" precision parton-level calculations at fixed order in perturbation theory. The basis of our analysis is also formed by the extrapolation of existing searches to 3/ab and eventually to 100 TeV.

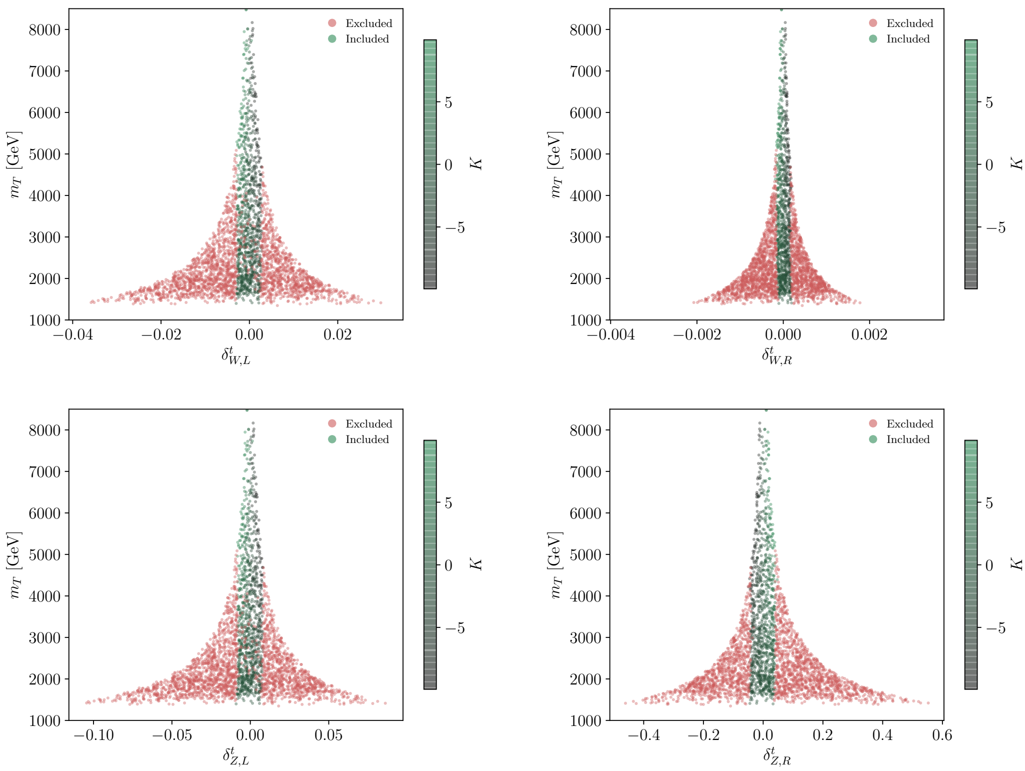

Figure 6.3: Top coupling correlations analogous to Fig. 6.1 for the FCC-hh analysis. See Fig. 6.4 and the text for uncertainty discussion.

When statistics is not a limiting factor, a more fine-grained picture can be obtained by leveraging differential information[1]. Due to the limiting factor in the indirect analysis considered here being tZ coupling constraints we have extended the inclusive tjZ cross–section to gauge the impact of differential measurements, including the differential cross–section with respect to both the tranverse momentum and rapidity of the Z boson in the tjZ channel.

The inclusion of these distributions did not result in a notable change in the sensitivity projections in Figs. 6.2 and 6.4, with a more in–depth study needed to identify maximally sensitive observables at hadron and lepton colliders. The identification of target observables and study of their impact on projected sensitivity at future colliders is, however, outwith the scope of this work.

[1]See also a recent proposal to employ polarisation information in non–top channels [216].

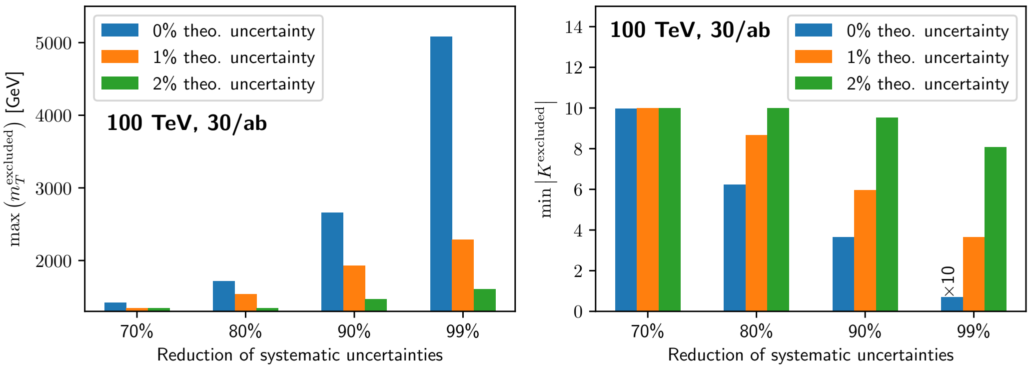

Figure 6.4: Same as Fig. 6.2 but for a centre-of-mass energy of $\sqrt{s} = 100$ TeV and a luminosity of $L = 30$/ab. The value of $\min|K^{\mathrm{excluded}}|$ for 99% reduction in systematic uncertainties and no theory uncertainty was multiplied by a factor of 10 to increase visibility in the plot on the right-hand side.

6.5 Top Resonance Searches

The existence of additional vector–like fermions in composite Higgs models admits the possibility of direct detection through resonance searches. We will focus on channels involving the lightest top partner resonance, denoted here by T, which may be produced as a pair through QCD interactions or in association with a quark through interactions with vector or Higgs bosons.

In the context of Section 6.4, modes $T \to tZ$ followed by decays of $tZ \to (q_1 q_2 b)(\ell^+\ell^-)$ are of particular interest as, in addition to directly correlating electroweak top quark property modifications with new resonant structures following Eqs. (6.8) and (6.11), they may allow separation of signal and background and the reconstruction of the top partner mass m_T. This is possible in the presence of two same–flavour, oppositely charged leptons ℓ^+, ℓ^- (electrons or muons) in the boosted final state and missing transverse energy as demonstrated in Ref. [209]. We will follow a similar cut–and–count analysis, adapted to FCC energies to enable comparison with the indirect constraints presented in Section 6.4. Relevant Standard Model background sources include Z+jets, $t\bar{t}Z$+jets, tZ+jets and $\bar{t}Z$+jets; the large mass of the top partner leads to a highly boosted Z boson, allowing us to omit background processes involving two vector bosons and jets.

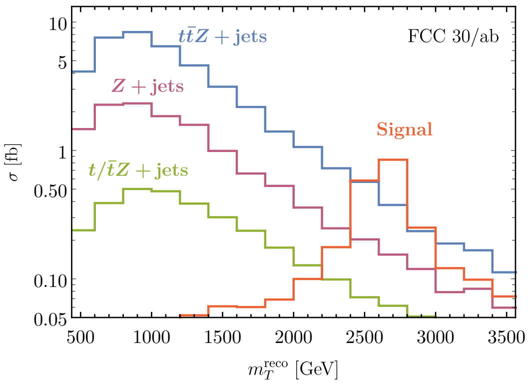

(a) Differential cross–sections.

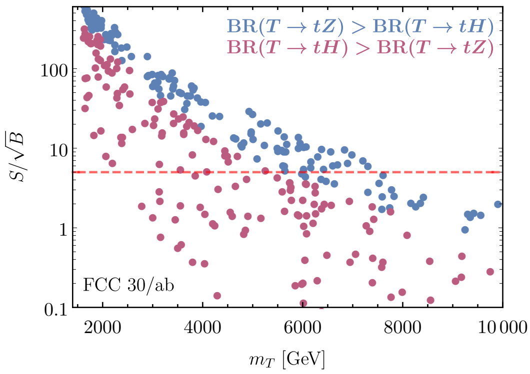

(b) Significance for different coupling points.

Figure 6.5: (a) Differential cross–sections for background and signal of a representative parameter point with a top partner mass of $m_T = 2700$ GeV. (b) Significance $S/\sqrt{B}$ for different coupling points at FCC 30/ab is displayed on the right. The dashed red line indicates $S/\sqrt{B} = 5$, where discovery can be achieved. For comparison, we include points dominantly decaying to tH to show where our tZ analysis is phenomenologically relevant.

The signal is modelled using FeynRules [217, 218], and events for both signal and background are generated with MadEvent [39, 40, 219]. Decays are included via MadSpin [47, 220] for the signal, $t\bar{t}Z$+jets, and $(t,\, \bar{t})Z$+jets background processes. All events are showered with Pythia8 [48] using the HepMC format [221] before passing them to Rivet [49] for a cut–and–count analysis, along with FastJet [222, 223] for jet clustering. The presence of a top in the boosted final state necessitates the use of jet–substructure methods for top–tagging, for which we adopt the Heidelberg-Eugene-Paris top-tagger (HepTopTagger) [224–226].

Final state leptons are required to be isolated[1] and have transverse momentum $p_T(\ell^\pm) \geq 20$ GeV and pseudorapidity $|\eta(\ell^\pm)| \leq 2.5$. Slim–jets are clustered with the anti–kT algorithm [227] with radius size of 0.4 and fat–jets are also simultaneously reconstructed with Cambridge–Aachen algorithm and a larger size of 1.5. Both types of jets must satisfy $p_T(j) \geq 20$ GeV and $|\eta(j)| \leq 4.9$.

Lepton selection cuts are also applied, requiring at least one pair of same flavour oppositely charged leptons with an invariant mass within 10 GeV of the Z boson

[1]For a lepton to be isolated we require the total p_T of charged particle candidates within the lepton's cone radius $\Delta R = 0.3$ to be less than 10% of the lepton's $p_T(\ell^\pm)$.

resonance, i.e. $|m_{\ell^+\ell^-} - m_Z| < 10$ GeV. Furthermore, we ensure the leptons are collimated by requiring that $\Delta R(\ell^+\ell^-) = \sqrt{[\Delta\eta(\ell^+\ell^-)]^2 + [\Delta\phi(\ell^+\ell^-)]^2} < 1.0$. Both leptons must have transverse momentum $p_T(\ell^\pm) > 25$ GeV, and if more than one candidate pair exists the one with invariant mass closest to $m_Z = 91.1$ GeV is selected to reconstruct the Z boson's four–momentum. The search region is restricted further by imposing the requirements $p_T(Z) > 225$ GeV and $|\eta(Z)| < 2.3$, with the former ensuring boosted kinematics and the latter allowing better discrimination from the Z+jets background of the SM.

As the hadronic part of the signal final state is characterised by large transverse momentum, stemming from the boosted nature of the top quark, we require the scalar sum of the transverse momenta to satisy $H_T > 700$ GeV for all identified slim–jets with $p_T(j) > 30$ GeV and $|\eta(j)| < 3$. In order to constrain the search region we require at least one fat–jet that is top–tagged with HepTopTagger and has $p_T(j) > 200$ GeV. Where more than one candidate exists we choose the top with $\Delta\phi(Z, t)$ closest to π, ensuring the Z and t candidates are back-to-back. B–jets are identified from slim–jets with at least one satisfying $p_T(b) > 40$ GeV being required to be within the top radius of $\Delta R(t, b) < 0.8$, implying that the b quark originated from the top. The b-tag efficiency is set to 80% and the mistagging probability of quarks at 1%. The reconstructed Z and t candidates are used to reconstruct the top partner's mass, m_T^{reco}, via the sum of the Z and t four momenta.

The efficiency of the cut–and–count analysis is determined by the resonance mass, which defines the kinematics of the final state particles. We scan over a range of top partner masses and perform an interpolation to eventually evaluate constraints in a fast and adapted way. The accuracy of this approach has been validated against additional points, as well as against the independence of the coupling values. We find that a signal region definition using the reconstructed top partner mass $m_T^{\text{reco}} \in [m_T - 0.2m_T, m_T + 0.15m_T]$ to be an appropriate choice to reduce backgrounds and retain enough signal events to set limits in the region $|K| < 1$ that we are interested in as discussed in Section 6.4; this ensures that the detailed search is well–controlled and phenomenologically relevant. For larger K values the $T \to ht$ decay receives sizeable momentum-dependent corrections [165], which quickly start to dominate the total decay width to a level where we can expect our analysis flow to become challenged due to non-perturbative parameter choices.

In the spirit of data–driven "bump hunts", we fit the m_T^{reco} distribution away from the signal region to obtain a background estimate in the signal region defined above. Such distribitions follow polynomial distributions on a logarithmic scale and are therefore rather straightforward to control in a data–driven approach; this can be seen in Fig. 6.5(a), where we show a m_T^{reco} histogram for a representative signal point $m_T \simeq 2.7$ TeV alongside background contributions. Such data–driven strategies also largely remove the influence of theoretical uncertainties at large momentum transfers, and are a commonly–deployed method in experimental analyses[1]. After all analysis steps are carried out we typically deal with a signal–to–background ratio $S/B \sim 0.1$, which means that our sensitivity is also not too limited by the background uncertainty resulting from such a fit. Identifying a resonance we can evaluate the significance, which is controlled by $S/\sqrt{B}$. In setting limits we assume a total integrated luminosity of 30/ab for 100 TeV FCC-hh collisions. Sensitivity projections are shown in Fig. 6.5(b), where it can be seen we have good discovery potential in tZ for parameter regions up to $m_T \simeq 7.3$ TeV with the additional exclusion potential $\sim S/\sqrt{S+B}$ reaching to $m_T \lesssim 10$ TeV at 95% CL. As previously mentioned the analysis outlined above is particularly suited for parameter regions with significant top partner decay into Zt pair — that is, regions in parameter space where modifications are most pronounced in the weak boson phenomenology rather than in Higgs-associated channels.

Whilst one particular analysis has been used here to provide additional context for the scan presented in Section 6.4 it is worth nothing that other channels present significant BSM discovery potential — see, e.g., Refs. [228, 229]. This could include $T \to ht$, for example, which would lead to b-rich final states and target partial compositeness in the Higgs sector [230, 231]. Such an analysis provides an avenue to clarify the Higgs sector's role analogous to the weak boson phenomenology studied in this work, albeit in phenomenologically more complicated final states when turning away from indirect Higgs precision analyses and $t\bar{t}h$ production. Searches for other exotic fermion resonances, such as B and the 5/3-charged Q, provide additional discriminating power [232, 233] and would be key in determining the parameter region of the model if a new discovery consistent with partial compositeness is made.

Comparing the direct sensitivity estimates of Fig. 6.5 with Fig. 6.3 we see that indirect searches for top compositeness as expressed through SM top electroweak coupling modifications provide additional information to resonance searches if uncertainties can be sufficiently well–controlled. The potential discovery of the top partner alone, for instance, is insufficient to verify or falsify the model studied in this

[1] See, e.g., Refs. [210, 211] for recent examples.

work; the correlated information of top quark coupling deviations is an additional crucial step in clarifying the underlying UV theory.

Extrapolating the current sensitivity estimates of the LHC alongside the uncertainties to the 3/ab phase, the HL-LHC will provide only limited insight from a measurement of top quark electroweak SM gauge interaction deformations, though can nonetheless lead to an interesting opportunity at the LHC; with the LHC obtaining a significant boost in sensitivity via direct searches [209, 232, 233], the potential discovery of a top partner at the LHC would make a clear case for pushing the energy frontier to explore the full composite spectrum, correlating these findings with an enhanced sensitivity to top coupling modifications.

6.6 Summary and Outlook

Due to the ability of high–statistics exploration at the LHC, top quark processes act as Standard Model "candles". The electroweak properties of the top quark are particularly relevant interactions, as deviations from Standard Model predictions are tell–tale signatures of new physics beyond the Standard Model with direct relevance to the nature of the TeV scale.

Using the example of top partial compositeness, and the extended MCHM5 implementation of Ref. [165] for concreteness, we demonstrate that the ongoing top EFT programme will provide important additional information to resonance searches as long as theoretical and experimental uncertainties can be brought under control. This is further highlighted at the energy frontier of a future hadron collider at 100 TeV. Backing up our electroweak top coupling analysis with a representative top partner resonance search, we demonstrate the increased sensitivity and discriminating power to pin down the top quark's electroweak properties at the FCC-hh.

Especially in case a discovery is made at the LHC that might act as a harbinger of a composite TeV scale, there is a clear case for further honing the sensitivity to the top's coupling properties whilst extending the available energy coverage. We additionally note that high–energy lepton colliders such as CLIC will be able to provide a very fine–grained picture of the top electroweak interactions, which can provide competitive indirect sensitivity [204, 234–238]. A more detailed comparison of the interplay of hadron and lepton colliders may prove to be fruitful.

Chapter 7

Improved Constraints using Edge Convolution Networks

The global and statistically rigorous fit to top sector data presented in Chapter 5 highlighted both the usefulness of broad and extensible fits to ever–expanding and evolving data and the fact that the experimental implementation of such a strategy is also far from trivial; the number of involved and independent effective interactions can be large, potentially limiting the sensitivity of any specific analysis.

In Chapter 6 we found that continued pursuit of the top EFT programme offers the potential for important additional data points, though the degree of said potential is subject to both experimental and theoretical uncertainty improvements. Poorly–controlled uncertainties can lead to weak constraints, giving only loose and perhaps non–perturbative limits when understood as UV constraints in concrete matching calculations; well–controlled uncertainties, however, will lead to improved limits when more data become available. Lower limits on the direct evidence of new states are predominantly driven by the available LHC centre-of-mass energy. The lower limit on Λ in our effective Lagrangian, which is driven by the energy coverage of the LHC, will not change dramatically in the future. Thus, any modelling improvement at scales $|Q^2| \ll \Lambda^2$ where the EFT expansion can be considered reliable will be reflected in improved constraints on the Wilson coefficients.

Another possibility is to pursue more comprehensive extraction of information from new and existing experimental data, with such strategies being highlighted in the recent resurgence of machine learning (ML) applications to particle physics [213, 214, 239–247] (in particular focusing also on experimental improvements [248, 249]). Commonly employed collider observables such as transverse momenta, angles and (pseudo)rapidities, alongside rectangular cuts on these, may be unable to fully capture the exclusion potential when all ad hoc modifications of correlations are considered; this is the key motivation of the EFT approach, particularly as regards the inclusion of systematic uncertainties [215].

It is the latter of these routes we will pursue here, focusing on EFT parameter constraints for the top sector [129, 130, 132, 133, 203, 206, 250, 251] using $pp \to t\bar{t}$ production with semi–leptonic top decays. We choose this process due to it providing a reasonably clean channel, with sufficient statistical control to enable discussion of ML–improved EFT strategies (see also Ref. [243]). To reflect expected correlations between the final state — fully showered and hadronised — objects, we employ Graph Neural Networks (GNNs) with Edge Convolution [252–255]. This exploits both the structure of data and correlations ('edges') of different intermediate and final state particles ('nodes'); it is, therefore, well motivated for particle physics applications [256–267].

This chapter is organised as follows: In Section 7.1 we discuss our simulation, analysis, and fit setup for this case study into $t\bar{t}$ production. Section 7.2 covers the machine learning aspects of the work, briefly outlining our baseline cuts with the experimental analysis of Ref. [268] as guidance. We also review our ML setup and discuss input parameters, training and classification. The performance improvements of an ML–informed top sector fit are presented in Section 7.3, and conclusions in Section 7.4.

7.1 Effective Interactions for Top Pair Production with Leptonic Decays

Exploiting the same piecewise construction discussed in Chapter 4 we use the SMEFTSim [45, 269] implementation to include the effective operators, interfaced with MadGraph5 [40] via FeynRules [218] and UFO [46] to generate the event samples at leading order (LO)[1] for

$$pp \to t\bar{t} \to \ell b\bar{b}j + \not{E}_T \,. \tag{7.1}$$

We use a $\sqrt{s} = 13$ TeV analysis by the CMS collaboration [268] as inspiration to investigate correlated differential measurements, with representative data binning as given in Table 7.1.

[1] In this work, we focus on GNN performance of EFT parameter fits and limit ourselves to a leading order analysis. We note that including higher order contributions for the SM hypothesis is crucial to obtain consistency with the measured data, but will not impact the qualitative results of this work. We have checked that the results of Table 7.2 are qualitatively reproduced by a full NLO fit using the TopFitter framework described in Chapter 4.

Distribution	Observable	Binning
$\frac{1}{\sigma}\frac{d\sigma}{d\lvert y_t^h\rvert}$	$\lvert y_t^h\rvert$	$[0.0, 0.2, 0.4, 0.7, 1.0, 1.3, 1.6, 2.5]$
$\frac{1}{\sigma}\frac{d\sigma}{d\lvert y_t^l\rvert}$	$\lvert y_t^l\rvert$	$[0.0, 0.2, 0.4, 0.7, 1.0, 1.3, 1.6, 2.5]$
$\frac{1}{\sigma}\frac{d\sigma}{d\lvert y_{t\bar{t}}\rvert}$	$\lvert y_{t\bar{t}}\rvert$	$[0.0, 0.2, 0.4, 0.6, 0.9, 1.3, 2.3]$
$\frac{1}{\sigma}\frac{d\sigma}{dp_\perp^{t,h}}$	$p_\perp^{t,h}$	$[0, 45, 90, 135, 180, 225, 270, 315, 400, 800]$ GeV
$\frac{1}{\sigma}\frac{d\sigma}{dp_\perp^{t,l}}$	$p_\perp^{t,l}$	$[0, 45, 90, 135, 180, 225, 270, 315, 400, 800]$ GeV
$\frac{1}{\sigma}\frac{d\sigma}{dm_{t\bar{t}}}$	$m_{t\bar{t}}$	$[300, 375, 450, 530, 625, 740, 850, 1100, 2000]$ GeV
$\frac{1}{\sigma}\frac{d\sigma}{d\lvert y_{t\bar{t}}\rvert dm_{t\bar{t}}}$	$\lvert y_{t\bar{t}}\rvert$	$[0.0, 0.2, 0.4, 0.6, 0.9, 1.3, 2.3]$
	$m_{t\bar{t}}$	$[300, 375, 450, 625, 850, 2000]$ GeV
$\frac{1}{\sigma}\frac{d\sigma}{dp_\perp^{t,h}d\lvert y_t^h\rvert}$	$p_\perp^{t,h}$	$[0, 45, 90, 135, 180, 225, 270, 315, 400, 800]$ GeV
	$\lvert y_t^h\rvert$	$[0.0, 0.5, 1.0, 1.5, 2.5]$

Table 7.1: Distributions provided in Ref. [268] and included in the fit in this work.

Standard Model predictions are injected as mock reference data[1] for the luminosity $\mathcal{L}_{\text{ref}} = 2.3\ \text{fb}^{-1}$ of Ref. [268]. Statistical uncertainties are scaled relative to this luminosity, using $\sqrt{\mathcal{L}_{\text{ref}}/\mathcal{L}}$ for extrapolations. Our implementation relies on Rivet [49, 270] and the routine described in Section 4.3.5, with Rivet processing events after showering with Pythia8 [48] before they enter the fit. Bounds for all relevant operators are again expressed in the dimensionless 'bar' notation, $\bar{C}_i = C_i \frac{v^2}{\Lambda^2}$, with electroweak expectation value $v \simeq 246$ GeV.

The standard approach taken by many analyses is to employ cut–and–count techniques, aiming to boost sensitivity to new physics by restricting the phase space region such that SM contamination is minimised. Rectangular cuts, however, often yield inferior sensitivity compared to phase space regions methodically selected by means of machine learning classifiers.

We posit that an efficient event–by–event classification using GNNs, separating the generated events into either pure SM or the SMEFT operators that sourced them, may lead to improvements on the EFT constraints after imposing cuts on the output score of the network.

[1]This allows the use of the TopFitter framework to perform fits in a similar manner to that discussed in 5, with the target being SM predictions rather than experimental results.

7.2 Graph Representation of Events

As implied by the name, our events must first be cast to a graph representation before they can be used as input for a Graph Neural Network. Whilst there exists multiple routes to defining a graph embedding — comprised of nodes, edges, and features — for final states or reconstructed objects we will here use a physically–motivated approach, basing our embedding on the structure of Eq. (7.1)[1].

Events are passed through a preselection stage before embedding, with events being vetoed unless meeting the following criteria: at least two non–b–tagged jets with transverse momentum $p_T(j) > 20$ GeV and pseudorapidity $|\eta| < 5$; at least two b–jets with $p_T(b) > 20$ GeV and one lepton ℓ in the central part of the detector, $|\eta(\ell)| < 2.5$. The events surviving preselection are then embedded as illustrated in Fig. 7.1 by defining the nodes, edges, and features of the graph representation.

The first node is defined using the missing transverse momentum (MTM), identified by balancing the net visible momenta, $-p(\text{visible})$, neglecting the longitudinal components. For each lepton we then attempt to reconstruct the W four–momentum as a sum of the lepton's four–momentum and the MTM. If the invariant mass of the W candidate satisfies $65\,\text{GeV} \leq m_W^{\text{cand.}} \leq 95\,\text{GeV}$, a node, labelled W_1, is added alongside a node labelled b_1 for the b–jet with the smallest separation $\Delta R = \sqrt{\Delta\eta^2 + \Delta\phi^2}$ from W_1; if there are multiple lepton–MTM combinations that satisfy the criteria we select the candidate closest to the W boson mass. The top from the leptonic decay chain adds another node, t_1, with the top being reconstructed using the four–momenta of ℓ, b_1, and the MTM. We also consider combinations of jets using a similar procedure, finding a pair with dijet invariant mass 70 GeV $\leq m(jj) \leq$ 90 GeV. If such a pair is found, we add nodes for the two jets j_1, j_2 and for the second boson W_2, otherwise nodes are added nodes for only the two leading jets. From the remaining b–jets a node is added for the leading one, b_2, as well as for the second top t_2 whose four–momentum is reconstructed using b_2, j_1 and j_2. We finally scan over the remaining particles and, if any are within $\Delta R < 0.8$ of an existing node, a node is added that will be connected only to the single closest node. Each node is assigned a feature vector, $[p_T, \eta, \phi, E, m, \text{PID}]$, containing the transverse momentum, pseudorapidity, azimuthal angle, energy, mass, and (PDG [10]) particle identification number.

[1] It was found that using the fully connected graph lead to decreasing performance as the number of edges, which carry less physics information, increased. A decay–chain inspired embedding gives better performance.

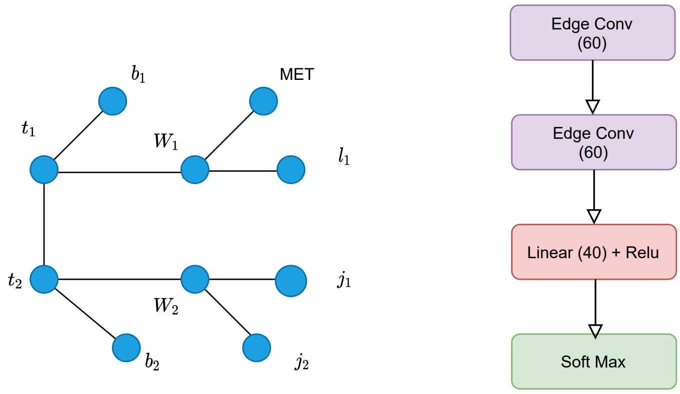

Figure 7.1: Representative diagrams of the input graph structure (left) and network architecture (right) used in this work.

With the nodes in place and associated with their respective features, we can finally construct our graph representation by adding edges to connect them; these connections between nodes create the adjacency matrix of the graph, with final state nodes being connected to the nodes of their preceding reconstructed objects as illustrated in Fig. 7.1. The MTM and lepton are first connected to W_1 and, subsequently, W_1 and b_1 are connected to the first top quark node. If a node labelled W_1 was not created the final states connect directly to t_1.[1]

The other leg of the decay chain is handled similarly; if W_2 was successfully reconstructed it is connected to the two jets used to reconstruct it, and both W_2 and b_2 are connected to the top quark node. Jet nodes are directly connected to the top if there is no node for W_2. Lastly, any node originating from the remaining final states is connected to the node of the object that satisfied $\Delta R < 0.8$.

Graph Neural Network with Edge Convolution

Due to their admitting the use of multi–scale localised spatial features, Convolutional Neural Networks (CNNs) have been (and continue to be) an active area of research and improvement in the ML space. CNNs do, however, exhibit the limitation of being suited to applications involving regular Euclidean data sources such as images, which in turn limits their usefulness in the particle physics use–case. Recent developments in GNNs have overcome this limitation, generalising CNNs to operate on graph structures and enabling the exploration of non–Euclidean domains [271];

[1] We expect that this will lead to a further enhancement of sensitivity when the non–resonant Λ^{-4} contributions are considered.

this was formalised for supervised learning applications as Message Passing Neural Networks (MPNNs) in Ref. [254], which generalises to the type of network, Edge Convolution (EdgeConv), used here. There are two main components to an MPNN: a message–passing phase and a graph readout layer. Message passing is defined as a mathematical operation between two nodes, i and j; we define $x_i^{(l)}$ as the features of the i^{th} node and $\mathbf{e}_{ij}^{(l)}$ as the edge connecting nodes i and j at the l^{th} step in time, where the vector sign represents the directed graph[1].

During the message-passing phase a message $\mathbf{m}_{ij}^{(l)}$ is calculated between the two nodes by the following operation,

$$\mathbf{m}_{ij}^{(l)} = \mathbf{M}^{(l)}(\mathbf{x}_i^{(l)}, \mathbf{x}_j^{(l)}, \mathbf{e}_{ij}^{(l)})\,. \tag{7.2}$$

The message function can be a linear activation function or a multilayer-perceptron (MLP), which is shared between the edges and is analogous to convolution operation; we will utilise a linear activation function for the message function here. Once the messages between all connected nodes have been calculated in a layer, each node feature is updated using an aggregation function

$$\mathbf{x}_i^{(l+1)} = \mathbf{A}(\mathbf{x}_i^{(l)}, \{\mathbf{m}_{ij}^{(l)} \,|\, j \in \mathcal{N}(i)\})\,, \tag{7.3}$$

where $\mathcal{N}(i)$ are the nodes which are connected to i^{th} node, $\mathbf{A}$ is the permutation–invariant function — for instance the mean, maximum, or sum — and the vector $\mathbf{x}^{(l+1)}$ is the input to the next message passing layer. For graph classification, after some message passing operation L we perform a permutation invariant graph readout operation $\square$ on the final node features $x_i^{(L)}$,

$$\mathbf{X} = \square(\mathbf{x}_i^{(L)} | i \in G), \tag{7.4}$$

where G denotes the input graph. This gives us fixed–length representation of (possibly variable–length) graphs to be fed into a downstream neural network.

We use an EdgeConv network in this study, which is an ideally suited network for exploiting the edge features from given node features. The edge convolution operation is defined with the following message–passing function

$$\mathbf{x}_i^{(l+1)} = \frac{1}{|\mathcal{N}(i)|} \sum_{j \in \mathcal{N}(i)} \text{ReLU}\left(\Theta(\mathbf{x}_j^{(l)} - \mathbf{x}_i^{(l)}) + \Phi(\mathbf{x}_i^{(l)})\right), \tag{7.5}$$

where aggregation for each node is done using the mean, after which the features of each node are updated. The linear layers Θ and Φ take the inputs and map them to identical dimensional spaces. We use $L = 2$ and mean graph–readout.

[1] A graph can be undirected or directed, with bi–directed graphs used for this study.

Network Architecture and Training

The graphs and networks used to classify the different EFT (signal) and SM (background) contributions are constructed using Deep Graph Library [272] and PyTorch [273]. Models with different architectures are trained on data samples that consist of 70,000 events for each class, with a split of 80%, 10% and 10% for training, validation and testing respectively. The network models considered incorporate EdgeConv layers followed by hidden linear layers. ReLU is used as the activation function for each layer. Probabilities for each class can be obtained from the output layer by applying the softmax function. We choose the categorical cross–entropy loss function for the multi–class classification problem and use the Adam optimiser, with a learning rate of 0.001, to minimise the loss function. The learning rate decays with a factor of 0.1 if the loss function has not decreased for three consecutive epochs. We train the models for 100 epochs in mini–batches of 100 graphs and an early stopping condition when no loss decrease has occurred for ten epochs.

By varying the number of layers and nodes, and training the different models on the data, we find that the configuration of two EdgeConv layers of 60 nodes and one hidden linear layer of 40 nodes performs particularly well for our scenario. Any event used during training or validation is not considered further in any other part of this work. The loss and accuracy curves for the classifying events have been checked to avoid overtraining, and it is worth highlighting that signs of overtraining are observed when we deeper networks are considered. The good performance of a relatively shallow network signifies that non–resonant physics can be characterised using relatively few phenomenological properties; this observation is consistent with the findings of traditional differential EFT fits such as Ref. [274], and will form the baseline of the qualitative discussion of a two–operator example in Section 7.3.1.

7.3 GNN-improved Wilson Coefficient Constraints

7.3.1 A Minimal Example

For illustration purposes, we first limit our study to a three–class classification problem. The network output in this example returns the probability of an event belonging to each of the three classes, with the event being assigned to the EFT or SM class with the greatest corresponding probability. Generalising this to a larger number of Wilson coefficients will be the focus of Section 7.3.2.

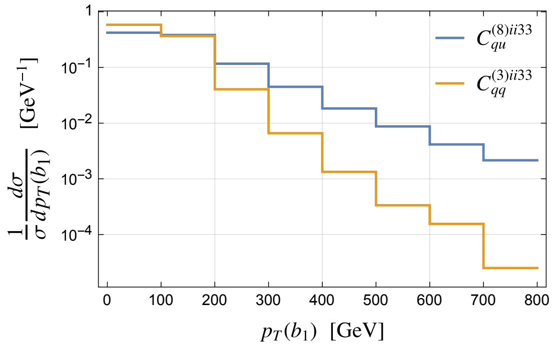

Figure 7.2: The normalised $p_T(b_1)$ distributions at the 13 TeV LHC for the two operators of the three-class example, Eq. (7.6).

The restriction employed in this section is motivated from the generic modifications that can be expected from EFT interactions. Momentum–dependent interactions will typically enhance the tails of momentum–dependent distributions compared to the SM, while interactions that modify SM couplings (feeding into, e.g., a modified top quark width) will predominantly lead to a modified inclusive rate with momentum-related distributions similar to the SM. This is reflected in our choice of operators for this section:

$$\begin{aligned} \mathcal{O}_{qu}^{(8)ii33} &= (\bar{q}_i \gamma_\mu T^A q_i)(\bar{u_3}\gamma^\mu T^A u_3)\,, \\ \mathcal{O}_{qq}^{(3)ii33} &= (\bar{q}_i \gamma_\mu \tau^I q_i)(\bar{q}_3 \gamma^\mu \tau^I q_3)\,. \end{aligned} \tag{7.6}$$

The distributions of the hardest b jet for these operators are given in Fig. 7.2. Correlated with the events hardness are more central final states and characteristically modified angular and rapidity separations. Identifying the most appropriate superposition of physical observables is therefore critical for a particularly sensitive EFT analysis. We consider the two operators of Eq. (7.6) as they exhibit distinct phenomenology, however they will also allow us to discuss the limitations of using different approaches to ML–informed limit setting.

In Fig. 7.3 (left), the probabilities calculated for each event to be a result of each SMEFT insertion are shown; as can be expected, events arising from $\mathcal{O}_{qu}^{8(ii33)}$ are more commonly located in the upper left region — large $\mathcal{O}_{qu}^{8(ii33)}$ probability, small $\mathcal{O}_{qq}^{3(ii33)}$ probability — while events from $\mathcal{O}_{qq}^{3(ii33)}$ are in the bottom right. In contrast, SM events usually end up in a region where the probabilities for $\mathcal{O}_{qu}^{8(ii33)}$ and $\mathcal{O}_{qq}^{3(ii33)}$ are both low and the probability of belonging to the SM is high due to the normalisation of probabilities. The network is able to discriminate efficiently among the three classes and different regions can be efficiently removed by cuts on the two output probabilities. In Fig. 7.3 (right), the Receiver Operator Characteristic (ROC) curves are shown. These are calculated in a one–vs–rest scheme by first

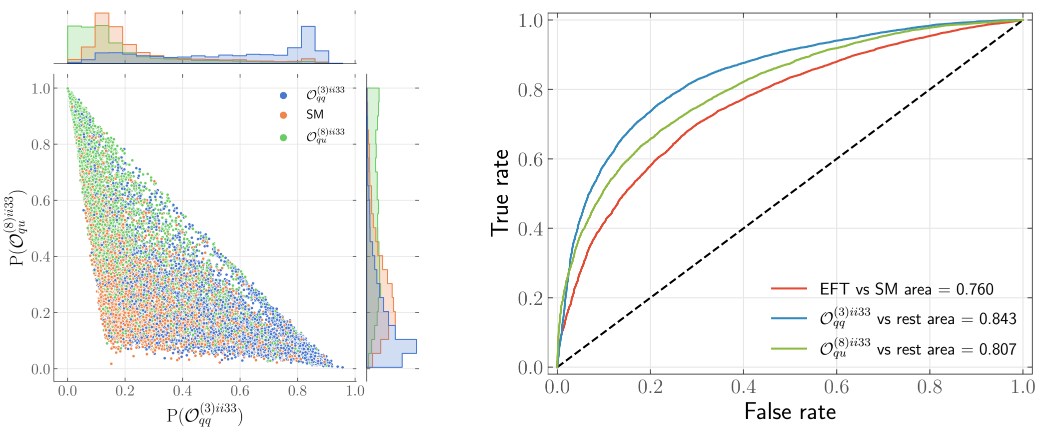

Figure 7.3: The probabilities calculated for each event to be a result of each SMEFT insertion is shown. On the right the Receiver Operator Characteristic (ROC) curves are shown. We calculate these in a one–vs–rest scheme for each operator.

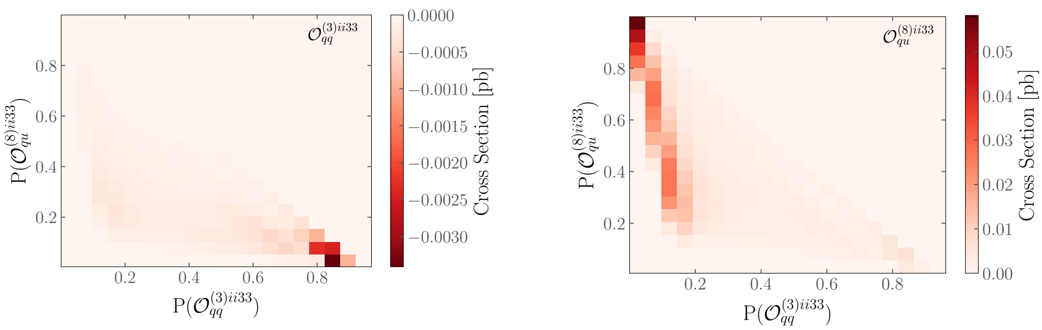

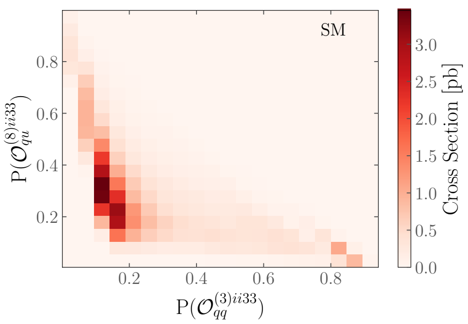

Figure 7.4: Example two-dimensional histograms for each contribution, normalised to the cross section rate.

binarising the labels and using the network score output for each coefficient. We also show an EFT vs SM ROC curve where all EFT labels are marked as signal and the SM as background. We construct the ROC curve using the summed scores for each new physics Wilson Coefficient, which we later generalise when more than two contributions are non–zero.

To examine the improvement of the network performance for this simplified test case of two WCs modifying SM production, we performed a χ^2 fit for each operator to derive bounds on the WCs. To construct the χ^2 (for details see Ref. [130]), we use the distribution $p_T(b_1)$, the transverse momentum of the leading b-jet. To gain as much statistical control as possible, we also extrapolate the results to an integrated luminosity of 3/ab, in line with the expected performance of the High-Luminosity LHC (HL–LHC). The qualitative pattern of results, however, is independent of the luminosity chosen. Performing this analysis on the full dataset gives the contours shown in black in Fig. 7.5, establishing a baseline against which we can evaluate the improvement in the constraints from applying the GNN results.

To demonstrate the power of the GNN approach, we cut on the datasets based on the probability assigned by the network of belonging to a given class; only events with a probability greater than an optimised value of belonging to one operator class are used in the χ^2 fit. The correlation of Fig. 7.3 (left) allows us to select a threshold probability to cut on, which has the effect of substantially reducing the SM background and the contamination from the other operator, resulting in a relative boost to signal effect and thus a tighter constraint on the WC for the operator in

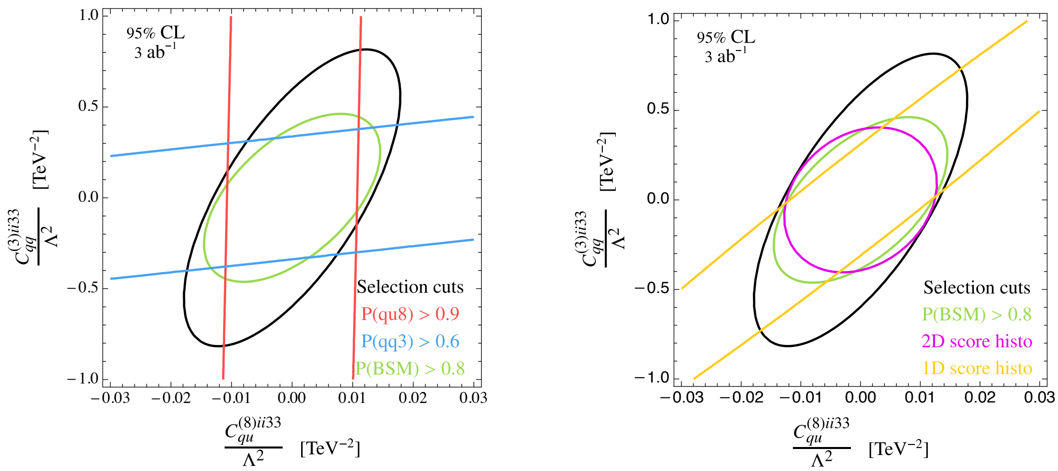

Figure 7.5: WC constraint contours at the 95% C.L. from χ^2 fitting; in black from the data of the baseline selection of Section 7.1 which also passes the network requirements. The left plot shows the contours from cuts on the NN scores at the optimal value of these score cuts, with the analysis performed using $p_T(b_1)$ distributions. The right plot shows the BSM score cut as in the left plot, along with the contour from the 2D score histogram of Fig. 7.4 (with no score cuts) analysis, as well as an analysis using the 1D BSM score histogram. For details see text.

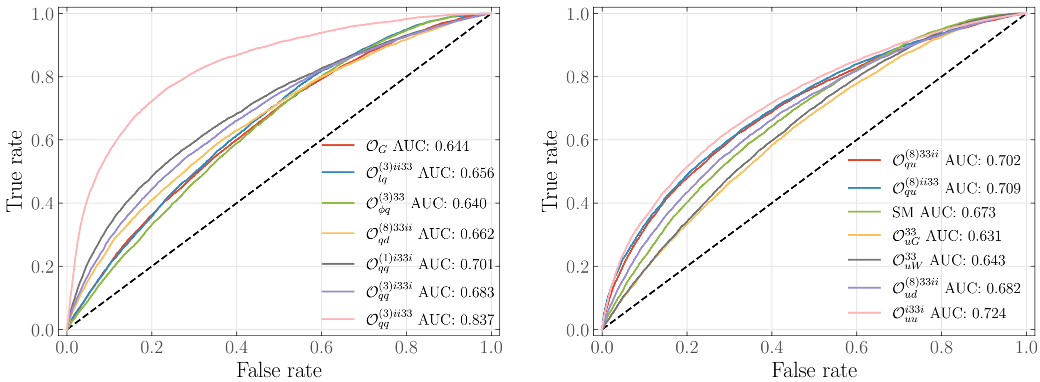

Figure 7.6: ROC curves for the scenario where multi-class classification is performed on thirteen SMEFT operators and the SM.

question. This is shown in the blue and red contours in Fig. 7.5, where the values of the cuts have been tuned to give maximal performance for each operator respectively whilst avoiding completely depleting bins in the SM $p_T(b_1)$ distribution; to do so would lead to unrealistic bounds due to loss of statistical control.

Due to this optimisation the bounds on individual coefficients improve, yet the other coefficient is essentially free, with expectedly far worse performance than in the original case with the full dataset. To resolve this, and improve the combined bounds, we consider the probability P(BSM) which is simply the sum of the network assigned probabilities of each operator,

$$\mathrm{P(BSM)} = \mathrm{P}(\mathcal{O}_{qu}^{(8)ii33}) + \mathrm{P}(\mathcal{O}_{qq}^{(3)ii33})\,,$$

for the two operator classification considered here. This does indeed result in a combined bound that is superior to the original analysis.

An alternative approach to formulating constraints is to directly employ the output of the GNN, i.e., using 2D histograms of the probabilities from the network (see, for example, the individual histograms from each contribution in Fig. 7.4), in place of the $p_T(b_1)$ distributions of Fig. 7.2. A d-dimensional classification can be converted into a $d-1$ dimensional probability histogram. This can act as a template for limit setting using the information that has condensed down the phenomenologically available information into the operator classification. Considering again $\mathcal{O}_{qu}^{(8)ii33}$ and $\mathcal{O}_{qq}^{(3)ii33}$, this is demonstrated in Fig. 7.4. The three histograms can be used to construct a χ^2 in the same way as the 1D $p_T(b_1)$ distributions, allowing the information of all three histograms to contribute. The resulting contour from this method is shown on the right plot of Fig. 7.5. This method also improves the

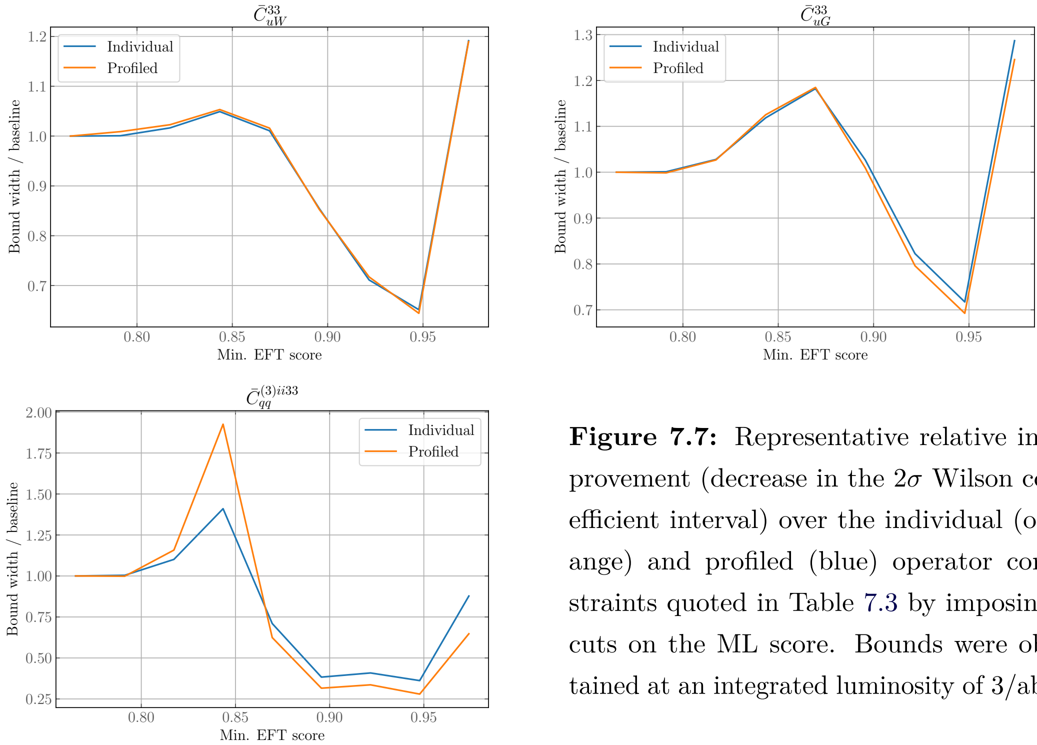

Figure 7.7: Representative relative improvement (decrease in the 2σ Wilson coefficient interval) over the individual (orange) and profiled (blue) operator constraints quoted in Table 7.3 by imposing cuts on the ML score. Bounds were obtained at an integrated luminosity of 3/ab.

bounds on the WCs compared to the original $p_T(b_1)$ distribution analysis with no cuts on the probabilities required. This approach is feasible when we consider only a small set of relevant interactions, as turning to the full $d-1$ dimensional histogram very quickly increases the statistical uncertainty. As can be seen from the qualitative similarity of the two approaches, a minimisation of

$$\mathrm{P(SM)} = 1 - \mathrm{P(BSM)}$$

appears to be adequate for multi–dimensional EFT analyses, particularly at luminosities below 3 ab^{-1}.

It should be noted that the one–dimensional P(BSM) histogram could be used to construct a χ^2 as well, in order to obtain the contours on the $C_{qq}^{(3)ii33} - C_{qu}^{(8)ii33}$ plane. However, the sensitivity is limited compared to the other approaches along certain directions, as shown in Fig. 7.5, due to the loss of information in the projection of the two–dimensional output to a one–dimensional score and we therefore have not explored this approach further.

7.3.2 Fit Constraints with GNN Selections

Extending the qualitative discussion of the previous section to the thirteen dimensional SMEFT parameter space, we show the Receiver Operator Characteristic

(ROC) curves of the full classification in Fig. 7.6. The ROC curves are calculated with the generalised procedure discussed above. Again we see that the network[1] is capable of distinguishing operators adequately.

	$2.3\ \mathrm{fb}^{-1}$		$3\ \mathrm{ab}^{-1}$	
	Individual	Profiled	Individual	Profiled
$\bar{C}_G$	$(-0.0543, 0.0535)$	$(-0.1785, 0.1776)$	$(-0.0015, 0.0015)$	$(-0.0047, 0.0047)$
$\bar{C}_{\varphi q}^{(3)33}$	$(-0.0317, 0.0326)$	$(-0.0806, 0.0758)$	$(-0.0009, 0.0009)$	$(-0.0022, 0.0022)$
$\bar{C}_{uG}^{33}$	$(-0.0253, 0.0247)$	$(-0.0622, 0.0655)$	$(-0.0007, 0.0007)$	$(-0.0017, 0.0017)$
$\bar{C}_{uW}^{33}$	$(-0.0234, 0.0228)$	$(-0.0544, 0.0580)$	$(-0.0006, 0.0006)$	$(-0.0015, 0.0016)$
$\bar{C}_{qd}^{(8)33ii}$	$(-0.1543, 0.1558)$	$(-0.3789, 0.3698)$	$(-0.0043, 0.0043)$	$(-0.0104, 0.0104)$
$\bar{C}_{qq}^{(1)i33i}$	$(-0.0202, 0.0204)$	$(-0.0495, 0.0484)$	$(-0.0006, 0.0006)$	$(-0.0014, 0.0014)$
$\bar{C}_{qq}^{(3)i33i}$	$(-0.0101, 0.0102)$	$(-0.0247, 0.0241)$	$(-0.0003, 0.0003)$	$(-0.0007, 0.0007)$
$\bar{C}_{qq}^{(3)ii33}$	$(-3.2964, 3.3259)$	–	$(-0.0917, 0.0917)$	$(-0.3045, 0.3046)$
$\bar{C}_{qu}^{(8)33ii}$	$(-0.0867, 0.0875)$	$(-0.2127, 0.2079)$	$(-0.0024, 0.0024)$	$(-0.0058, 0.0058)$
$\bar{C}_{qu}^{(8)ii33}$	$(-0.0577, 0.0583)$	$(-0.1416, 0.1383)$	$(-0.0016, 0.0016)$	$(-0.0039, 0.0039)$
$\bar{C}_{ud}^{(8)33ii}$	$(-0.1598, 0.1613)$	$(-0.3923, 0.3824)$	$(-0.0044, 0.0044)$	$(-0.0107, 0.0107)$
$\bar{C}_{uu}^{i33i}$	$(-0.0225, 0.0228)$	$(-0.0553, 0.0540)$	$(-0.0006, 0.0006)$	$(-0.0015, 0.0015)$
$\bar{C}_{lq}^{(3)ii33}$	–	–	$(-0.3289, 0.3288)$	$(-1.8493, 1.8930)$

Table 7.2: Baseline 2σ bounds for different luminosities.

Starting from the baseline sensitivity quoted in Table 7.2 (see also Section 7.1), we first show how contributing operators are impacted by imposing ML score cuts in Fig. 7.6. Sizeable improvements can be obtained when the momentum enhancement is present, for example in the case of $\bar{C}_{uG}^{33}$. Similarly, the graph network performs well in discriminating the non–resonant top decay contributions such as $\bar{C}_{uW}^{33}$. Improvements ranging between 5% and 60% are achievable in such instances (see Table 7.3) depending on the operators under consideration. Maximum improvements are found to require stringent cuts on the ML score, with statistical control being lost as score cuts approach unity. Representative operator improvements as a function of the ML score are given in Fig. 7.7. Operators showing a relatively small improvement are

[1] By optimising the hyperparameters for this scenario we conclude that the architecture used for the two operators case continues to perform particularly well. Deeper networks do not significantly improve the performance and often suffer from longer training times and overtraining risk.

	2.3 fb^{-1}		3 ab^{-1}	
	Individual	Profiled	Individual	Profiled
$\bar{C}_G$	0.07%	14.12%	0.07%	11.09%
$\bar{C}_{\varphi q}^{(3)33}$	33.74%	34.19%	33.73%	33.48%
$\bar{C}_{uG}^{33}$	28.29%	32.18%	28.28%	30.74%
$\bar{C}_{uW}^{33}$	34.86%	35.35%	34.85%	35.53%
$\bar{C}_{qd}^{(8)33ii}$	4.71%	4.68%	4.71%	4.76%
$\bar{C}_{qq}^{(1)i33i}$	3.50%	3.45%	3.50%	4.73%
$\bar{C}_{qq}^{(3)i33i}$	4.35%	4.28%	4.35%	5.00%
$\bar{C}_{qq}^{(3)ii33}$	63.83%	–	63.83%	71.91%
$\bar{C}_{qu}^{(8)33ii}$	3.45%	3.51%	3.45%	3.48%
$\bar{C}_{qu}^{(8)ii33}$	3.74%	3.72%	3.74%	3.77%
$\bar{C}_{ud}^{(8)33ii}$	4.62%	4.46%	4.62%	4.79%
$\bar{C}_{uu}^{i33i}$	3.38%	3.35%	3.38%	1.95%
$\bar{C}_{lq}^{(3)ii33}$	–	–	10.57%	35.52%

Table 7.3: Maximum improvements in 2σ bounds.

already reasonably well–controlled via the inclusive rate and the baseline selection, which establishes good sensitivity to such non–SM interactions. In particular this holds for the $\bar{C}_G$ direction, which can be constrained in more adapted ways by exploiting multi–jet production [275, 276].

Since individual constraints focus on one operator it is common practice to produce profiled bounds using all coefficients, determining their value such that the χ^2 function is minimised. In the scenario where the analysis is particularly sensitive to the presence of any additional operator, a significant decrease in sensitivity will arise. We calculate the improvement in the case of profiled constraints which, as shown in Fig. 7.7, remains similar to the individual case. This is expected as the network selection removes background contributions but keeps new–physics effects. We note, however, that the improvement on profiled bounds can be greater than on individual ones as in Fig. 7.7. This occurs when the cut on the EFT score selects a region where the impact on the bounds of a particular operator by the presence of additional ones is reduced, even though the robustness of one class against variations of others is not taken into account here.

7.4 Summary and Outlook

Given the current lack of direct evidence of new physics beyond the Standard Model, there is a strong motivation to pursue avenues toward more indirect searches. Effective field theory methods offer well–motivated approaches in this direction, however the plethora of ad hoc new physics interactions in the SMEFT approach requires tailored approaches to achieve optimal sensitivity. In this sense, limiting analyses to a handful of (however well–motivated) differential distributions is not necessarily beneficial for enhancing sensitivity. Machine learning techniques that identify and exploit correlations in data provides a route to enhance the sensitivity that can be achieved at not only the LHC but also other, future, collider experiments.

In this work, we have focused employing on GNNs for EFT limit setting. GNNs are particularly well–suited for this purpose as they allow us to directly reflect the graph structure which is imposed by EFT interactions in the classification and eventual limit setting. We base our analysis on the semileptonic $t\bar{t}$ final states, finding that significant improvements in sensitivity are achievable when correlations are not yet fully exploited in the inclusive base selection. This demonstrates that machine learning of multi–labelled collider data provides an excellent avenue towards improving the sensitivity of EFT–related measurements at colliders. We find that this improvement translates from individual to profiled bounds; our results also indicate a strategic approach to improve profiled constraints by tensioning operators against each other, which is not directly accessible by minimising the SM probability. This highlights the relative operator probabilities as another, possibly fruitful, area of research. Along these lines, we also note that optimisations of the ML score can be achieved via different weightings of the individual class probabilities in order to reflect more model–specific interpretations of EFT constraints at the machine learning stage; this should, in principle, lead to further sensitivity enhancements.

We note that the results of our exploratory study presented here are based on a Monte Carlo analysis and that the comparison of actual data is affected by a range of theoretical and experimental uncertainties. Whilst our results do not include such uncertainties, in principle it is possible to treat them via Generative Adversarial Neural Networks [212, 277]. This would discriminate between the different (labelled) hypotheses, effectively removing modelled uncertainty parameters from the classifier score. In general, this will lead to decreased sensitivity compared to the idealised situation of the proof–of–principle analysis presented here. There are examples of such approaches to treat theoretical [215] and experimental [278] uncertainties.

Chapter 8

Conclusions

In this thesis we have discussed Effective Field Theory as a powerful approach, in the absence of direct measurement of new physics, toward performing both global and more narrowly–targeted indirect searches for signs of as–yet undiscovered physics at energy scales current particle colliders are unable to probe directly.

The Standard Model was introduced as our current — and incredibly well–tested — best guess as to the nature of physics at high energies, as well as some reasons to believe that it *cannot* be complete, in Chapter 1. In Chapter 2 we discussed the concept of Effective Field Theory; in particular that the SM may be considered as the low(er) energy tail of some unknown, more fundamental, description of physics that we may be able to study indirectly through low–energy effects of this unknown physics causing deviations from SM expectations. An overview of the methods by which fundamental particle physics is probed experimentally, alongside sources of uncertainty and commonly measured quantities applicable to indirect searches, was presented in Chapter 3. These methods and uncertainties are, indeed, the avenue by which we may be able to leverage measured deviations from expected results to constrain our EFT operators.

Bringing this together in Chapter 4, we introduced the extensible and modular TopFitter framework which was designed and implemented to enable efficient EFT fits to an ever–expanding amount and variety of experimental results. Specifically, we discussed: the structure of the EFT–extended Langrangian and its exploitation to construct theory predictions in a piecewise fashion using a physics–inspired data structure; the implementation of event generation and experimentally–matched analyses using arbitrary models and parton distribution function sets; the direct exploration of the theory parameter space, with plugin–driven calculation of systematic uncertainties and application of per–analysis K–factors; and the general purpose, plugin–based functionality to determine both individual and profiled constraints for a given set of Wilson coefficients. This framework is designed to allow the quick inclusion of new data and theory improvements as and when they arise.

A specific application of the TopFitter framework to top quark measurements was described in Chapter 5, where a large portion of available experimental results was used to obtain constraints on 31 dimension six operators contributing to top–relevant processes. This global and statistically rigorous fit included the use of processes involving top quark decay, leveraging analytical predictions of the top decay width to apply dynamic corrections to predictions at arbitrary points in our parameter space. We found the majority of operators to be well–controlled and to have good agreement with the Standard Model within their 95% confidence intervals, except a set of four–quark octet operators. This tension appears to arise from a single 13 TeV, double differential, analysis and the root cause is as–yet undetermined. Operators contributing only to top quark production and decay in association with the Z boson were found to admit the weakest bounds due to the smaller number, and larger statistical uncertainties, of such measurements.

The TopFitter framework is well–placed to take advantage of an increased number and variety of inclusive and differential measurements of these channels as they become available. Results using the described framework and methodology were compared with a contemporaneous publication utilising a different approach and input data set. Competitive limits with good qualitative agreement, including with the aforementioned octet operators, were observed. That results using leading order EFT contributions were competitive is encouraging, as the model–agnostic nature of the framework leave open the possibility of studying the impact of EFT contributions at NLO in QCD as and when such models are available for inclusion.

As well as global fits, the framework also enables more targeted fits and studies for (sub)sets of operators; this could be an arbitrary choice, or those operators admitted by a model or class of models. In Chapter 6 we demonstrated, using the example of top partial compositeness, that the ongoing top EFT programme may provide important additional information to resonance searches as long as theoretical and experimental uncertainties can be brought under control. This was further highlighted at the energy frontier, using projections to a future hadron collider at 100 TeV. The increase in sensitivity and ability to investigate the electroweak properties of the top quark at the FCC–hh was also demonstrated using a representative top partner resonance search. Whilst future improvements in sensitivity and reach in energy scales are anticipated to prove useful, in particular providing opportunities for greater discriminating power as regards top EFT studies, it remains the case that uncertainties are a major limiting factor for indirect searches.

As overcoming this limiting factor is likely to require significant time and effort, it may be prudent to explore possible avenues toward maximising the achievable sensitivity of the experimental and theoretical infrastructure we have currently. With this in mind, an additional route to boosting EFT sensitivity was explored in Chapter 7, wherein we discussed the improvements that may be captured by (at least partially) eschewing standard rectangular cuts in favour of ML–driven classification of events using a DGNN architecture. Graph Neural Networks are well–suited for the EFT limit setting approach, as they directly reflect the graph structure of EFT interactions. Whilst wide–ranging, we found that such an approach can indeed provide significant improvements where available inclusive and multi–differential data proves insufficient to discriminate between operators. We found that this improvement translated from individual to profiled bounds, with indications of a possible strategic approach to improving profiled constraints through operator tension. This approach is not directly accessible by minimising the SM probability alone, which raises relative operator probabilities a possibly fruitful area of research.

We have introduced a fitting framework and rigorous statistical methodology designed to allow for rapid iteration and the inclusion of new experimental results in addition to theoretical and computational improvements as they become available. This framework was used to perform a global fit with constraining power competitive with contemporaneous studies, a more narrowly focused study into top partner resonances and future colliders, and to investigate the possible utility of ML–driven event classifications as a means to improve sensitivity to new physics using the tools at our disposal at the present time.

The TopFitter framework stands ready to exploit improvements as they arise; be that increased reporting of experimental covariance matrices allowing an increase in usable measurements, improved uncertainties on existing measurements mitigating the major limiting factor for EFT studies, new kinematic observables or distributions which allows better separation of EFT operators, or theory improvements such as a full treatment of SMEFT contributions at higher orders in QCD.

Until then, however, the Standard Model stands bloodied, but unbowed, and we have little choice but to remember our ABCDEFs:

Always be collecting data experimentally.[1]

[1]The ‘F’ is left as an exercise for the motivated reader.

Appendix A

Top Quark Width in Decay

Processes with top decay, for example $pp \to t\bar{t} \to b\bar{b}\ell^+\ell^-\nu_\ell\bar{\nu}_\ell$, depend on the top quark width Γ_t. In particular the width appears in the denominator of the top quark propagator; in the narrow-width approximation of the top quark propagator we obtain

$$\frac{1}{(p^2 - m_t^2) - \Gamma_t^2 m_t^2} \to \frac{\pi}{\Gamma_t m_t}\delta(p^2 - m_t^2)\,. \tag{A.1}$$

Each decaying top quark in the process therefore gives a factor of $1/\Gamma_t$, with Γ_t depending on the Wilson coefficients

$$\Gamma_t = \Gamma_t^{\mathrm{SM}} + C_i\Gamma_{t,i}^{(1)} + C_iC_j\Gamma_{t,ij}^{(1)}\,. \tag{A.2}$$

The appearance of the top quark width in the denominator means that the cross–section at any point $\mathbf{C}$ in Wilson coefficient space cannot be generated by simply combining σ^{SM}, $\sigma_i^{(1)}$ and $\sigma_{ij}^{(2)}$ — we must also know Γ_t^{SM}, $\Gamma_{t,i}^{(1)}$ and $\Gamma_{t,ij}^{(1)}$.

The decay width Γ_t factors out of the cross–section because it does not depend on the kinematics of the process, allowing construction of the cross–section σ for any point $\mathbf{C}$ in the Wilson coefficient space as

$$\sigma(\mathbf{C}) = \frac{\tilde{\sigma}(\mathbf{C})}{\Gamma_t(\mathbf{C})^n} = \frac{\tilde{\sigma}^{\mathrm{SM}} + C_i\tilde{\sigma}_i^{(1)} + C_iC_j\tilde{\sigma}_{ij}^{(2)}}{\left(\Gamma_t^{\mathrm{SM}} + C_i\Gamma_{t,i}^{(1)} + C_iC_j\Gamma_{t,ij}^{(2)}\right)^n}\,, \tag{A.3}$$

where $\tilde{\sigma}$ and Γ_t need only be computed once. We determine the coefficients $\tilde{\sigma}^{\mathrm{SM}}$, $\tilde{\sigma}_i^{(1)}$ and $\tilde{\sigma}_{ij}^{(2)}$ by generating the process with different values for the Wilson coefficient, as in the case of processes without decay, using the SM decay width Γ_t^{SM} and multiplying the resulting cross–sections by Γ_t^{SM}

$$\tilde{\sigma}^{\mathrm{SM}}_{n\times t} = \sigma^{\mathrm{SM}}_{n\times t}\left(\Gamma_t^{\mathrm{SM}}\right)^n\,, \quad \tilde{\sigma}^{(1)i}_{n\times t} = \sigma^{(1)i}_{n\times t}\left(\Gamma_t^{\mathrm{SM}}\right)^n\,, \quad \tilde{\sigma}^{(2)ij}_{n\times t} = \sigma^{(2)ij}_{n\times t}\left(\Gamma_t^{\mathrm{SM}}\right)^n\,, \tag{A.4}$$

where n is the number of decaying top quarks and antiquarks in the process.

The general structure of the top quark decay matrix element is given by

$$
\begin{aligned}
\frac{v^2}{m_t^4}|\mathcal{M}_P^x|^2 = \left(1 + C_{\varphi q}^{(3)33}\right) \Big\{ & \left(1 + C_{\varphi q}^{(3)33}\right) m_P^{(0,x)} |V_{tb}|^2 \\
& + m_{P,[uW]}^{(1,x)} |V_{tb}|^2 \mathrm{Re}\left[C_{uW}^{33}\right] + m_{P,[dW]}^{(1,x)} |V_{tb}|^2 \mathrm{Re}\left[C_{dW}^{33}\right] + m_{P,[\varphi ud]}^{(1,x)} \mathrm{Re}\left[C_{\varphi ud}^{33} V_{tb}^*\right] \Big\} \\
& + m_{P,[uW][dW]}^{(2,x)} |V_{tb}|^2 \mathrm{Re}\left[C_{uW}^{33} C_{dW}^{33}\right] + m_{P,[uW][\varphi ud]}^{(2,x)} \mathrm{Re}\left[C_{uW}^{33} C_{\varphi ud}^{33} V_{tb}^*\right] \\
& + m_{P,[duW][\varphi ud]}^{(2,x)} \mathrm{Re}\left[C_{dW}^{33} C_{\varphi ud}^{33*} V_{tb}\right] + m_{P,[uW]}^{(2,x)} |V_{tb}|^2 |C_{uW}^{33}|^2 \\
& + m_{P,[dW]}^{(2,x)} |V_{tb}|^2 |C_{dW}^{33}|^2 + m_{P,[\varphi ud]}^{(2,x)} |C_{\varphi ud}^{33}|^2 \,,
\end{aligned}
$$

where the superscript $x = m_b, \not{m}_b$ indicates whether the b quark is massive or massless, the subscript $P = 0,\, L,\, R$ indicates the W polarisation, and the numbers in the superscript distinguish contributions. Explicit expressions for matrix element contributions are provided in Table A.1 and expanded in Eq. (A.5).

	Unpolarised		R		L		0	
	m_b	$\not{m}_b$	m_b	$\not{m}_b$	m_b	$\not{m}_b$	m_b	$\not{m}_b$
$m_P^{(0,x)}$	$4M_1$		$4M_6$	0	$4M_8$		$4M_{14}$	
$m_{P,[uW]}^{(1,x)}$	$6M_4$		$2M_{11}$	0	$-2M_{12}$		$2M_4$	
$m_{P,[dW]}^{(1,x)}$	$6M_3$	0	$2M_{10}$	0	$-2M_{13}$	0	$2M_3$	0
$m_{P,[\varphi ud]}^{(1,x)}$	$3M_5$	0	M_5	0	M_5	0	M_5	0
$m_{P,[uW][dW]}^{(2,x)}$	$-12M_5$	0	$-4M_5$	0	$-4M_5$	0	$-4M_5$	0
$m_{P,[uW][\varphi ud]}^{(2,x)}$	$-3M_3$	0	M_{13}	0	$-M_{10}$	0	$-M_3$	0
$m_{P,[dW][\varphi ud]}^{(2,x)}$	$-3M_4$		M_{12}		$-M_{11}$	0	$-M_4$	
$m_{P,[uW]}^{(2,x)}$	M_2		M_9	0	M_7		M_{15}	
$m_{P,[dW]}^{(2,x)}$	M_2		M_7		M_9	0	M_{15}	
$m_{P,[\varphi ud]}^{(2,x)}$	M_1		M_8		M_6	0	M_{14}	

Table A.1: SM and EFT contributions to the top quark decay matrix element

The full expressions for matrix element contributions outlined in Table A.1 are

$$
\begin{aligned}
M_1 &= \frac{1}{4}\left(-2x^4 + x^2\left(y^2+1\right) + \left(y^2-1\right)^2\right) , \\
M_2 &= -2\left(x^4 + x^2\left(y^2+1\right) - 2\left(y^2-1\right)^2\right) , \\
M_3 &= \sqrt{2}xy\left(x^2 - y^2 + 1\right) , \\
M_4 &= \sqrt{2}x\left(x^2 + y^2 - 1\right) , \\
M_5 &= 2x^2y\,, \\
M_6 &= -\frac{1}{4}x^2\left(\sqrt{\lambda} + x^2 - y^2 - 1\right) , \\
M_7 &= 2\left(-y^2\left(\sqrt{\lambda} + x^2 + 2\right) + \sqrt{\lambda} - x^2 + y^4 + 1\right) , \\
M_8 &= \frac{1}{4}x^2\left(\sqrt{\lambda} - x^2 + y^2 + 1\right) , \\
M_9 &= 2\left(\sqrt{\lambda}\left(y^2-1\right) + x^2\left(-\left(y^2+1\right)\right) + \left(y^2-1\right)^2\right) , \\
M_{10} &= \sqrt{2}xy\left(\sqrt{\lambda} + x^2 - y^2 + 1\right) , \\
M_{11} &= \sqrt{2}x\left(\sqrt{\lambda} + x^2 + y^2 - 1\right) , \\
M_{12} &= -\sqrt{2}x\left(-\sqrt{\lambda} + x^2 + y^2 - 1\right) , \\
M_{13} &= \sqrt{2}xy\left(\sqrt{\lambda} - x^2 + y^2 - 1\right) , \\
M_{14} &= \frac{1}{4}\left(\left(y^2-1\right)^2 - x^2\left(y^2+1\right)\right) , \\
M_{15} &= 2x^2\left(-x^2 + y^2 + 1\right) ,
\end{aligned} \tag{A.5}
$$

where $x = M_W/m_t$, $y = m_b/m_t$, and $\lambda = x^4 - 2x^2y^2 - 2x^2 + y^4 - 2y^2 + 1$. Note also that there are additional relationships between M_i, with

$$
\begin{aligned}
M_1 &= M_6 + M_8 + M_{14}, \\
M_2 &= M_7 + M_9 + M_{15}, \\
2M_3 &= M_{10} - M_{13}, \text{ and} \\
2M_4 &= M_{11} - M_{12}.
\end{aligned}
$$

The top quark decay width is then given by

$$
\Gamma_t = \frac{\sqrt{\lambda}}{16\pi m_t}\mathcal{M},
$$

meaning we can include analytical predictions of the value for arbitrary points in our Wilson coefficient space. We will now discuss the process and results of verifying this approach numerically.

Contribution	Γ_t^{SM}	$\Gamma_{t,1}^{(1)}$	$\Gamma_{t,2}^{(1)}$	$\Gamma_{t,11}^{(1)}$	$\Gamma_{t,22}^{(1)}$	$\Gamma_{t,12}^{(1)}$
Value [GeV]	1.5069	−0.25074	0.1827	0.017198	0.0055381	−0.0152008

Table A.2: Contributions to the top quark decay width calculated by MadGraph with $m_t = 173.2$ GeV, $m_W = 79.831336$ GeV, and $m_b = 0$ GeV. Statistical uncertainties are $< 10^{-5}$.

We first check that we can construct the top quark width for an arbitrary point in Wilson coefficient space using Eq. (A.2). Choosing the Wilson coefficients $C_1 \equiv C_{uW}^{33}$ and $C_2 \equiv C_{\varphi q}^{(3)33}$ as an example, we generate ten random points $\left(C_{uW}^{33}, C_{\varphi q}^{(3)33}\right)$ and compare the directly generated top width and that calculated according to Eq. (A.2) using the coefficients in Table A.2.

The result of this test is presented in Table A.3, showing that we can indeed calculate the top width for an arbitrary point **C** in Wilson coefficient space according to Eq. (A.2). We need know, therefore, only the SM top decay width and $k(k+3)/2$ coefficients where k is the number of Wilson coefficients. For this test we used $k = 2$ different Wilson coefficients, with Table A.2 containing five Γ coefficients from the EFT contributions.

Coefficient		Γ_t [GeV]	
C_{uW}^{33}	$C_{\varphi q}^{(3)33}$	Generated	Calculated
1.95	1.17	1.2700	1.2700
1.46	1.69	1.4645	1.4646
1.48	1.30	1.3911	1.3911
1.79	0.31	1.1619	1.1619
1.38	0.86	1.3368	1.3368
0.68	0.71	1.4695	1.4695
0.64	0.44	1.4306	1.4307
0.36	0.62	1.5308	1.5309
0.60	0.26	1.4081	1.4082
1.80	0.25	1.1504	1.1505

Table A.3: Comparison between generated and calculated top width.

Contribution	$\tilde{\sigma}^{\mathrm{SM}}$	$\tilde{\sigma}_1^{(1)}$	$\tilde{\sigma}_2^{(1)}$	$\tilde{\sigma}_{11}^{(2)}$	$\tilde{\sigma}_{22}^{(2)}$	$\tilde{\sigma}_{12}^{(2)}$
σ_i [pb]	32.88	-10.516	7.972	1.555	0.7250	-1.914
$\Delta\sigma_i$ [pb]	0.03	0.009	0.007	0.001	0.0006	0.002

Table A.4: Contributions to $t\bar{t}$ production and dileptonic decay.

With validation for Γ_t in place, we will now check our approach for inclusive cross–section, again considering the Wilson coefficients $C_1 = C_{uW}^{33}$ and $C_2 = C_{\varphi q}^{(3)33}$, choosing the process $pp \to t\bar{t} \to b\bar{b}\ell^+\ell^-\nu_\ell\bar{\nu}_\ell$.

We determine the coefficients $\tilde{\sigma}$ in Eq. (A.4) by generating the cross–sections using the SM top quark width ($\Gamma_t^{\mathrm{SM}} = 1.508336$ GeV), with results listed in Table A.4. Generating ten random points $\left(C_{uW}^{33}, C_{\varphi q}^{(3)33}\right)$ in Wilson coefficient space, we compare the generated cross–sections with those calculated using Eq. (A.3). Results are presented in Table A.5, showing excellent agreement and therefore serving as a numerical validation of Eq. (A.3) at the level of inclusive cross–sections.

Coefficient		Cross–section [pb]	
C_{uW}^{33}	$C_{\varphi q}^{(3)33}$	Generated	Calculated
1.11	1.26	14.68 ± 0.01	14.69 ± 0.02
0.39	1.69	14.50 ± 0.01	14.53 ± 0.01
0.36	1.18	14.54 ± 0.01	14.54 ± 0.01
1.96	0.58	15.22 ± 0.01	15.24 ± 0.03
1.55	0.12	15.03 ± 0.01	15.06 ± 0.02
1.18	1.24	14.71 ± 0.01	14.71 ± 0.02
1.10	1.76	14.66 ± 0.01	14.67 ± 0.01
1.13	1.58	14.68 ± 0.01	14.69 ± 0.01
0.89	0.00	14.71 ± 0.01	14.71 ± 0.02
0.96	0.16	14.73 ± 0.01	14.72 ± 0.02

Table A.5: Comparison between generated and calculated cross–sections.

Now that we have verified Eq. (A.3) for the inclusive cross–section, it is interesting to know what effect the $\mathbf{C}$–dependent top quark decay width $\Gamma_t(\mathbf{C})$ has on the inclusive cross–section. The ratio between the cross–section with SM width and $\mathbf{C}$–dependent width is given by

$$R(\mathbf{C}) = \frac{\sigma\left(\Gamma_t^{\mathrm{SM}}\right)}{\sigma\left(\Gamma_t^{\mathrm{EFT}}\right)} = \left(\frac{\Gamma_t(\mathbf{C})}{\Gamma_t^{\mathrm{SM}}}\right)^2 . \tag{A.6}$$

As an example we present in Table A.6 the deviation $\delta R = R - 1$ for the random values of C_{uW}^{33} and $C_{\varphi q}^{(3)33}$ from Table A.5.

C_{uW}^{33}	1.11	0.39	0.36	1.96	1.55	1.18	1.10	1.13	0.89	0.96
$C_{\varphi q}^{(3)33}$	1.26	1.69	1.18	0.58	0.12	1.24	1.76	1.58	0.00	0.16
δR [%]	-5.2	31.2	17.8	-39.5	-38.8	-7.7	7.3	1.9	-25.9	-24.5

Table A.6: Deviation $\delta R = 1 - R$ between inclusive cross–sections calculated with Γ_t^{SM} and $\Gamma_t\,(\mathbf{C})$ for different values of C_{uW}^{33} and $C_{\varphi q}^{(3)33}$.

The results in Table A.6 shows clearly that the deviations can be quite large for generic points in Wilson coefficient space if the $\mathbf{C}$-dependent top quark width is not taken into account but instead the SM width is used.

While Table A.5 shows excellent agreement between calculated and generated *inclusive* cross–sections, we must also confirm this level of agreement for *differential* cross–sections. The method of calculating the differential cross–sections is analogous to Eq. (A.4), using

$$\frac{\mathrm{d}\tilde{\sigma}_{t\bar{t}}^{\mathrm{SM}}}{\mathrm{d}X} = \frac{\mathrm{d}\sigma_{t\bar{t}}^{\mathrm{SM}}}{\mathrm{d}X}\left(\Gamma_t^{\mathrm{SM}}\right)^2 , \quad \frac{\mathrm{d}\tilde{\sigma}_{t\bar{t}}^{(1)i}}{\mathrm{d}X} = \frac{\mathrm{d}\sigma_{t\bar{t}}^{(1)i}}{\mathrm{d}X}\left(\Gamma_t^{\mathrm{SM}}\right)^2 , \quad \frac{\mathrm{d}\tilde{\sigma}_{t\bar{t}}^{(2)ij}}{\mathrm{d}X} = \frac{\mathrm{d}\sigma_{t\bar{t}}^{(2)ij}}{\mathrm{d}X}\left(\Gamma_t^{\mathrm{SM}}\right)^2 ,$$

where X stands for any observable. These contributions, as well as those in Table A.2, were used to calculate the differential cross–section for a selection of points in Wilson coefficient space as

$$\frac{\mathrm{d}\sigma(\mathbf{C})}{\mathrm{d}X} = \left[\frac{\mathrm{d}\tilde{\sigma}_{t\bar{t}}^{\mathrm{SM}}}{\mathrm{d}X} + C_i\frac{\mathrm{d}\tilde{\sigma}_{t\bar{t}}^{(1)i}}{\mathrm{d}X} + C_iC_j\frac{\mathrm{d}\tilde{\sigma}_{t\bar{t}}^{(2)ij}}{\mathrm{d}X}\right]\left[\Gamma_t^{\mathrm{SM}} + C_i\Gamma_{t,i}^{(1)} + C_iC_j\Gamma_{t,ij}^{(2)}\right]^{-2} .$$

Using the process $pp \to t\bar{t} \to b\bar{b}\ell^+\ell^-\nu_\ell\bar{\nu}_\ell$, we investigate the differential cross–section with respect to six different observables. The results, presented in Tables A.7–A.36, exhibit good agreement with an average standard deviation of $\lesssim 1\sigma$ per bin.

$p_{\perp,\ell^+}$ [GeV]	σ_{calc} [pb]	$\Delta\sigma_{\text{calc}}$ [pb]	σ_{gen} [pb]	$\Delta\sigma_{\text{gen}}$ [pb]	STD
[0, 30]	3.710	0.030	3.760	0.020	1.42
[30, 60]	5.890	0.030	5.850	0.030	0.98
[60, 90]	2.960	0.020	2.990	0.020	0.91
[90, 120]	1.240	0.020	1.220	0.010	1.07
[120, 150]	0.484	0.009	0.496	0.009	0.93
[150, 180]	0.213	0.006	0.205	0.005	0.98
[180, 210]	0.084	0.004	0.091	0.004	1.35
[210, 240]	0.038	0.003	0.037	0.002	0.30
[240, 270]	0.021	0.002	0.016	0.002	2.00
[270, 300]	0.009	0.001	0.008	0.001	0.24
Total	14.65	0.050	14.67	0.050	0.28
Average					1.02 ± 0.49
$p_{\perp,\ell^-}$ [GeV]	σ_{calc} [pb]	$\Delta\sigma_{\text{calc}}$ [pb]	σ_{gen} [pb]	$\Delta\sigma_{\text{gen}}$ [pb]	STD
[0, 30]	3.730	0.030	3.760	0.020	0.82
[30, 60]	5.840	0.030	5.870	0.030	0.80
[60, 90]	3.000	0.020	2.950	0.020	1.64
[90, 120]	1.250	0.020	1.230	0.010	1.07
[120, 150]	0.482	0.009	0.497	0.009	1.21
[150, 180]	0.196	0.006	0.203	0.005	0.87
[180, 210]	0.085	0.004	0.088	0.004	0.59
[210, 240]	0.040	0.003	0.039	0.002	0.26
[240, 270]	0.018	0.002	0.016	0.002	0.83
[270, 300]	0.010	0.001	0.011	0.001	0.67
Total	14.65	0.050	14.67	0.050	0.23
Average					0.88 ± 0.35

Table A.7: Comparison of calculated and generated differential cross section w.r.t. $p_{\perp,\ell^+}$ and $p_{\perp,\ell^-}$ for $C_{uW}^{33} = 1.11$ and $C_{\varphi q}^{(3)33} = 1.26$. Bins are not divided by bin width. The last column shows the standard deviation (STD). 'Total' refers to the sum over all bins and 'Average' is the average STD over all bins.

$\lvert y_{\ell^+}\rvert$	σ_{calc} [pb]	$\Delta\sigma_{\text{calc}}$ [pb]	σ_{gen} [pb]	$\Delta\sigma_{\text{gen}}$ [pb]	STD
[0.0, 0.5]	4.15	0.03	4.18	0.02	0.66
[0.5, 1.0]	3.73	0.03	3.79	0.02	1.67
[1.0, 1.5]	3.11	0.02	3.05	0.02	1.81
[1.5, 2.0]	2.24	0.02	2.22	0.02	0.68
[2.0, 2.5]	1.43	0.02	1.44	0.01	0.46
Total	14.66	0.05	14.68	0.05	0.25
Average					1.06 ± 0.57
$\lvert y_{\ell^-}\rvert$	σ_{calc} [pb]	$\Delta\sigma_{\text{calc}}$ [pb]	σ_{gen} [pb]	$\Delta\sigma_{\text{gen}}$ [pb]	STD
[0.0, 0.5]	4.11	0.03	4.17	0.02	1.73
[0.5, 1.0]	3.77	0.03	3.76	0.02	0.27
[1.0, 1.5]	3.09	0.02	3.09	0.02	0.13
[1.5, 2.0]	2.24	0.02	2.23	0.02	0.06
[2.0, 2.5]	1.46	0.02	1.42	0.01	1.43
Total	14.66	0.05	14.68	0.05	0.25
Average					0.73 ± 0.71
$\lvert\Delta\phi_{\ell\ell}\rvert$ [π]	σ_{calc} [pb]	$\Delta\sigma_{\text{calc}}$ [pb]	σ_{gen} [pb]	$\Delta\sigma_{\text{gen}}$ [pb]	STD
[0.0, 0.1]	0.90	0.01	0.91	0.01	0.69
[0.1, 0.2]	1.14	0.01	1.10	0.01	2.08
[0.2, 0.3]	1.20	0.02	1.20	0.01	0.22
[0.3, 0.4]	1.25	0.02	1.28	0.01	1.44
[0.4, 0.5]	1.35	0.02	1.35	0.01	0.14
[0.5, 0.6]	1.53	0.02	1.49	0.01	1.65
[0.6, 0.7]	1.63	0.02	1.65	0.02	0.85
[0.7, 0.8]	1.76	0.02	1.80	0.02	1.62
[0.8, 0.9]	1.89	0.02	1.90	0.02	0.55
[0.9, 1.0]	2.02	0.02	2.00	0.02	0.73
Total	14.66	0.05	14.68	0.05	0.25
Average					1.00 ± 0.63

Table A.8: Comparison of calculated and generated differential cross section w.r.t. $\lvert y_{\ell^+}\rvert$, $\lvert y_{\ell^-}\rvert$, and $\lvert\Delta\phi_{\ell\ell}\rvert$ for $C_{uW}^{33} = 1.11$ and $C_{\varphi q}^{(3)33} = 1.26$. Bins are not divided by bin width.

$\cos\theta_+ \cos\theta_-$	σ_{calc} [pb]	$\Delta\sigma_{\text{calc}}$ [pb]	σ_{gen} [pb]	$\Delta\sigma_{\text{gen}}$ [pb]	STD
[-1.0, -0.9]	0.028	0.002	0.027	0.002	0.30
[-0.9, -0.8]	0.124	0.005	0.126	0.004	0.25
[-0.8, -0.7]	0.225	0.007	0.235	0.006	1.13
[-0.7, -0.6]	0.352	0.008	0.346	0.007	0.56
[-0.6, -0.5]	0.473	0.010	0.474	0.008	0.09
[-0.5, -0.4]	0.610	0.010	0.632	0.010	1.59
[-0.4, -0.3]	0.840	0.010	0.830	0.010	0.24
[-0.3, -0.2]	1.050	0.010	1.060	0.010	0.73
[-0.2, -0.1]	1.450	0.020	1.430	0.010	0.90
[-0.1, -0.0]	2.440	0.020	2.440	0.020	0.02
[-0.0, 0.1]	2.390	0.020	2.390	0.020	0.07
[0.1, 0.2]	1.320	0.020	1.290	0.010	1.43
[0.2, 0.3]	0.900	0.010	0.890	0.010	0.13
[0.3, 0.4]	0.640	0.010	0.644	0.010	0.52
[0.4, 0.5]	0.485	0.010	0.476	0.008	0.67
[0.5, 0.6]	0.321	0.008	0.347	0.007	2.44
[0.6, 0.7]	0.222	0.007	0.228	0.006	0.60
[0.7, 0.8]	0.127	0.005	0.131	0.004	0.54
[0.8, 0.9]	0.063	0.004	0.074	0.003	2.31
[0.9, 1.0]	0.018	0.002	0.018	0.002	0.07
Total	14.06	0.050	14.10	0.050	0.48
Average					0.73 ± 0.70

Table A.9: Comparison of calculated and generated differential cross section w.r.t. $\cos\theta_+ \cos\theta_-$ for $C_{uW}^{33} = 1.11$ and $C_{\varphi q}^{(3)33} = 1.26$. Bins are not divided by bin width. The last column shows the standard deviation (STD). 'Total' refers to the sum over all bins and 'Average' is the average STD over all bins.

$p_{\perp,\ell^+}$ [GeV]	σ_{calc} [pb]	$\Delta\sigma_{\text{calc}}$ [pb]	σ_{gen} [pb]	$\Delta\sigma_{\text{gen}}$ [pb]	STD
[0, 30]	3.8000	0.0200	3.810	0.020	0.29
[30, 60]	5.8100	0.0200	5.790	0.030	0.71
[60, 90]	2.8700	0.0200	2.880	0.020	0.22
[90, 120]	1.1900	0.0100	1.180	0.010	0.27
[120, 150]	0.4660	0.0070	0.484	0.008	1.64
[150, 180]	0.2030	0.0040	0.199	0.005	0.63
[180, 210]	0.0810	0.0030	0.082	0.003	0.36
[210, 240]	0.0360	0.0020	0.038	0.002	0.46
[240, 270]	0.0190	0.0010	0.018	0.002	0.67
[270, 300]	0.0084	0.0009	0.011	0.001	1.51
Total	14.49	0.04	14.49	0.05	0.00
Average					0.68 ± 0.48
$p_{\perp,\ell^-}$ [GeV]	σ_{calc} [pb]	$\Delta\sigma_{\text{calc}}$ [pb]	σ_{gen} [pb]	$\Delta\sigma_{\text{gen}}$ [pb]	STD
[0, 30]	3.8100	0.0200	3.820	0.020	0.13
[30, 60]	5.7700	0.0200	5.790	0.030	0.59
[60, 90]	2.9100	0.0200	2.840	0.020	2.46
[90, 120]	1.2000	0.0100	1.210	0.010	0.28
[120, 150]	0.4660	0.0070	0.478	0.008	1.15
[150, 180]	0.1870	0.0040	0.202	0.005	2.27
[180, 210]	0.0810	0.0030	0.087	0.004	1.25
[210, 240]	0.0370	0.0020	0.038	0.002	0.06
[240, 270]	0.0170	0.0010	0.016	0.002	0.23
[270, 300]	0.0092	0.0009	0.009	0.001	0.23
Total	14.49	0.04	14.49	0.05	0.02
Average					0.86 ± 0.85

Table A.10: Comparison of calculated and generated differential cross section w.r.t. $p_{\perp,\ell^+}$ and $p_{\perp,\ell^-}$ for $C_{uW}^{33} = 0.39$ and $C_{\varphi q}^{(3)33} = 1.69$. Bins are not divided by bin width. The last column shows the standard deviation (STD). 'Total' refers to the sum over all bins and 'Average' is the average STD over all bins.

$\|y_{\ell^+}\|$	σ_{calc} [pb]	$\Delta\sigma_{\text{calc}}$ [pb]	σ_{gen} [pb]	$\Delta\sigma_{\text{gen}}$ [pb]	STD
[0.0, 0.5]	4.11	0.02	4.13	0.02	0.73
[0.5, 1.0]	3.71	0.02	3.72	0.02	0.37
[1.0, 1.5]	3.06	0.02	3.03	0.02	1.04
[1.5, 2.0]	2.21	0.01	2.22	0.02	0.55
[2.0, 2.5]	1.42	0.01	1.40	0.01	1.08
Total	14.50	0.04	14.50	0.05	0.02
Average					0.76 ± 0.27
$\|y_{\ell^-}\|$	σ_{calc} [pb]	$\Delta\sigma_{\text{calc}}$ [pb]	σ_{gen} [pb]	$\Delta\sigma_{\text{gen}}$ [pb]	STD
[0.0, 0.5]	4.07	0.02	4.11	0.02	1.16
[0.5, 1.0]	3.74	0.02	3.74	0.02	0.26
[1.0, 1.5]	3.05	0.02	3.06	0.02	0.28
[1.5, 2.0]	2.21	0.01	2.18	0.02	1.18
[2.0, 2.5]	1.43	0.01	1.40	0.01	1.41
Total	14.50	0.04	14.50	0.05	0.02
Average					0.86 ± 0.49
$\|\Delta\phi_{\ell\ell}\|$ [π]	σ_{calc} [pb]	$\Delta\sigma_{\text{calc}}$ [pb]	σ_{gen} [pb]	$\Delta\sigma_{\text{gen}}$ [pb]	STD
[0.0, 0.1]	0.887	0.009	0.88	0.01	0.38
[0.1, 0.2]	1.130	0.010	1.10	0.01	1.69
[0.2, 0.3]	1.190	0.010	1.18	0.01	0.61
[0.3, 0.4]	1.240	0.010	1.27	0.01	1.41
[0.4, 0.5]	1.340	0.010	1.34	0.01	0.33
[0.5, 0.6]	1.500	0.010	1.48	0.01	0.89
[0.6, 0.7]	1.620	0.010	1.61	0.02	0.19
[0.7, 0.8]	1.740	0.010	1.77	0.02	1.07
[0.8, 0.9]	1.870	0.010	1.90	0.02	1.41
[0.9, 1.0]	1.990	0.010	1.97	0.02	0.90
Total	14.50	0.04	14.50	0.05	0.02
Average					0.89 ± 0.48

Table A.11: Comparison of calculated and generated differential cross section w.r.t. $|y_{\ell^+}|$, $|y_{\ell^-}|$, and $|\Delta\phi_{\ell\ell}|$ for $C_{uW}^{33} = 0.39$ and $C_{\varphi q}^{(3)33} = 1.69$. Bins are not divided by bin width.

$\cos\theta_+ \cos\theta_-$	σ_{calc} [pb]	$\Delta\sigma_{\text{calc}}$ [pb]	σ_{gen} [pb]	$\Delta\sigma_{\text{gen}}$ [pb]	STD
[-1.0, -0.9]	0.028	0.002	0.031	0.002	1.01
[-0.9, -0.8]	0.123	0.003	0.113	0.004	1.84
[-0.8, -0.7]	0.223	0.005	0.216	0.006	1.01
[-0.7, -0.6]	0.345	0.006	0.349	0.007	0.41
[-0.6, -0.5]	0.469	0.007	0.479	0.008	0.96
[-0.5, -0.4]	0.609	0.008	0.623	0.010	1.15
[-0.4, -0.3]	0.825	0.009	0.810	0.010	1.12
[-0.3, -0.2]	1.040	0.010	1.070	0.010	1.80
[-0.2, -0.1]	1.440	0.010	1.430	0.010	0.36
[-0.1, -0.0]	2.420	0.020	2.430	0.020	0.25
[-0.0, 0.1]	2.360	0.020	2.340	0.020	0.95
[0.1, 0.2]	1.310	0.010	1.290	0.010	0.70
[0.2, 0.3]	0.886	0.009	0.890	0.010	0.07
[0.3, 0.4]	0.633	0.008	0.635	0.010	0.17
[0.4, 0.5]	0.472	0.007	0.467	0.008	0.48
[0.5, 0.6]	0.318	0.006	0.325	0.007	0.83
[0.6, 0.7]	0.219	0.005	0.223	0.006	0.61
[0.7, 0.8]	0.126	0.004	0.133	0.004	1.22
[0.8, 0.9]	0.063	0.003	0.067	0.003	0.93
[0.9, 1.0]	0.017	0.001	0.018	0.002	0.39
Total	13.92	0.04	13.93	0.04	0.17
Average					0.81 ± 0.48

Table A.12: Comparison of calculated and generated differential cross section w.r.t. $\cos\theta_+ \cos\theta_-$ for $C_{uW}^{33} = 0.39$ and $C_{\varphi q}^{(3)33} = 1.69$. Bins are not divided by bin width. The last column shows the standard deviation (STD). 'Total' refers to the sum over all bins and 'Average' is the average STD over all bins.

$p_{\perp,\ell^+}$ [GeV]	σ_{calc} [pb]	$\Delta\sigma_{\text{calc}}$ [pb]	σ_{gen} [pb]	$\Delta\sigma_{\text{gen}}$ [pb]	STD
[0, 30]	3.81	0.02	3.82	0.02	0.57
[30, 60]	5.82	0.03	5.79	0.03	0.59
[60, 90]	2.87	0.02	2.90	0.02	1.06
[90, 120]	1.19	0.01	1.19	0.01	0.04
[120, 150]	0.466	0.007	0.479	0.008	1.16
[150, 180]	0.202	0.005	0.190	0.005	1.74
[180, 210]	0.080	0.003	0.086	0.004	1.30
[210, 240]	0.036	0.002	0.035	0.002	0.25
[240, 270]	0.020	0.001	0.019	0.002	0.10
[270, 300]	0.0083	0.0010	0.008	0.001	0.43
Total	14.50	0.04	14.53	0.05	0.46
Average					0.72 ± 0.54
$p_{\perp,\ell^-}$ [GeV]	σ_{calc} [pb]	$\Delta\sigma_{\text{calc}}$ [pb]	σ_{gen} [pb]	$\Delta\sigma_{\text{gen}}$ [pb]	STD
[0, 30]	3.82	0.02	3.85	0.02	1.09
[30, 60]	5.78	0.03	5.80	0.03	0.63
[60, 90]	2.91	0.02	2.88	0.02	0.87
[90, 120]	1.20	0.01	1.18	0.01	1.37
[120, 150]	0.465	0.007	0.466	0.008	0.04
[150, 180]	0.187	0.005	0.192	0.005	0.71
[180, 210]	0.081	0.003	0.090	0.004	1.84
[210, 240]	0.038	0.002	0.038	0.002	0.05
[240, 270]	0.017	0.001	0.019	0.002	1.23
[270, 300]	0.009	0.001	0.008	0.001	0.61
Total	14.50	0.04	14.53	0.05	0.44
Average					0.84 ± 0.54

Table A.13: Comparison of calculated and generated differential cross section w.r.t. $p_{\perp,\ell^+}$ and $p_{\perp,\ell^-}$ for $C_{uW}^{33} = 0.36$ and $C_{\varphi q}^{(3)33} = 1.18$. Bins are not divided by bin width. The last column shows the standard deviation (STD). 'Total' refers to the sum over all bins and 'Average' is the average STD over all bins.

$\lvert y_{\ell^+}\rvert$	σ_{calc} [pb]	$\Delta\sigma_{\mathrm{calc}}$ [pb]	σ_{gen} [pb]	$\Delta\sigma_{\mathrm{gen}}$ [pb]	STD
[0.0, 0.5]	4.11	0.02	4.16	0.02	1.41
[0.5, 1.0]	3.71	0.02	3.74	0.02	0.92
[1.0, 1.5]	3.06	0.02	3.05	0.02	0.42
[1.5, 2.0]	2.21	0.02	2.20	0.02	0.66
[2.0, 2.5]	1.42	0.01	1.40	0.01	1.06
Total	14.51	0.04	14.54	0.05	0.44
Average					0.90 ± 0.34
$\lvert y_{\ell^-}\rvert$	σ_{calc} [pb]	$\Delta\sigma_{\mathrm{calc}}$ [pb]	σ_{gen} [pb]	$\Delta\sigma_{\mathrm{gen}}$ [pb]	STD
[0.0, 0.5]	4.07	0.02	4.10	0.02	0.92
[0.5, 1.0]	3.74	0.02	3.74	0.02	0.02
[1.0, 1.5]	3.05	0.02	3.06	0.02	0.18
[1.5, 2.0]	2.21	0.02	2.22	0.02	0.53
[2.0, 2.5]	1.43	0.01	1.41	0.01	1.05
Total	14.51	0.04	14.54	0.05	0.44
Average					0.54 ± 0.40
$\lvert\Delta\phi_{\ell\ell}\rvert$ [π]	σ_{calc} [pb]	$\Delta\sigma_{\mathrm{calc}}$ [pb]	σ_{gen} [pb]	$\Delta\sigma_{\mathrm{gen}}$ [pb]	STD
[0.0, 0.1]	0.89	0.01	0.90	0.01	0.47
[0.1, 0.2]	1.13	0.01	1.11	0.01	0.90
[0.2, 0.3]	1.19	0.01	1.19	0.01	0.02
[0.3, 0.4]	1.24	0.01	1.27	0.01	1.42
[0.4, 0.5]	1.34	0.01	1.34	0.01	0.12
[0.5, 0.6]	1.50	0.01	1.46	0.01	2.34
[0.6, 0.7]	1.62	0.01	1.65	0.02	1.66
[0.7, 0.8]	1.75	0.01	1.75	0.02	0.11
[0.8, 0.9]	1.87	0.01	1.90	0.02	1.36
[0.9, 1.0]	1.99	0.02	1.98	0.02	0.39
Total	14.51	0.04	14.54	0.05	0.44
Average					0.88 ± 0.75

Table A.14: Comparison of calculated and generated differential cross section w.r.t. $\lvert y_{\ell^+}\rvert$, $\lvert y_{\ell^-}\rvert$, and $\lvert\Delta\phi_{\ell\ell}\rvert$ for $C_{uW}^{33} = 0.36$ and $C_{\varphi q}^{(3)33} = 1.18$. Bins are not divided by bin width.

$\cos\theta_+ \cos\theta_-$	σ_{calc} [pb]	$\Delta\sigma_{\text{calc}}$ [pb]	σ_{gen} [pb]	$\Delta\sigma_{\text{gen}}$ [pb]	STD
[-1.0, -0.9]	0.028	0.002	0.030	0.002	0.77
[-0.9, -0.8]	0.123	0.004	0.123	0.004	0.05
[-0.8, -0.7]	0.223	0.005	0.238	0.006	1.95
[-0.7, -0.6]	0.346	0.006	0.347	0.007	0.08
[-0.6, -0.5]	0.470	0.007	0.479	0.008	0.77
[-0.5, -0.4]	0.609	0.008	0.623	0.010	1.13
[-0.4, -0.3]	0.825	0.010	0.82	0.01	0.39
[-0.3, -0.2]	1.04	0.01	1.06	0.01	1.13
[-0.2, -0.1]	1.44	0.01	1.43	0.01	0.59
[-0.1, -0.0]	2.42	0.02	2.44	0.02	0.54
[-0.0, 0.1]	2.36	0.02	2.37	0.02	0.36
[0.1, 0.2]	1.31	0.01	1.29	0.01	0.99
[0.2, 0.3]	0.89	0.01	0.87	0.01	1.16
[0.3, 0.4]	0.633	0.008	0.648	0.010	1.13
[0.4, 0.5]	0.473	0.007	0.455	0.008	1.69
[0.5, 0.6]	0.318	0.006	0.313	0.007	0.53
[0.6, 0.7]	0.219	0.005	0.225	0.006	0.81
[0.7, 0.8]	0.126	0.004	0.135	0.004	1.49
[0.8, 0.9]	0.063	0.003	0.068	0.003	1.24
[0.9, 1.0]	0.017	0.001	0.017	0.002	0.03
Total	13.93	0.04	13.97	0.05	0.67
Average					0.84 ± 0.52

Table A.15: Comparison of calculated and generated differential cross section w.r.t. $\cos\theta_+ \cos\theta_-$ for $C_{uW}^{33} = 0.36$ and $C_{\varphi q}^{(3)33} = 1.18$. Bins are not divided by bin width. The last column shows the standard deviation (STD). 'Total' refers to the sum over all bins and 'Average' is the average STD over all bins.

$p_{\perp,\ell^+}$ [GeV]	σ_{calc} [pb]	$\Delta\sigma_{\text{calc}}$ [pb]	σ_{gen} [pb]	$\Delta\sigma_{\text{gen}}$ [pb]	STD
[0, 30]	3.71	0.05	3.75	0.02	0.76
[30, 60]	6.13	0.06	6.10	0.03	0.39
[60, 90]	3.13	0.04	3.10	0.02	0.63
[90, 120]	1.33	0.03	1.35	0.01	0.68
[120, 150]	0.51	0.02	0.525	0.009	0.82
[150, 180]	0.23	0.01	0.215	0.006	0.90
[180, 210]	0.088	0.007	0.092	0.004	0.59
[210, 240]	0.040	0.004	0.041	0.003	0.21
[240, 270]	0.024	0.003	0.019	0.002	1.47
[270, 300]	0.009	0.002	0.013	0.001	1.44
Total	15.19	0.09	15.21	0.05	0.15
Average					0.79 ± 0.39
$p_{\perp,\ell^-}$ [GeV]	σ_{calc} [pb]	$\Delta\sigma_{\text{calc}}$ [pb]	σ_{gen} [pb]	$\Delta\sigma_{\text{gen}}$ [pb]	STD
[0, 30]	3.76	0.05	3.77	0.02	0.35
[30, 60]	6.06	0.06	6.08	0.03	0.40
[60, 90]	3.17	0.04	3.12	0.02	1.14
[90, 120]	1.33	0.03	1.30	0.01	1.23
[120, 150]	0.51	0.02	0.540	0.009	1.86
[150, 180]	0.209	0.010	0.224	0.006	1.24
[180, 210]	0.090	0.007	0.092	0.004	0.31
[210, 240]	0.045	0.005	0.044	0.003	0.12
[240, 270]	0.020	0.003	0.023	0.002	0.87
[270, 300]	0.011	0.002	0.012	0.001	0.66
Total	15.20	0.09	15.21	0.05	0.12
Average					0.82 ± 0.52

Table A.16: Comparison of calculated and generated differential cross section w.r.t. $p_{\perp,\ell^+}$ and $p_{\perp,\ell^-}$ for $C_{uW}^{33} = 1.96$ and $C_{\varphi q}^{(3)33} = 0.58$. Bins are not divided by bin width. The last column shows the standard deviation (STD). 'Total' refers to the sum over all bins and 'Average' is the average STD over all bins.

$\lvert y_{\ell^+}\rvert$	σ_{calc} [pb]	$\Delta\sigma_{\text{calc}}$ [pb]	σ_{gen} [pb]	$\Delta\sigma_{\text{gen}}$ [pb]	STD
[0.0, 0.5]	4.31	0.05	4.35	0.03	0.85
[0.5, 1.0]	3.84	0.05	3.93	0.02	1.68
[1.0, 1.5]	3.25	0.04	3.17	0.02	1.65
[1.5, 2.0]	2.32	0.04	2.31	0.02	0.44
[2.0, 2.5]	1.49	0.03	1.47	0.01	0.78
Total	15.21	0.09	15.22	0.05	0.13
Average					1.08 ± 0.50
$\lvert y_{\ell^-}\rvert$	σ_{calc} [pb]	$\Delta\sigma_{\text{calc}}$ [pb]	σ_{gen} [pb]	$\Delta\sigma_{\text{gen}}$ [pb]	STD
[0.0, 0.5]	4.24	0.05	4.34	0.03	1.79
[0.5, 1.0]	3.90	0.05	3.89	0.02	0.11
[1.0, 1.5]	3.22	0.04	3.21	0.02	0.31
[1.5, 2.0]	2.32	0.04	2.31	0.02	0.30
[2.0, 2.5]	1.53	0.03	1.48	0.01	1.61
Total	15.21	0.09	15.22	0.05	0.13
Average					0.83 ± 0.72
$\lvert\Delta\phi_{\ell\ell}\rvert$ [π]	σ_{calc} [pb]	$\Delta\sigma_{\text{calc}}$ [pb]	σ_{gen} [pb]	$\Delta\sigma_{\text{gen}}$ [pb]	STD
[0.0, 0.1]	0.92	0.02	0.94	0.01	0.55
[0.1, 0.2]	1.17	0.03	1.16	0.01	0.52
[0.2, 0.3]	1.25	0.03	1.21	0.01	1.30
[0.3, 0.4]	1.29	0.03	1.31	0.01	0.55
[0.4, 0.5]	1.39	0.03	1.38	0.01	0.45
[0.5, 0.6]	1.59	0.03	1.55	0.02	1.15
[0.6, 0.7]	1.68	0.03	1.69	0.02	0.51
[0.7, 0.8]	1.83	0.03	1.87	0.02	1.03
[0.8, 0.9]	1.96	0.03	2.02	0.02	1.50
[0.9, 1.0]	2.12	0.03	2.10	0.02	0.58
Total	15.21	0.09	15.22	0.05	0.13
Average					0.82 ± 0.37

Table A.17: Comparison of calculated and generated differential cross section w.r.t. $|y_{\ell^+}|$, $|y_{\ell^-}|$, and $|\Delta\phi_{\ell\ell}|$ for $C_{uW}^{33} = 1.96$ and $C_{\varphi q}^{(3)33} = 0.58$. Bins are not divided by bin width.

$\cos\theta_+ \cos\theta_-$	σ_{calc} [pb]	$\Delta\sigma_{\mathrm{calc}}$ [pb]	σ_{gen} [pb]	$\Delta\sigma_{\mathrm{gen}}$ [pb]	STD
[-1.0, -0.9]	0.029	0.004	0.035	0.002	1.33
[-0.9, -0.8]	0.126	0.008	0.130	0.004	0.39
[-0.8, -0.7]	0.23	0.01	0.237	0.006	0.52
[-0.7, -0.6]	0.37	0.01	0.363	0.007	0.45
[-0.6, -0.5]	0.48	0.02	0.481	0.009	0.18
[-0.5, -0.4]	0.61	0.02	0.651	0.010	1.75
[-0.4, -0.3]	0.86	0.02	0.83	0.01	1.28
[-0.3, -0.2]	1.08	0.02	1.10	0.01	0.44
[-0.2, -0.1]	1.50	0.03	1.50	0.02	0.11
[-0.1, -0.0]	2.53	0.04	2.52	0.02	0.28
[-0.0, 0.1]	2.48	0.04	2.45	0.02	0.66
[0.1, 0.2]	1.37	0.03	1.38	0.01	0.29
[0.2, 0.3]	0.93	0.02	0.94	0.01	0.42
[0.3, 0.4]	0.65	0.02	0.67	0.01	0.88
[0.4, 0.5]	0.52	0.02	0.477	0.009	2.47
[0.5, 0.6]	0.33	0.01	0.359	0.007	1.61
[0.6, 0.7]	0.24	0.01	0.239	0.006	0.29
[0.7, 0.8]	0.130	0.009	0.139	0.005	0.88
[0.8, 0.9]	0.064	0.006	0.078	0.003	1.95
[0.9, 1.0]	0.018	0.003	0.016	0.002	0.47
Total	14.56	0.09	14.59	0.05	0.31
Average					0.83 ± 0.66

Table A.18: Comparison of calculated and generated differential cross section w.r.t. $|\Delta\phi_{\ell\ell}|$ and $\cos\theta_+ \cos\theta_-$ for $C_{uW}^{33} = 1.96$ and $C_{\varphi q}^{(3)33} = 0.58$. Bins are not divided by bin width. The last column shows the standard deviation (STD). 'Total' refers to the sum over all bins and 'Average' is the average STD over all bins.

$p_{\perp,\ell^+}$ [GeV]	σ_{calc} [pb]	$\Delta\sigma_{\text{calc}}$ [pb]	σ_{gen} [pb]	$\Delta\sigma_{\text{gen}}$ [pb]	STD
[0, 30]	3.72	0.04	3.75	0.02	0.56
[30, 60]	6.05	0.05	6.02	0.03	0.51
[60, 90]	3.08	0.04	3.06	0.02	0.48
[90, 120]	1.29	0.02	1.29	0.01	0.01
[120, 150]	0.50	0.01	0.523	0.009	1.36
[150, 180]	0.218	0.010	0.210	0.006	0.75
[180, 210]	0.085	0.006	0.095	0.004	1.39
[210, 240]	0.039	0.004	0.046	0.003	1.59
[240, 270]	0.023	0.003	0.021	0.002	0.75
[270, 300]	0.009	0.002	0.008	0.001	0.32
Total	15.02	0.08	15.02	0.05	0.05
Average					0.77 ± 0.49
$p_{\perp,\ell^-}$ [GeV]	σ_{calc} [pb]	$\Delta\sigma_{\text{calc}}$ [pb]	σ_{gen} [pb]	$\Delta\sigma_{\text{gen}}$ [pb]	STD
[0, 30]	3.76	0.04	3.75	0.02	0.17
[30, 60]	5.99	0.05	6.00	0.03	0.20
[60, 90]	3.11	0.04	3.08	0.02	0.67
[90, 120]	1.30	0.02	1.30	0.01	0.15
[120, 150]	0.50	0.01	0.509	0.009	0.78
[150, 180]	0.204	0.009	0.216	0.006	1.08
[180, 210]	0.088	0.006	0.094	0.004	0.86
[210, 240]	0.044	0.004	0.039	0.002	1.12
[240, 270]	0.019	0.003	0.022	0.002	1.06
[270, 300]	0.010	0.002	0.009	0.001	0.52
Total	15.02	0.08	15.02	0.05	0.01
Average					0.66 ± 0.37

Table A.19: Comparison of calculated and generated differential cross section w.r.t. $p_{\perp,\ell^+}$ and $p_{\perp,\ell^-}$ for $C_{uW}^{33} = 1.55$ and $C_{\varphi q}^{(3)33} = 0.12$. Bins are not divided by bin width. The last column shows the standard deviation (STD). 'Total' refers to the sum over all bins and 'Average' is the average STD over all bins.

$\lvert y_{\ell^+}\rvert$	σ_{calc} [pb]	$\Delta\sigma_{\text{calc}}$ [pb]	σ_{gen} [pb]	$\Delta\sigma_{\text{gen}}$ [pb]	STD
[0.0, 0.5]	4.26	0.04	4.27	0.03	0.23
[0.5, 1.0]	3.80	0.04	3.87	0.02	1.28
[1.0, 1.5]	3.20	0.04	3.15	0.02	1.12
[1.5, 2.0]	2.29	0.03	2.31	0.02	0.36
[2.0, 2.5]	1.47	0.03	1.43	0.01	1.22
Total	15.03	0.08	15.03	0.05	0.02
Average					0.84 ± 0.45
$\lvert y_{\ell^-}\rvert$	σ_{calc} [pb]	$\Delta\sigma_{\text{calc}}$ [pb]	σ_{gen} [pb]	$\Delta\sigma_{\text{gen}}$ [pb]	STD
[0.0, 0.5]	4.19	0.04	4.28	0.03	1.75
[0.5, 1.0]	3.86	0.04	3.84	0.02	0.35
[1.0, 1.5]	3.18	0.04	3.13	0.02	1.11
[1.5, 2.0]	2.29	0.03	2.31	0.02	0.47
[2.0, 2.5]	1.50	0.03	1.46	0.01	1.30
Total	15.03	0.08	15.03	0.05	0.02
Average					1.00 ± 0.52
$\lvert\Delta\phi_{\ell\ell}\rvert$ [π]	σ_{calc} [pb]	$\Delta\sigma_{\text{calc}}$ [pb]	σ_{gen} [pb]	$\Delta\sigma_{\text{gen}}$ [pb]	STD
[0.0, 0.1]	0.92	0.02	0.91	0.01	0.11
[0.1, 0.2]	1.16	0.02	1.12	0.01	1.57
[0.2, 0.3]	1.24	0.02	1.19	0.01	1.57
[0.3, 0.4]	1.28	0.02	1.27	0.01	0.65
[0.4, 0.5]	1.38	0.03	1.41	0.01	1.09
[0.5, 0.6]	1.57	0.03	1.53	0.02	1.30
[0.6, 0.7]	1.66	0.03	1.69	0.02	0.83
[0.7, 0.8]	1.81	0.03	1.84	0.02	0.97
[0.8, 0.9]	1.93	0.03	1.97	0.02	1.20
[0.9, 1.0]	2.08	0.03	2.09	0.02	0.41
Total	15.03	0.08	15.03	0.05	0.02
Average					0.97 ± 0.45

Table A.20: Comparison of calculated and generated differential cross section w.r.t. $\lvert y_{\ell^+}\rvert$, $\lvert y_{\ell^-}\rvert$, and $\lvert\Delta\phi_{\ell\ell}\rvert$ for $C_{uW}^{33} = 1.55$ and $C_{\varphi q}^{(3)33} = 0.12$. Bins are not divided by bin width.

$\cos\theta_+ \cos\theta_-$	σ_{calc} [pb]	$\Delta\sigma_{\text{calc}}$ [pb]	σ_{gen} [pb]	$\Delta\sigma_{\text{gen}}$ [pb]	STD
[-1.0, -0.9]	0.028	0.004	0.031	0.002	0.69
[-0.9, -0.8]	0.126	0.008	0.120	0.004	0.61
[-0.8, -0.7]	0.23	0.01	0.228	0.006	0.03
[-0.7, -0.6]	0.37	0.01	0.356	0.007	0.70
[-0.6, -0.5]	0.48	0.02	0.481	0.009	0.19
[-0.5, -0.4]	0.61	0.02	0.654	0.010	2.12
[-0.4, -0.3]	0.85	0.02	0.85	0.01	0.37
[-0.3, -0.2]	1.07	0.02	1.07	0.01	0.01
[-0.2, -0.1]	1.48	0.03	1.45	0.01	1.03
[-0.1, -0.0]	2.50	0.03	2.49	0.02	0.26
[-0.0, 0.1]	2.45	0.03	2.43	0.02	0.51
[0.1, 0.2]	1.35	0.03	1.35	0.01	0.04
[0.2, 0.3]	0.92	0.02	0.93	0.01	0.63
[0.3, 0.4]	0.65	0.02	0.68	0.01	1.81
[0.4, 0.5]	0.51	0.02	0.482	0.009	1.71
[0.5, 0.6]	0.33	0.01	0.338	0.007	0.66
[0.6, 0.7]	0.23	0.01	0.236	0.006	0.46
[0.7, 0.8]	0.128	0.008	0.141	0.005	1.39
[0.8, 0.9]	0.063	0.006	0.074	0.003	1.69
[0.9, 1.0]	0.018	0.003	0.019	0.002	0.37
Total	14.40	0.08	14.42	0.05	0.20
Average					0.76 ± 0.63

Table A.21: Comparison of calculated and generated differential cross section w.r.t. $\cos\theta_+ \cos\theta_-$ for $C_{uW}^{33} = 1.55$ and $C_{\varphi q}^{(3)33} = 0.12$. Bins are not divided by bin width. The last column shows the standard deviation (STD). 'Total' refers to the sum over all bins and 'Average' is the average STD over all bins.

$p_{\perp,\ell^+}$ [GeV]	σ_{calc} [pb]	$\Delta\sigma_{\text{calc}}$ [pb]	σ_{gen} [pb]	$\Delta\sigma_{\text{gen}}$ [pb]	STD
[0, 30]	3.70	0.03	3.75	0.02	1.14
[30, 60]	5.90	0.03	5.87	0.03	0.50
[60, 90]	2.97	0.02	2.96	0.02	0.31
[90, 120]	1.24	0.02	1.25	0.01	0.23
[120, 150]	0.486	0.010	0.499	0.009	1.01
[150, 180]	0.214	0.006	0.211	0.006	0.31
[180, 210]	0.084	0.004	0.091	0.004	1.36
[210, 240]	0.038	0.003	0.038	0.002	0.04
[240, 270]	0.021	0.002	0.018	0.002	1.17
[270, 300]	0.009	0.001	0.010	0.001	0.61
Total	14.67	0.06	14.70	0.05	0.42
Average					0.67 ± 0.44
$p_{\perp,\ell^-}$ [GeV]	σ_{calc} [pb]	$\Delta\sigma_{\text{calc}}$ [pb]	σ_{gen} [pb]	$\Delta\sigma_{\text{gen}}$ [pb]	STD
[0, 30]	3.73	0.03	3.76	0.02	0.93
[30, 60]	5.84	0.03	5.83	0.03	0.18
[60, 90]	3.01	0.02	3.00	0.02	0.42
[90, 120]	1.26	0.02	1.22	0.01	1.76
[120, 150]	0.484	0.010	0.507	0.009	1.82
[150, 180]	0.196	0.006	0.211	0.006	1.80
[180, 210]	0.085	0.004	0.089	0.004	0.63
[210, 240]	0.040	0.003	0.039	0.002	0.22
[240, 270]	0.018	0.002	0.022	0.002	1.58
[270, 300]	0.010	0.001	0.014	0.001	1.89
Total	14.67	0.06	14.70	0.05	0.36
Average					1.12 ± 0.68

Table A.22: Comparison of calculated and generated differential cross section w.r.t. $p_{\perp,\ell^+}$ and $p_{\perp,\ell^-}$ for $C_{uW}^{33} = 1.18$ and $C_{\varphi q}^{(3)33} = 1.24$. Bins are not divided by bin width. The last column shows the standard deviation (STD). 'Total' refers to the sum over all bins and 'Average' is the average STD over all bins.

$\lvert y_{\ell^+}\rvert$	σ_{calc} [pb]	$\Delta\sigma_{\text{calc}}$ [pb]	σ_{gen} [pb]	$\Delta\sigma_{\text{gen}}$ [pb]	STD
[0.0, 0.5]	4.16	0.03	4.18	0.02	0.65
[0.5, 1.0]	3.74	0.03	3.79	0.02	1.56
[1.0, 1.5]	3.11	0.03	3.08	0.02	1.01
[1.5, 2.0]	2.24	0.02	2.24	0.02	0.12
[2.0, 2.5]	1.44	0.02	1.42	0.01	0.77
Total	14.68	0.06	14.71	0.05	0.39
Average					0.82 ± 0.47
$\lvert y_{\ell^-}\rvert$	σ_{calc} [pb]	$\Delta\sigma_{\text{calc}}$ [pb]	σ_{gen} [pb]	$\Delta\sigma_{\text{gen}}$ [pb]	STD
[0.0, 0.5]	4.11	0.03	4.16	0.02	1.26
[0.5, 1.0]	3.78	0.03	3.81	0.02	0.88
[1.0, 1.5]	3.10	0.03	3.10	0.02	0.08
[1.5, 2.0]	2.24	0.02	2.23	0.02	0.47
[2.0, 2.5]	1.46	0.02	1.42	0.01	1.64
Total	14.68	0.06	14.71	0.05	0.39
Average					0.87 ± 0.55
$\lvert\Delta\phi_{\ell\ell}\rvert$ [π]	σ_{calc} [pb]	$\Delta\sigma_{\text{calc}}$ [pb]	σ_{gen} [pb]	$\Delta\sigma_{\text{gen}}$ [pb]	STD
[0.0, 0.1]	0.90	0.01	0.91	0.01	0.66
[0.1, 0.2]	1.14	0.02	1.13	0.01	0.63
[0.2, 0.3]	1.21	0.02	1.19	0.01	0.80
[0.3, 0.4]	1.26	0.02	1.27	0.01	0.57
[0.4, 0.5]	1.35	0.02	1.38	0.01	1.34
[0.5, 0.6]	1.53	0.02	1.47	0.01	2.58
[0.6, 0.7]	1.63	0.02	1.64	0.02	0.54
[0.7, 0.8]	1.76	0.02	1.79	0.02	1.13
[0.8, 0.9]	1.89	0.02	1.92	0.02	1.02
[0.9, 1.0]	2.02	0.02	2.02	0.02	0.17
Total	14.68	0.06	14.71	0.05	0.39
Average					0.94 ± 0.63

Table A.23: Comparison of calculated and generated differential cross section w.r.t. $|y_{\ell^+}|$, $|y_{\ell^-}|$, and $|\Delta\phi_{\ell\ell}|$ for $C_{uW}^{33} = 1.18$ and $C_{\varphi q}^{(3)33} = 1.24$. Bins are not divided by bin width.

$\cos\theta_+ \cos\theta_-$	σ_{calc} [pb]	$\Delta\sigma_{\text{calc}}$ [pb]	σ_{gen} [pb]	$\Delta\sigma_{\text{gen}}$ [pb]	STD
[-1.0, -0.9]	0.028	0.002	0.029	0.002	0.33
[-0.9, -0.8]	0.124	0.005	0.122	0.004	0.36
[-0.8, -0.7]	0.225	0.007	0.223	0.006	0.18
[-0.7, -0.6]	0.353	0.009	0.347	0.007	0.51
[-0.6, -0.5]	0.473	0.010	0.484	0.008	0.83
[-0.5, -0.4]	0.61	0.01	0.621	0.010	0.86
[-0.4, -0.3]	0.84	0.01	0.83	0.01	0.68
[-0.3, -0.2]	1.05	0.01	1.08	0.01	1.63
[-0.2, -0.1]	1.45	0.02	1.43	0.01	0.86
[-0.1, -0.0]	2.44	0.02	2.45	0.02	0.27
[-0.0, 0.1]	2.39	0.02	2.40	0.02	0.34
[0.1, 0.2]	1.32	0.02	1.32	0.01	0.10
[0.2, 0.3]	0.90	0.01	0.88	0.01	1.01
[0.3, 0.4]	0.64	0.01	0.655	0.010	1.16
[0.4, 0.5]	0.486	0.010	0.466	0.008	1.53
[0.5, 0.6]	0.321	0.008	0.333	0.007	1.11
[0.6, 0.7]	0.223	0.007	0.221	0.006	0.23
[0.7, 0.8]	0.127	0.005	0.140	0.005	1.83
[0.8, 0.9]	0.063	0.004	0.068	0.003	0.97
[0.9, 1.0]	0.018	0.002	0.020	0.002	0.82
Total	14.08	0.05	14.12	0.05	0.57
Average					0.78 ± 0.49

Table A.24: Comparison of calculated and generated differential cross section w.r.t. $\cos\theta_+ \cos\theta_-$ for $C_{uW}^{33} = 1.18$ and $C_{\varphi q}^{(3)33} = 1.24$. Bins are not divided by bin width. The last column shows the standard deviation (STD). 'Total' refers to the sum over all bins and 'Average' is the average STD over all bins.

$p_{\perp,\ell^+}$ [GeV]	σ_{calc} [pb]	$\Delta\sigma_{\text{calc}}$ [pb]	σ_{gen} [pb]	$\Delta\sigma_{\text{gen}}$ [pb]	STD
[0, 30]	3.72	0.03	3.73	0.02	0.55
[30, 60]	5.88	0.03	5.85	0.03	0.67
[60, 90]	2.95	0.02	2.97	0.02	0.56
[90, 120]	1.24	0.01	1.23	0.01	0.24
[120, 150]	0.483	0.009	0.498	0.009	1.27
[150, 180]	0.213	0.006	0.205	0.005	1.10
[180, 210]	0.084	0.004	0.090	0.004	1.29
[210, 240]	0.038	0.002	0.043	0.003	1.45
[240, 270]	0.021	0.002	0.017	0.002	1.53
[270, 300]	0.009	0.001	0.010	0.001	0.77
Total	14.63	0.05	14.65	0.05	0.28
Average					0.94 ± 0.42
$p_{\perp,\ell^-}$ [GeV]	σ_{calc} [pb]	$\Delta\sigma_{\text{calc}}$ [pb]	σ_{gen} [pb]	$\Delta\sigma_{\text{gen}}$ [pb]	STD
[0, 30]	3.74	0.03	3.75	0.02	0.54
[30, 60]	5.83	0.03	5.87	0.03	0.92
[60, 90]	3.00	0.02	2.96	0.02	1.28
[90, 120]	1.25	0.01	1.22	0.01	1.32
[120, 150]	0.482	0.009	0.491	0.008	0.78
[150, 180]	0.195	0.005	0.204	0.005	1.13
[180, 210]	0.085	0.004	0.085	0.004	0.03
[210, 240]	0.039	0.002	0.039	0.002	0.01
[240, 270]	0.018	0.002	0.021	0.002	1.08
[270, 300]	0.010	0.001	0.010	0.001	0.15
Total	14.64	0.05	14.65	0.05	0.23
Average					0.72 ± 0.49

Table A.25: Comparison of calculated and generated differential cross section w.r.t. $p_{\perp,\ell^+}$ and $p_{\perp,\ell^-}$ for $C_{uW}^{33} = 1.1$ and $C_{\varphi q}^{(3)33} = 1.76$. Bins are not divided by bin width. The last column shows the standard deviation (STD). ‘Total’ refers to the sum over all bins and ‘Average’ is the average STD over all bins.

$\lvert y_{\ell^+}\rvert$	σ_{calc} [pb]	$\Delta\sigma_{\text{calc}}$ [pb]	σ_{gen} [pb]	$\Delta\sigma_{\text{gen}}$ [pb]	STD
[0.0, 0.5]	4.15	0.03	4.17	0.02	0.62
[0.5, 1.0]	3.73	0.02	3.78	0.02	1.49
[1.0, 1.5]	3.10	0.02	3.09	0.02	0.56
[1.5, 2.0]	2.23	0.02	2.23	0.02	0.34
[2.0, 2.5]	1.43	0.02	1.40	0.01	1.38
Total	14.65	0.05	14.66	0.05	0.27
Average					0.88 ± 0.47
$\lvert y_{\ell^-}\rvert$	σ_{calc} [pb]	$\Delta\sigma_{\text{calc}}$ [pb]	σ_{gen} [pb]	$\Delta\sigma_{\text{gen}}$ [pb]	STD
[0.0, 0.5]	4.10	0.03	4.12	0.02	0.30
[0.5, 1.0]	3.77	0.02	3.78	0.02	0.45
[1.0, 1.5]	3.09	0.02	3.09	0.02	0.04
[1.5, 2.0]	2.23	0.02	2.23	0.02	0.07
[2.0, 2.5]	1.45	0.02	1.45	0.01	0.25
Total	14.65	0.05	14.66	0.05	0.27
Average					0.22 ± 0.15
$\lvert\Delta\phi_{\ell\ell}\rvert$ [π]	σ_{calc} [pb]	$\Delta\sigma_{\text{calc}}$ [pb]	σ_{gen} [pb]	$\Delta\sigma_{\text{gen}}$ [pb]	STD
[0.0, 0.1]	0.90	0.01	0.89	0.01	0.47
[0.1, 0.2]	1.14	0.01	1.13	0.01	0.26
[0.2, 0.3]	1.20	0.01	1.20	0.01	0.18
[0.3, 0.4]	1.25	0.01	1.25	0.01	0.04
[0.4, 0.5]	1.35	0.01	1.37	0.01	1.21
[0.5, 0.6]	1.52	0.02	1.47	0.01	2.44
[0.6, 0.7]	1.62	0.02	1.63	0.02	0.06
[0.7, 0.8]	1.76	0.02	1.79	0.02	1.19
[0.8, 0.9]	1.89	0.02	1.92	0.02	1.43
[0.9, 1.0]	2.02	0.02	2.01	0.02	0.13
Total	14.65	0.05	14.66	0.05	0.27
Average					0.74 ± 0.76

Table A.26: Comparison of calculated and generated differential cross section w.r.t. $\lvert y_{\ell^+}\rvert$, $\lvert y_{\ell^-}\rvert$, and $\lvert\Delta\phi_{\ell\ell}\rvert$ for $C_{uW}^{33} = 1.1$ and $C_{\varphi q}^{(3)33} = 1.76$. Bins are not divided by bin width.

$\cos\theta_+ \cos\theta_-$	σ_{calc} [pb]	$\Delta\sigma_{\text{calc}}$ [pb]	σ_{gen} [pb]	$\Delta\sigma_{\text{gen}}$ [pb]	STD
[-1.0, -0.9]	0.028	0.002	0.032	0.002	1.06
[-0.9, -0.8]	0.124	0.004	0.128	0.004	0.66
[-0.8, -0.7]	0.225	0.006	0.217	0.006	0.87
[-0.7, -0.6]	0.350	0.008	0.345	0.007	0.48
[-0.6, -0.5]	0.471	0.009	0.469	0.008	0.19
[-0.5, -0.4]	0.61	0.01	0.642	0.010	2.37
[-0.4, -0.3]	0.84	0.01	0.82	0.01	1.03
[-0.3, -0.2]	1.05	0.01	1.09	0.01	2.21
[-0.2, -0.1]	1.45	0.02	1.45	0.01	0.25
[-0.1, -0.0]	2.44	0.02	2.46	0.02	0.81
[-0.0, 0.1]	2.38	0.02	2.34	0.02	1.52
[0.1, 0.2]	1.32	0.01	1.31	0.01	0.54
[0.2, 0.3]	0.89	0.01	0.90	0.01	0.45
[0.3, 0.4]	0.64	0.01	0.640	0.010	0.19
[0.4, 0.5]	0.482	0.009	0.468	0.008	1.18
[0.5, 0.6]	0.321	0.007	0.322	0.007	0.15
[0.6, 0.7]	0.222	0.006	0.221	0.006	0.16
[0.7, 0.8]	0.127	0.005	0.131	0.004	0.64
[0.8, 0.9]	0.063	0.003	0.065	0.003	0.51
[0.9, 1.0]	0.018	0.002	0.019	0.002	0.52
Total	14.05	0.05	14.08	0.05	0.44
Average					0.79 ± 0.62

Table A.27: Comparison of calculated and generated differential cross section w.r.t. $\cos\theta_+ \cos\theta_-$ for $C_{uW}^{33} = 1.1$ and $C_{\varphi q}^{(3)33} = 1.76$. Bins are not divided by bin width. The last column shows the standard deviation (STD). 'Total' refers to the sum over all bins and 'Average' is the average STD over all bins.

$p_{\perp,\ell^+}$ [GeV]	σ_{calc} [pb]	$\Delta\sigma_{\text{calc}}$ [pb]	σ_{gen} [pb]	$\Delta\sigma_{\text{gen}}$ [pb]	STD
[0, 30]	3.71	0.03	3.72	0.02	0.34
[30, 60]	5.89	0.03	5.89	0.03	0.06
[60, 90]	2.96	0.02	2.96	0.02	0.10
[90, 120]	1.24	0.01	1.24	0.01	0.09
[120, 150]	0.484	0.009	0.487	0.008	0.25
[150, 180]	0.214	0.006	0.206	0.005	0.92
[180, 210]	0.084	0.004	0.091	0.004	1.35
[210, 240]	0.038	0.002	0.039	0.002	0.36
[240, 270]	0.021	0.002	0.021	0.002	0.09
[270, 300]	0.009	0.001	0.008	0.001	0.19
Total	14.64	0.05	14.66	0.05	0.25
Average					0.37 ± 0.41
$p_{\perp,\ell^-}$ [GeV]	σ_{calc} [pb]	$\Delta\sigma_{\text{calc}}$ [pb]	σ_{gen} [pb]	$\Delta\sigma_{\text{gen}}$ [pb]	STD
[0, 30]	3.73	0.03	3.74	0.02	0.28
[30, 60]	5.83	0.03	5.85	0.03	0.47
[60, 90]	3.00	0.02	2.97	0.02	1.04
[90, 120]	1.25	0.01	1.24	0.01	0.69
[120, 150]	0.482	0.009	0.508	0.009	2.07
[150, 180]	0.196	0.006	0.196	0.005	0.10
[180, 210]	0.085	0.004	0.084	0.004	0.16
[210, 240]	0.039	0.003	0.041	0.002	0.55
[240, 270]	0.018	0.002	0.020	0.002	0.93
[270, 300]	0.010	0.001	0.010	0.001	0.13
Total	14.65	0.05	14.66	0.05	0.21
Average					0.64 ± 0.57

Table A.28: Comparison of calculated and generated differential cross section w.r.t. $p_{\perp,\ell^+}$ and $p_{\perp,\ell^-}$ for $C_{uW}^{33} = 1.13$ and $C_{\varphi q}^{(3)33} = 1.58$. Bins are not divided by bin width. The last column shows the standard deviation (STD). 'Total' refers to the sum over all bins and 'Average' is the average STD over all bins.

$\lvert y_{\ell^+}\rvert$	σ_{calc} [pb]	$\Delta\sigma_{\text{calc}}$ [pb]	σ_{gen} [pb]	$\Delta\sigma_{\text{gen}}$ [pb]	STD
[0.0, 0.5]	4.15	0.03	4.18	0.02	0.83
[0.5, 1.0]	3.73	0.03	3.78	0.02	1.34
[1.0, 1.5]	3.11	0.02	3.05	0.02	1.83
[1.5, 2.0]	2.24	0.02	2.21	0.02	0.82
[2.0, 2.5]	1.43	0.02	1.45	0.01	0.97
Total	14.66	0.05	14.68	0.05	0.27
Average					1.16 ± 0.39
$\lvert y_{\ell^-}\rvert$	σ_{calc} [pb]	$\Delta\sigma_{\text{calc}}$ [pb]	σ_{gen} [pb]	$\Delta\sigma_{\text{gen}}$ [pb]	STD
[0.0, 0.5]	4.11	0.03	4.16	0.02	1.35
[0.5, 1.0]	3.77	0.03	3.77	0.02	0.10
[1.0, 1.5]	3.09	0.02	3.10	0.02	0.30
[1.5, 2.0]	2.24	0.02	2.24	0.02	0.34
[2.0, 2.5]	1.45	0.02	1.40	0.01	2.49
Total	14.66	0.05	14.68	0.05	0.27
Average					0.92 ± 0.90
$\lvert\Delta\phi_{\ell\ell}\rvert$ [π]	σ_{calc} [pb]	$\Delta\sigma_{\text{calc}}$ [pb]	σ_{gen} [pb]	$\Delta\sigma_{\text{gen}}$ [pb]	STD
[0.0, 0.1]	0.90	0.01	0.88	0.01	0.95
[0.1, 0.2]	1.14	0.01	1.11	0.01	1.33
[0.2, 0.3]	1.20	0.01	1.21	0.01	0.53
[0.3, 0.4]	1.25	0.01	1.28	0.01	1.36
[0.4, 0.5]	1.35	0.02	1.36	0.01	0.35
[0.5, 0.6]	1.52	0.02	1.48	0.01	2.13
[0.6, 0.7]	1.63	0.02	1.62	0.02	0.43
[0.7, 0.8]	1.76	0.02	1.83	0.02	2.81
[0.8, 0.9]	1.89	0.02	1.91	0.02	0.98
[0.9, 1.0]	2.02	0.02	2.00	0.02	0.81
Total	14.66	0.05	14.68	0.05	0.27
Average					1.17 ± 0.74

Table A.29: Comparison of calculated and generated differential cross section w.r.t. $\lvert y_{\ell^+}\rvert$, $\lvert y_{\ell^-}\rvert$, and $\lvert\Delta\phi_{\ell\ell}\rvert$ for $C_{uW}^{33} = 1.13$ and $C_{\varphi q}^{(3)33} = 1.58$. Bins are not divided by bin width.

$\cos\theta_+ \cos\theta_-$	σ_{calc} [pb]	$\Delta\sigma_{\text{calc}}$ [pb]	σ_{gen} [pb]	$\Delta\sigma_{\text{gen}}$ [pb]	STD
[-1.0, -0.9]	0.028	0.002	0.025	0.002	0.97
[-0.9, -0.8]	0.124	0.005	0.122	0.004	0.31
[-0.8, -0.7]	0.225	0.006	0.225	0.006	0.03
[-0.7, -0.6]	0.351	0.008	0.349	0.007	0.14
[-0.6, -0.5]	0.472	0.009	0.483	0.008	0.91
[-0.5, -0.4]	0.61	0.01	0.638	0.010	2.05
[-0.4, -0.3]	0.84	0.01	0.82	0.01	1.15
[-0.3, -0.2]	1.05	0.01	1.07	0.01	1.05
[-0.2, -0.1]	1.45	0.02	1.44	0.01	0.62
[-0.1, -0.0]	2.44	0.02	2.44	0.02	0.10
[-0.0, 0.1]	2.38	0.02	2.37	0.02	0.52
[0.1, 0.2]	1.32	0.02	1.29	0.01	1.43
[0.2, 0.3]	0.89	0.01	0.90	0.01	0.14
[0.3, 0.4]	0.64	0.01	0.648	0.010	0.78
[0.4, 0.5]	0.483	0.009	0.477	0.008	0.48
[0.5, 0.6]	0.321	0.008	0.332	0.007	1.11
[0.6, 0.7]	0.222	0.006	0.221	0.006	0.17
[0.7, 0.8]	0.127	0.005	0.135	0.004	1.19
[0.8, 0.9]	0.063	0.003	0.069	0.003	1.27
[0.9, 1.0]	0.018	0.002	0.020	0.002	0.86
Total	14.06	0.05	14.07	0.05	0.13
Average					0.76 ± 0.52

Table A.30: Comparison of calculated and generated differential cross section w.r.t. $\cos\theta_+ \cos\theta_-$ for $C_{uW}^{33} = 1.13$ and $C_{\varphi q}^{(3)33} = 1.58$. Bins are not divided by bin width. The last column shows the standard deviation (STD). 'Total' refers to the sum over all bins and 'Average' is the average STD over all bins.

$p_{\perp,\ell^+}$ [GeV]	σ_{calc} [pb]	$\Delta\sigma_{\text{calc}}$ [pb]	σ_{gen} [pb]	$\Delta\sigma_{\text{gen}}$ [pb]	STD
[0, 30]	3.74	0.03	3.80	0.02	1.43
[30, 60]	5.90	0.04	5.87	0.03	0.62
[60, 90]	2.96	0.03	2.97	0.02	0.21
[90, 120]	1.23	0.02	1.22	0.01	0.35
[120, 150]	0.48	0.01	0.493	0.009	0.87
[150, 180]	0.207	0.007	0.203	0.005	0.44
[180, 210]	0.082	0.005	0.084	0.004	0.35
[210, 240]	0.037	0.003	0.038	0.002	0.25
[240, 270]	0.021	0.002	0.019	0.002	0.78
[270, 300]	0.008	0.001	0.007	0.001	0.67
Total	14.66	0.06	14.70	0.05	0.44
Average					0.60 ± 0.35
$p_{\perp,\ell^-}$ [GeV]	σ_{calc} [pb]	$\Delta\sigma_{\text{calc}}$ [pb]	σ_{gen} [pb]	$\Delta\sigma_{\text{gen}}$ [pb]	STD
[0, 30]	3.77	0.03	3.78	0.02	0.28
[30, 60]	5.84	0.04	5.91	0.03	1.30
[60, 90]	2.99	0.03	2.92	0.02	1.91
[90, 120]	1.24	0.02	1.23	0.01	0.51
[120, 150]	0.48	0.01	0.502	0.009	1.77
[150, 180]	0.194	0.007	0.196	0.005	0.28
[180, 210]	0.084	0.005	0.092	0.004	1.32
[210, 240]	0.041	0.003	0.042	0.002	0.26
[240, 270]	0.017	0.002	0.016	0.002	0.57
[270, 300]	0.010	0.002	0.007	0.001	1.32
Total	14.67	0.06	14.70	0.05	0.39
Average					0.95 ± 0.61

Table A.31: Comparison of calculated and generated differential cross section w.r.t. $p_{\perp,\ell^+}$ and $p_{\perp,\ell^-}$ for $C_{uW}^{33} = 0.89$ and $C_{\varphi q}^{(3)33} = 0.0$. Bins are not divided by bin width. The last column shows the standard deviation (STD). 'Total' refers to the sum over all bins and 'Average' is the average STD over all bins.

$\lvert y_{\ell^+} \rvert$	σ_{calc} [pb]	$\Delta\sigma_{\text{calc}}$ [pb]	σ_{gen} [pb]	$\Delta\sigma_{\text{gen}}$ [pb]	STD
[0.0, 0.5]	4.16	0.03	4.15	0.02	0.14
[0.5, 1.0]	3.74	0.03	3.73	0.02	0.19
[1.0, 1.5]	3.11	0.03	3.13	0.02	0.49
[1.5, 2.0]	2.24	0.03	2.27	0.02	1.09
[2.0, 2.5]	1.43	0.02	1.43	0.01	0.31
Total	14.68	0.06	14.71	0.05	0.38
Average					0.44 ± 0.34
$\lvert y_{\ell^-} \rvert$	σ_{calc} [pb]	$\Delta\sigma_{\text{calc}}$ [pb]	σ_{gen} [pb]	$\Delta\sigma_{\text{gen}}$ [pb]	STD
[0.0, 0.5]	4.11	0.03	4.19	0.02	2.13
[0.5, 1.0]	3.78	0.03	3.78	0.02	0.02
[1.0, 1.5]	3.10	0.03	3.10	0.02	0.09
[1.5, 2.0]	2.24	0.03	2.23	0.02	0.21
[2.0, 2.5]	1.46	0.02	1.40	0.01	2.30
Total	14.68	0.06	14.71	0.05	0.38
Average					0.95 ± 1.04
$\lvert\Delta\phi_{\ell\ell}\rvert$ [π]	σ_{calc} [pb]	$\Delta\sigma_{\text{calc}}$ [pb]	σ_{gen} [pb]	$\Delta\sigma_{\text{gen}}$ [pb]	STD
[0.0, 0.1]	0.90	0.02	0.90	0.01	0.25
[0.1, 0.2]	1.14	0.02	1.13	0.01	0.27
[0.2, 0.3]	1.21	0.02	1.22	0.01	0.45
[0.3, 0.4]	1.26	0.02	1.25	0.01	0.16
[0.4, 0.5]	1.35	0.02	1.34	0.01	0.31
[0.5, 0.6]	1.53	0.02	1.49	0.01	1.58
[0.6, 0.7]	1.63	0.02	1.64	0.02	0.27
[0.7, 0.8]	1.77	0.02	1.80	0.02	1.23
[0.8, 0.9]	1.88	0.02	1.93	0.02	1.49
[0.9, 1.0]	2.01	0.02	2.00	0.02	0.38
Total	14.68	0.06	14.71	0.05	0.38
Average					0.64 ± 0.53

Table A.32: Comparison of calculated and generated differential cross section w.r.t. $|y_{\ell^+}|$, $|y_{\ell^-}|$, and $|\Delta\phi_{\ell\ell}|$ for $C_{uW}^{33} = 0.89$ and $C_{\varphi q}^{(3)33} = 0.0$. Bins are not divided by bin width.

$\cos\theta_+ \cos\theta_-$	σ_{calc} [pb]	$\Delta\sigma_{\text{calc}}$ [pb]	σ_{gen} [pb]	$\Delta\sigma_{\text{gen}}$ [pb]	STD
[-1.0, -0.9]	0.028	0.003	0.033	0.002	1.42
[-0.9, -0.8]	0.124	0.006	0.124	0.004	0.09
[-0.8, -0.7]	0.224	0.008	0.226	0.006	0.20
[-0.7, -0.6]	0.356	0.010	0.345	0.007	0.91
[-0.6, -0.5]	0.48	0.01	0.474	0.008	0.23
[-0.5, -0.4]	0.61	0.01	0.640	0.010	1.99
[-0.4, -0.3]	0.83	0.02	0.82	0.01	0.67
[-0.3, -0.2]	1.05	0.02	1.09	0.01	1.76
[-0.2, -0.1]	1.45	0.02	1.46	0.01	0.47
[-0.1, -0.0]	2.45	0.03	2.47	0.02	0.68
[-0.0, 0.1]	2.39	0.03	2.39	0.02	0.00
[0.1, 0.2]	1.32	0.02	1.29	0.01	1.53
[0.2, 0.3]	0.90	0.02	0.91	0.01	0.44
[0.3, 0.4]	0.63	0.01	0.653	0.010	1.10
[0.4, 0.5]	0.49	0.01	0.450	0.008	2.70
[0.5, 0.6]	0.319	0.009	0.329	0.007	0.82
[0.6, 0.7]	0.222	0.008	0.223	0.006	0.07
[0.7, 0.8]	0.125	0.006	0.130	0.004	0.56
[0.8, 0.9]	0.063	0.004	0.065	0.003	0.47
[0.9, 1.0]	0.018	0.002	0.019	0.002	0.56
Total	14.08	0.06	14.13	0.05	0.72
Average					0.83 ± 0.70

Table A.33: Comparison of calculated and generated differential cross section w.r.t. $\cos\theta_+ \cos\theta_-$ for $C_{uW}^{33} = 0.89$ and $C_{\varphi q}^{(3)33} = 0.0$. Bins are not divided by bin width. The last column shows the standard deviation (STD). ‘Total’ refers to the sum over all bins and ‘Average’ is the average STD over all bins.

$p_{\perp,\ell^+}$ [GeV]	σ_{calc} [pb]	$\Delta\sigma_{\text{calc}}$ [pb]	σ_{gen} [pb]	$\Delta\sigma_{\text{gen}}$ [pb]	STD
[0, 30]	3.73	0.03	3.80	0.02	1.70
[30, 60]	5.90	0.04	5.85	0.03	0.97
[60, 90]	2.96	0.03	2.95	0.02	0.46
[90, 120]	1.24	0.02	1.24	0.01	0.34
[120, 150]	0.48	0.01	0.497	0.009	1.08
[150, 180]	0.209	0.007	0.217	0.006	0.89
[180, 210]	0.082	0.005	0.089	0.004	1.24
[210, 240]	0.037	0.003	0.041	0.002	1.00
[240, 270]	0.021	0.002	0.019	0.002	0.85
[270, 300]	0.008	0.001	0.008	0.001	0.13
Total	14.67	0.06	14.72	0.05	0.56
Average					0.87 ± 0.43
$p_{\perp,\ell^-}$ [GeV]	σ_{calc} [pb]	$\Delta\sigma_{\text{calc}}$ [pb]	σ_{gen} [pb]	$\Delta\sigma_{\text{gen}}$ [pb]	STD
[0, 30]	3.76	0.03	3.77	0.02	0.17
[30, 60]	5.85	0.04	5.90	0.03	1.03
[60, 90]	2.99	0.03	2.96	0.02	1.04
[90, 120]	1.25	0.02	1.23	0.01	0.75
[120, 150]	0.48	0.01	0.497	0.009	1.32
[150, 180]	0.194	0.007	0.202	0.005	0.87
[180, 210]	0.084	0.005	0.091	0.004	1.23
[210, 240]	0.041	0.003	0.040	0.002	0.38
[240, 270]	0.017	0.002	0.018	0.002	0.39
[270, 300]	0.010	0.002	0.010	0.001	0.35
Total	14.68	0.06	14.71	0.05	0.49
Average					0.75 ± 0.39

Table A.34: Comparison of calculated and generated differential cross section w.r.t. $p_{\perp,\ell^+}$ and $p_{\perp,\ell^-}$ for $C_{uW}^{33} = 0.96$ and $C_{\varphi q}^{(3)33} = 0.16$. Bins are not divided by bin width. The last column shows the standard deviation (STD). 'Total' refers to the sum over all bins and 'Average' is the average STD over all bins.

$\lvert y_{\ell^+}\rvert$	σ_{calc} [pb]	$\Delta\sigma_{\text{calc}}$ [pb]	σ_{gen} [pb]	$\Delta\sigma_{\text{gen}}$ [pb]	STD
[0.0, 0.5]	4.16	0.03	4.21	0.02	1.12
[0.5, 1.0]	3.74	0.03	3.83	0.02	2.22
[1.0, 1.5]	3.11	0.03	3.08	0.02	1.04
[1.5, 2.0]	2.24	0.02	2.21	0.02	1.10
[2.0, 2.5]	1.44	0.02	1.41	0.01	0.99
Total	14.69	0.06	14.73	0.05	0.51
Average					1.29 ± 0.47
$\lvert y_{\ell^-}\rvert$	σ_{calc} [pb]	$\Delta\sigma_{\text{calc}}$ [pb]	σ_{gen} [pb]	$\Delta\sigma_{\text{gen}}$ [pb]	STD
[0.0, 0.5]	4.11	0.03	4.18	0.02	1.62
[0.5, 1.0]	3.78	0.03	3.80	0.02	0.40
[1.0, 1.5]	3.10	0.03	3.09	0.02	0.22
[1.5, 2.0]	2.24	0.02	2.25	0.02	0.36
[2.0, 2.5]	1.46	0.02	1.41	0.01	1.92
Total	14.69	0.06	14.73	0.05	0.51
Average					0.90 ± 0.72
$\lvert\Delta\phi_{\ell\ell}\rvert$ [π]	σ_{calc} [pb]	$\Delta\sigma_{\text{calc}}$ [pb]	σ_{gen} [pb]	$\Delta\sigma_{\text{gen}}$ [pb]	STD
[0.0, 0.1]	0.90	0.02	0.89	0.01	0.36
[0.1, 0.2]	1.14	0.02	1.13	0.01	0.58
[0.2, 0.3]	1.21	0.02	1.21	0.01	0.32
[0.3, 0.4]	1.26	0.02	1.27	0.01	0.43
[0.4, 0.5]	1.35	0.02	1.39	0.01	1.46
[0.5, 0.6]	1.53	0.02	1.49	0.01	1.66
[0.6, 0.7]	1.63	0.02	1.61	0.02	0.84
[0.7, 0.8]	1.77	0.02	1.79	0.02	0.75
[0.8, 0.9]	1.89	0.02	1.93	0.02	1.56
[0.9, 1.0]	2.02	0.02	2.02	0.02	0.23
Total	14.69	0.06	14.73	0.05	0.51
Average					0.82 ± 0.52

Table A.35: Comparison of calculated and generated differential cross section w.r.t. $\lvert y_{\ell^+}\rvert$, $\lvert y_{\ell^-}\rvert$, and $\lvert\Delta\phi_{\ell\ell}\rvert$ for $C_{uW}^{33} = 0.96$ and $C_{\varphi q}^{(3)33} = 0.16$. Bins are not divided by bin width.

$\cos\theta_+ \cos\theta_-$	σ_{calc} [pb]	$\Delta\sigma_{\text{calc}}$ [pb]	σ_{gen} [pb]	$\Delta\sigma_{\text{gen}}$ [pb]	STD
[-1.0, -0.9]	0.028	0.003	0.032	0.002	1.08
[-0.9, -0.8]	0.124	0.006	0.122	0.004	0.29
[-0.8, -0.7]	0.224	0.008	0.236	0.006	1.16
[-0.7, -0.6]	0.356	0.010	0.362	0.007	0.50
[-0.6, -0.5]	0.48	0.01	0.475	0.008	0.12
[-0.5, -0.4]	0.61	0.01	0.635	0.010	1.71
[-0.4, -0.3]	0.83	0.02	0.81	0.01	1.57
[-0.3, -0.2]	1.05	0.02	1.05	0.01	0.07
[-0.2, -0.1]	1.45	0.02	1.48	0.01	1.28
[-0.1, -0.0]	2.45	0.03	2.46	0.02	0.48
[-0.0, 0.1]	2.39	0.03	2.39	0.02	0.07
[0.1, 0.2]	1.32	0.02	1.29	0.01	1.22
[0.2, 0.3]	0.90	0.02	0.90	0.01	0.14
[0.3, 0.4]	0.64	0.01	0.647	0.010	0.73
[0.4, 0.5]	0.49	0.01	0.473	0.008	1.09
[0.5, 0.6]	0.319	0.009	0.344	0.007	2.11
[0.6, 0.7]	0.223	0.008	0.221	0.006	0.14
[0.7, 0.8]	0.126	0.006	0.132	0.004	0.85
[0.8, 0.9]	0.063	0.004	0.064	0.003	0.18
[0.9, 1.0]	0.018	0.002	0.017	0.002	0.33
Total	14.08	0.06	14.15	0.05	0.87
Average					0.76 ± 0.60

Table A.36: Comparison of calculated and generated differential cross section w.r.t. $\cos\theta_+ \cos\theta_-$ for $C_{uW}^{33} = 0.96$ and $C_{\varphi q}^{(3)33} = 0.16$. Bins are not divided by bin width. The last column shows the standard deviation (STD). 'Total' refers to the sum over all bins and 'Average' is the average STD over all bins.

Appendix B

Electroweak Top Couplings

B.1 Propagating Top Partners as EFT Contributions

In addition to the coupling modifications of the top–associated currents, amplitudes receive corrections from propagating top partners. Similarly, a composite top substructure can lead to additional anomalous magnetic moments [230, 279, 280] as observed in nuclear physics [281]. At the considered order in the chiral expansion in this work such terms arise at loop level [282, 283], and at tree level via the direct propagation of top partners. It is interesting to understand the latter contributions from an EFT perspective as they not only give rise to dimension six effects and cancellations can occur. In the mass eigenbasis, the propagating degrees of freedom lead to dimension eight effects. For instance, $t\bar{t} \to WW$ scattering in the mass eigenbasis receives corrections from b, B as well as from the 5/3-charged Q. The resulting Lorentz structure of contact $t\bar{t}W^+W^-$ amplitude in the EFT limit is described by a combination of

$$
\begin{aligned}
\mathcal{O}_{tW} &= \bar{Q}_L \sigma^{\mu\nu} \tilde{\varphi}\, \tau^a t_R W^a_{\mu\nu}\,, \\
\mathcal{O}_{tH} &= (D_\mu \varphi^\dagger D^\mu \varphi) \bar{Q}_L \tilde{\varphi}\, t_R\,,
\end{aligned}
$$

leading to

$$
\mathcal{M}(t\bar{t} \to W^+W^-) = \frac{C_{tW}}{\Lambda^2} \langle \mathcal{O}_{tW} \rangle + \frac{C_{tH}}{\Lambda^4} \langle \mathcal{O}_{th} \rangle + \ldots
$$

where the ellipses refer to momentum–dependent corrections that become relevant for $Q^2 \sim m_X^2$ and

$$
\begin{aligned}
\frac{C_{tW}}{\Lambda^2} &= -\frac{g_W}{4m_t} \left(\frac{c_L^{tB} c_R^{tB}}{m_B} - \frac{c_L^{tX} c_R^{tX}}{m_X} \right)\,, \\
\frac{C_{tH}}{\Lambda^4} &= -\frac{g_W^2}{16 m_t m_W^2} \left(\frac{c_L^{tB} c_R^{tB}}{m_B} + \frac{c_L^{tX} c_R^{tX}}{m_X} \right)\,,
\end{aligned}
$$

where $e\, c_{L,R}^{tX}, e\, c_{L,R}^{tB}$ are the left and right–chiral W couplings of the top with the respective top partner in the mass basis.

B.2 EFT Parametrisation of Anomalous Weak Top Quark Couplings

The effective dimension six operators (in the Warsaw basis [30]) that modify the vectorial couplings of the top quark to the W and Z bosons are given by

$$
\begin{aligned}
\mathcal{O}_{\varphi q}^{(1)} &= (\varphi^\dagger i \overleftrightarrow{D}_\mu \varphi)(\bar{Q}\gamma^\mu Q)\,, \\
\mathcal{O}_{\varphi q}^{(3)} &= (\varphi^\dagger i \overleftrightarrow{D}^I_\mu \varphi)(\bar{Q}\tau^I\gamma^\mu Q)\,, \\
\mathcal{O}_{\varphi u} &= (\varphi^\dagger i \overleftrightarrow{D}_\mu \varphi)(\bar{t}_R\gamma^\mu t_R)\,, \\
\mathcal{O}_{\varphi ud} &= i(\widetilde{\varphi}^\dagger D_\mu \varphi)(\bar{t}_R\gamma^\mu b_R)\,,
\end{aligned}
$$

with the associated Wilson coefficients $C_{\varphi q}^{(1)}$, $C_{\varphi q}^{(3)}$, $C_{\varphi u}$, and $C_{\varphi ud}$. See also Ref. [284] for a detailed recent discussion beyond tree–level. $Q = (t_L, b_L)^T$ denotes the quark $SU(2)_L$ doublet of the third generation with t_L and b_L the left–handed top and bottom quarks, respectively. The rest of the notation is aligned with Ref. [30].

The anomalous couplings of the top quark to W and Z bosons are related to the Wilson coefficients as follows

$$
\delta^t_{Z,L} = -\frac{C^Z_{\varphi q} v^2}{\Lambda^2}\left(1 - \frac{4}{3}\sin^2\theta_W\right)^{-1}\,, \tag{B.1a}
$$

$$
\delta^t_{Z,R} = \frac{C_{\varphi u} v^2}{\Lambda^2}\frac{3}{4\sin^2\theta_W}\,, \tag{B.1b}
$$

$$
\delta_{W,L} = \frac{C^W_{\varphi q} v^2}{\Lambda^2}\,, \tag{B.1c}
$$

$$
\delta_{W,R} = -\frac{1}{2}\frac{C_{\varphi ud} v^2}{\Lambda^2}\,. \tag{B.1d}
$$

In Eqs. (B.1a) and (B.1c) we have introduced two new Wilson coefficients which correspond to the operators

$$
\begin{aligned}
\mathcal{O}^W_{Hq} &= \mathcal{O}^{(3)}_{\varphi q}\,, \\
\mathcal{O}^Z_{Hq} &= \mathcal{O}^{(1)}_{\varphi q} - \mathcal{O}^{(3)}_{\varphi q}\,.
\end{aligned}
$$

This change of basis ensures that each of the four operators $\mathcal{O}^W_{Hq}$, $\mathcal{O}^Z_{Hq}$, $\mathcal{O}_{\varphi u}$ and $\mathcal{O}_{\varphi ud}$ contributes to exactly one kind of W and Z coupling in Section 6.3. The relations of Eq. (B.1) allow us to directly relate constraints on the Wilson coefficients to constraints on the coupling modifications δ.

List of Figures

List of Tables

Bibliography

[1] S. Brown, A. Buckley, C. Englert, J. Ferrando, P. Galler, D. J. Miller, L. Moore, M. Russell, C. White, and N. Warrack, "*TopFitter: Fitting top-quark Wilson Coefficients to Run II data*", PoS **ICHEP2018**, 293 (2019), arXiv:`1901.03164 [hep-ph]`.

[2] S. Brown, A. Buckley, C. Englert, J. Ferrando, P. Galler, D. Miller, C. Wanotayaroj, N. Warrack, and C. White, "*New results from TopFitter*", PoS **ICHEP2020**, 322 (2021).

[3] S. Brown, C. Englert, P. Galler, and P. Stylianou, "*Electroweak top couplings, partial compositeness, and top partner searches*", Phys. Rev. D **102**, 075021 (2020), arXiv:`2006.09112 [hep-ph]`.

[4] O. Atkinson, A. Bhardwaj, S. Brown, C. Englert, D. J. Miller, and P. Stylianou, "*Improved constraints on effective top quark interactions using edge convolution networks*", JHEP **04**, 137 (2022), arXiv:`2111.01838 [hep-ph]`.

[5] P. Galler, Private communication.

[6] M. E. Peskin and D. V. Schroeder, *An Introduction to quantum field theory* (Addison-Wesley, Reading, USA, 1995).

[7] A. Zee, *Quantum field theory in a nutshell*, second edition (Princeton University Press, 2010).

[8] N. Cabibbo, "*Unitary Symmetry and Leptonic Decays*", Phys. Rev. Lett. **10**, 531–533 (1963).

[9] M. Kobayashi and T. Maskawa, "*CP-Violation in the Renormalizable Theory of Weak Interaction*", Progress of Theoretical Physics **49**, 652–657 (1973), eprint: `https://academic.oup.com/ptp/article-pdf/49/2/652/5257692/49-2-652.pdf`.

[10] **Particle Data Group**, R. Workman et al., "*Review of Particle Physics*", Progress of Theoretical and Experimental Physics **2022**, 083C01 (2022).

[11] L. Wolfenstein, "*Parametrization of the Kobayashi-Maskawa Matrix*", Phys. Rev. Lett. **51**, 1945–1947 (1983).

[12] Z. Maki, M. Nakagawa, and S. Sakata, "*Remarks on the Unified Model of Elementary Particles*", Progress of Theoretical Physics **28**, 870–880 (1962).

[13] A. A. Petrov and A. E. Blechman, *Effective Field Theories* (World Scientific, 2016).

[14] C. Burgess, *Introduction to Effective Field Theory: Thinking Effectively about Hierarchies of Scale* (Cambridge University Press, 2020).

[15] B. Gripaios, *Lectures on Effective Field Theory*, 2015, arXiv:1506.05039 [hep-ph].

[16] A. V. Manohar, "*Effective field theories*", Lect. Notes Phys. **479**, 311–362 (1997), arXiv:hep-ph/9606222 [hep-ph].

[17] S. Liem, G. Bertone, F. Calore, R. Ruiz de Austri, T. M. P. Tait, R. Trotta, and C. Weniger, "*Effective field theory of dark matter: a global analysis*", JHEP **09**, 077 (2016), arXiv:1603.05994 [hep-ph].

[18] A. De Simone and T. Jacques, "*Simplified models vs. effective field theory approaches in dark matter searches*", Eur. Phys. J. **C76**, 367 (2016), arXiv:1603.08002 [hep-ph].

[19] J. K. Bloomfield, E. E. Flanagan, M. Park, and S. Watson, "*Dark energy or modified gravity? An effective field theory approach*", JCAP **1308**, 010 (2013), arXiv:1211.7054 [astro-ph.CO].

[20] A. Banerjee and H. Khanchandani, "*Constraining parameters of effective field theory of inflation from Planck data*", (2015), arXiv:1509.00328 [hep-th].

[21] M. Raveri, B. Hu, N. Frusciante, and A. Silvestri, "*Effective Field Theory of Cosmic Acceleration: constraining dark energy with CMB data*", Phys. Rev. **D90**, 043513 (2014), arXiv:1405.1022 [astro-ph.CO].

[22] P. F. Bedaque and U. van Kolck, "*Effective field theory for few nucleon systems*", Ann. Rev. Nucl. Part. Sci. **52**, 339–396 (2002), arXiv:nucl-th/0203055 [nucl-th].

[23] M. P. Valderrama, "*Power Counting and Wilsonian Renormalization in Nuclear Effective Field Theory*", Int. J. Mod. Phys. **E25**, 1641007 (2016), arXiv:1604.01332 [nucl-th].

[24] S. S. Gershtein and Y. B. Zeldovich, "*Meson corrections in the theory of beta decay*", Zh. Eksp. Teor. Fiz. **29**, 698–699 (1955).

[25] M. Dohse, "*TikZ-FeynHand: Basic User Guide*", (2018), arXiv:1802.00689 [cs.OH].

[26] D. B. Kaplan, "*Five lectures on effective field theory*", in (2005), arXiv:nucl-th/0510023 [nucl-th].

[27] A. Lesov, "*The Weak Force: From Fermi to Feynman*", ArXiv e-prints (2009), arXiv:0911.0058 [physics.hist-ph].

[28] W. Buchmüller and D. Wyler, "*Effective lagrangian analysis of new interactions and flavour conservation*", Nuclear Physics B **268**, 621–653 (1986).

[29] B. Grzadkowski, Z. Hioki, K. Ohkuma, and J. Wudka, "*Probing anomalous top quark couplings induced by dimension-six operators at photon colliders*", Nucl. Phys. **B689**, 108–126 (2004), arXiv:hep-ph/0310159 [hep-ph].

[30] B. Grzadkowski, M. Iskrzynski, M. Misiak, and J. Rosiek, "*Dimension-Six Terms in the Standard Model Lagrangian*", JHEP **10**, 085 (2010), arXiv:1008.4884 [hep-ph].

[31] G. F. Giudice, C. Grojean, A. Pomarol, and R. Rattazzi, "*The Strongly-Interacting Light Higgs*", JHEP **06**, 045 (2007), arXiv:hep-ph/0703164 [hep-ph].

[32] K. Hagiwara, S. Ishihara, R. Szalapski, and D. Zeppenfeld, "*Low-energy effects of new interactions in the electroweak boson sector*", Phys. Rev. **D48**, 2182–2203 (1993).

[33] A. Buckley, C. White, and M. White, *Practical Collider Physics*, 2053-2563 (IOP Publishing, 2021).

[34] F. Maltoni, D. Pagani, and I. Tsinikos, "*Associated production of a top-quark pair with vector bosons at NLO in QCD: impact on* $\mathrm{t\bar{t}H}$ *searches at the LHC*", JHEP **02**, 113 (2016), arXiv:1507.05640 [hep-ph].

[35] T.-J. Hou, J. Gao, T. J. Hobbs, K. Xie, S. Dulat, M. Guzzi, J. Huston, P. Nadolsky, J. Pumplin, C. Schmidt, I. Sitiwaldi, D. Stump, and C.-P. Yuan, "*New CTEQ global analysis of quantum chromodynamics with high-precision data from the LHC*", Physical Review D **103**, 10.1103/physrevd.103.014013 (2021), arXiv:1912.10053 [hep-ph].

[36] A. H. Hoang, "*What is the Top Quark Mass?*", Ann. Rev. Nucl. Part. Sci. **70**, 225–255 (2020), arXiv:2004.12915 [hep-ph].

[37] **ATLAS**, *Top cross section summary plots - September 2023*, tech. rep. (CERN, Geneva, 2023).

[38] **ATLAS**, M. Aaboud et al., "*Measurements of $t\bar{t}$ differential cross-sections of highly boosted top quarks decaying to all-hadronic final states in pp collisions at $\sqrt{s} = 13$ TeV using the ATLAS detector*", Phys. Rev. D **98**, 012003 (2018), arXiv:1801.02052 [hep-ex].

[39] J. Alwall, M. Herquet, F. Maltoni, O. Mattelaer, and T. Stelzer, "*MadGraph 5: Going Beyond*", JHEP **06**, 128 (2011), arXiv:1106.0522 [hep-ph].

[40] J. Alwall, R. Frederix, S. Frixione, V. Hirschi, F. Maltoni, O. Mattelaer, H. .-. Shao, T. Stelzer, P. Torrielli, and M. Zaro, "*The automated computation of tree-level and next-to-leading order differential cross sections, and their matching to parton shower simulations*", JHEP **07**, 079 (2014), arXiv:1405.0301 [hep-ph].

[41] S. Hoyer and J. Hamman, "*xarray: N-D labeled arrays and datasets in Python*", Journal of Open Research Software **5**, 10.5334/jors.148 (2017).

[42] W. McKinney, "*Data Structures for Statistical Computing in Python*", in *Proceedings of the 9th Python in Science Conference*, edited by S. van der Walt and J. Millman (2010), pp. 56–61.

[43] S. K. Lam, A. Pitrou, and S. Seibert, "*Numba: A LLVM-based Python JIT Compiler*", in *Proceedings of the Second Workshop on the LLVM Compiler Infrastructure in HPC*, LLVM '15 (2015), 7:1–7:6.

[44] E. Conte, B. Fuks, and G. Serret, "*MadAnalysis 5, A User-Friendly Framework for Collider Phenomenology*", Comput. Phys. Commun. **184**, 222–256 (2013), arXiv:1206.1599 [hep-ph].

[45] I. Brivio, Y. Jiang, and M. Trott, "*The SMEFTsim package, theory and tools*", JHEP **12**, 070 (2017), arXiv:1709.06492 [hep-ph].

[46] C. Degrande, C. Duhr, B. Fuks, D. Grellscheid, O. Mattelaer, and T. Reiter, "*UFO - The Universal FeynRules Output*", Comput. Phys. Commun. **183**, 1201–1214 (2012), arXiv:1108.2040 [hep-ph].

[47] P. Artoisenet, R. Frederix, O. Mattelaer, and R. Rietkerk, "*Automatic spin-entangled decays of heavy resonances in Monte Carlo simulations*", JHEP **03**, 015 (2013), arXiv:1212.3460 [hep-ph].

[48] T. Sjöstrand, S. Ask, J. R. Christiansen, R. Corke, N. Desai, P. Ilten, S. Mrenna, S. Prestel, C. O. Rasmussen, and P. Z. Skands, "*An introduction to PYTHIA 8.2*", Comput. Phys. Commun. **191**, 159–177 (2015), arXiv:1410.3012 [hep-ph].

[49] A. Buckley, J. Butterworth, L. Lonnblad, D. Grellscheid, H. Hoeth, J. Monk, H. Schulz, and F. Siegert, "*Rivet user manual*", Comput. Phys. Commun. **184**, 2803–2819 (2013), arXiv:1003.0694 [hep-ph].

[50] E. Boos et al., "*Generic User Process Interface for Event Generators*", arXiv e-prints, hep-ph/0109068, hep–ph/0109068 (2001), arXiv:hep-ph/0109068 [hep-ph].

[51] J. Alwall et al., "*A standard format for Les Houches Event Files*", Computer Physics Communications **176**, 300–304 (2007), arXiv:hep-ph/0609017 [hep-ph].

[52] P. Virtanen et al., "*SciPy 1.0: Fundamental Algorithms for Scientific Computing in Python*", Nature Methods **17**, 261–272 (2020).

[53] **ATLAS**, G. Aad et al., "*Measurement of the top quark pair production cross-section with ATLAS in the single lepton channel*", Phys. Lett. B **711**, 244–263 (2012), arXiv:1201.1889 [hep-ex].

[54] **ATLAS**, G. Aad et al., "*Measurement of the top quark pair cross section with ATLAS in pp collisions at $\sqrt{s} = 7$ TeV using final states with an electron or a muon and a hadronically decaying τ lepton*", Phys. Lett. B **717**, 89–108 (2012), arXiv:1205.2067 [hep-ex].

[55] **ATLAS**, G. Aad et al., "*Measurement of the W boson polarization in top quark decays with the ATLAS detector*", JHEP **06**, 088 (2012), arXiv:1205.2484 [hep-ex].

[56] **ATLAS**, G. Aad et al., "*Measurement of the ttbar production cross section in the tau+jets channel using the ATLAS detector*", Eur. Phys. J. C **73**, 2328 (2013), arXiv:1211.7205 [hep-ex].

[57] **ATLAS**, G. Aad et al., "*Measurement of the top quark pair production charge asymmetry in proton-proton collisions at $\sqrt{s} = 7$ TeV using the ATLAS detector*", JHEP **02**, 107 (2014), arXiv:1311.6724 [hep-ex].

[58] **ATLAS**, G. Aad et al., "*Measurement of the $t\bar{t}$ production cross-section using $e\mu$ events with b-tagged jets in pp collisions at $\sqrt{s} = 7$ and 8 TeV with the ATLAS detector*", Eur. Phys. J. C **74**, [Addendum: Eur.Phys.J.C 76, 642 (2016)], 3109 (2014), arXiv:1406.5375 [hep-ex].

[59] **ATLAS**, G. Aad et al., "*Comprehensive measurements of t-channel single top-quark production cross sections at $\sqrt{s} = 7$ TeV with the ATLAS detector*", Phys. Rev. D **90**, 112006 (2014), arXiv:1406.7844 [hep-ex].

[60] **ATLAS**, G. Aad et al., "*Measurements of normalized differential cross sections for $t\bar{t}$ production in pp collisions at $\sqrt{s} = 7$ TeV using the ATLAS detector*", Phys. Rev. D **90**, 072004 (2014), arXiv:1407.0371 [hep-ex].

[61] **ATLAS**, G. Aad et al., "*Simultaneous measurements of the $t\bar{t}$, W^+W^-, and $Z/\gamma^* \to \tau\tau$ production cross-sections in pp collisions at $\sqrt{s} = 7$ TeV with the ATLAS detector*", Phys. Rev. D **91**, 052005 (2015), arXiv:1407.0573 [hep-ex].

[62] **ATLAS**, G. Aad et al., "*Measurements of spin correlation in top-antitop quark events from proton-proton collisions at $\sqrt{s} = 7$ TeV using the ATLAS detector*", Phys. Rev. D **90**, 112016 (2014), arXiv:1407.4314 [hep-ex].

[63] **ATLAS**, G. Aad et al., "*Measurement of the $t\bar{t}W$ and $t\bar{t}Z$ production cross sections in pp collisions at $\sqrt{s} = 8$ TeV with the ATLAS detector*", JHEP **11**, 172 (2015), arXiv:1509.05276 [hep-ex].

[64] **ATLAS**, G. Aad et al., "*Measurement of the correlations between the polar angles of leptons from top quark decays in the helicity basis at $\sqrt{s} = 7$ TeV using the ATLAS detector*", Phys. Rev. D **93**, 012002 (2016), arXiv:1510.07478 [hep-ex].

[65] **ATLAS**, G. Aad et al., "*Measurement of the charge asymmetry in highly boosted top-quark pair production in $\sqrt{s} =$ 8 TeV pp collision data collected by the ATLAS experiment*", Phys. Lett. B **756**, 52–71 (2016), arXiv:1512.06092 [hep-ex].

[66] **ATLAS**, M. Aaboud et al., "*Measurement of the $t\bar{t}$ production cross-section using $e\mu$ events with b-tagged jets in pp collisions at $\sqrt{s}$=13 TeV with the ATLAS detector*", Phys. Lett. B **761**, [Erratum: Phys.Lett.B 772, 879–879 (2017)], 136–157 (2016), arXiv:1606.02699 [hep-ex].

[67] **ATLAS**, M. Aaboud et al., "*Measurement of top quark pair differential cross-sections in the dilepton channel in pp collisions at $\sqrt{s}$ = 7 and 8 TeV with ATLAS*", Phys. Rev. D **94**, [Addendum: Phys.Rev.D 101, 119901 (2020)], 092003 (2016), arXiv:1607.07281 [hep-ex].

[68] **ATLAS**, M. Aaboud et al., "*Measurement of the inclusive cross-sections of single top-quark and top-antiquark t-channel production in pp collisions at* $\sqrt{s}$ *= 13 TeV with the ATLAS detector*", JHEP **04**, 086 (2017), arXiv:1609.03920 [hep-ex].

[69] **ATLAS**, M. Aaboud et al., "*Measurement of the W boson polarisation in* $t\bar{t}$ *events from pp collisions at* $\sqrt{s}$ *= 8 TeV in the lepton + jets channel with ATLAS*", Eur. Phys. J. C **77**, [Erratum: Eur.Phys.J.C 79, 19 (2019)], 264 (2017), arXiv:1612.02577 [hep-ex].

[70] **ATLAS**, M. Aaboud et al., "*Measurement of the cross-section for producing a W boson in association with a single top quark in pp collisions at* $\sqrt{s} = 13$ *TeV with ATLAS*", JHEP **01**, 063 (2018), arXiv:1612.07231 [hep-ex].

[71] **ATLAS**, M. Aaboud et al., "*Probing the* Wtb *vertex structure in t-channel single-top-quark production and decay in pp collisions at* $\sqrt{s} = 8$ *TeV with the ATLAS detector*", JHEP **04**, 124 (2017), arXiv:1702.08309 [hep-ex].

[72] **ATLAS**, M. Aaboud et al., "*Measurement of the* $t\bar{t}$ *production cross section in the* τ *+ jets final state in pp collisions at* $\sqrt{s} = 8$ *TeV using the ATLAS detector*", Phys. Rev. D **95**, 072003 (2017), arXiv:1702.08839 [hep-ex].

[73] **ATLAS**, M. Aaboud et al., "*Analysis of the* Wtb *vertex from the measurement of triple-differential angular decay rates of single top quarks produced in the t-channel at* $\sqrt{s}$ *= 8 TeV with the ATLAS detector*", JHEP **12**, 017 (2017), arXiv:1707.05393 [hep-ex].

[74] **ATLAS**, M. Aaboud et al., "*Direct top-quark decay width measurement in the* $t\bar{t}$ *lepton+jets channel at* $\sqrt{s}$*=8 TeV with the ATLAS experiment*", Eur. Phys. J. C **78**, 129 (2018), arXiv:1709.04207 [hep-ex].

[75] **ATLAS**, M. Aaboud et al., "*Measurement of the production cross-section of a single top quark in association with a Z boson in proton–proton collisions at 13 TeV with the ATLAS detector*", Phys. Lett. B **780**, 557–577 (2018), arXiv:1710.03659 [hep-ex].

[76] **ATLAS**, M. Aaboud et al., "*Measurement of the* $t\bar{t}Z$ *and* $t\bar{t}W$ *cross sections in proton-proton collisions at* $\sqrt{s} = 13$ *TeV with the ATLAS detector*", Phys. Rev. D **99**, 072009 (2019), arXiv:1901.03584 [hep-ex].

[77] **ATLAS**, M. Aaboud et al., "*Measurements of top-quark pair spin correlations in the eμ channel at $\sqrt{s} = 13$ TeV using pp collisions in the ATLAS detector*", Eur. Phys. J. C **80**, 754 (2020), arXiv:1903.07570 [hep-ex].

[78] **ATLAS**, G. Aad et al., "*Observation of the associated production of a top quark and a Z boson in pp collisions at $\sqrt{s} = 13$ TeV with the ATLAS detector*", JHEP **07**, 124 (2020), arXiv:2002.07546 [hep-ex].

[79] **ATLAS, CMS**, M. Aaboud et al., "*Combination of inclusive and differential* $\mathrm{t\bar{t}}$ *charge asymmetry measurements using ATLAS and CMS data at $\sqrt{s} = 7$ and 8 TeV*", JHEP **04**, 033 (2018), arXiv:1709.05327 [hep-ex].

[80] **ATLAS, CMS**, M. Aaboud et al., "*Combinations of single-top-quark production cross-section measurements and $|f_{LV} V_{tb}|$ determinations at $\sqrt{s} = 7$ and 8 TeV with the ATLAS and CMS experiments*", JHEP **05**, 088 (2019), arXiv:1902.07158 [hep-ex].

[81] **CDF**, T. Aaltonen et al., "*First Measurement of the t anti-t Differential Cross Section d sigma/dM(t anti-t) in p anti-p Collisions at s**(1/2)=1.96-TeV*", Phys. Rev. Lett. **102**, 222003 (2009), arXiv:0903.2850 [hep-ex].

[82] **CDF**, T. Aaltonen et al., "*Measurement of W-Boson Polarization in Top-quark Decay using the Full CDF Run II Data Set*", Phys. Rev. D **87**, 031104 (2013), arXiv:1211.4523 [hep-ex].

[83] **CDF**, T. Aaltonen et al., "*Measurement of the Differential Cross Section $d\sigma/d(\cos\theta t)$ for Top-Quark Pair Production in $p-\bar{p}$ Collisions at $\sqrt{s} = 1.96$ TeV*", Phys. Rev. Lett. **111**, 182002 (2013), arXiv:1306.2357 [hep-ex].

[84] **CDF**, T. A. Aaltonen et al., "*Direct Measurement of the Total Decay Width of the Top Quark*", Phys. Rev. Lett. **111**, 202001 (2013), arXiv:1308.4050 [hep-ex].

[85] **CDF**, T. A. Aaltonen et al., "*Updated Measurement of the Single Top Quark Production Cross Section and Vtb in the Missing Transverse Energy Plus Jets Topology in $p\bar{p}$ Collisions at $\sqrt{s} = 1.96$ TeV*", Phys. Rev. D **93**, 032011 (2016), arXiv:1410.4909 [hep-ex].

[86] **CDF**, T. A. Aaltonen et al., "*Measurement of the forward–backward asymmetry of top-quark and antiquark pairs using the full CDF Run II data set*", Phys. Rev. D **93**, 112005 (2016), arXiv:1602.09015 [hep-ex].

[87] **CDF, D0**, T. A. Aaltonen et al., "*Combination of Measurements of the Top-Quark Pair Production Cross Section from the Tevatron Collider*", Phys. Rev. D **89**, 072001 (2014), arXiv:1309.7570 [hep-ex].

[88] **CDF, D0**, T. A. Aaltonen et al., "*Observation of s-channel production of single top quarks at the Tevatron*", Phys. Rev. Lett. **112**, 231803 (2014), arXiv:1402.5126 [hep-ex].

[89] **CDF, D0**, T. A. Aaltonen et al., "*Tevatron Combination of Single-Top-Quark Cross Sections and Determination of the Magnitude of the Cabibbo-Kobayashi-Maskawa Matrix Element* $\mathbf{V_{tb}}$", Phys. Rev. Lett. **115**, 152003 (2015), arXiv:1503.05027 [hep-ex].

[90] **CDF, D0**, T. A. Aaltonen et al., "*Combined Forward-Backward Asymmetry Measurements in Top-Antitop Quark Production at the Tevatron*", Phys. Rev. Lett. **120**, 042001 (2018), arXiv:1709.04894 [hep-ex].

[91] **CMS**, S. Chatrchyan et al., "*Measurement of the top quark pair production cross section in pp collisions at* $\sqrt{s} = 7$ *TeV in dilepton final states containing a* τ", Phys. Rev. D **85**, 112007 (2012), arXiv:1203.6810 [hep-ex].

[92] **CMS**, S. Chatrchyan et al., "*Measurement of the Single-Top-Quark* t*-Channel Cross Section in pp Collisions at* $\sqrt{s} = 7$ *TeV*", JHEP **12**, 035 (2012), arXiv:1209.4533 [hep-ex].

[93] **CMS**, S. Chatrchyan et al., "*Measurement of Differential Top-Quark Pair Production Cross Sections in pp collisions at* $\sqrt{s} = 7$ *TeV*", Eur. Phys. J. C **73**, 2339 (2013), arXiv:1211.2220 [hep-ex].

[94] **CMS**, S. Chatrchyan et al., "*Measurement of the* $t\bar{t}$ *Production Cross Section in the* τ *+Jets Channel in pp Collisions at* $\sqrt{s} = 7$ *TeV*", Eur. Phys. J. C **73**, 2386 (2013), arXiv:1301.5755 [hep-ex].

[95] **CMS**, S. Chatrchyan et al., "*Measurement of the* $t\bar{t}$ *Production Cross Section in the All-Jet Final State in pp Collisions at* $\sqrt{s} = 7$ *TeV*", JHEP **05**, 065 (2013), arXiv:1302.0508 [hep-ex].

[96] **CMS**, S. Chatrchyan et al., "*Measurement of the W-Boson Helicity in Top-Quark decays from* $t\bar{t}$ *Production in Lepton + Jets Events in pp Collisions at* $\sqrt{s} = 7$ *TeV*", JHEP **10**, 167 (2013), arXiv:1308.3879 [hep-ex].

[97] **CMS**, S. Chatrchyan et al., "*Measurements of the $t\bar{t}$ charge asymmetry using the dilepton decay channel in pp collisions at $\sqrt{s}$ = 7 TeV*", JHEP **04**, 191 (2014), arXiv:1402.3803 [hep-ex].

[98] **CMS**, V. Khachatryan et al., "*Measurement of the t-channel single-top-quark production cross section and of the $\mid V_{tb} \mid$ CKM matrix element in pp collisions at $\sqrt{s}$= 8 TeV*", JHEP **06**, 090 (2014), arXiv:1403.7366 [hep-ex].

[99] **CMS**, V. Khachatryan et al., "*Measurement of the differential cross section for top quark pair production in pp collisions at $\sqrt{s} = 8$ TeV*", Eur. Phys. J. C **75**, 542 (2015), arXiv:1505.04480 [hep-ex].

[100] **CMS**, V. Khachatryan et al., "*Observation of top quark pairs produced in association with a vector boson in pp collisions at $\sqrt{s} = 8$ TeV*", JHEP **01**, 096 (2016), arXiv:1510.01131 [hep-ex].

[101] **CMS**, V. Khachatryan et al., "*Measurement of Top Quark Polarisation in T-Channel Single Top Quark Production*", JHEP **04**, 073 (2016), arXiv:1511.02138 [hep-ex].

[102] **CMS**, V. Khachatryan et al., "*Measurements of t t-bar spin correlations and top quark polarization using dilepton final states in pp collisions at sqrt(s) = 8 TeV*", Phys. Rev. D **93**, 052007 (2016), arXiv:1601.01107 [hep-ex].

[103] **CMS**, V. Khachatryan et al., "*Measurements of the* $\mathrm{t\bar{t}}$ *production cross section in lepton+jets final states in pp collisions at 8 TeV and ratio of 8 to 7 TeV cross sections*", Eur. Phys. J. C **77**, 15 (2017), arXiv:1602.09024 [hep-ex].

[104] **CMS**, V. Khachatryan et al., "*Measurement of the t-tbar production cross section in the e-mu channel in proton-proton collisions at sqrt(s) = 7 and 8 TeV*", JHEP **08**, 029 (2016), arXiv:1603.02303 [hep-ex].

[105] **CMS**, V. Khachatryan et al., "*Measurements of $t\bar{t}$ charge asymmetry using dilepton final states in pp collisions at $\sqrt{s} = 8$ TeV*", Phys. Lett. B **760**, 365–386 (2016), arXiv:1603.06221 [hep-ex].

[106] **CMS**, V. Khachatryan et al., "*Measurement of the W boson helicity fractions in the decays of top quark pairs to lepton + jets final states produced in pp collisions at $\sqrt{s}$ = 8TeV*", Phys. Lett. B **762**, 512–534 (2016), arXiv:1605.09047 [hep-ex].

[107] **CMS**, A. M. Sirunyan et al., "*Measurement of the $t\bar{t}$ production cross section using events with one lepton and at least one jet in pp collisions at $\sqrt{s}$ = 13 TeV*", JHEP **09**, 051 (2017), arXiv:1701.06228 [hep-ex].

[108] **CMS**, A. M. Sirunyan et al., "*Measurement of double-differential cross sections for top quark pair production in pp collisions at $\sqrt{s} = 8$ TeV and impact on parton distribution functions*", Eur. Phys. J. C **77**, 459 (2017), arXiv:1703.01630 [hep-ex].

[109] **CMS**, A. M. Sirunyan et al., "*Measurement of normalized differential* $\mathrm{t\bar{t}}$ *cross sections in the dilepton channel from pp collisions at $\sqrt{s} = 13$ TeV*", JHEP **04**, 060 (2018), arXiv:1708.07638 [hep-ex].

[110] **CMS**, A. M. Sirunyan et al., "*Measurement of the cross section for top quark pair production in association with a W or Z boson in proton-proton collisions at $\sqrt{s}$ = 13 TeV*", JHEP **08**, 011 (2018), arXiv:1711.02547 [hep-ex].

[111] **CMS**, A. M. Sirunyan et al., "*Measurement of the production cross section for single top quarks in association with W bosons in proton-proton collisions at $\sqrt{s} = 13$ TeV*", JHEP **10**, 117 (2018), arXiv:1805.07399 [hep-ex].

[112] **CMS**, A. M. Sirunyan et al., "*Measurements of* $\mathrm{t\bar{t}}$ *differential cross sections in proton-proton collisions at $\sqrt{s}$ = 13 TeV using events containing two leptons*", JHEP **02**, 149 (2019), arXiv:1811.06625 [hep-ex].

[113] **CMS**, A. M. Sirunyan et al., "*Observation of Single Top Quark Production in Association with a Z Boson in Proton-Proton Collisions at $\sqrt{s}$ =13 TeV*", Phys. Rev. Lett. **122**, 132003 (2019), arXiv:1812.05900 [hep-ex].

[114] **CMS**, A. M. Sirunyan et al., "*Measurement of the* $\mathrm{t\bar{t}}$ *production cross section, the top quark mass, and the strong coupling constant using dilepton events in pp collisions at $\sqrt{s}$ = 13 TeV*", Eur. Phys. J. C **79**, 368 (2019), arXiv:1812.10505 [hep-ex].

[115] **CMS**, A. M. Sirunyan et al., "*Measurement of the single top quark and antiquark production cross sections in the t channel and their ratio in proton-proton collisions at $\sqrt{s}$ = 13 TeV*", Phys. Lett. B **800**, 135042 (2020), arXiv:1812.10514 [hep-ex].

[116] **CMS**, A. M. Sirunyan et al., "*Measurement of* tt *normalised multi-differential cross sections in pp collisions at $\sqrt{s} = 13$ TeV, and simultaneous determination*

of the strong coupling strength, top quark pole mass, and parton distribution functions", Eur. Phys. J. C **80**, 658 (2020), arXiv:1904.05237 [hep-ex].

[117] **CMS**, A. M. Sirunyan et al., "*Measurement of the top quark polarization and* tt *spin correlations using dilepton final states in proton-proton collisions at $\sqrt{s}$ = 13 TeV*", Phys. Rev. D **100**, 072002 (2019), arXiv:1907.03729 [hep-ex].

[118] **CMS**, A. M. Sirunyan et al., "*Measurement of top quark pair production in association with a Z boson in proton-proton collisions at $\sqrt{s} = 13$ TeV*", (2019), arXiv:1907.11270 [hep-ex].

[119] **D0**, V. M. Abazov et al., "*Measurement of the W Boson Helicity in Top Quark Decays using 5.4 fb^{-1} of $p\bar{p}$ Collision Data*", Phys. Rev. D **83**, 032009 (2011), arXiv:1011.6549 [hep-ex].

[120] **D0**, V. M. Abazov et al., "*An Improved determination of the width of the top quark*", Phys. Rev. D **85**, 091104 (2012), arXiv:1201.4156 [hep-ex].

[121] **D0**, V. M. Abazov et al., "*Measurement of the Asymmetry in Angular Distributions of Leptons Produced in Dilepton $t\bar{t}$ Final States in $p\bar{p}$ Collisions at $\sqrt{s}$=1.96 TeV*", Phys. Rev. D **88**, 112002 (2013), arXiv:1308.6690 [hep-ex].

[122] **D0**, V. M. Abazov et al., "*Measurement of differential $t\bar{t}$ production cross sections in $p\bar{p}$ collisions*", Phys. Rev. D **90**, 092006 (2014), arXiv:1401.5785 [hep-ex].

[123] **D0**, V. M. Abazov et al., "*Measurement of the Forward-Backward Asymmetry in Top Quark-Antiquark Production in $p\bar{p}$ Collisions using the Lepton+Jets Channel*", Phys. Rev. D **90**, 072011 (2014), arXiv:1405.0421 [hep-ex].

[124] **D0**, V. M. Abazov et al., "*Measurement of the Inclusive $t\bar{t}$ Production Cross Section in $p\bar{p}$ Collisions at $\sqrt{s} = 1.96$ TeV and Determination of the Top Quark Pole Mass*", Phys. Rev. D **94**, 092004 (2016), arXiv:1605.06168 [hep-ex].

[125] F. Krauss, S. Kuttimalai, and T. Plehn, "*LHC multijet events as a probe for anomalous dimension-six gluon interactions*", Phys. Rev. D **95**, 035024 (2017).

[126] V. Hirschi, F. Maltoni, I. Tsinikos, and E. Vryonidou, "*Constraining anomalous gluon self-interactions at the LHC: a reappraisal*", Journal of High Energy Physics **2018**, 10.1007/jhep07(2018)093 (2018).

[127] C. Degrande, G. Durieux, F. Maltoni, K. Mimasu, E. Vryonidou, and C. Zhang, "*Automated one-loop computations in the standard model effective field theory*", Phys. Rev. D **103**, 096024 (2021), arXiv:2008.11743 [hep-ph].

[128] M. Aliev, H. Lacker, U. Langenfeld, S. Moch, P. Uwer, and M. Wiedermann, "*HATHOR: HAdronic Top and Heavy quarks crOss section calculatoR*", Comput. Phys. Commun. **182**, 1034–1046 (2011), arXiv:1007.1327 [hep-ph].

[129] A. Buckley, C. Englert, J. Ferrando, D. J. Miller, L. Moore, M. Russell, and C. D. White, "*Global fit of top quark effective theory to data*", Phys. Rev. **D92**, 091501 (2015), arXiv:1506.08845 [hep-ph].

[130] A. Buckley, C. Englert, J. Ferrando, D. J. Miller, L. Moore, M. Russell, and C. D. White, "*Constraining top quark effective theory in the LHC Run II era*", JHEP **04**, 015 (2016), arXiv:1512.03360 [hep-ph].

[131] J. Butterworth et al., "*PDF4LHC recommendations for LHC Run II*", J. Phys. **G43**, 023001 (2016), arXiv:1510.03865 [hep-ph].

[132] N. P. Hartland, F. Maltoni, E. R. Nocera, J. Rojo, E. Slade, E. Vryonidou, and C. Zhang, "*A Monte Carlo global analysis of the Standard Model Effective Field Theory: the top quark sector*", JHEP **04**, 100 (2019), arXiv:1901.05965 [hep-ph].

[133] D. Barducci et al., "*Interpreting top-quark LHC measurements in the standard-model effective field theory*", edited by J. A. Aguilar-Saavedra, C. Degrande, G. Durieux, F. Maltoni, E. Vryonidou, and C. Zhang (2018), arXiv:1802.07237 [hep-ph].

[134] R. Contino, "*The Higgs as a Composite Nambu-Goldstone Boson*", in *Physics of the large and the small, TASI 09, proceedings of the Theoretical Advanced Study Institute in Elementary Particle Physics, Boulder, Colorado, USA, 1-26 June 2009* (2011), pp. 235–306, arXiv:1005.4269 [hep-ph].

[135] G. Panico and A. Wulzer, "*The Composite Nambu-Goldstone Higgs*", Lect. Notes Phys. **913**, pp.1–316 (2016), arXiv:1506.01961 [hep-ph].

[136] S. Dawson, C. Englert, and T. Plehn, "*Higgs Physics: It ain't over till it's over*", Phys. Rept. **816**, 1–85 (2019), arXiv:1808.01324 [hep-ph].

[137] G. Cacciapaglia, C. Pica, and F. Sannino, "*Fundamental Composite Dynamics: A Review*", (2020), arXiv:2002.04914 [hep-ph].

[138] **FCC**, A. Abada et al., "*FCC-hh: The Hadron Collider*", Eur. Phys. J. ST **228**, 755–1107 (2019).

[139] K. Agashe, R. Contino, and R. Sundrum, "*Top compositeness and precision unification*", Phys. Rev. Lett. **95**, 171804 (2005), arXiv:hep-ph/0502222 [hep-ph].

[140] K. Kumar, T. M. P. Tait, and R. Vega-Morales, "*Manifestations of Top Compositeness at Colliders*", JHEP **05**, 022 (2009), arXiv:0901.3808 [hep-ph].

[141] G. Ferretti and D. Karateev, "*Fermionic UV completions of Composite Higgs models*", JHEP **03**, 077 (2014), arXiv:1312.5330 [hep-ph].

[142] G. Ferretti, "*Gauge theories of Partial Compositeness: Scenarios for Run-II of the LHC*", JHEP **06**, 107 (2016), arXiv:1604.06467 [hep-ph].

[143] R. Contino, Y. Nomura, and A. Pomarol, "*Higgs as a holographic pseudo-Goldstone boson*", Nucl. Phys. **B671**, 148–174 (2003), arXiv:hep-ph/0306259 [hep-ph].

[144] K. Agashe, R. Contino, and A. Pomarol, "*The Minimal composite Higgs model*", Nucl. Phys. **B719**, 165–187 (2005), arXiv:hep-ph/0412089 [hep-ph].

[145] R. Contino, L. Da Rold, and A. Pomarol, "*Light custodians in natural composite Higgs models*", Phys. Rev. **D75**, 055014 (2007), arXiv:hep-ph/0612048 [hep-ph].

[146] B. Bellazzini, C. Csáki, and J. Serra, "*Composite Higgses*", Eur. Phys. J. **C74**, 2766 (2014), arXiv:1401.2457 [hep-ph].

[147] D. Marzocca, M. Serone, and J. Shu, "*General Composite Higgs Models*", JHEP **08**, 013 (2012), arXiv:1205.0770 [hep-ph].

[148] A. Pomarol and F. Riva, "*The Composite Higgs and Light Resonance Connection*", JHEP **08**, 135 (2012), arXiv:1205.6434 [hep-ph].

[149] M. Redi and A. Tesi, "*Implications of a Light Higgs in Composite Models*", JHEP **10**, 166 (2012), arXiv:1205.0232 [hep-ph].

[150] H. Terazawa, K. Akama, and Y. Chikashige, "*Unified Model of the Nambu-Jona-Lasinio Type for All Elementary Particle Forces*", Phys. Rev. **D15**, 480 (1977).

[151] H. Terazawa, "*t quark mass predicted from a sum rule for lepton and quark masses*", Phys. Rev. **D22**, [Erratum: Phys. Rev.D41,3541(1990)], 2921–2921 (1980).

[152] D. B. Kaplan, "*Flavor at SSC energies: A New mechanism for dynamically generated fermion masses*", Nucl. Phys. **B365**, 259–278 (1991).

[153] R. Contino, T. Kramer, M. Son, and R. Sundrum, "*Warped/composite phenomenology simplified*", JHEP **05**, 074 (2007), arXiv:hep-ph/0612180 [hep-ph].

[154] M. Golterman and Y. Shamir, "*Top quark induced effective potential in a composite Higgs model*", Phys. Rev. **D91**, 094506 (2015), arXiv:1502.00390 [hep-ph].

[155] L. Del Debbio, C. Englert, and R. Zwicky, "*A UV Complete Compositeness Scenario: LHC Constraints Meet The Lattice*", JHEP **08**, 142 (2017), arXiv:1703.06064 [hep-ph].

[156] M. Gillioz, R. Grober, C. Grojean, M. Muhlleitner, and E. Salvioni, "*Higgs Low-Energy Theorem (and its corrections) in Composite Models*", JHEP **10**, 004 (2012), arXiv:1206.7120 [hep-ph].

[157] A. Hietanen, R. Lewis, C. Pica, and F. Sannino, "*Fundamental Composite Higgs Dynamics on the Lattice: SU(2) with Two Flavors*", JHEP **07**, 116 (2014), arXiv:1404.2794 [hep-lat].

[158] T. DeGrand, Y. Liu, E. T. Neil, Y. Shamir, and B. Svetitsky, "*Spectroscopy of SU(4) gauge theory with two flavors of sextet fermions*", Phys. Rev. **D91**, 114502 (2015), arXiv:1501.05665 [hep-lat].

[159] V. Ayyar, T. DeGrand, M. Golterman, D. C. Hackett, W. I. Jay, E. T. Neil, Y. Shamir, and B. Svetitsky, "*Spectroscopy of SU(4) composite Higgs theory with two distinct fermion representations*", Phys. Rev. **D97**, 074505 (2018), arXiv:1710.00806 [hep-lat].

[160] V. Ayyar, T. Degrand, D. C. Hackett, W. I. Jay, E. T. Neil, Y. Shamir, and B. Svetitsky, "*Baryon spectrum of SU(4) composite Higgs theory with two distinct fermion representations*", Phys. Rev. **D97**, 114505 (2018), arXiv:1801.05809 [hep-ph].

[161] V. Ayyar, T. DeGrand, D. C. Hackett, W. I. Jay, E. T. Neil, Y. Shamir, and B. Svetitsky, "*Partial compositeness and baryon matrix elements on the lattice*", Phys. Rev. **D99**, 094502 (2019), arXiv:1812.02727 [hep-ph].

[162] T. DeGrand and E. T. Neil, "*Repurposing lattice QCD results for composite phenomenology*", Phys. Rev. **D101**, 034504 (2020), arXiv:1910.08561 [hep-ph].

[163] S. R. Coleman, J. Wess, and B. Zumino, "*Structure of phenomenological Lagrangians. 1.*", Phys. Rev. **177**, 2239–2247 (1969).

[164] C. G. Callan Jr., S. R. Coleman, J. Wess, and B. Zumino, "*Structure of phenomenological Lagrangians. 2.*", Phys. Rev. **177**, 2247–2250 (1969).

[165] G. Ferretti, "*UV Completions of Partial Compositeness: The Case for a SU(4) Gauge Group*", JHEP **06**, 142 (2014), arXiv:1404.7137 [hep-ph].

[166] G. Cacciapaglia and F. Sannino, "*An Ultraviolet Chiral Theory of the Top for the Fundamental Composite (Goldstone) Higgs*", Phys. Lett. **B755**, 328–331 (2016), arXiv:1508.00016 [hep-ph].

[167] M. Golterman and Y. Shamir, "*Effective potential in ultraviolet completions for composite Higgs models*", Phys. Rev. **D97**, 095005 (2018), arXiv:1707.06033 [hep-ph].

[168] T. A. DeGrand, M. Golterman, W. I. Jay, E. T. Neil, Y. Shamir, and B. Svetitsky, "*Radiative contribution to the effective potential in composite Higgs models from lattice gauge theory*", Phys. Rev. **D94**, 054501 (2016), arXiv:1606.02695 [hep-lat].

[169] A. Belyaev, G. Cacciapaglia, H. Cai, G. Ferretti, T. Flacke, A. Parolini, and H. Serodio, "*Di-boson signatures as Standard Candles for Partial Compositeness*", JHEP **01**, [Erratum: JHEP12,088(2017)], 094 (2017), arXiv:1610.06591 [hep-ph].

[170] C. Englert, P. Schichtel, and M. Spannowsky, "*Same-sign W pair production in composite Higgs models*", Phys. Rev. **D95**, 055002 (2017), arXiv:1610.07354 [hep-ph].

[171] P. Ko, C. Yu, and T.-C. Yuan, "*Probing a new strongly interacting sector via composite diboson resonances*", Phys. Rev. **D95**, 115034 (2017), arXiv:1603.08802 [hep-ph].

[172] F. Sannino, A. Strumia, A. Tesi, and E. Vigiani, "*Fundamental partial compositeness*", JHEP **11**, 029 (2016), arXiv:1607.01659 [hep-ph].

[173] G. Cacciapaglia, H. Gertov, F. Sannino, and A. E. Thomsen, "*Minimal Fundamental Partial Compositeness*", Phys. Rev. **D98**, 015006 (2018), arXiv:1704.07845 [hep-ph].

[174] A. De Simone, O. Matsedonskyi, R. Rattazzi, and A. Wulzer, "*A First Top Partner Hunter's Guide*", JHEP **04**, 004 (2013), arXiv:1211.5663 [hep-ph].

[175] K. Agashe, R. Contino, L. Da Rold, and A. Pomarol, "*A Custodial symmetry for $Zb\bar{b}$*", Phys. Lett. **B641**, 62–66 (2006), arXiv:hep-ph/0605341 [hep-ph].

[176] J. M. Cline, "*B decay anomalies and dark matter from vectorlike confinement*", Phys. Rev. **D97**, 015013 (2018), arXiv:1710.02140 [hep-ph].

[177] **CDF, D0**, T. A. Aaltonen et al., "*Tevatron Combination of Single-Top-Quark Cross Sections and Determination of the Magnitude of the Cabibbo-Kobayashi-Maskawa Matrix Element* $\mathbf{V_{tb}}$", Phys. Rev. Lett. **115**, 152003 (2015), arXiv:1503.05027 [hep-ex].

[178] **ATLAS**, G. Aad et al., "*Comprehensive measurements of t-channel single top-quark production cross sections at $\sqrt{s} = 7$ TeV with the ATLAS detector*", Phys. Rev. **D90**, 112006 (2014), arXiv:1406.7844 [hep-ex].

[179] **ATLAS, CMS**, M. Aaboud et al., "*Combinations of single-top-quark production cross-section measurements and $|f_{\rm LV}V_{tb}|$ determinations at $\sqrt{s} = 7$ and 8 TeV with the ATLAS and CMS experimentsCombinations of single-top-quark production cross-section measurements and $|f_{LV}\, V_{tb}|$ determinations at $\sqrt{s} =$ 7 and 8 TeV with the ATLAS and CMS experiments*", JHEP **05**, 088 (2019), arXiv:1902.07158 [hep-ex].

[180] **ATLAS**, M. Aaboud et al., "*Measurement of the inclusive cross-sections of single top-quark and top-antiquark t-channel production in pp collisions at $\sqrt{s}$ = 13 TeV with the ATLAS detector*", JHEP **04**, 086 (2017), arXiv:1609.03920 [hep-ex].

[181] **CMS**, A. M. Sirunyan et al., "*Measurement of the single top quark and antiquark production cross sections in the t channel and their ratio in proton-proton collisions at $\sqrt{s}$ = 13 TeV*", Phys. Lett. **B800**, 135042 (2020), arXiv:1812.10514 [hep-ex].

[182] **ATLAS**, M. Aaboud et al., "*Measurement of the cross-section for producing a W boson in association with a single top quark in pp collisions at* $\sqrt{s} = 13$ *TeV with ATLAS*", JHEP **01**, 063 (2018), arXiv:1612.07231 [hep-ex].

[183] **CMS**, A. M. Sirunyan et al., "*Measurement of the production cross section for single top quarks in association with W bosons in proton-proton collisions at* $\sqrt{s} = 13$ *TeV*", JHEP **10**, 117 (2018), arXiv:1805.07399 [hep-ex].

[184] **ATLAS**, M. Aaboud et al., "*Measurement of the production cross-section of a single top quark in association with a Z boson in proton–proton collisions at 13 TeV with the ATLAS detector*", Phys. Lett. **B780**, 557–577 (2018), arXiv:1710.03659 [hep-ex].

[185] **CMS**, A. M. Sirunyan et al., "*Observation of Single Top Quark Production in Association with a Z Boson in Proton-Proton Collisions at* $\sqrt{s}$ *=13 TeV*", Phys. Rev. Lett. **122**, 132003 (2019), arXiv:1812.05900 [hep-ex].

[186] **ATLAS**, G. Aad et al., "*Measurement of the* $t\bar{t}W$ *and* $t\bar{t}Z$ *production cross sections in pp collisions at* $\sqrt{s} = 8$ *TeV with the ATLAS detector*", JHEP **11**, 172 (2015), arXiv:1509.05276 [hep-ex].

[187] **CMS**, V. Khachatryan et al., "*Observation of top quark pairs produced in association with a vector boson in pp collisions at* $\sqrt{s} = 8$ *TeV*", JHEP **01**, 096 (2016), arXiv:1510.01131 [hep-ex].

[188] **ATLAS**, M. Aaboud et al., "*Measurement of the* $t\bar{t}Z$ *and* $t\bar{t}W$ *cross sections in proton-proton collisions at* $\sqrt{s} = 13$ *TeV with the ATLAS detector*", Phys. Rev. **D99**, 072009 (2019), arXiv:1901.03584 [hep-ex].

[189] **CDF**, T. Aaltonen et al., "*Measurement of W-Boson Polarization in Top-quark Decay using the Full CDF Run II Data Set*", Phys. Rev. **D87**, 031104 (2013), arXiv:1211.4523 [hep-ex].

[190] **ATLAS**, G. Aad et al., "*Measurement of the W boson polarization in top quark decays with the ATLAS detector*", JHEP **06**, 088 (2012), arXiv:1205.2484 [hep-ex].

[191] **CMS**, S. Chatrchyan et al., "*Measurement of the W-Boson Helicity in Top-Quark decays from* $t\bar{t}$ *Production in Lepton + Jets Events in pp Collisions at* $\sqrt{s} = 7$ *TeV*", JHEP **10**, 167 (2013), arXiv:1308.3879 [hep-ex].

[192] **ATLAS**, M. Aaboud et al., “*Measurement of the W boson polarisation in $t\bar{t}$ events from pp collisions at $\sqrt{s}$ = 8 TeV in the lepton + jets channel with ATLAS*”, Eur. Phys. J. **C77**, [Erratum: Eur. Phys. J.C79,no.1,19(2019)], 264 (2017), arXiv:1612.02577 [hep-ex].

[193] **D0**, V. M. Abazov et al., “*An Improved determination of the width of the top quark*”, Phys. Rev. **D85**, 091104 (2012), arXiv:1201.4156 [hep-ex].

[194] **CDF**, T. A. Aaltonen et al., “*Direct Measurement of the Total Decay Width of the Top Quark*”, Phys. Rev. Lett. **111**, 202001 (2013), arXiv:1308.4050 [hep-ex].

[195] **ATLAS**, M. Aaboud et al., “*Direct top-quark decay width measurement in the $t\bar{t}$ lepton+jets channel at $\sqrt{s}$=8 TeV with the ATLAS experiment*”, Eur. Phys. J. **C78**, 129 (2018), arXiv:1709.04207 [hep-ex].

[196] **CMS**, A. M. Sirunyan et al., “*Projected performance of Higgs analyses at the HL-LHC for ECFA 2016*”, (2017), eprint: CMS-PAS-FTR-16-002.

[197] A. Efrati, A. Falkowski, and Y. Soreq, “*Electroweak constraints on flavorful effective theories*”, JHEP **07**, 018 (2015), arXiv:1503.07872 [hep-ph].

[198] M. Redi and A. Weiler, “*Flavor and CP Invariant Composite Higgs Models*”, JHEP **11**, 108 (2011), arXiv:1106.6357 [hep-ph].

[199] M. Redi, “*Composite MFV and Beyond*”, Eur. Phys. J. **C72**, 2030 (2012), arXiv:1203.4220 [hep-ph].

[200] O. Matsedonskyi, G. Panico, and A. Wulzer, “*Light Top Partners for a Light Composite Higgs*”, JHEP **01**, 164 (2013), arXiv:1204.6333 [hep-ph].

[201] “*Addendum to the report on the physics at the HL-LHC, and perspectives for the HE-LHC: Collection of notes from ATLAS and CMS*”, CERN Yellow Rep. Monogr. **7**, Addendum (2019), arXiv:1902.10229 [hep-ex].

[202] “*Perspectives on the determination of systematic uncertainties at HL-LHC*”, Workshop on the physics of HL-LHC, and perspectives at HE-LHC, 2018.

[203] N. Castro, J. Erdmann, C. Grunwald, K. Kröninger, and N.-A. Rosien, “*EFTfitter—A tool for interpreting measurements in the context of effective field theories*”, Eur. Phys. J. C **76**, 432 (2016), arXiv:1605.05585 [hep-ex].

[204] G. Durieux, M. Perelló, M. Vos, and C. Zhang, “*Global and optimal probes for the top-quark effective field theory at future lepton colliders*”, JHEP **10**, 168 (2018), arXiv:1807.02121 [hep-ph].

[205] D. Barducci et al., "*Interpreting top-quark LHC measurements in the standard-model effective field theory*", edited by J. A. Aguilar-Saavedra, C. Degrande, G. Durieux, F. Maltoni, E. Vryonidou, and C. Zhang (2018), arXiv:1802.07237 [hep-ph].

[206] I. Brivio, S. Bruggisser, F. Maltoni, R. Moutafis, T. Plehn, E. Vryonidou, S. Westhoff, and C. Zhang, "*O new physics, where art thou? A global search in the top sector*", JHEP **02**, 131 (2020), arXiv:1910.03606 [hep-ph].

[207] G. Durieux, A. Irles, V. Miralles, A. Peñuelas, R. Pöschl, M. Perelló, and M. Vos, "*The electro-weak couplings of the top and bottom quarks — Global fit and future prospects*", JHEP **12**, [Erratum: JHEP 01, 195 (2021)], 98 (2019), arXiv:1907.10619 [hep-ph].

[208] **FCC**, A. Abada et al., "*FCC Physics Opportunities: Future Circular Collider Conceptual Design Report Volume 1*", Eur. Phys. J. C **79**, 474 (2019).

[209] J. Reuter and M. Tonini, "*Top Partner Discovery in the $T \to tZ$ channel at the LHC*", JHEP **01**, 088 (2015), arXiv:1409.6962 [hep-ph].

[210] **ATLAS**, M. Aaboud et al., "*Observation of Higgs boson production in association with a top quark pair at the LHC with the ATLAS detector*", Phys. Lett. **B784**, 173–191 (2018), arXiv:1806.00425 [hep-ex].

[211] **ATLAS**, G. Aad et al., "*Search for $t\bar{t}$ resonances in fully hadronic final states in pp collisions at $\sqrt{s} = 13$ TeV with the ATLAS detector*", (2020), arXiv:2005.05138 [hep-ex].

[212] G. Louppe, M. Kagan, and K. Cranmer, "*Learning to Pivot with Adversarial Networks*", (2016), arXiv:1611.01046 [stat.ML].

[213] J. Brehmer, K. Cranmer, G. Louppe, and J. Pavez, "*Constraining Effective Field Theories with Machine Learning*", Phys. Rev. Lett. **121**, 111801 (2018), arXiv:1805.00013 [hep-ph].

[214] J. Brehmer, K. Cranmer, G. Louppe, and J. Pavez, "*A Guide to Constraining Effective Field Theories with Machine Learning*", Phys. Rev. D **98**, 052004 (2018), arXiv:1805.00020 [hep-ph].

[215] C. Englert, P. Galler, P. Harris, and M. Spannowsky, "*Machine Learning Uncertainties with Adversarial Neural Networks*", Eur. Phys. J. C **79**, 4 (2019), arXiv:1807.08763 [hep-ph].

[216] Q.-H. Cao, B. Yan, C. P. Yuan, and Y. Zhang, "*Probing $Zt\bar{t}$ couplings using Z boson polarization in ZZ production at hadron colliders*", Phys. Rev. D **102**, 055010 (2020), arXiv:2004.02031 [hep-ph].

[217] N. D. Christensen and C. Duhr, "*FeynRules - Feynman rules made easy*", Comput. Phys. Commun. **180**, 1614–1641 (2009), arXiv:0806.4194 [hep-ph].

[218] A. Alloul, N. D. Christensen, C. Degrande, C. Duhr, and B. Fuks, "*FeynRules 2.0 - A complete toolbox for tree-level phenomenology*", Comput. Phys. Commun. **185**, 2250–2300 (2014), arXiv:1310.1921 [hep-ph].

[219] P. de Aquino, W. Link, F. Maltoni, O. Mattelaer, and T. Stelzer, "*ALOHA: Automatic Libraries Of Helicity Amplitudes for Feynman Diagram Computations*", Comput. Phys. Commun. **183**, 2254–2263 (2012), arXiv:1108.2041 [hep-ph].

[220] S. Frixione, E. Laenen, P. Motylinski, and B. R. Webber, "*Angular correlations of lepton pairs from vector boson and top quark decays in Monte Carlo simulations*", JHEP **04**, 081 (2007), arXiv:hep-ph/0702198 [HEP-PH].

[221] M. Dobbs and J. B. Hansen, "*The HepMC C++ Monte Carlo event record for High Energy Physics*", Comput. Phys. Commun. **134**, 41–46 (2001).

[222] M. Cacciari, G. P. Salam, and G. Soyez, "*FastJet User Manual*", Eur. Phys. J. **C72**, 1896 (2012), arXiv:1111.6097 [hep-ph].

[223] M. Cacciari and G. P. Salam, "*Dispelling the N^3 myth for the k_t jet-finder*", Phys. Lett. **B641**, 57–61 (2006), arXiv:hep-ph/0512210 [hep-ph].

[224] T. Plehn, M. Spannowsky, M. Takeuchi, and D. Zerwas, "*Stop Reconstruction with Tagged Tops*", JHEP **10**, 078 (2010), arXiv:1006.2833 [hep-ph].

[225] G. Kasieczka, T. Plehn, T. Schell, T. Strebler, and G. P. Salam, "*Resonance Searches with an Updated Top Tagger*", JHEP **06**, 203 (2015), arXiv:1503.05921 [hep-ph].

[226] T. Plehn, G. P. Salam, and M. Spannowsky, "*Fat Jets for a Light Higgs*", Phys. Rev. Lett. **104**, 111801 (2010), arXiv:0910.5472 [hep-ph].

[227] M. Cacciari, G. P. Salam, and G. Soyez, "*The anti-k_t jet clustering algorithm*", JHEP **04**, 063 (2008), arXiv:0802.1189 [hep-ph].

[228] T. Golling et al., "*Physics at a 100 TeV pp collider: beyond the Standard Model phenomena*", CERN Yellow Rep., 441–634 (2017), arXiv:1606.00947 [hep-ph].

[229] O. Matsedonskyi, G. Panico, and A. Wulzer, "*On the Interpretation of Top Partners Searches*", JHEP **12**, 097 (2014), arXiv:1409.0100 [hep-ph].

[230] D. Barducci, M. Fabbrichesi, and A. Tonero, "*Constraints on top quark nonstandard interactions from Higgs and $t\bar{t}$ production cross sections*", Phys. Rev. **D96**, 075022 (2017), arXiv:1704.05478 [hep-ph].

[231] H.-L. Li, L.-X. Xu, J.-H. Yu, and S.-H. Zhu, "*EFTs meet Higgs Nonlinearity, Compositeness and (Neutral) Naturalness*", JHEP **09**, 010 (2019), arXiv:1904.05359 [hep-ph].

[232] A. Azatov, M. Salvarezza, M. Son, and M. Spannowsky, "*Boosting Top Partner Searches in Composite Higgs Models*", Phys. Rev. **D89**, 075001 (2014), arXiv:1308.6601 [hep-ph].

[233] **CMS**, A. M. Sirunyan et al., "*Search for top quark partners with charge 5/3 in the same-sign dilepton and single-lepton final states in proton-proton collisions at $\sqrt{s} = 13$ TeV*", JHEP **03**, 082 (2019), arXiv:1810.03188 [hep-ex].

[234] C. Englert and M. Russell, "*Top quark electroweak couplings at future lepton colliders*", Eur. Phys. J. **C77**, 535 (2017), arXiv:1704.01782 [hep-ph].

[235] A. Escamilla, A. O. Bouzas, and F. Larios, "*Single top production at linear e^-e^+ colliders*", Phys. Rev. **D97**, 033004 (2018), arXiv:1712.02763 [hep-ph].

[236] **CLICdp, ILC Physics Study**, N. van der Kolk, "*Toward Precision Top Quark Measurements in e^+e^- Collisions at Linear Colliders*", PoS **EPS-HEP2017**, 470 (2017).

[237] M. Boronat, E. Fullana, J. Fuster, P. Gomis, A. Hoang, V. Mateu, M. Vos, and A. Widl, "*Top quark mass measurement in radiative events at electron-positron colliders*", Phys. Lett. **B804**, 135353 (2020), arXiv:1912.01275 [hep-ph].

[238] **CLICdp**, H. Abramowicz et al., "*Top-Quark Physics at the CLIC Electron-Positron Linear Collider*", JHEP **11**, 003 (2019), arXiv:1807.02441 [hep-ex].

[239] J. Brehmer, F. Kling, T. Plehn, and T. M. P. Tait, "*Better Higgs-CP Tests Through Information Geometry*", Phys. Rev. D **97**, 095017 (2018), arXiv:1712.02350 [hep-ph].

[240] C. W. Bauer, M. Freytsis, and B. Nachman, "*Simulating Collider Physics on Quantum Computers Using Effective Field Theories*", Phys. Rev. Lett. **127**, 212001 (2021), arXiv:2102.05044 [hep-ph].

[241] M. Feickert and B. Nachman, "*A Living Review of Machine Learning for Particle Physics*", (2021), arXiv:2102.02770 [hep-ph].

[242] J. Brehmer, K. Cranmer, F. Kling, and T. Plehn, "*Better Higgs boson measurements through information geometry*", Phys. Rev. D **95**, 073002 (2017), arXiv:1612.05261 [hep-ph].

[243] J. D'Hondt, A. Mariotti, K. Mimasu, S. Moortgat, and C. Zhang, "*Learning to pinpoint effective operators at the LHC: a study of the* $\mathrm{t\bar{t}b\bar{b}}$ *signature*", JHEP **11**, 131 (2018), arXiv:1807.02130 [hep-ph].

[244] S. Chatterjee, N. Frohner, L. Lechner, R. Schöfbeck, and D. Schwarz, "*Tree boosting for learning EFT parameters*", (2021), arXiv:2107.10859 [hep-ph].

[245] J. Y. Araz and M. Spannowsky, "*Combine and Conquer: Event Reconstruction with Bayesian Ensemble Neural Networks*", JHEP **04**, 296 (2021), arXiv:2102.01078 [hep-ph].

[246] P. Konar, V. S. Ngairangbam, and M. Spannowsky, "*Energy-weighted Message Passing: an infra-red and collinear safe graph neural network algorithm*", (2021), arXiv:2109.14636 [hep-ph].

[247] G. Karagiorgi, G. Kasieczka, S. Kravitz, B. Nachman, and D. Shih, "*Machine Learning in the Search for New Fundamental Physics*", (2021), arXiv:2112.03769 [hep-ph].

[248] E. A. Moreno, O. Cerri, J. M. Duarte, H. B. Newman, T. Q. Nguyen, A. Periwal, M. Pierini, A. Serikova, M. Spiropulu, and J.-R. Vlimant, "*JEDI-net: a jet identification algorithm based on interaction networks*", Eur. Phys. J. C **80**, 58 (2020), arXiv:1908.05318 [hep-ex].

[249] J. Pata, J. Duarte, J.-R. Vlimant, M. Pierini, and M. Spiropulu, "*MLPF: Efficient machine-learned particle-flow reconstruction using graph neural networks*", Eur. Phys. J. C **81**, 381 (2021), arXiv:2101.08578 [physics.data-an].

[250] M. Vos et al., "*Top physics at high-energy lepton colliders*", (2016), arXiv:1604.08122 [hep-ex].

[251] J. J. Ethier, G. Magni, F. Maltoni, L. Mantani, E. R. Nocera, J. Rojo, E. Slade, E. Vryonidou, and C. Zhang, "*Combined SMEFT interpretation of Higgs, diboson, and top quark data from the LHC*", (2021), arXiv:2105.00006 [hep-ph].

[252] J. Zhou, G. Cui, Z. Zhang, C. Yang, Z. Liu, L. Wang, C. Li, and M. Sun, "*Graph neural networks: A review of methods and applications*", (2018), arXiv:1812.08434 [cs].

[253] Z. Wu, S. Pan, F. Chen, G. Long, C. Zhang, and P. S. Yu, "*A Comprehensive Survey on Graph Neural Networks*", IEEE Transactions on Neural Networks and Learning Systems **32**, 4–24 (2021), arXiv:1901.00596 [cs].

[254] J. Gilmer, S. S. Schoenholz, P. F. Riley, O. Vinyals, and G. E. Dahl, "*Neural message passing for quantum chemistry*", in *International Conference on Machine Learning* (PMLR, 2017), pp. 1263–1272, arXiv:1704.01212 [cs].

[255] Y. Wang, Y. Sun, Z. Liu, S. E. Sarma, M. M. Bronstein, and J. M. Solomon, "*Dynamic graph cnn for learning on point clouds*", Acm Transactions On Graphics (tog) **38**, 1–12 (2019), arXiv:1801.07829 [cs].

[256] F. A. Dreyer and H. Qu, "*Jet tagging in the Lund plane with graph networks*", JHEP **03**, 052 (2021), arXiv:2012.08526 [hep-ph].

[257] M. Abdughani, J. Ren, L. Wu, and J. M. Yang, "*Probing stop pair production at the LHC with graph neural networks*", JHEP **08**, 055 (2019), arXiv:1807.09088 [hep-ph].

[258] J. Duarte and J.-R. Vlimant, "*Graph Neural Networks for Particle Tracking and Reconstruction*", (2020), arXiv:2012.01249 [hep-ph].

[259] X. Ju and B. Nachman, "*Supervised Jet Clustering with Graph Neural Networks for Lorentz Boosted Bosons*", Phys. Rev. **D102**, 075014 (2020), arXiv:2008.06064 [hep-ph].

[260] A. Blance and M. Spannowsky, "*Unsupervised Event Classification with Graphs on Classical and Photonic Quantum Computers*", (2021), arXiv:2103.03897 [hep-ph].

[261] O. Atkinson, A. Bhardwaj, C. Englert, V. S. Ngairangbam, and M. Spannowsky, "*Anomaly detection with Convolutional Graph Neural Networks*", (2021), arXiv:2105.07988 [hep-ph].

[262] H. Qu and L. Gouskos, "*ParticleNet: Jet Tagging via Particle Clouds*", Phys. Rev. D **101**, 056019 (2020), arXiv:1902.08570 [hep-ph].

[263] T. Dorigo, M. Fumanelli, C. Maccani, M. Mojsovska, G. C. Strong, and B. Scarpa, "*RanBox: Anomaly Detection in the Copula Space*", (2021), arXiv:2106.05747 [physics.data-an].

[264] V. Mikuni and F. Canelli, "*ABCNet: An attention-based method for particle tagging*", Eur. Phys. J. Plus **135**, 463 (2020), arXiv:2001.05311 [physics.data-an].

[265] O. Knapp, O. Cerri, G. Dissertori, T. Q. Nguyen, M. Pierini, and J.-R. Vlimant, "*Adversarially Learned Anomaly Detection on CMS Open Data: re-discovering the top quark*", Eur. Phys. J. Plus **136**, 236 (2021), arXiv:2005.01598 [hep-ex].

[266] V. Mikuni and F. Canelli, "*Unsupervised clustering for collider physics*", Phys. Rev. D **103**, 092007 (2021), arXiv:2010.07106 [physics.data-an].

[267] G. Dezoort, S. Thais, I. Ojalvo, P. Elmer, V. Razavimaleki, J. Duarte, M. Atkinson, and M. Neubauer, "*Charged particle tracking via edge-classifying interaction networks*", (2021), arXiv:2103.16701 [hep-ex].

[268] **CMS**, V. Khachatryan et al., "*Measurement of differential cross sections for top quark pair production using the lepton+jets final state in proton-proton collisions at 13 TeV*", Phys. Rev. D **95**, 092001 (2017), arXiv:1610.04191 [hep-ex].

[269] I. Brivio, "*SMEFTsim 3.0 — a practical guide*", JHEP **04**, 073 (2021), arXiv:2012.11343 [hep-ph].

[270] C. Bierlich et al., "*Robust Independent Validation of Experiment and Theory: Rivet version 3*", SciPost Phys. **8**, 026 (2020), arXiv:1912.05451 [hep-ph].

[271] Y. Lecun, L. Bottou, Y. Bengio, and P. Haffner, "*Gradient-based learning applied to document recognition*", Proceedings of the IEEE **86**, 2278–2324 (1998).

[272] M. Wang, D. Zheng, Z. Ye, Q. Gan, M. Li, X. Song, J. Zhou, C. Ma, L. Yu, Y. Gai, T. Xiao, T. He, G. Karypis, J. Li, and Z. Zhang, *Deep Graph Library: A Graph-Centric, Highly-Performant Package for Graph Neural Networks*, 2020, arXiv:1909.01315 [cs.LG].

[273] A. Paszke, S. Gross, F. Massa, A. Lerer, J. Bradbury, G. Chanan, T. Killeen, Z. Lin, N. Gimelshein, L. Antiga, A. Desmaison, A. Köpf, E. Yang, Z. DeVito, M. Raison, A. Tejani, S. Chilamkurthy, B. Steiner, L. Fang, J. Bai, and S. Chintala, *PyTorch: An Imperative Style, High-Performance Deep Learning Library*, 2019, arXiv:1912.01703 [cs.LG].

[274] C. Englert, R. Kogler, H. Schulz, and M. Spannowsky, "*Higgs characterisation in the presence of theoretical uncertainties and invisible decays*", Eur. Phys. J. C **77**, 789 (2017), arXiv:1708.06355 [hep-ph].

[275] H. K. Dreiner, A. Duff, and D. Zeppenfeld, "*How well do we know the three gluon vertex?*", Phys. Lett. B **282**, 441–447 (1992).

[276] L. J. Dixon and Y. Shadmi, "*Testing gluon selfinteractions in three jet events at hadron colliders*", Nucl. Phys. B **423**, [Erratum: Nucl.Phys.B 452, 724–724 (1995)], 3–32 (1994), arXiv:hep-ph/9312363.

[277] R. Kansal, J. Duarte, H. Su, B. Orzari, T. Tomei, M. Pierini, M. Touranakou, J.-R. Vlimant, and D. Gunopulos, "*Particle Cloud Generation with Message Passing Generative Adversarial Networks*", (2021), arXiv:2106.11535 [cs.LG].

[278] M. Bellagente, A. Butter, G. Kasieczka, T. Plehn, and R. Winterhalder, "*How to GAN away Detector Effects*", SciPost Phys. **8**, 070 (2020), arXiv:1912.00477 [hep-ph].

[279] C. Englert, A. Freitas, M. Spira, and P. M. Zerwas, "*Constraining the Intrinsic Structure of Top-Quarks*", Phys. Lett. **B721**, 261–268 (2013), arXiv:1210.2570 [hep-ph].

[280] D. Buarque Franzosi and A. Tonero, "*Top-quark Partial Compositeness beyond the effective field theory paradigm*", JHEP **04**, 040 (2020), arXiv:1908.06996 [hep-ph].

[281] B. R. Holstein, "*Introduction to effective field theory*", Nucl. Phys. **A689**, 135–146 (2001), arXiv:nucl-th/0010015 [nucl-th].

[282] J. S. Schwinger, "*On Quantum electrodynamics and the magnetic moment of the electron*", Phys. Rev. **73**, 416–417 (1948).

[283] J. Jersak, E. Laermann, and P. M. Zerwas, "*Electroweak Production of Heavy Quarks in e+ e- Annihilation*", Phys. Rev. **D25**, [Erratum: Phys. Rev.D36,310(1987)], 1218 (1982).

[284] Q.-H. Cao, B. Yan, J.-H. Yu, and C. Zhang, "*A General Analysis of Wtb anomalous Couplings*", Chin. Phys. **C41**, 063101 (2017), arXiv:1504.03785 [hep-ph].